TENSILE STRENGTH, SHEAR STRENGTH, AND EFFECTIVE
STRESS FOR UNSATURATED SAND

A Dissertation
Presented to
the Faculty of the Graduate School
University of Missouri – Columbia

In Partial Fulfillment
of the Requirements for the Degree

Doctor of Philosophy

By
RAFAEL BALTODANO GOULDING

Dr. William J. Likos, Dissertation Supervisor

MAY 2006

The undersigned, appointed by the Dean of the Graduate School,
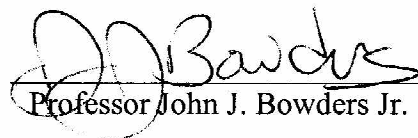have examined the dissertation entitled

TENSILE STRENGTH, SHEAR STRENGTH, AND EFFECTIVE STRESS FOR
UNSATURATED SAND

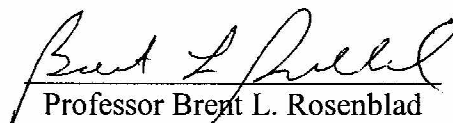Presented by Rafael Baltodano Goulding

A candidate for the degree of Doctor of Philosophy in Civil Engineering
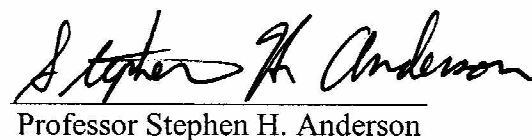
And hereby certify that in their opinion it is worthy of acceptance.

Professor William J. Likos

Professor John J. Bowders Jr.

Professor J. Eric Loehr

Professor Brent L. Rosenblad

Professor Stephen H. Anderson

Abstract

It is generally accepted in geotechnical engineering that non-cohesive materials such as sands exhibit no or negligible tensile strength. However, there is significant evidence that interparticle forces arising from capillary and other pore-scale force mechanisms increase both the shear and tensile strength of soils. The general behavior of these pore-scale forces, their role in macroscopic stress, strength, and deformation behavior, and the changes that occur in the field under natural or imposed changes in water content remain largely uncertain.

The primary objective of this research was to experimentally examine the manifestation of capillary-induced interparticle forces in partially saturated sands to macroscopic shear strength, tensile strength, and deformation behavior. This was accomplished by conducting a large suite of direct shear and direct tension tests using three gradations of Ottawa sand prepared to relatively "loose" and relatively "dense" conditions over a range of degrees saturation. Results were compared with previous experimental results from similar tests, existing theoretical formulations to define effective stress in unsaturated soil, and a hypothesis proposed to define a direct relationship between tensile strength and effective stress.

The major conclusions obtained from this research include: Theoretical models tended to underpredict measured tensile strength. Analysis of results indicates that shear strength may be reasonably predicted using the sum of tensile strength and total normal stress as an equivalent effective stress ($\sigma' = \sigma_t + \sigma_n$). Analysis also indicates that Bishop's (1959) effective stress formulation is a reasonable representation for effective stress by setting $\chi = S$ and by back-calculating χ from shear tests. Tensile strength and apparent cohesion measured exhibited double-peak behavior as a function of degree of saturation. Relatively dense specimen with water contents approaching the capillary regime start behaving as a loose specimen. Horizontal displacement at failure in tension exhibited double-peak behavior as a function of saturation. The two-peak behavior tends to flatten out as the grain size increases.

Keywords: Unsaturated Soils, Effective Stress, Shear Strength, Apparent Cohesion, Tensile Strength

Acknowledgement

I would like to thank my advisor Dr William J. Likos because he always supported me and helped me during the completion of this work, showing real interest in high quality academics. I also want to thank my committee, Dr John Bowders, Dr Erik Loehr, Dr Stephen Anderson, Dr David Hammer, and Dr Brett Rosenblad for all the help and invaluable advice given throughout my coursework, research, qualifiers, and comprehensive examinations, and their review of this work.

I wish to thank Mr. Richard Wells for helping me build all the necessary equipment for this research, and all the staff of Civil and Environmental Engineering Department office for their assistance in my time as TA and RA.

Special thanks to my family who always supported me emotionally during my whole life, but especially during the last five years, especially my grandfather Dr Walter S. Goulding for being such a good life example, and to all of those friends that have been part of my life.

Table of Contents

List of Tables

1   Introduction

1.1 Statement of the Problem

It is generally accepted in geotechnical engineering practice that non-cohesive materials such as sands exhibit only shear strength and no or negligible tensile strength. Cohesive materials such as clays, on the other hand, may exhibit both shear and tensile strength, where, following the conventional Mohr-Coulomb failure criterion, the former is captured as a function of normal stress via the friction angle (ϕ) term and the latter is indirectly captured via the cohesion term (c). For design purposes, it is typically assumed that soils are either fully saturated or completely dry to calculate stress, strength, and deformation parameters and corresponding system response. A variety of problems, however, present situations where water content does not correspond to the saturated state or to dry conditions, including shallow slope stability, lateral earth pressure, fill compaction, and shallow footing design. There is significant evidence that interparticle forces arising from capillary and other pore-scale force mechanisms increase both the shear and tensile strength of soils. However, the general behavior of these pore-scale forces, their role in macroscopic stress, strength, and deformation behavior, and the changes that occur in the field under natural or imposed changes in water content (e.g., from precipitation, evaporation, water table lowering) remain largely uncertain.

The increase in cohesion associated with partial saturation in materials such as sands has been historically referred to as "apparent" cohesion. This is primarily intended to reflect the fact that the cohesive strength may drop to near zero if the soil subsequently becomes saturated. Lu and Likos (2004) noted that apparent cohesion embeds two terms:

classical cohesion c', which represents the mobilization of interparticle physicochemical forces such as van der Waals attraction to shearing resistance, and capillary cohesion c'', which represents the mobilization of capillary interparticle forces to shearing resistance. For clays, both terms are significant over a wide range of saturation. For sands, classical cohesion is generally negligible, while capillary cohesion varies from near zero at saturation and becomes a complex function of degree of saturation or matric suction thereafter. Examining the macroscopic behavior of partially saturated sand over a wide range of saturation allows the role of capillary mechanisms to be more effectively isolated and forms the general motivation and scope of this research.

1.2 Goals and Objectives

The primary objective of this research is to experimentally examine the manifestation of capillary-induced interparticle forces in partially saturated sands to macroscopic shear strength, tensile strength, and deformation behavior. This was accomplished by conducting a large suite of direct shear and direct tension tests using three gradations of Ottawa sand prepared to relatively "loose" and relatively "dense" conditions over a wide range of saturation. Results were compared with previous experimental results from similar tests, existing theoretical models for predicting tensile strength in the pendular, funicular, and capillary water content regimes, existing formulations to define effective stress in unsaturated soil, and a new hypothesis was proposed to describe the relationship between tensile strength and an equivalent effective stress.

1.3 Scope

The specific scope of the work includes the following.

1. A background literature review was conducted to summarize theoretical models developed to predict the tensile strength of granular materials, experimental tensile strength testing approaches, formulations for the state of stress in unsaturated soil, and suction measurement techniques.

2. Test materials were characterized in terms of grain size distribution, specific gravity, compaction behavior, water retention behavior (soil-water characteristic curves), and particle morphology by scanning electron microscope (SEM) imaging (e.g., roundness, smoothness). Test materials include three different gradations of Ottawa sand (F-40, F-55, and F-75), which were selected to represent relatively coarse, medium, and fine sand, respectively.

3. A suite of direct shear tests was conducted for Ottawa sand specimens compacted to relatively loose ($e \sim 0.75$) and relatively dense ($e \sim 0.60$) conditions at water contents ranging through the pendular, funicular, and capillary regimes.

4. A suite of direct tension tests was conducted for Ottawa sand specimens compacted to relatively loose ($e \sim 0.75$) and relatively dense ($e \sim 0.60$) conditions at water contents ranging through the pendular, funicular, and capillary regimes. Tensile deformations prior to failure were also measured.

5. Results from the direct tension testing series were compared with existing theoretical formulations for the tensile strength of partially saturated materials.

6. Results from the direct shear and direct tension tests were analyzed to investigate the behavior of apparent cohesion and tensile strength as functions of grain size,

void ratio, water content, and corresponding matric suction. Results were
compared with similar shear and tensile strength results reported by Kim (2001)
for Ottawa sand at relatively low applied normal stresses. Combined results were
interpreted in light of existing formulations for the state of stress in unsaturated
soil, including Bishop's (1969) effective stress formulism, the Khalili and
Khabbaz (1998) empirical formulism. Results were also analyzed to test a
hypothesis that tensile strength measured from direct tension tests may be treated
as an equivalent effective stress resulting from capillary interparticle forces.

7. Specimen deformations obtained during direct shear and direct tension testing
    were considered to examine stress-strain and critical state behavior and compared
    with results for saturated soils.

1.4 Organization of Thesis

This work includes six chapters including the introduction chapter and three
appendices. Chapter two contains a theoretical background where two main concepts are
presented. First, soil suction, its components and measurement techniques are discussed.
An overview of the soil water characteristic curve, capillary phenomena, and suction
stress is also addressed in that section. Second, a theoretical tensile strength overview is
presented, where tensile strength prediction models, measurement techniques, and
previous tension and shear tests in sands are described.

Chapter three explains the materials and methods used to develop this research.
This chapter includes soil properties, and soil water characteristic curves determined for
the soils tested in this work as well as measurement methods and models used. In
addition, present in Chapter three are the apparatuses description, experimental program,

procedure, and data reduction for the direct shear and tensile strength testing. The results for this testing program are shown in Chapter four.

In Chapter five the discussion and analysis of the results is presented. Tensile strength models predictions are compared to the results obtained. The relationship between tensile strength and shear strength at low and high normal stresses is discussed. In addition a double-peak behavior observed in the results, the failure surfaces, and stress-deformation behavior of the soils are addressed. The stress-deformation behavior includes analysis of the shear stress-horizontal displacement, volumetric strain, critical state line, and tensile deformations. Chapter six summarizes the conclusions and recommendations derived from this work. References cited, and appendices including additional direct shear, tensile strength results, and a proposed suction-controlled tension test device follow chapter six.

2 Background

2.1 Soil Suction

2.1.1 Components of soil suction

The concept of soil suction was developed by the soil physics field in the early 1900's. This theory was developed mainly in relation to the soil-water-plant system. Its importance in the mechanical behavior of unsaturated soils applicable to engineering problems was introduced at the Road Research Laboratory in England (Fredlund and Rahardjo, 1993).

Soil suction can be defined conceptually as the ability for an unsaturated soil to attract or retain water in terms of pressure. If gravity, temperature, and inertial effects are neglected, mechanisms responsible for this attraction are capillarity, short-range hydration mechanisms, and osmotic mechanisms. Hydration and osmotic mechanisms can occur in either a saturated or an unsaturated soil. The capillary mechanism is unique of unsaturated soil.

Short-range absorptive effects arise primarily from electrical and van der Waals force fields near the solid-liquid interface, i.e. the soil-pore ware interface. Hydration mechanisms are a function of both the surface area and charge properties of the solid, and thus are particularly important for fine-grained soils. Osmotic effects are produced by dissolved solutes in the pore water, which may be present as externally introduced solutes or naturally occurring solutes adsorbed by the soil mineral surfaces. Capillary effects

include curvature of the air-water interface and negative pore water pressure in the three-phase unsaturated soil system.

Total soil suction quantifies the thermodynamic potential of soil pore water relative to a reference potential of free water. Free water may be defined as water that does not contain any dissolved solutes and experiences no interactions with other phases that produce curvature in the air-water interface. The free energy of soil water can be measured in terms of its partial vapor pressure. The thermodynamic relationship between soil suction and the partial pressure of the pore-water vapor can be expressed as

$$\psi_t = -\frac{RT}{v_w \omega_v} \ln\left(\frac{\bar{u}_v}{\bar{u}_{vo}}\right) \tag{2.1}$$

where ψ is total suction, R is the universal gas constant, T is absolute temperature, v_{wo} is the specific volume of water, ω_v is the molecular mass of water vapor, $\bar{u}_v$ is the partial pressure of pore-water vapor, and $\bar{u}_{vo}$ is the saturation pressure of water vapor over a flat surface of pure water at the same temperature.

The reduction in pore water potential described by eq. 2.1 represents that contributed by the effects of hydration, dissolved solutes, and capillary mechanisms. Total soil suction is considered to be the algebraic sum of a matric suction component and an osmotic suction component. This may be expressed as $\psi_t = \psi_m + \psi_o$, where ψ_t is the total suction, ψ_o is the osmotic suction, and ψ_m is the matric suction. In pressure terms, matric suction can also be expressed as $(u_a - u_w)$, where u_a is the pore-air pressure, and u_w is the pore-water pressure. Potential reduction produced from the effects of capillarity and short- range adsorption is combined to form the matric component of

total suction. Potential reduction produced from the presence of dissolved solutes forms the osmotic component of total suction. Thus, matric suction originates from physical interaction effect and the osmotic suction originates from chemical interaction effects.

According to Aitchison (1965a) total, matric, and osmotic suction may be qualitatively defined as follows:

"Matric or capillary components of free energy: In suction terms, it is the equivalent suction derived from the measurement of the partial pressure of the water vapor in equilibrium with the soil water, relative to the partial pressure of the water vapor in equilibrium with a solution identical in composition with the soil water.

Osmotic (or solute) components of free water: In suction terms, it is the equivalent suction derived from the measurement of the partial pressure of the water vapor in equilibrium with a solution identical in composition with the soil water, relative to the partial pressure of water vapor in equilibrium with free pure water.

Total suction or free energy of the soil water: In suction terms, it is the equivalent suction derived from the measurement of the partial pressure of the water vapor in equilibrium with a solution identical in composition with the soil water, relative to the partial pressure of water vapor in equilibrium with free pure water."

2.1.2 Measurement of soil suction

Soil suction measurement techniques can be classified as either laboratory or field methods and by the component of suction that is measured, e.g. matric or total suction. Laboratory measurements require undisturbed specimens to account for the sensitivity of suction to soil fabric. Disturbance effects become less critical at higher

values of suction, which are governed primarily by short-range effects that are relatively insensitive to soil fabric. Table 2.1 summarizes common suction measurement techniques and applicable measurement ranges.

Table 2. 1: *Summary of Common Laboratory and Field Techniques for Measuring Soil Suction. (after Lu & Likos, 2004)*

Suction Component Measured	Technique/Sensor	Practical Suction Range (kPa)	Lab/Field
Matric Suction	Tensiometers	0-100	Lab and Field
	Axis Translation	0-1,500	Lab
	Electrical/thermal conductivity sensors	0-400	Lab and Field
	Contact filter paper	0-1,000,000	Lab and Field
Total Suction	Thermocouple psychrometers	100-8,000	Lab and Field
	Chilled-mirror hygrometers	1,000-450,000	Lab
	Resistance/capacitance sensors	0-1,000,000	Lab
	Isopiestic humidity control	10,000-600,000	Lab
	Two-pressure humidity control	10,000-600,000	Lab
	Non-contact filter paper	1,000-500,000	Lab and Field

2.1.3 Soil Water Characteristic Curve

The soil water characteristic curve (SWCC) or water retention curve (WRC) describes the relationship between soil suction and soil water content. This curve describes the thermodynamic potential of the soil pore water related to free water as a function of the water that is absorbed by the system. At relatively low water contents or degrees of saturation, the pore water potential is significantly reduced relative to free

water, thus producing relatively high soil suction. At relatively high water contents, the

difference between the pore water potential and the potential of free water decreases, thus

the soil suction is low. When the potential of pore water is equal to the potential of free

water, the soil suction is equal to zero. This happens when the degree of saturation is

close to 100%. Figure 2.1 shows typical SWCCs for sand, silt, and clay. In general, for a

given water content, soil suction is inversely proportional to particle size. Fine-grained

materials are capable of sustaining significant suction over a wide range of water content.
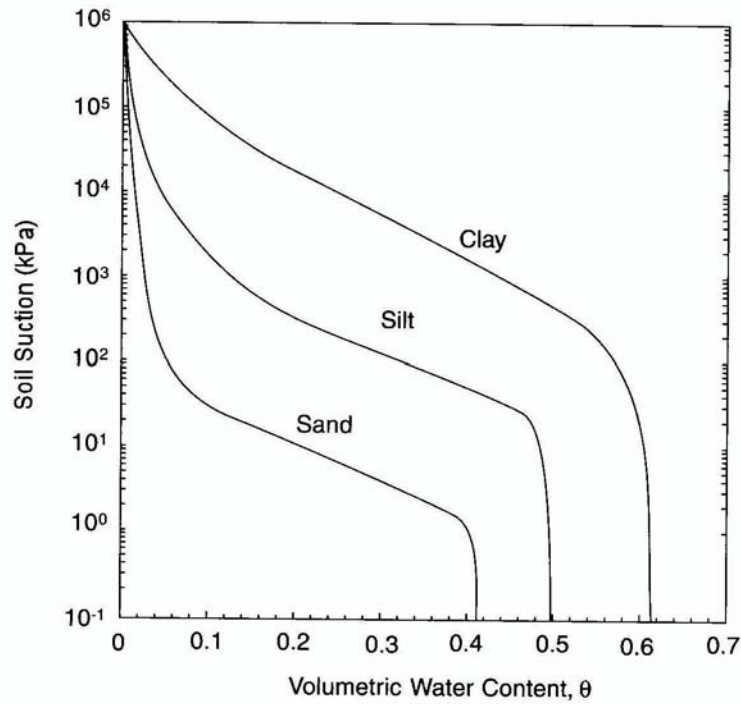
Figure 2. 1: *Typical soil-water characteristic curves for sand, silt, and clay (Lu and Likos, 2004).*

2.1.4 Capillary Phenomena

Capillary phenomena are associated with the matric component of total suction.

Figure 2.2, for example, shows mechanical equilibrium for capillary rise in a small

diameter tube. The vertical resultant of the surface tension is responsible for holding the

weight of the water column to a critical height h_c. From vertical force equilibrium arises the expression

$$2\pi r T_s \cos\alpha = \pi r^2 h_c \rho_w g \tag{2.2}$$

where r is the radius of the capillary tube, T_s is the surface tension of water, α is the solid-liquid contact angle, h_c is the height of capillary rise, and g is gravitational acceleration. If this expression is rearranged, an expression for the ultimate height of capillary rise is

$$h_c = \frac{2T_s}{\rho_w g r} \tag{2.3}$$

which indicates the capillary rise is inversely proportional to the radius of the capillary tube. The water in the capillary tube experiences a pressure deficit with respect to the air pressure with a suction head h_c at the air water interface, or a matric suction $(u_a - u_w) = h_c \gamma_w$, where γ_w is the unit weight of water.

For more complex interface geometries (e.g., in menisci between soil particles), a double-curvature or "toroidal" model may be used to describe the curvature of the air-water interface. An expression that relates matric suction and the interface geometry is

$$u_a - u_w = T_s \left(\frac{1}{R_1} + \frac{1}{R_2} \right) \tag{2.4}$$

where R_1 and R_2 are two principal radii of curvature of the air-water interface. For particles with a water bridge between them, the pressure deficit described by the above equation and surface tension at the air-water interface produces a net force that acts to pull the particles together, thus increasing the normal contact force between them. For bulk systems of unsaturated particles, this force increases the frictional component of

shear strength and produces bulk tensile strength. The magnitude of the interparticle force

is a complex function of water content, matric suction, and the particle and pore size

properties. The corresponding stress may be referred to as suction stress.

T_s: Surface Tension
d: Diameter
h_c: Capillary rise
U_a: Water pressure
α: Contact angle
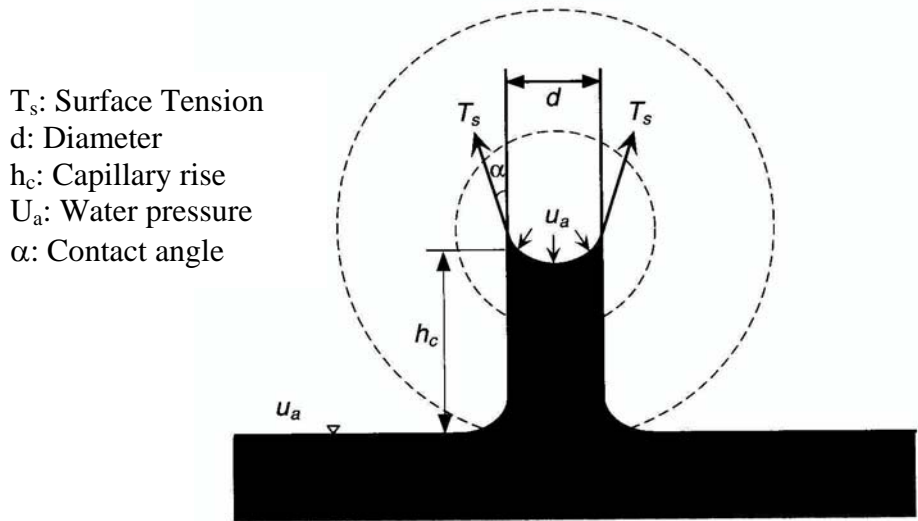
Figure 2. 2: *Mechanical equilibrium for capillary rise in small diameter tube. Lu & Likos (2004)*

2.1.5   Suction Stress

Effective stress in unsaturated soil includes macroscopic stresses such as total

stress, pore air pressure, and pore-water pressure, as well as components resulting from

microscopic interparticle forces such as physicochemical and capillary forces. In

unsaturated soil, it is necessary to distinguish between these mechanisms because pore

pressure as a macroscopic stress disintegrates into several microscopic interparticle forces

acting near the grain contacts, including surface tension forces and interparticle forces

produced by negative pore water pressure.

Suction stress may be defined as the net interparticle stress generated from

capillary mechanisms in a bulk matrix of unsaturated granular particles. This force is due

to the combined effect of negative pore water pressure and the surface tension of water acting at air-water interfaces within menisci. From the macroscopic point of view, suction stress tends to pull the soil particles toward one another, which has a similar effect as overburden stress or surcharge loading. Lu and Likos (2004), for example, described a microscopic approach that may be used to evaluate the magnitude of suction stress for idealized two-particle systems in the pendular (isolated water bridge) regime of saturation. This approach considers the microscale forces acting between ideal spheres. Interparticle forces are produced by the presence of the air-water-solid interface defining the pore water menisci among the soil grains. Figure 2.3 shows the approach used to analyze the magnitude of capillary force arising from the liquid bridge by considering the local geometry of the air-water-solid interface.
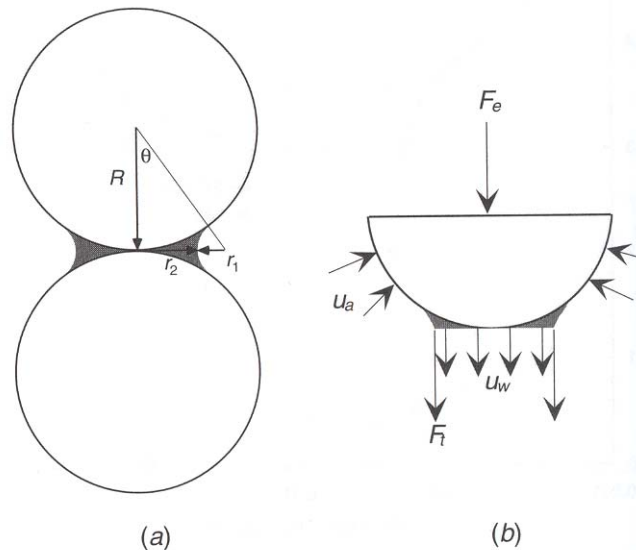
Figure 2. 3: *Air-water-solid interaction for two spherical particles and water meniscus.*
Lu & Likos (2004)

The free body diagram shown on the right side of Figure 2.3 includes the contribution from pore air pressure, pore water pressure, surface tension, and applied

external force. The resultant capillary force between the particles is the sum of all forces

and can be expressed as

$$F_{sum} = F_a + F_t + F_w \tag{2.5}$$

where F_a, F_t, and F_w are interparticle forces resulting from air pressure, surface tension,

and water pressure, respectively, The total force due to the air pressure is

$$F_a = u_a \left(\pi R^2 - \pi r_2^2 \right) \tag{2.6}$$

where u_a is the air pressure, R is the radius of a particle, and r_2 is a radius describing the

meniscus geometry (Figure 2.3). The total force due to surface tension is

$$F_t = -T_s 2\pi r_2 \tag{2.7}$$

where T_s is the surface tension of water. The total force due to water pressure acting on

the water-solid interface in the vertical direction is

$$F_w = u_w \pi r_2^2 \tag{2.8}$$

The interparticle stress due to the resultant of these interparticle forces can be

evaluated by considering the area over which it acts (cross-sectional area of one particle).

$$\sigma_w = u_a - \frac{r_2^2}{R^2} \frac{r_2 + r_1}{r_2 - r_1} \left(u_a - u_w \right) \tag{2.9}$$

such that the effective stress σ'under a total stress σ is

$$\sigma' = \sigma - \sigma_w = \sigma - u_a + \frac{r_2^2}{R^2} \frac{r_2 + r_1}{r_2 - r_1} \left(u_a - u_w \right) \tag{2.10}$$

The above analysis for an idealized two-particle system in the pendular saturation

regime illustrates on a very basic level that for positive values of matric suction capillary

interparticle force mechanisms contribute an additional component of effective stress.

The magnitude of this stress is a complex function of matric suction ($u_a - u_w$), particle

size (R), and water content or degree of saturation (e.g., described by the radii r_1 and r_2). Theoretical and experimental investigations to evaluate the magnitude and behavior of the stress component resulting from capillary mechanisms in unsaturated soils over a wide range of water content (e.g., beyond the pendular regime) remains an active area of research.

2.2 Tensile Strength

2.2.1 Tensile Strength Models

As shown on Figure 2.4, there are three general regimes of saturation in soil with negative pore water pressure or suction: the capillary regime, the funicular regime, and the pendular regime. Prior to desaturation, pore water may be under negative pressure within a regime referred to as the capillary regime. When the suction pressure increases, water starts draining from the saturated specimen and air-water interfaces or menisci are produced between and among the soil grains. The suction pressure that first causes air to enter the coarsest pores is known as air-entry pressure. Air-entry pressure depends on the size of the pores, and thus the grain size and grain size distribution of the particle matrix. In general, the finer the grain size, the finer the pore size, and the higher the air entry pressure. A suction increases beyond the air-entry pressure, air continues to break into the soil pores but the water still forms a continuous phase. As indicated on Figure 2.4, the pore water resides as menisci or "liquid bridges" between soil particles or groups of soil particles, but may concurrently reside within saturated pores at other locations. This regime is known as the funicular regime. Because the liquid water phase

remains continuous, any local change in water pressure is rapidly homogenized throughout the soil. Finally, the pendular regime, which corresponds to relatively high suction pressures, describes a regime where water exists primarily as liquid bridges between and among particles and as thin films of water around the particles. The border point between the funicular and the pendular regimes is known generally as residual saturation. After this point, a very large suction change is required to remove additional water from the soil.

Pendular	Funicular	Capillary
(a)	(b)	(c)
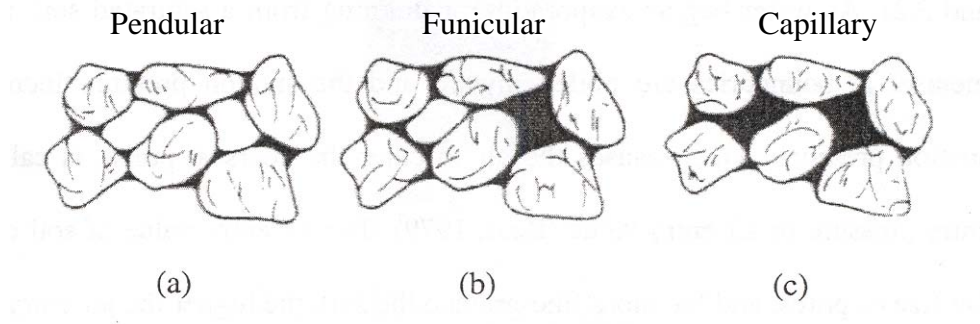
Figure 2. 4: *States of Saturation in Unsaturated Soils (after Kim, 2001)*

Capillary forces associated with these saturation regimes contribute to tensile strength and shear strength. Capillary forces in the pendular regime result from a surface tension force that acts along the water-solid contact line and the net force due to the pressure deficit in the water bridge with respect to the pore air pressure. In the funicular regime, water bridges and pores filled with water are both present, which means that both capillary forces due to the water bridges, and capillary forces due to regions filled with water, contribute to the total bonding force. Within the capillary regime, negative pore water pressure acts isotropically and contributes directly to total stress. The net tensile force in each of these regimes contributes to macroscopic tensile strength. The net tensile

force also contributes to shear strength by increasing the normal forces among the soil particles, and thus the frictional resistance of the bulk system.

Numerous expressions have been developed in the literature to predict tensile strength for idealized two-particle systems and for bulk particle systems within the pendular regime (e.g., Fisher, 1926; Dallavalle, 1943; Orr et al., 1975; Dobbs and Yeomans, 1982; Lian et al., 1993; Molencamp and Nazami, 2003; Likos and Lu, 2004). Recent studies (e.g., Molencamp and Nazami, 2003; Lechman and Lu, 2005) show that most of the theories predict both water retention and capillary stress reasonably well. Considering the simple two-particle system shown in Figure 2.5, for example, tensile stress between two identical contacting spherical particles due to a water bridge in the pendular regime can be conveniently expressed as (Lu and Likos, 2004):

$$\sigma_t = \frac{r_2}{R^2}\frac{r_1 + r_2}{r_1}T_s \tag{2.11}$$

where R is the particle radius, T_s is the surface tension of water (~72 mN/m), and r_1 and r_2 are radii describing the geometry of the water bridge. The radii r_1 and r_2 may be expressed in terms of the particle radius R, "filling" angle θ, and the solid-water contact angle α as:

$$r_1 = R\frac{1 - \cos\theta}{\cos(\theta + \alpha)} \tag{2.12}$$

$$r_2 = R\tan\theta - r_1\left(1 - \frac{\sin\alpha}{\cos\theta}\right) \tag{2.13}$$

The filling angle θ captures the general size of the meniscus and corresponding water content or degree of saturation for the system. The contact angle α is a material property dependent on the pore water properties, soil surface properties, and direction of

wetting. This angle, designated herein as α, defines the angle measured inside the liquid phase from the solid surface to a point tangent to the liquid-air interface. Contact angles less than 90° indicate a wetting, or hydrophilic, solid-liquid interaction. Contact angles greater than 90° indicate a non-wetting, or hydrophobic, solid-liquid interaction. Experimental studies based on capillary rise or horizontal infiltration testing have shown that wetting contact angles in sands can be as high as 60° to 80° (*e.g*., Letey et al., 1962; Kumar and Malik, 1990). Drying contact angles, on the other hand, have been estimated from 0° to as much as 20° to 30° smaller than the wetting angles (e.g., Laroussi and DeBacker, 1979).

$\angle EBC = \pi/2 - \theta - \alpha$
$\angle ECB = \pi/2 + \theta$
$\angle CEB = \alpha$
$\angle ECD = \pi/2 - \theta$
$\angle EFD = \theta + \alpha$
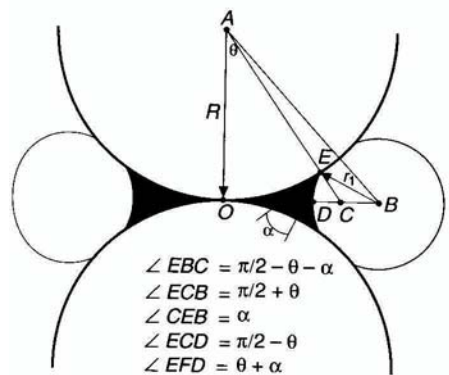
Figure 2. 5: *Meniscus geometry for calculating tensile forces between contacting mono-sized particles with a non-zero contact angle (Lu and Likos, 2004)*

Models to predict the tensile strength of unsaturated particle agglomerates have been developed by Rumpf (1961) and Schubert (1984). The Rumpf model is applicable for predicting tensile strength in the pendular regime. The Schubert model combines two terms to be applicable over the capillary regime and the funicular regime. Rumpf (1961) proposed a theory for non-contacting spherical particles that may be upscaled to predict

the tensile strength of unsaturated particle systems in the pendular regime. Figure 2.6 shows a non-contacting particle system for particles with diameter d, separation distance a, filling angle θ, and contact angle α.
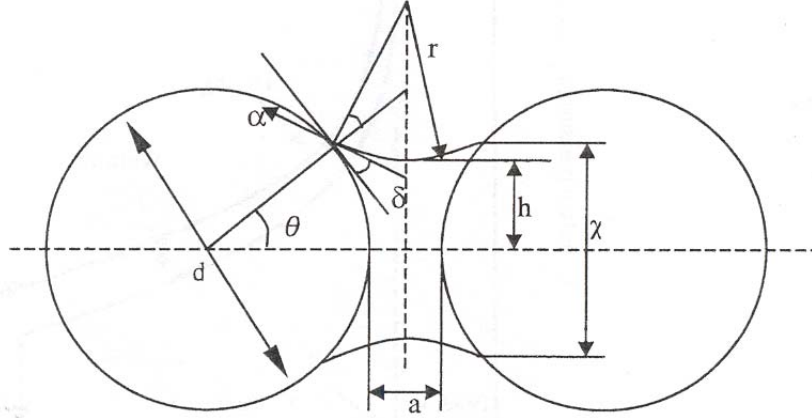
Figure 2. 6: *Meniscus geometry for calculating tensile forces between non-contacting mono-sized particles with a non-zero contact angle (Kim, 2001)*

The model assumes that all the particles are spheres with the same size and distributed uniformly. The model also assumes that the bonds are statistically distributed along the surface and in all directions. Thus, the effective bonding forces are distributed in a way that allows a mean value to be used for calculations of macroscopic tensile strength as follows:

$$\sigma_{tp} = \frac{(1-n)}{n}\frac{F_t}{d^2} = \frac{(1-n)}{n}\frac{\pi T_s}{d}\sin\theta\left[\sin(\theta+\alpha)+\frac{\sin\theta}{4}\left(\frac{1}{r^*}-\frac{1}{h^*}\right)\right] \qquad (2.14)$$

where r^* and h^* are dimensionless radii of curvature describing the water bridge, F_t is the total dimensionless bonding force (between two particles), θ is the filling angle, T_s and α are the surface tension and contact angle respectively, d is the diameter of the

particles, and n is bulk porosity. Expressions used to calculate the two radii of curvature are

$$h^* = \frac{h}{d} = \frac{\sin\theta}{2} + \frac{r}{d}\left[\sin(\theta+\alpha)-1\right] \tag{2.15}$$

and

$$r^* = \frac{r}{d} = \frac{(1-\cos\theta)+\dfrac{a}{d}}{2\cos(\theta+\alpha)} \tag{2.16}$$

where a/d is a dimensionless particle separation distance. Filling angle θ may be related to gravimetric water content for the bulk system w and the specific gravity G_s of the soil phase as (Pietsch and Rumpf, 1967):

$$
\begin{aligned}
w = \frac{6k}{G_s}\frac{V_{bridge}}{2\pi d^3} &= \frac{6k}{G_s}\{\left[r^{*2}+(r^*+h^*)^2\right]r^*\cos(\theta+\alpha)-\frac{r^{*3}\cos^3(\theta+\alpha)}{3} \\
&-r^{*2}(r^*+h^*)\left[\cos(\theta+\alpha)\sin(\theta+\alpha)\left(\frac{\pi}{2}-\theta-\alpha\right)\right]-\frac{1}{24}(2+\cos\theta)(1-\cos\theta)^2\}
\end{aligned}
\tag{2.17}
$$

where k is the mean number of particle-particle contact points per particle (coordination number). A corresponding degree of saturation S may also be written in terms of water content if the void ratio e and specific gravity G_s are known:

$$S = \frac{wG_s}{e} \tag{2.18}$$

The validity of the above expressions is constrained for degrees of saturation within the pendular regime. For evenly-sized particles oriented in simple cubic (SC) packing order (Figure 2.7), where $k = 6$, $n = 47.6\%$, and $e = 0.91$, the water content filling angle is limited to 45°. For particles in tetrahedral (TH) packing order ($k = 12$, $n = 26.0\%$, $e = 0.34$), the water content filling angle is limited to 30°. The corresponding upper limit

of gravimetric water content for SC packing is 0.063 g/g and the upper limit for TH

packing is 0.032 g/g.
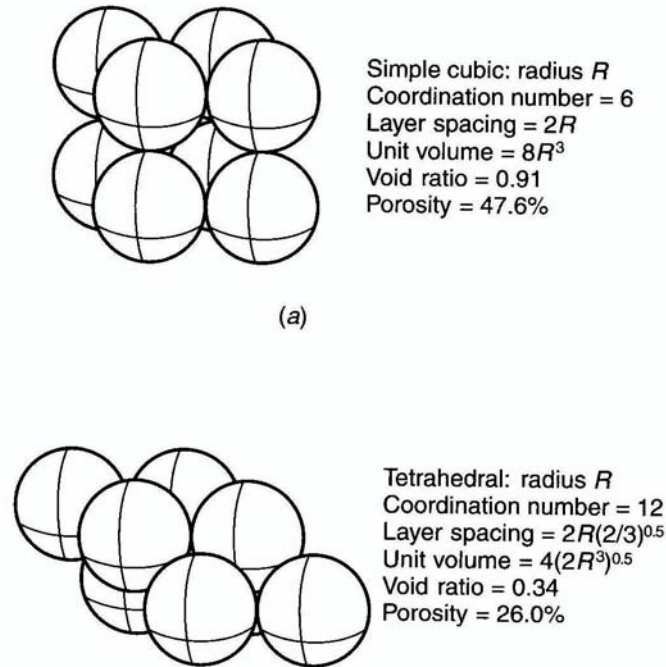
Figure 2. 7: *Uniform spheres in simple cubic (a) and tetrahedral (b) packing order.*

As implied in equation 2.14, tensile strength is inversely proportional to the size

of the particles. Contact angle, porosity, and particle separation distance also play central

roles. The dependency of tensile strength on particle size, porosity contact angle,

separation distance, and degree of saturation is illustrated in Figures 2.8 through 2.12.

Spherical particle systems arranged in SC and TH packing order are considered to

illustratively examine two extreme cases in porosity.

Figure 2.8 shows the effect of dimensionless separation distance for particles in

TH packing with contact angle $\alpha = 0°$, $G_s = 2.65$, and $T_s = 72$ mN/m. The results indicate

that tensile stress decreases as particle separation increases.
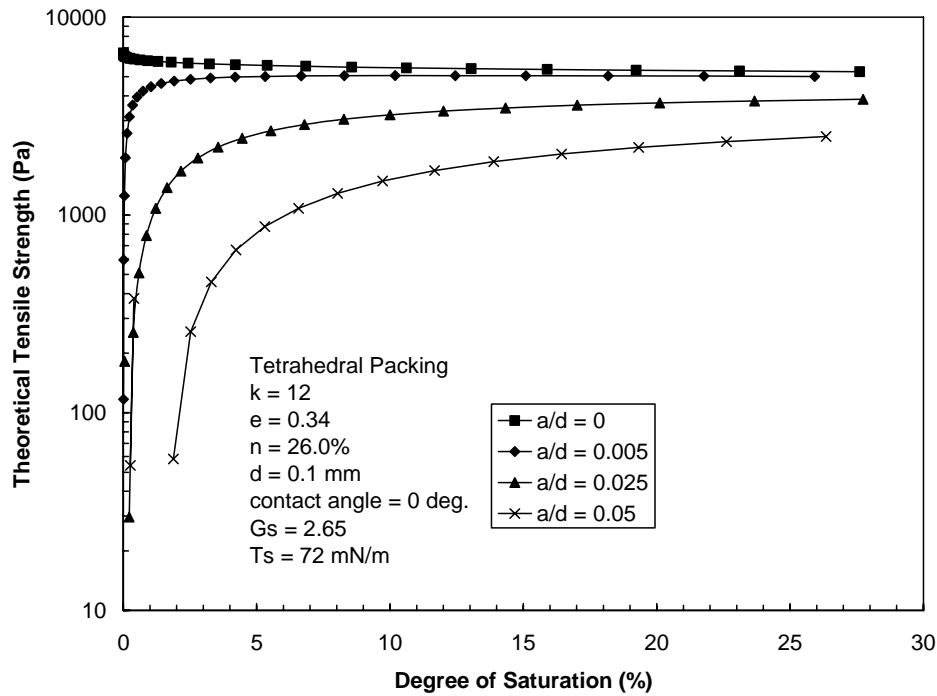
Figure 2. 8: *Theoretical tensile strength for spherical particles in TH packing order as a function of particle separation distance.*

Figures 2.9 and 2.10 show the effects of particle size ranging from $d = 0.01$ mm (*e.g.*, silt or fine sand) to $d = 1$ mm (*e.g.*, medium to coarse sand) for particles in SC and TH packing, respectively. The results illustrate that tensile strength in sand-sized particles can vary from tens of Pa for coarse sand to several kPa for fine sand. Tensile strength for silts may be on the order of several tens of kPa. Figure 2.11 illustrates the effect of packing geometry (porosity) by directly comparing tensile strength for 0.1-mm diameter particles in SC and TH packing. These results illustrate the important effect of packing density on tensile strength, which may be significantly greater for densely packed systems.
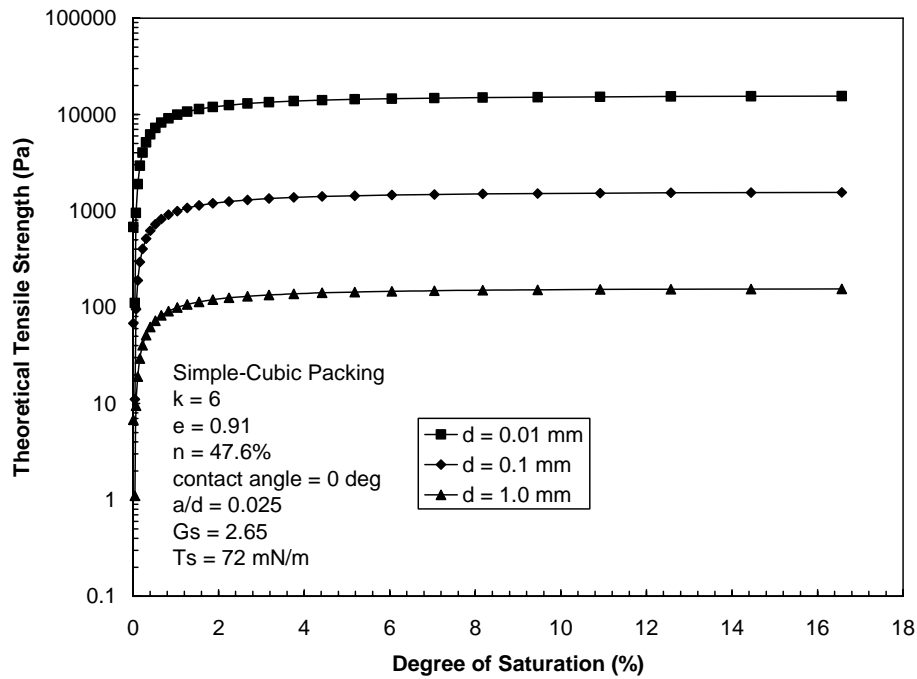
Figure 2. 9: *Theoretical tensile strength for spherical particles in SC packing order as a function of particle size.*
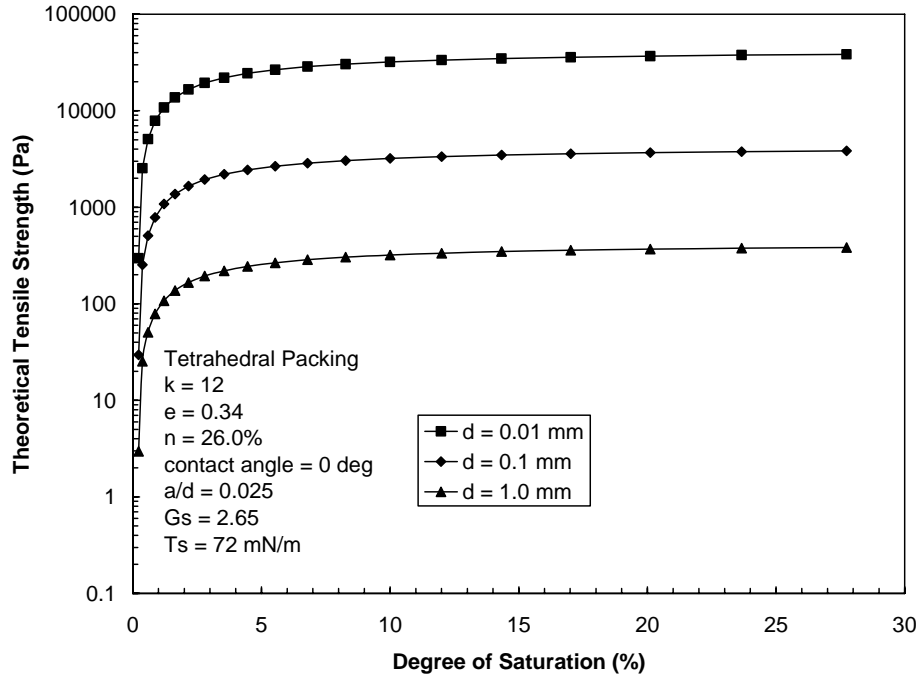
Figure 2. 10: *Theoretical tensile strength for spherical particles in TH packing order as a function of particle size.*
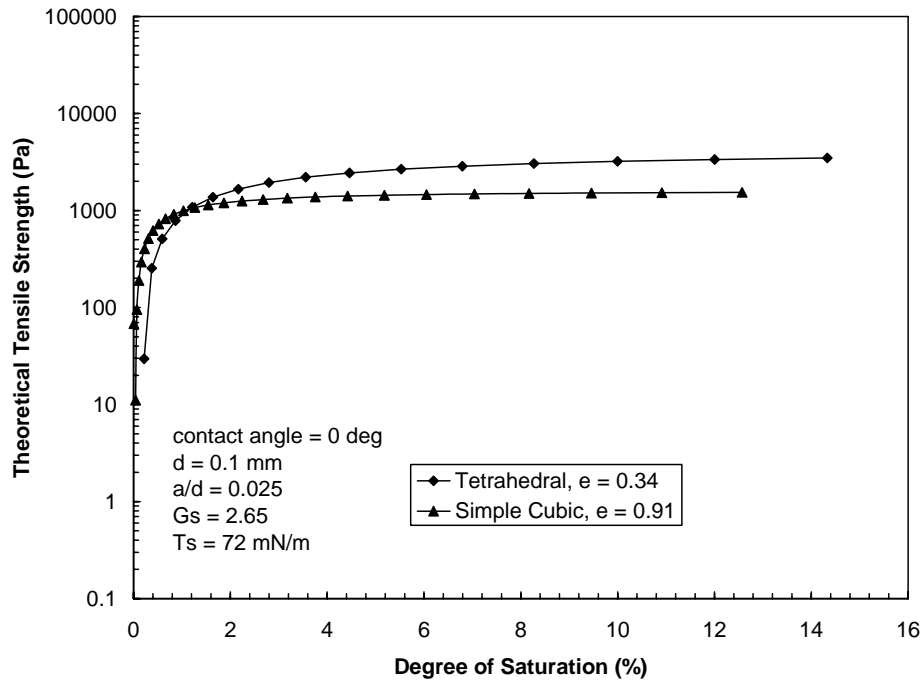
Figure 2. 11: *Theoretical tensile strength for 0.1 mm spherical particles in SC and TH packing order.*

Finally, Figure 2.12 isolates the effect of contact angle α for 0.1-mm diameter particles in SC packing order. Here, relatively small contact angles are representative of a drying process, while relatively large contact angles are representative of a wetting process. The results suggest that tensile strength during wetting may be appreciably less than that during drying.
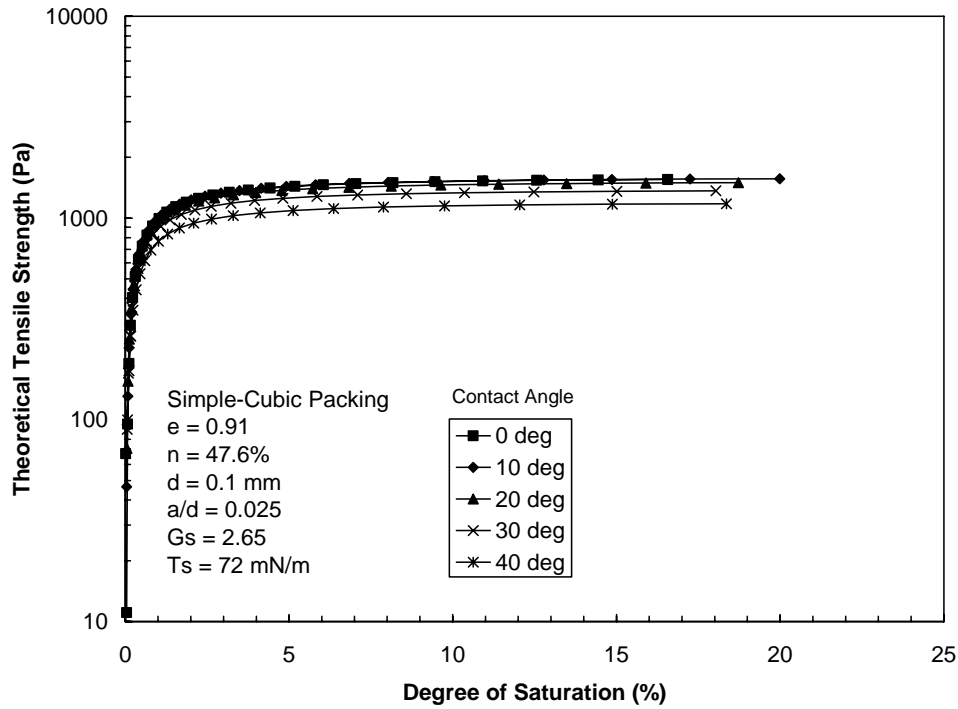
Figure 2. 12: *Theoretical tensile strength for 0.1 mm spherical particles in SC packing order as a function of contact angle.*

The preceding analyses are applicable for predicting tensile strength at relatively low water contents or degrees of saturation in the pendular regime. Schubert (1984) proposed a model for tensile strength in the capillary regime (saturated under negative pore water pressure) as follows:

$$\sigma_{tc} = S * P_c \tag{2.19}$$

where S is the degree of saturation and P_c is the capillary pressure (matric suction), which may be determined directly from the SWCC or estimated as (Shubert, 1984):

$$P_c = a' \frac{1-n}{n} \frac{T_s}{d} \tag{2.20}$$

where a' is a constant that changes with particle size. For particles with a narrow size range, $a' = 6{\sim}8$ and for particles with a wider particle size range, $a' = 1.9{\sim}14.5$. Note that

for a degree of saturation equal to 1.0 (*i.e.*, prior to air-entry), the predicted tensile strength is equal to the matric suction, which reflects the fact the pore pressure acts isotropically as long as the system remains saturated.

Schubert (1984) also proposed a model for predicting tensile strength (σ_{tf}) in the funicular state (concurrent liquid bridges and saturated pores) by combining the previous expression for tensile strength in the pendular regime (eq. 2.14) with the above expression for tensile strength in the capillary regime (eq. 2.19) as follows:

$$\sigma_{tf} = \sigma_{tp} \frac{S_c - S}{S_c - S_f} + \sigma_{tc} \frac{S - S_f}{S_c - S_f} \tag{2.21}$$

where S is degree of saturation, and σ_{tp} and σ_{tc} are tensile strength for the pendular and capillary regimes, respectively. Each term is normalized by establishing saturation boundaries between the capillary, funicular, and pendular states such that S_c and S_f are the upper saturation limits for the funicular and pendular states, respectively. These boundaries may be inferred from the general shape of the SWCC for degrees of saturation near the air-entry pressure and residual water content.

Figure 2.13 illustrates the general form of eq. (2.21) for a typical sand specimen. The SWCC (Fig. 2.13a) has been modeled using the van Genuchten (1980) model (Section 3.2.2) and the modeling parameters shown. The corresponding tensile strength is shown as a function of S as Figure 2.13b and has been differentiated into strength attributable to the pendular regime term and strength attributable to the capillary regime term. These terms reach peak values near the residual water content and air-entry pressure, respectively. The peak tensile strength in the capillary regime is approximately

the air-entry pressure. The shape of the tensile strength function in the pendular regime depends primarily on the pore size distribution of the soil.
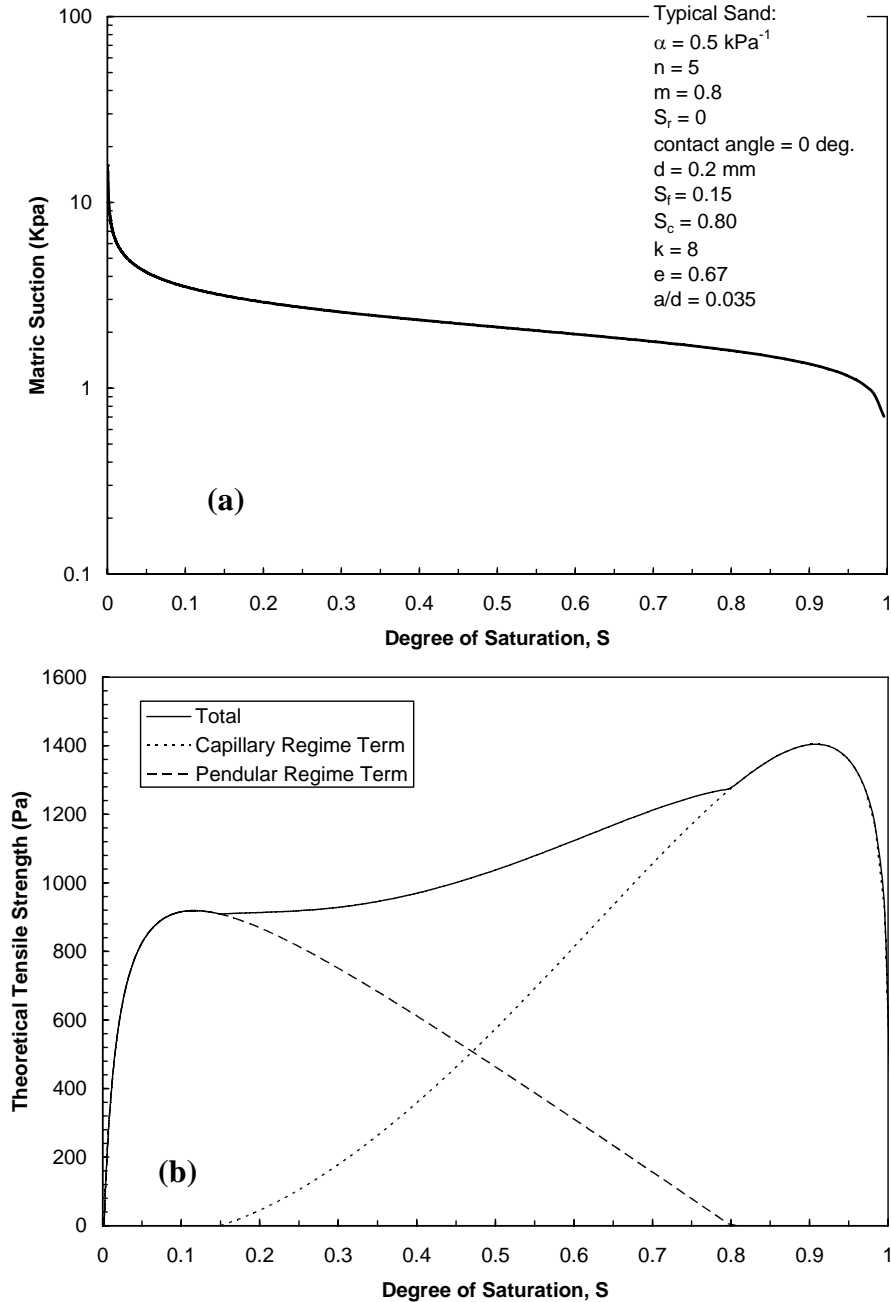
Figure 2. 13: *Suction (a) and theoretical tensile strength (b) as a function of saturation for a typical sand specimen.*

2.2.2   Review of Tensile Strength Testing Techniques

Unconfined tension tests on soft clayey silt were performed by Conlon (1966). The specimen used for these tests was similar to the one used in conventional triaxial devices with the exception of the central part of the specimen. Figure 2.14a shows how the central part of the specimen was necked down to create a failure zone and reduce the necking effects. In order to hold the specimen and be able to apply pure tension to the soil, split rings were clamped at the ends of the specimen and the loading head. The inside of the split rings had a fine emery paper to grip the soil. To avoid eccentricities during application force, a ball and socket arrangement was used at both ends. This apparatus was able to measure maximum tensile strength and axial deformation. Some disadvantages of this device are that the split rings around the specimen may cause stress concentrations at the ends, and since the effective length of the specimen was not accurately known the strain measurements are not reliable.

A similar test to a triaxial extension tests was used by Bishop & Garga (1969) to determine the tensile strength of soils. Confining pressure was used to produce tensile stresses instead of pulling the ends of the specimen. They also used a necked down specimen, thus an increase in confining stress pushed the upper and lower part of the soil apart to create a tension failure in this central portion. To perform these tests, they used a triaxial apparatus as shown in Figure 2.14b, with specimen diameters between 2.54 cm and 1.27 cm at the ends, and 14.24-cm high. The central part was necked to 1.9 cm in diameter. These tests accurately determined the tensile strength of soils, but not the strain measurement because only the necked part can be considered to be in pure tension.

Bofinger (1970) used a prismatic specimen 30.48 cm long with 7.74 cm by 7.74 cm cross section shown in Figure 2.14c. This test showed a concave stress-strain curve as opposed to the convex curve normally seen in compression tests. The ends of the specimen were bonded to steel plates with quick-setting polyester. Tensile force was applied using a cap with a spherical seating to reduce the effect of end rotation. This system had the advantage of reducing the effects of stress concentration at the ends; however it had problems with slippage and strain measurements.
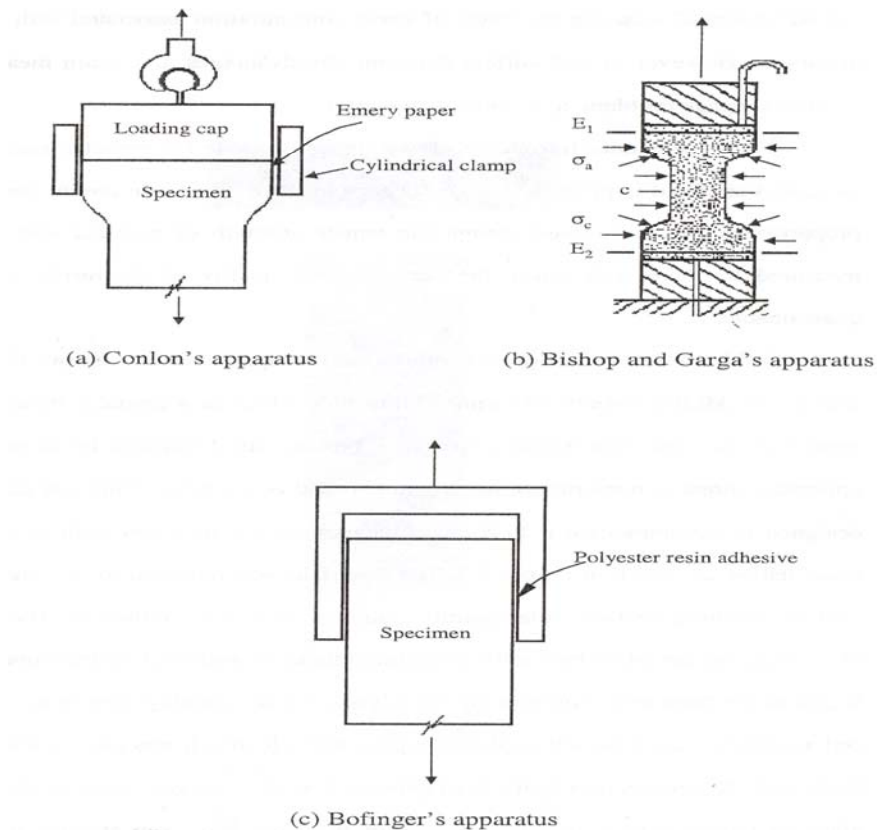
Figure 2. 14: *Tensile Strength Testing Systems (from Kim, 2001)*

Al-Hussaini & Townsend (1974) used a hollow cylinder apparatus to measure the tensile strength of soils (Figure 2.15). The hollow cylinder specimen is placed between two smooth annular platens, where the upper platen has a 4-in inside diameter, a 6-in

outside diameter and 1-in height. The lower platen has a 4-in inside diameter, a 7-in outside diameter and a 1 ¼-in height. The specimen cover has a spherical seating to receive the tip of the ram, which is pinned in a fixed position to prevent upward movement of the upper platen. The hollow cylinder test is based on the principle that when a hydrostatic pressure is applied to the internal surface of the specimen, a tangential tensile stress is generated. When this stress exceeds the tensile strength of the material the specimen fails in tension.
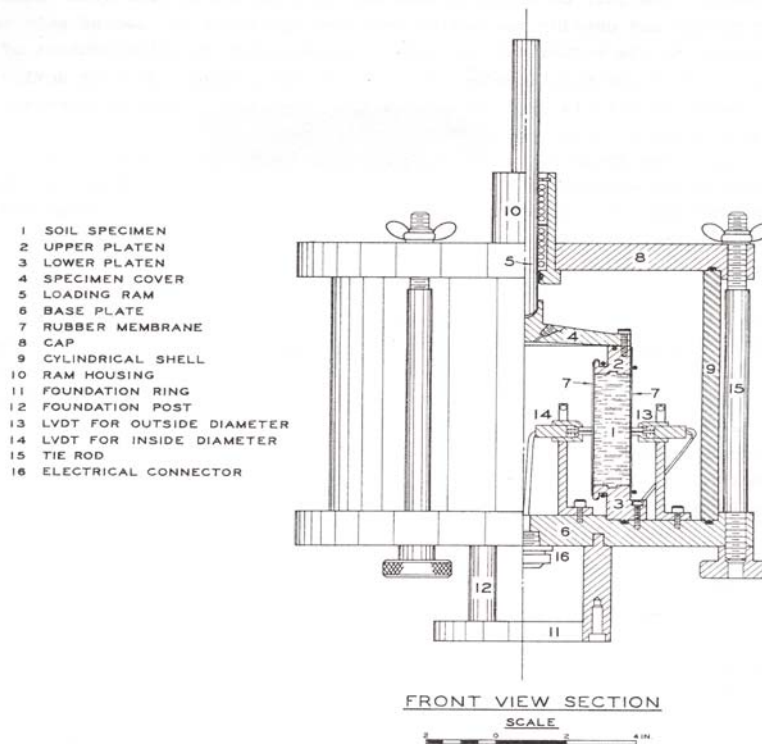
Figure 2. 15: *Hollow cylinder apparatus. Al-Hussaini & Townsend (1974)*

Al-Hussaini & Townsend (1974) mentioned that Carneiro and Barcellos 1953 (Brazil) as well as Akazawa 1953 (Japan) developed an indirect tensile test for concrete (Figure 2.16). This test consists of placing a cylindrical specimen horizontally between two plane loading surfaces in order to apply compression along the diameter. Tensile

strength can be calculated by knowing the imposed load and the geometry of specimens using elasticity theory.
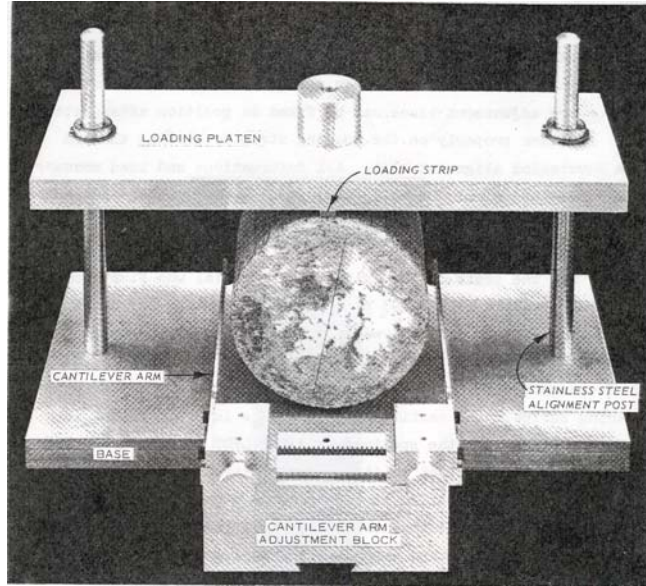
Figure 2. 16: *Indirect Tensile Test Apparatus. Al-Hussaini & Townsend (1974)*

Al-Hussaini and Townsend (1974) also used a double-punch test for determining the tensile strength of soils (Figure 2.17). Calculation of tensile strength is based on the limit analysis derived by Chen and Ducker (1969). The expression that can be used to determine the tensile strength is

$$S_d = \frac{P}{\pi\left(rH - c^2\right)} \tag{2.22}$$

where S_d is tensile strength, P is the applied load, r is the specimen radius, H is the height of the specimen, and c is the radius of the loading disk.
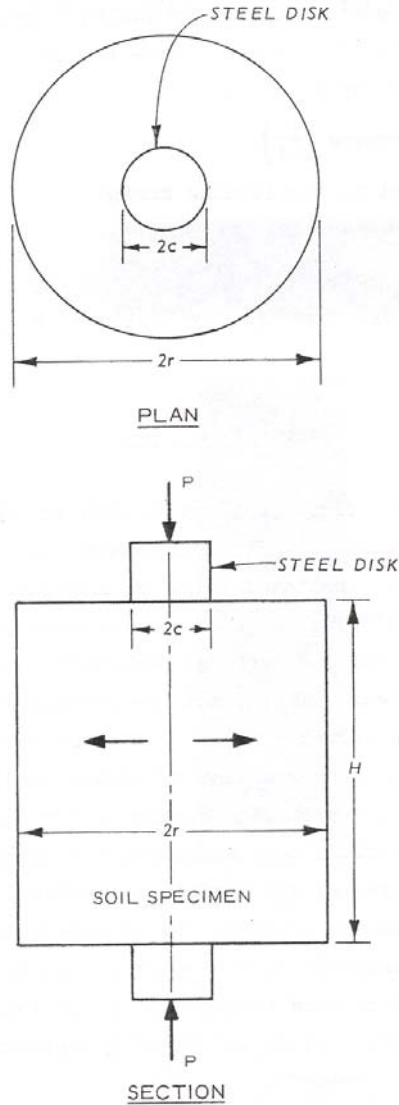
Figure 2. 17: *Schematic diagram of double-punch test. Al-Hussaini & Townsend (1974)*

Mesbah et al. (2004) used a direct-tension test that had problem of anchorage failure. To overcome this problem, the block was sawed along a section at mid-height to create a weak cross section. During load application movement of the ram was measured to provide displacement of the crack. Tang & Graham (2000) used a tensile strength test device for unsaturated soils as shown in Figure 2.18. This device consists of a

conventional motor-driven mechanical load frame for applying either compressive or tensile force to specimens at a constant displacement rate. The mold has two separate half-cylindrical forms that are welded to short lengths of channel and connected to the platen and crosshead of the load frame.
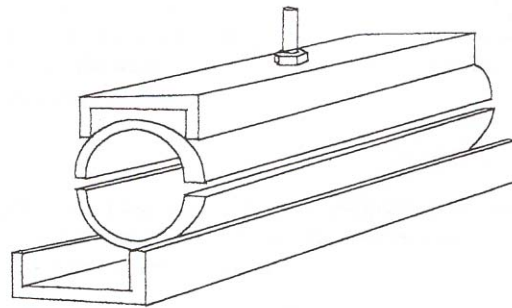
FIG. 1—*Oblique view of tensile mold.*
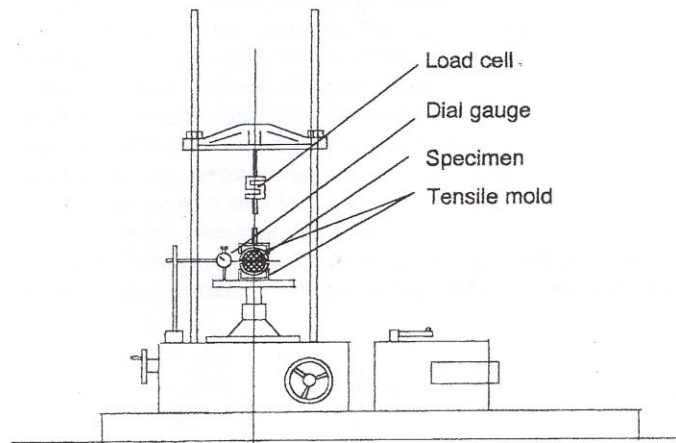
Figure 2. 18: *Side view of tensile mold and load frame. Tang & Graham (2000)*

Munkholm et al. (2002) used a direct tension test that consists of an automatically operated mechanical press. This device is a two-piece cylinder, where the lower half is fixed in a rigid frame by three screws horizontally driven against the cylinder wall. A

plastic cap is put in the upper half of the cylinder and is connected to a pressure transducer by an adjustable steel bar.

Tamrakar et.al. (2005) developed the tensile strength apparatus shown in Figure 2.19. This device consists of a split box comprising fixed and movable halves resting on a horizontal platform. The tensile mold consists of two separate "C" structures which have an inner shape that is almost circular, except at the portion where the two halves join. One part of the apparatus is fixed to the horizontal platform while the other part can move on the horizontal platform. A load cell placed between the movable box and a motor measures the tensile load. The tensile strength is obtained by dividing the tensile load by the area of the tensile crack perpendicular to horizontal pulling.
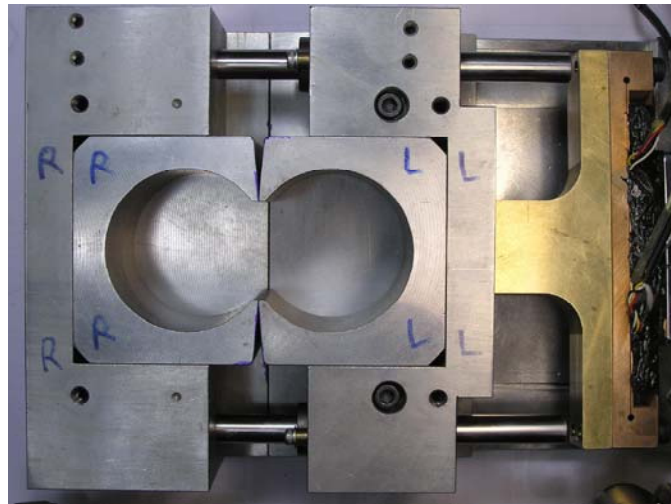
Figure 2. 19: *View of tensile test device. Tamrakar et.al. (2005)*

Perkins (1991) developed the direct tension testing device shown on Figure 2.20. The specimen was a 17.8 cm cubical specimen compacted into a split box. The front half of the box was mounted on a lateral guide rail by 8.89-cm roller bearing blocks placed at

the bottom of the box. The rear part of the box rested on two solid aluminum blocks to align it to the same vertical height as the front part. This device also had a motor and load cell mounted on the base plate. Experimental results were expressed as the average stress on the vertical plane of failure versus the displacement of the box.
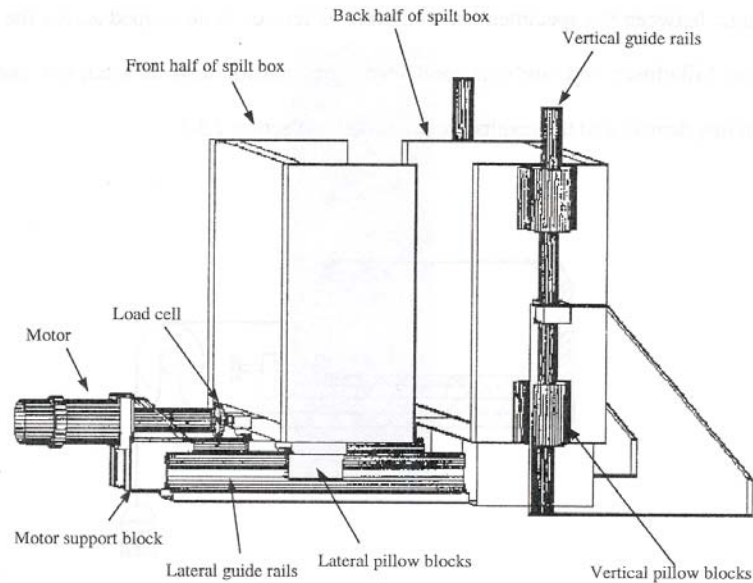
Figure 2. 20: *Direct Tension Apparatus. Perkins (1991)*

Figure 2.21 shows a direct tension device developed by Mikulitsch and Gudehus (1995) that is similar to the one developed by Perkins (1991). The specimen was kept in place by angled walls where one part of the box was fixed and the other part rested on a ball bearing system. The angled internal walls facilitate contact between the specimen and the box to develop tension across the center plane. Tensile forces were imposed by filling a bucket hanging from the movable half of the box with water.
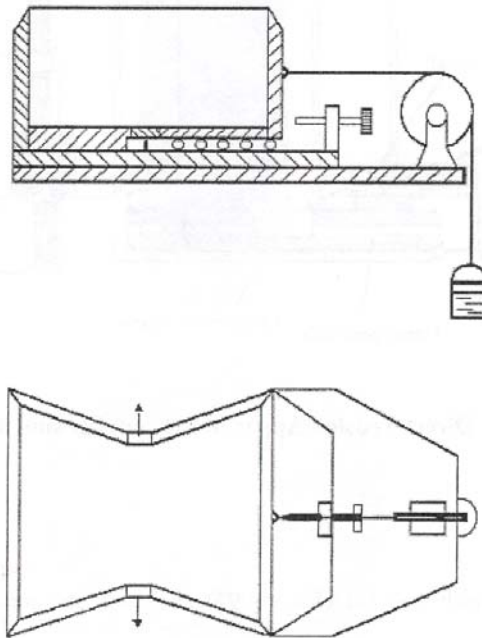
Figure 2. 21: *Device for Tension Tests. Mikulitsch & Gudehus (1995)*

Kim (2001) developed the direct tension apparatus shown as Figure 2.22. The sample container consists of a 17.8-cm by 17.8-cm by 17.8-cm box split in two equal halves. The movable front half is mounted on two sets of precision roller bearings attached to the bottom of the device. The rear half rests on two aluminum blocks to position it at the same height as the front part. Four wedges are attached inside the box to facilitate contact between the specimen and the box as tension is developed across the plane of separation. The wedges were designed with angles (20º) larger than the dilatancy angle of the material to prevent movement of the soil particles, and to achieve a relatively uniform stress distribution on the failure plane. The device rests on a loading table with two pulleys installed to connect loading wires to the movable half of the box. The rear loading container attached to the movable half is used to initially balance the system

against the front loading bucket. Tensile load is applied by introducing water into the front loading container.
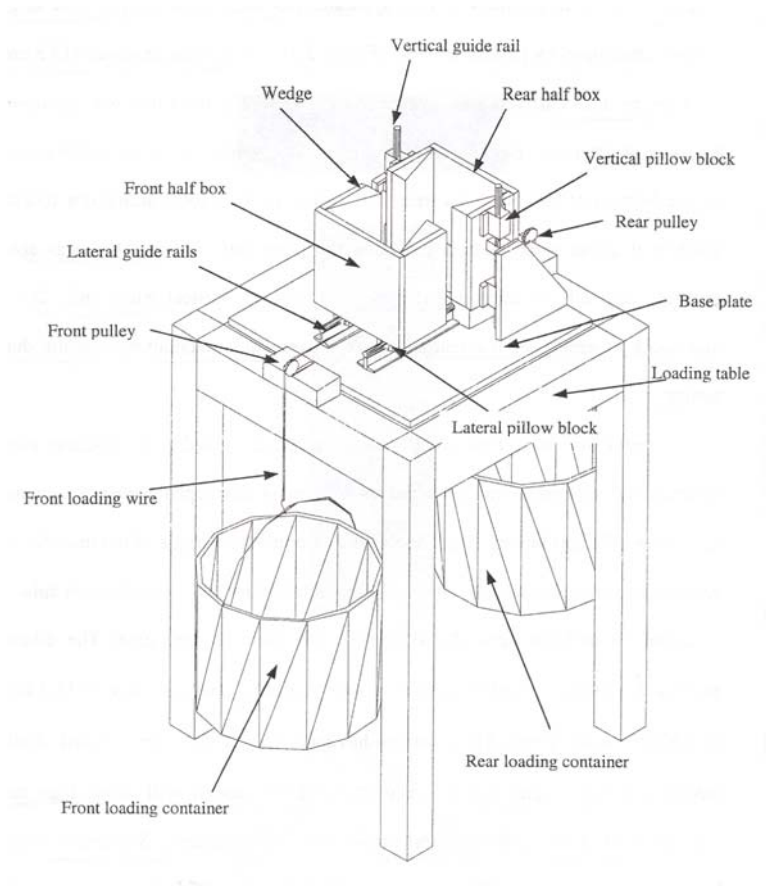
Figure 2. 22: *Direct Tension Apparatus. Kim (2001)*

Lu et.al. (2005) developed a tensile strength apparatus for cohesionless soils shown in Figure 2.23. The apparatus consists of a specimen confining tube (split in the middle), mounting plate, adjustable table for inclining the specimen tube, and a digital probe for measuring inclination angle. The specimen tube has two sections that are clamped together during sample preparation and released prior to testing. One section is fixed on the table, and the other part is free to slide on roller bearings. The table is inclined progressively to increase the gravity force along the longitudinal direction of the

sample, thus applying a tensile force. The inclination angle is recorded when the sample

fails and used to back-calculate tensile strength from the mass of the movable section.
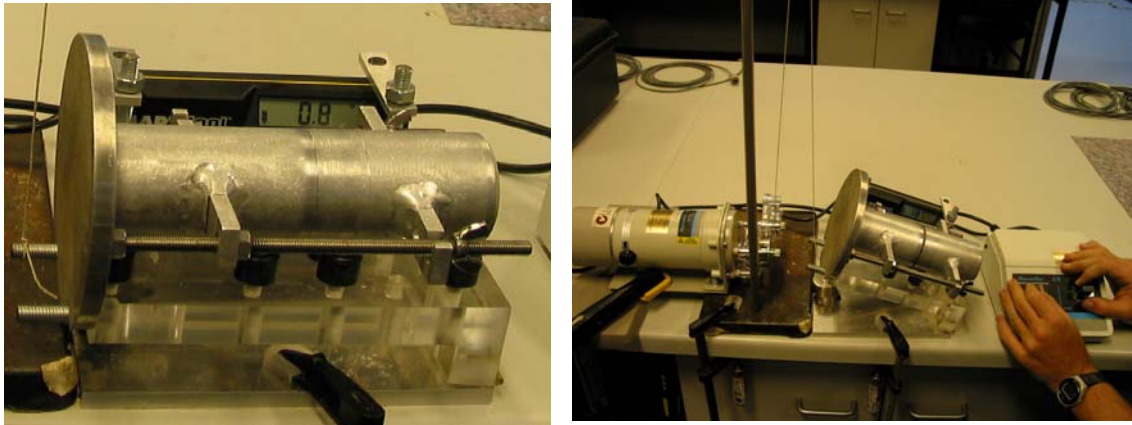
Figure 2. 23: *View of tensile test device. Lu et.al. (2005)*

2.2.3 Review of Tension and Shear Test Results for Sand

Kim (2001) used the direct tension apparatus shown in Figure 2.22 to measure the

tensile strength of clean F-75 gradation Ottawa sand (F-75-C) and F-75 Ottawa sand

containing fines (F-75-F) as a function of water content. Table 2.2 and Figure 2.24

summaries results for F-75-C sand specimens at gravimetric water content ranging from

approximately 0.3% to 4.0% and compacted to relatively loose ($D_r \sim 30$) and relatively

dense ($D_r \sim 70$) conditions (D_r = relative density). Maximum and minimum void ratios

reported were $e_{max} = 0.805$ and $e_{min} = 0.486$. Table 2.3 and Figure 2.25 summarize similar

results reported for F-75 Ottawa Sand containing 2.0% fines (F-75-F).

In general, for water contents between 0.3% and 4.0%, the tensile strength of

moist sands increases with increasing water content, and this trend is more noticeable

with increasing density. Results for sand with the addition of fines showed and increase

in tensile strength. The effects of density and fines on tensile strength are greatly influenced by the water content, and this effect is more pronounced at high water contents. However, at certain water content levels, the tensile strength decreases with increasing water content. These results were interpreted to propose empirical models for predicting tensile strength as a function of water content, relative density, and fines content for F-75 Ottawa sand at relatively low water content levels:

$$\frac{\sigma_t}{P_r \ln(D_r)} = 69 \ln(w) + 170 \tag{2.23}$$

for F-75 Ottawa Clean Sand, and

$$\frac{\sigma_t}{P_r \ln(D_r)} = 77 \ln(w) + 186 \tag{2.24}$$

for F-75 Ottawa sand with fines, where P_r is a reference pressure (1 Pa), w is water content (%), D_r is relative density (%), and σ_t is tensile strength (Pa).

Table 2. 2: *Summary of Direct Tension Test Results for F-75-C sand wetted at* $0.3\% < w < 4.0\%$ *and at the loose and dense states. Kim (2001)*

W (%)	S (%)	Dr (%)	Tensile Stress (Pa)
Direct Tension Test, Loose			
0.3	1.2	29	321.5
0.5	1.7	32	409.7
1.0	3.8	30	580.7
1.1	4.0	28	586.1
2.1	7.8	27	704.9
4.0	14.8	26	873.0
4.0	14.9	28	850.6
Direct Tension Test, Dense			
W (%)	S (%)	Dr (%)	Tensile Stress (Pa)
0.37	1.7	70	392.6
0.47	2.1	71	498.5
1.02	4.7	72	730.5
1.04	4.7	70	732.9
2.05	9.2	68	982.0
3.89	17.5	68	1164.5
4.06	18.0	65	1150.8
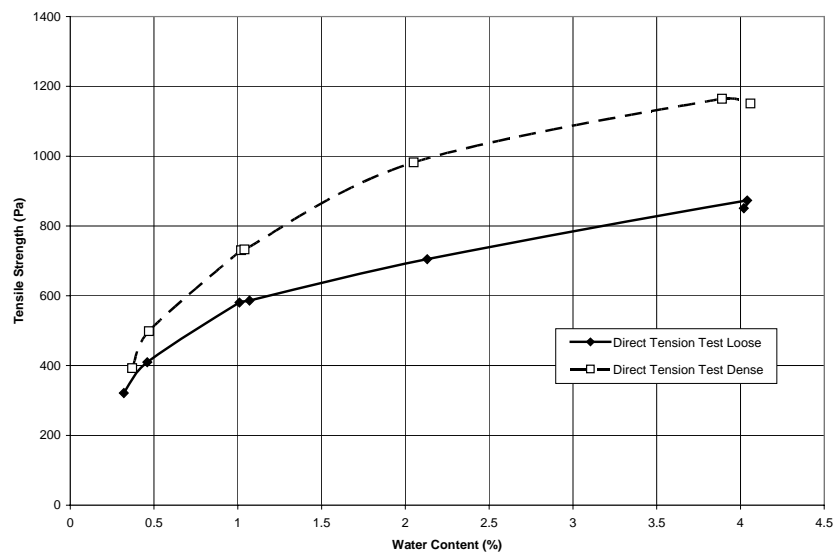
Figure 2. 24: *Relationship between Tensile Strength and Water Content for F-75-C Sand at different densities. Kim (2001)*

Table 2. 3: *Summary of Direct Tension Test Results for F-75-F sand wetted at* $0.3\% < w < 4.0\%$ *and at the loose and dense states. Kim (2001)*

Direct Tension Test Loose			
W (%)	S (%)	Dr (%)	Tensile Stress (Pa)
0.3	1.1	30	310.1
0.47	1.8	30	425.5
1.02	3.8	29	608.7
2.05	7.6	27	811.4
2	7.4	28	744.0
4.03	15.0	29	951.1
4.06	15.0	28	914.6
Direct Tension Test Dense			
W (%)	S (%)	Dr (%)	Tensile Stress (Pa)
0.29	1.3	71	430.3
0.41	1.9	72	524.1
1.01	4.6	69	823.3
2.03	9.2	70	1065.4
2.03	9.3	70	1051.0
4	18.1	69	1346.7
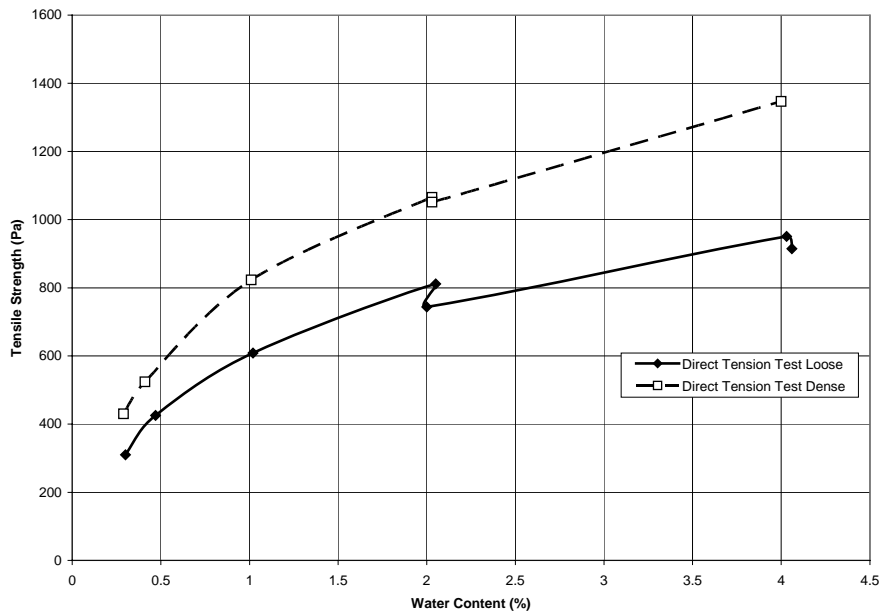
Figure 2. 25: *Relationship between Tensile Strength and Water Content for F-75-F Sand at different densities. Kim (2001)*

Kim (2001) also reported results from modified direct shear tests conducted for clean F-75-C Ottawa sand specimens and F-75-F specimens with 2% fines prepared to loose conditions ($D_r \sim 30\%$, $e \sim 0.71$). Tables 2.4 and 2.5 summarize results from direct shear testing for F-75-C and F-75-F, respectively.

Table 2. 4: *Summary of direct shear test results for F-75-C sand wetted at different water contents (approximated from Kim, 2001)(F-75-C, e~0.71)*

F-75-C (e ~ 0.71)

w (%)	S (%)	τ_f (Pa)			
		σ_n (Pa) 100	σ_n (Pa) 200	σ_n (Pa) 500	σ_n (Pa) 1000
0	0.0	220	300	400	780
0.5	1.9	390	600	800	1100
1	3.7	450	700	950	1300
10	37.3	750	930	1050	1380
15	56.0	790	950	1090	1430
17	63.5	790	950	1110	1410

Table 2. 5: *Summary of direct shear test results for F-75-F sand wetted at different water contents (approximated from Kim, 2001)(F-75-F, e~0.71)*

F-75-F (e ~ 0.71)

w (%)	S (%)	τ_f (Pa)			
		σ_n (Pa) 100	σ_n (Pa) 200	σ_n (Pa) 500	σ_n (Pa) 1000
0	0.0	220	350	500	700
0.5	1.9	400	600	850	1130
1	3.7	500	660	990	1300

Lu et al. (2005) used the system shown in Figure 2.23 to determine the tensile strength of clean sands commercially available from Western Australia (White Silica Mineral Sands, Cook Industrial Minerals Pty Ltd). This included silty sand with a mean particle size of 0.105 mm, a fine sand with a mean particle size of 0.167 mm, and a

medium sand with a mean particle size of 0.451 mm. Tensile strength for the silty sand

was obtained as a function of degree of saturation ranging from about 0% to 90% for

porosity equal to 45%, which reflects loose packing. Tensile strength for the fine sand

was obtained for two porosity values: one representing medium packing with a porosity

value of 37%, and the other representing loose packing with a porosity of 45%. Tensile

strength for the medium sand was obtained for two porosity values: 37% and 0.40%.

Results are shown in Figures 2.26 through 2.28.
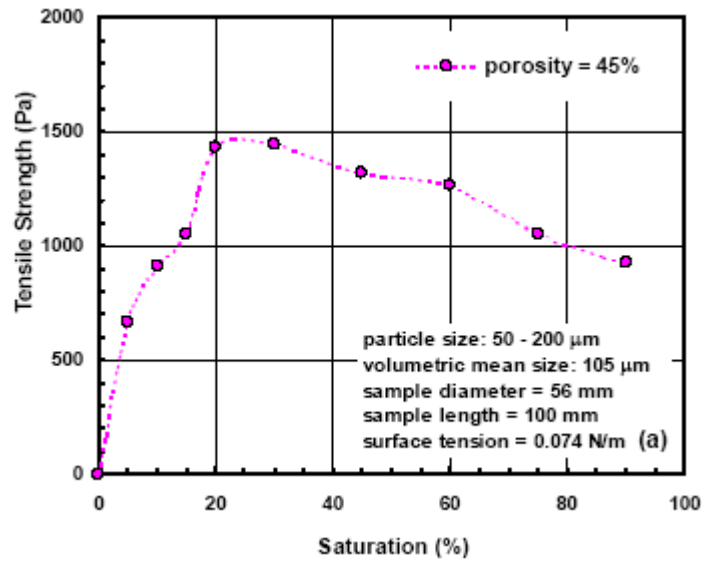
Figure 2. 26: *Tensile strength as a function of saturation for silty sand (Lu et al., 2005)*
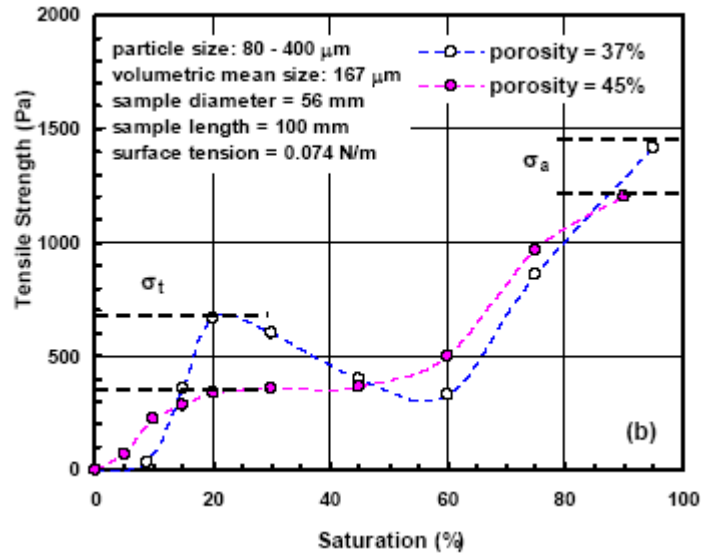
Figure 2. 27: *Tensile strength as a function of saturation for fine sand (Lu et al., 2005)*
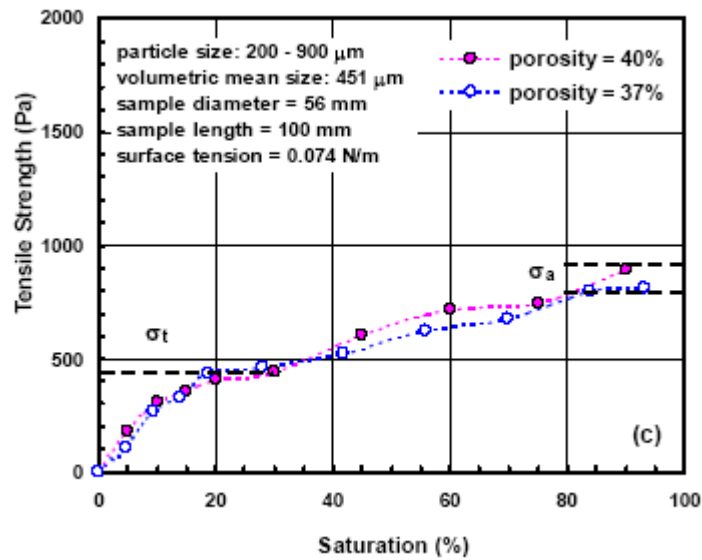
Figure 2. 28: *Tensile strength as a function of saturation for medium sand (Lu et al., 2005)*

3 Materials and Methods

This chapter describes in detail the material used for this research, including the soil properties grain size distribution, specific gravity, matric suction characteristics, and particle morphology. The methods used to determine these properties are summarized. Equipment that was used for performing the soil-water characteristic curve tests, direct shear tests, and tensile strength tests is also described. Finally, the overall experimental program (testing matrix) is summarized.

3.1 Soil Properties

One of the primary objectives of this research is to isolate the role of capillary interparticle forces on the tensile strength, shear strength, and deformation behavior of soils. Effective stress controls soil behavior and strength, and, as described in the preceding chapter, the effective stress in unsaturated soil is affected in part by suction stress. Effective stress in unsaturated (or saturated) soil is also affected by physicochemical forces such as van der Waals attraction and electrical double layer forces, which may change in magnitude and behavior as a function of degree of saturation. To more effectively isolate the role of capillarity on unsaturated soil behavior, therefore, it is desirable to select test materials where physicochemical effects are relatively minor. It is also desirable to examine behavior over a wide range of total stress and water content to clarify the relative importance of suction stress in contributing to effective stress. Finally, it is desirable to examine relatively well-rounded materials such that the observed experimental behavior may be more readily compared with the previously introduced micro-structural theories based on spherical particle geometries.

Materials selected for this research included three gradations of Ottawa sand.

Gradations selected included F-40, F-55, and F-75, which are progressively finer in grain

size. For all subsequent tests, specimens were compacted to relatively loose ($e \sim 0.75$)

and relatively dense ($e \sim 0.6$) conditions to examine the associated effects on shear and

tensile strength.

Figures 3.1, 3.2, and 3.3 show grain size distribution curves determined using

mechanical sieve analysis for the F-40, F-55, and F-75 sand respectively. Results are

compared with manufacturer-specified grain size distributions and are in relatively good

agreement. Mean particle sizes d_{10} are 0.25 mm, 0.18 mm, and 0.15 mm for the F-40, F-

55, and F-75 gradations, respectively. Specific gravity (G_s) was determined following the

procedures described in ASTM D-854 and found to be equal to 2.65.

Table 3. 1: *Summary of grain size parameters for test sands.*

Soil Type	d_{60}	d_{10}	C_u	C_c
Ottawa Sand F-40	0.38	0.25	1.52	0.77
Ottawa Sand F-55	0.27	0.18	1.50	1.09
Ottawa Sand F-75	0.26	0.15	1.73	0.83
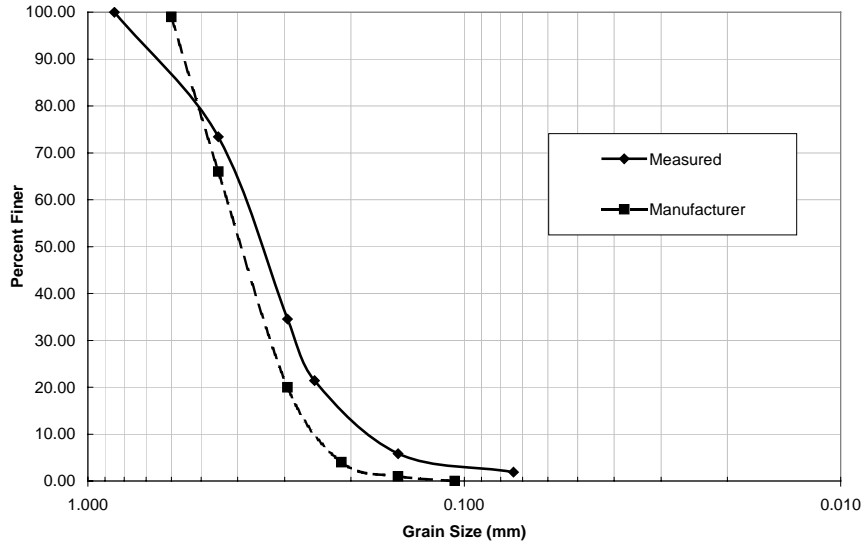
Figure 3. 1: *Grain size distribution curve for F-40 Ottawa sand*
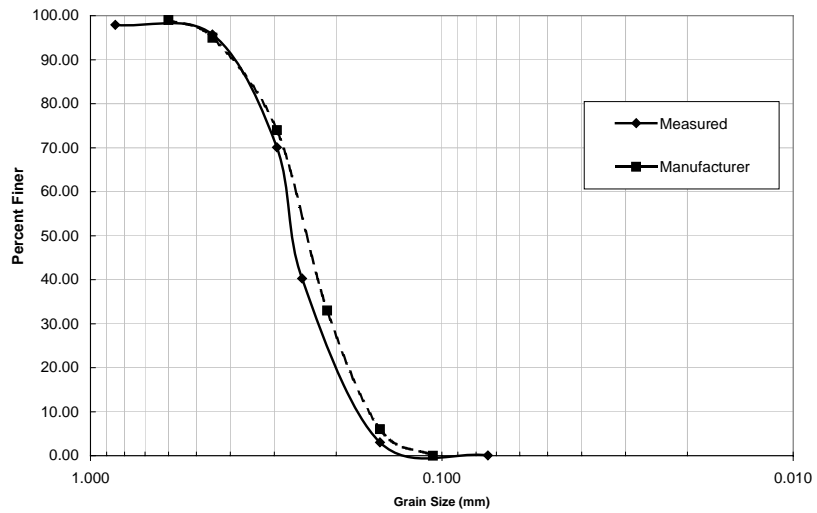
Figure 3. 2: *Grain size distribution curve for F-55 Ottawa sand*
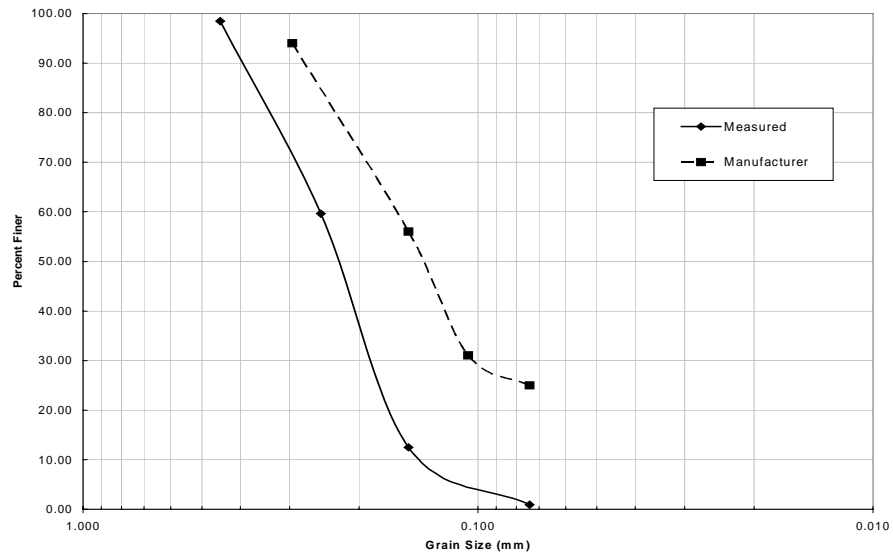
Figure 3. 3: *Grain size distribution curve for F-75 Ottawa sand*

Figure 3.4 shows a scanning electron micrograph of the F-55 sand, where it can be seen that the material is generally sub-rounded to rounded in shape. It should also be noted that numerous cracks and fissures are evident on the particle surfaces that might facilitate adsorption and retention of water by mechanisms other than capillary adsorption in the larger-scale pore space.

(a)
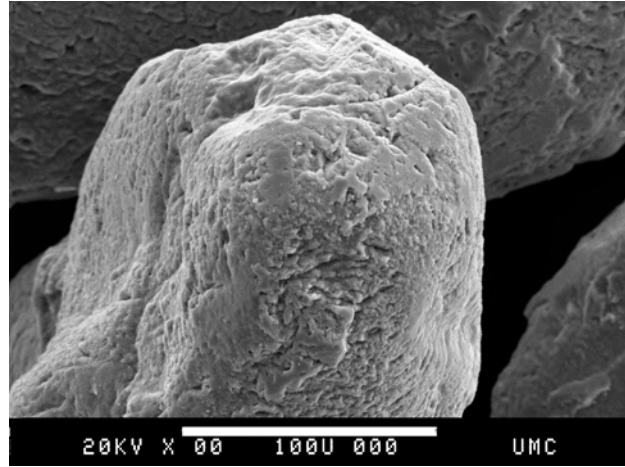
(b)

Figure 3. 4: *Scanning Electron Microscope Images of F-55 Ottawa Sand (a)*

Magnified 200 times (b) Magnified 510 times

Figure 3.5 and 3.6 summarize minimum and maximum void ratios (*e*) for all three

sands, respectively. The finest gradation (F-75) generally packs to the loosest condition.

Theoretical maximum and minimum void ratios for uniform spheres in simple cubic

packing (loosest) and tetrahedral close packing (densest) geometries are *e* = 0.91 and

0.34, respectively.
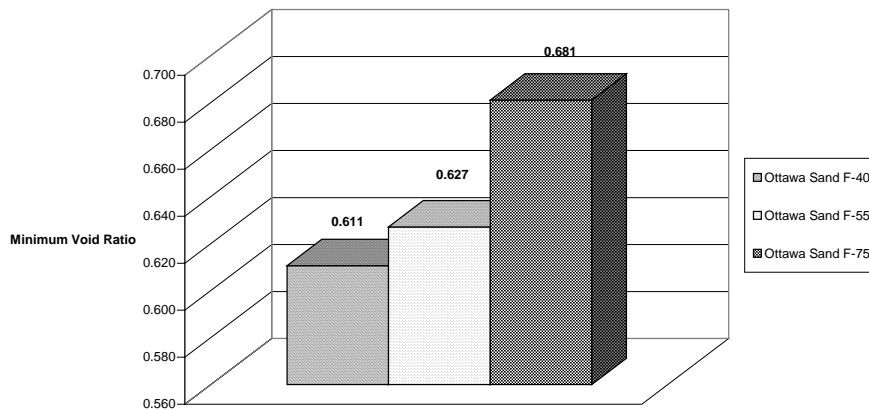
Figure 3. 5: *Measured minimum void ratio for all soil types used*
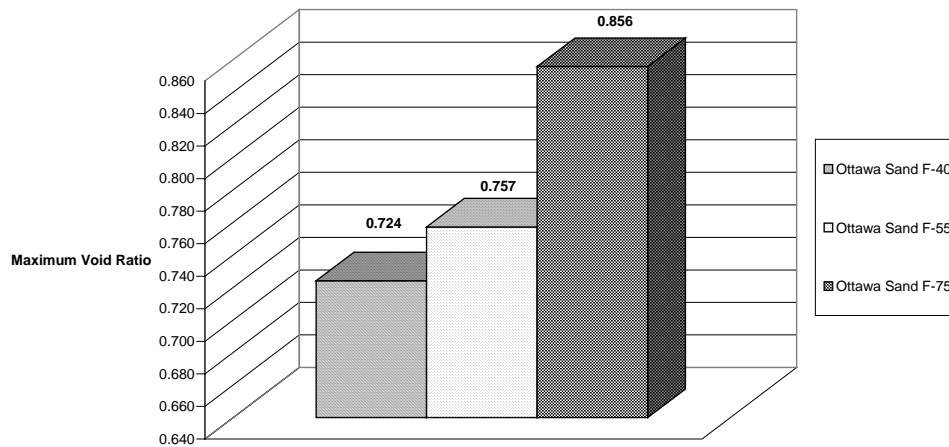
Figure 3. 6: *Measured maximum void ratio for all soil types used*

Compaction curves were determined using the standard Proctor compaction test procedure (ASTM D698). An additional series of compaction curves was also obtained for specimens compacted directly into Tempe pressure cells (*i.e.*, smaller molds than used for standard tests). These specimens were compacted at the same energy as a standard Proctor compaction test and following a similar procedure. The objective of these tests was to provide guidelines for compacting materials directly into Tempe cell molds for subsequent determination of soil-water characteristic curves on compacted specimens.

Figures 3.7 and 3.9 show standard Proctor compaction curves and the Tempe Cell compaction curves, respectively. In general, the coarser material (F-40) compacts to a greater density, which was also reflected by the previous determination of maximum and minimum void ratios. A more detailed compaction curve for the F-40 sand in terms of corresponding degree of saturation is shown as Figure 3.8 for analysis in Chapter 5.
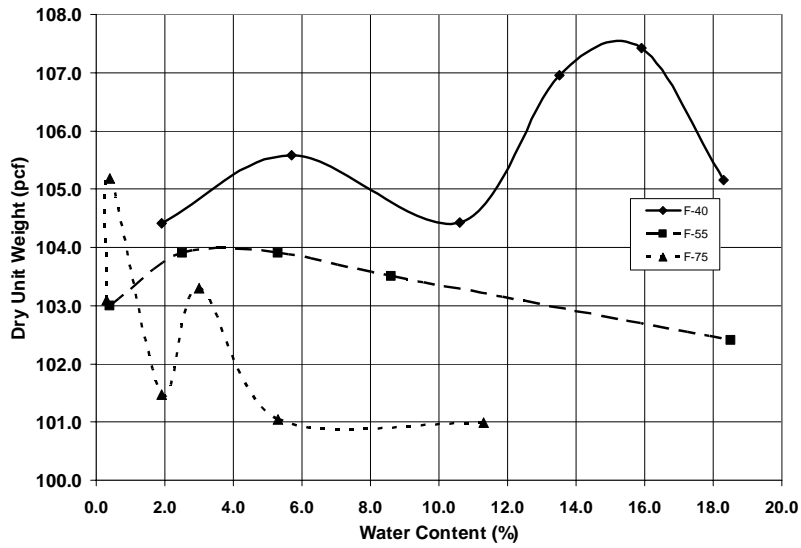
Figure 3. 7: *Standard Proctor compaction curves for all soils used*
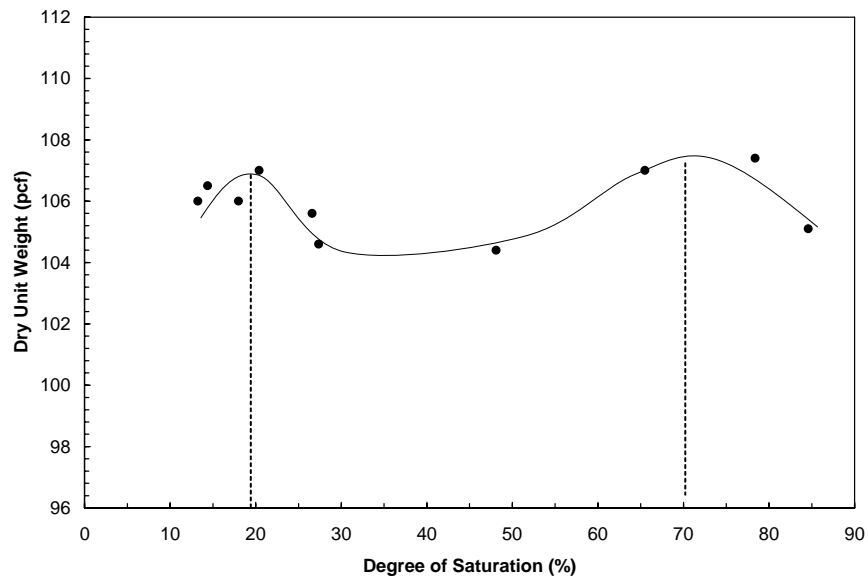
Figure 3. 8: *Standard Proctor compaction curve for F-40 sand as function of saturation*
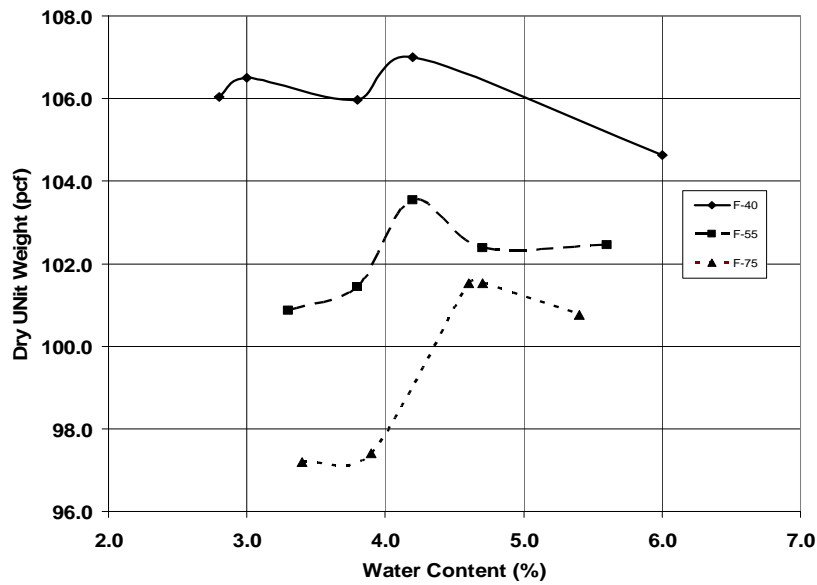
Figure 3. 9: *Tempe cell compaction curves for all soils used*

3.2 Soil Water Characteristic Curves

3.2.1 SWCC Measurement Methods

Three different methods were used to determine soil-water characteristic curves (SWCC). The first two methods used were axis translation techniques conducted using Tempe cells, initially by applying negative water pressure and atmospheric air pressure using a hanging column system, and subsequently by elevating pore air pressure while maintaining atmospheric water pressure. The third method involved measuring negative pore water pressure directly using tensiometers for specimens compacted to known water content values.

Axis translation refers to the process of maintaining a pressure difference between the air and water phases of unsaturated soil through the pores of a high-air-entry

(HAE) material (e.g., saturated ceramic disk). If the specimen is in good contact with the saturated HAE material, for example, it is possible to apply positive air pressure on one side and allow the specimen pore water to drain freely through the HAE material under atmospheric pressure on the other side. Alternatively, negative water pressure may be applied to the pore water phase (e.g., using a hanging column system) while maintaining the pore air pressure at atmospheric.

A Tempe cell consists of a saturated HAE ceramic disk separating air and water chambers in a closed vessel (Fig. 3.10). Air pressure is applied in the top part of the vessel and the bottom part is at atmospheric pressure. The air pressure for these tests was applied using a panel able to apply a maximum of 50 psi (~345 kPa), and with a resolution of 0.1 psi (~0.69 kPa). Water expelled from the specimen was measured volumetrically using a calibrated constant-head board (small diameter tube; Fig. 3.11).
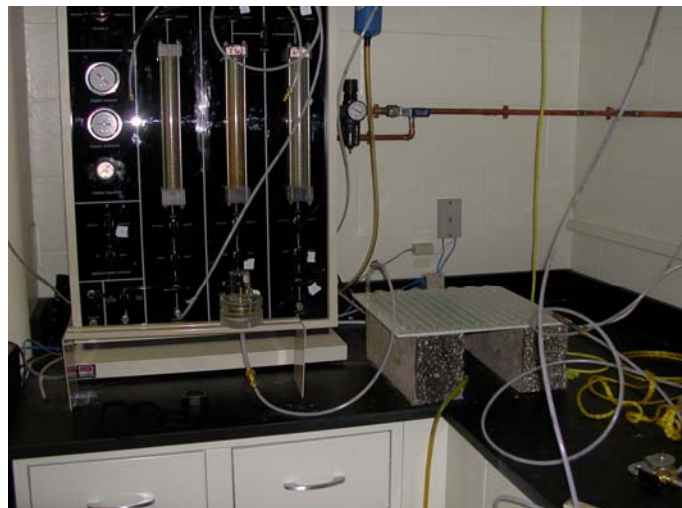
Figure 3. 10: *Tempe cell set up used for this research*
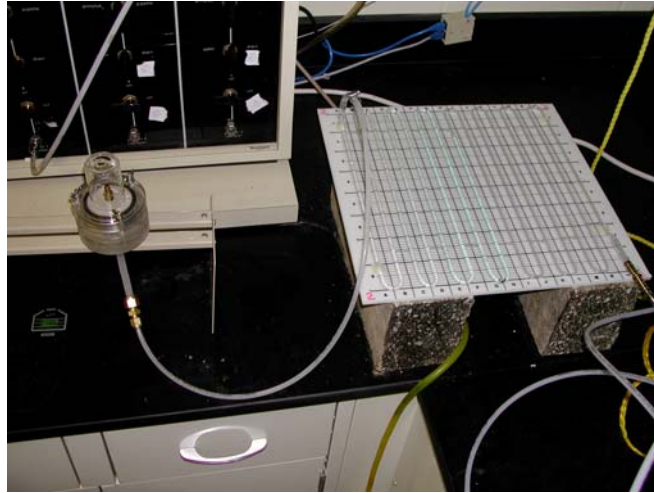
Figure 3. 11: *System used to measure outflow from the Tempe cell specimen*

The second axis translation method used was the hanging column method (e.g., Wang & Benson; 2004). This involves essentially the same procedures as just described; however, negative pore water pressure is applied directly by applying negative pressure head using water two reservoirs at different elevations (Figure 3.12). Pore air pressure was maintained atmospheric. The volume of water coming out of the specimen for increments in applied suction was measured using the previously described flowmeter. Figure 3.13, for example, shows the volume of pore water extracted from initially saturated F-75 sand compacted to a porosity of 41.2% ($e = 0.70$) as a function of time. Figure 3.14 shows the corresponding SWCC.
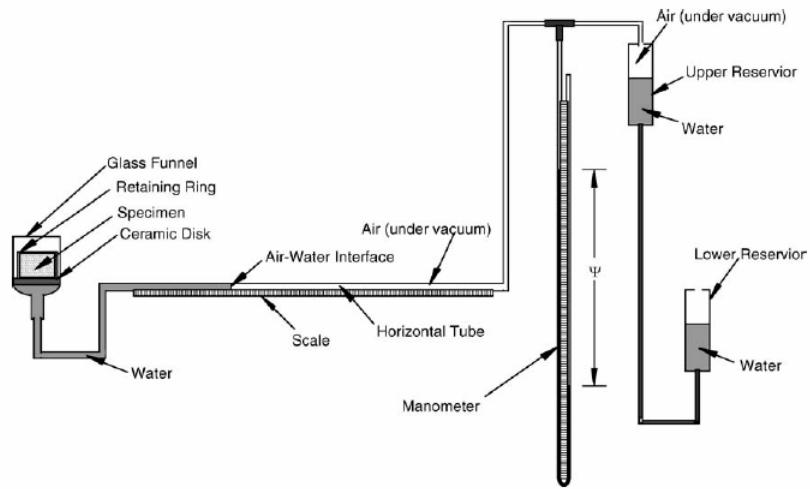
Figure 3. 12: *Schematic of hanging column system. Wang & Benson (2004)*
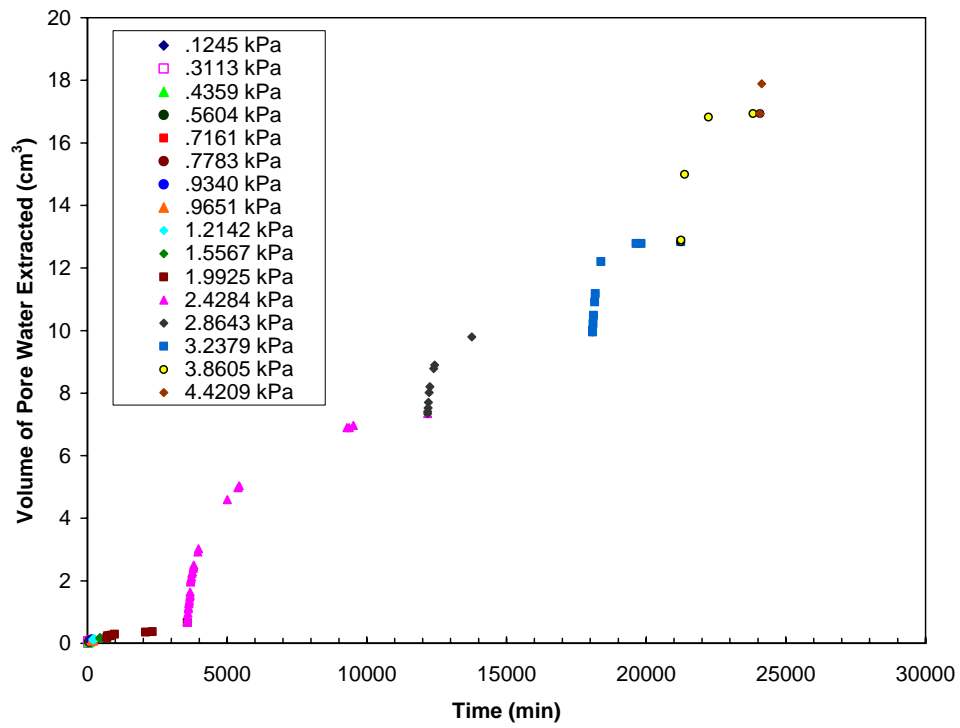
Figure 3. 13: *Extracted pore water as a function of time from hanging column SWCC test.*
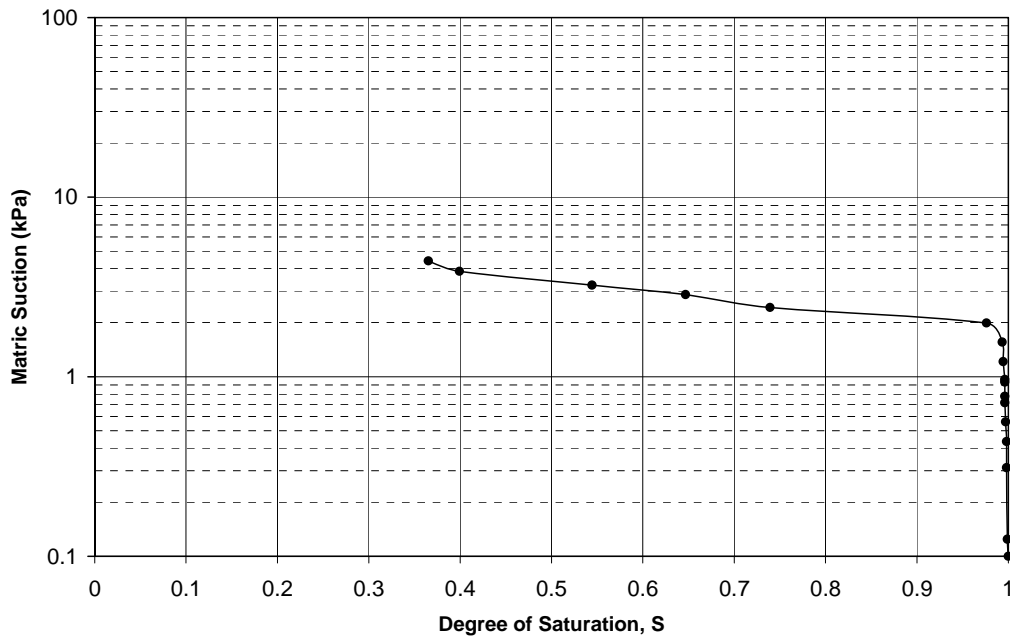
Figure 3. 14: *SWCC from hanging column test; F-75 sand.*

The third method to obtain the SWCC was using tensiometers. A tensiometer is a water-filled tube with an HAE ceramic tip at one end and a sensor for measuring negative water pressure at the other (Figure 3.15a). The ceramic tip is buried in a specimen. The tubing that connects the ceramic tip to the pressure sensor is saturated to create a hydraulic connection between negative pore water pressure in the specimen, the water in the tensiometer body, and the pressure sensing device. For these tests, soils were compacted to known density and water content into the Tempe Cell molds and a tensiometer was embedded in the soil to measure matric suction (Figure 3.15b).
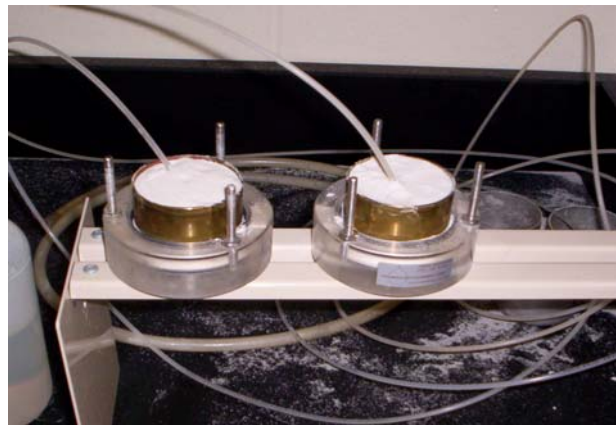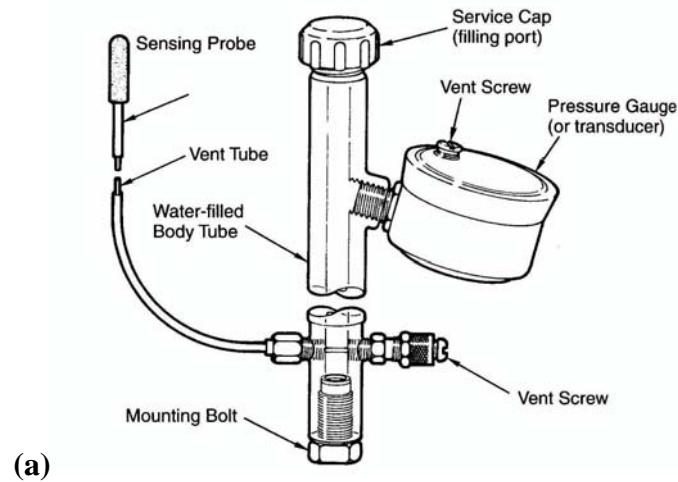
Figure 3. 15: *(a) Schematic diagram of a small-tip tensiometer (Soilmoisture Equipment Co); (b) Test specimens compacted into Tempe cells*

3.2.2 SWCC Models

Once matric suction values were obtained corresponding to different water contents for all three different gradations of sand, the SWCCs were plotted. Three different models were used to fit the experimental data: the Brooks & Corey (1964), van Genuchten (1980), and Fredlund & Xing (1994) models. The Brooks & Corey (1964) expression is a two-part model in the form:

$$S_e = 1 \qquad \psi < \psi_b \tag{3.1a}$$

$$S_e = \left(\frac{\psi_b}{\psi}\right)^{\lambda} \qquad \psi \geq \psi_b \tag{3.1b}$$

where S_e is the effective degree of saturation, ψ is matric suction, ψ_b is the air-entry pressure, and λ a pore size distribution index optimized to fit the model to experimental data.

The van Genuchten (1980) model is

$$S_e = \left[\frac{1}{1 + (a\psi)^n}\right]^m \tag{3.2a}$$

where a, n, and m are fitting parameters, where the latter is typically constrained to

$$m = 1 - \frac{1}{2n} \tag{3.2b}$$

The Fredlund & Xing (1994) expression is

$$S_e = \left[\frac{1}{\ln\left[e + \left(\frac{\psi}{a}\right)^n\right]}\right]^m \tag{3.3}$$

where e is the natural logarithmic constant and a, n, and m are fitting parameters.

Figures 3.16, 3.17, and 3.18 show SWCCs and corresponding models determined for F-40, F-55, and F-75 Ottawa Sand compacted to relatively loose conditions ($e = 0.75$). The experimental data reported was obtained from the tensiometer tests. Figures 3.19, 3.20, and 3.21 show similar results for specimens compacted to relatively dense ($e = 0.60$) conditions. Table 3.2 summarizes fitting parameters selected to model the results.
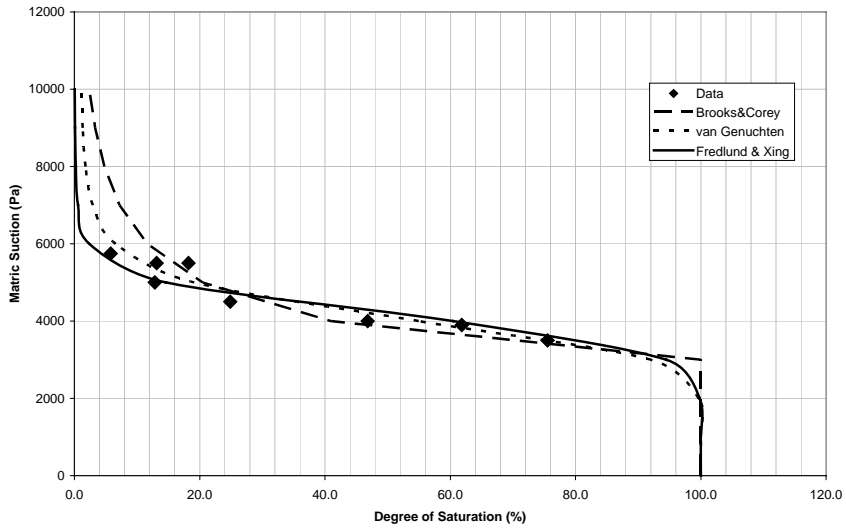
Figure 3. 16: *Soil Water Characteristic Curve Models for F-40 Ottawa Sand (e=0.75)*
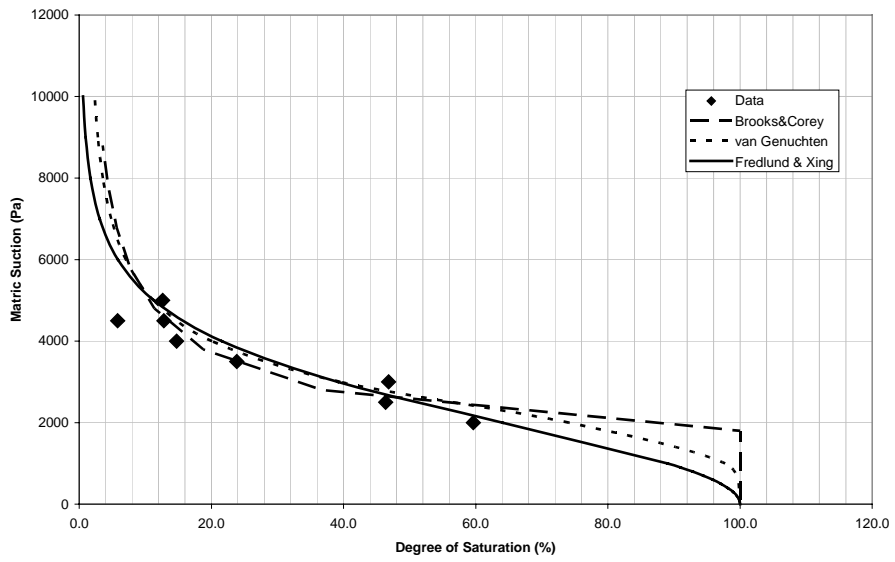
Figure 3. 17: *Soil Water Characteristic Curve Models for F-55 Ottawa Sand (e=0.75)*
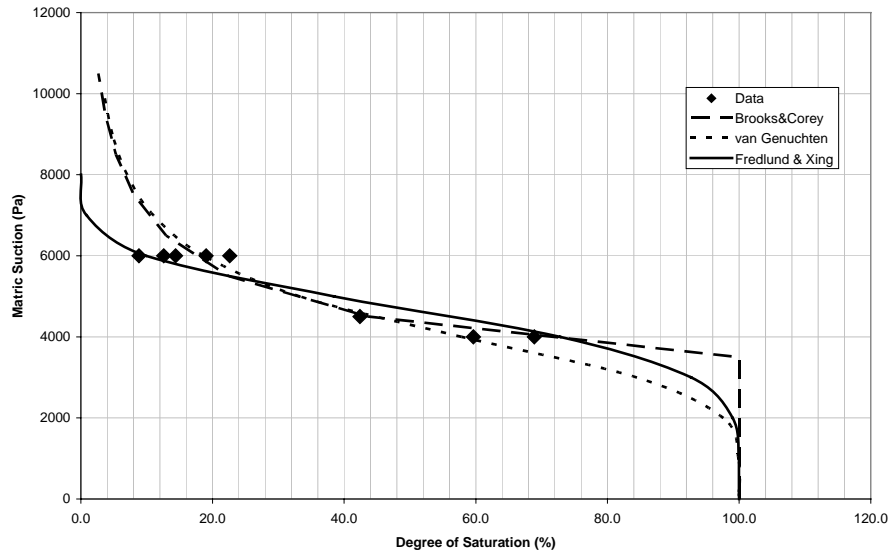
Figure 3. 18: *Soil Water Characteristic Curve Models for F-75 Ottawa Sand (e=0.75)*
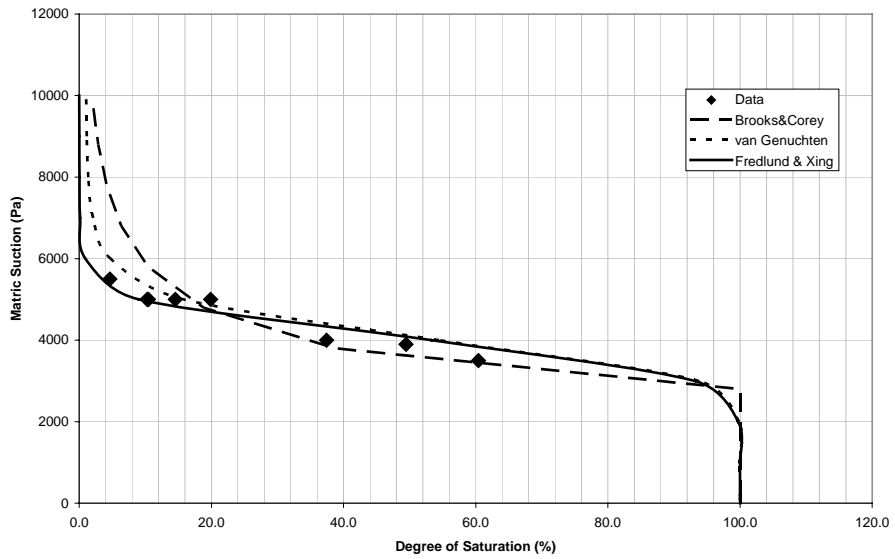
Figure 3. 19: *Soil Water Characteristic Curve Models for F-40 Ottawa Sand (e=0.60)*
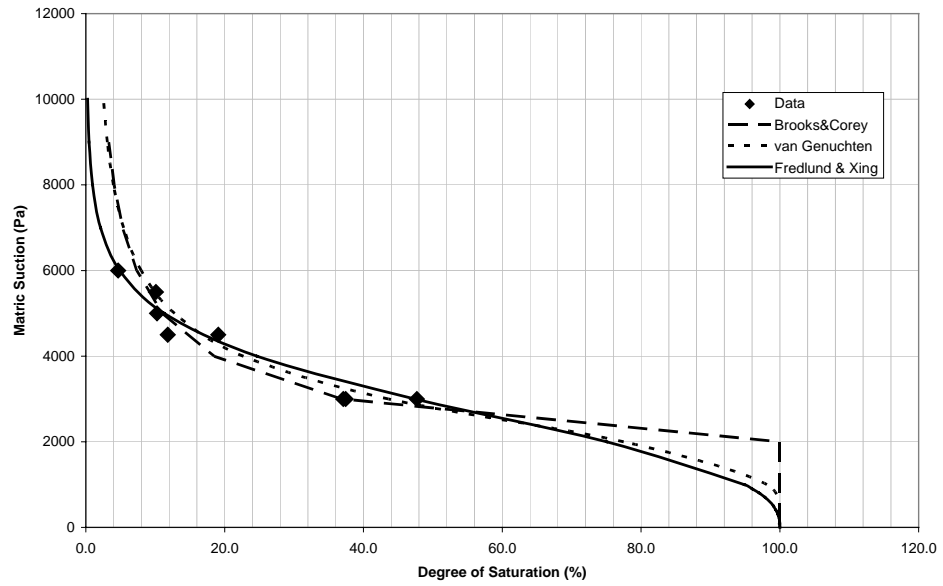
Figure 3. 20: Soil Water Characteristic Curve Models for F-55 Ottawa Sand (e=0.60)
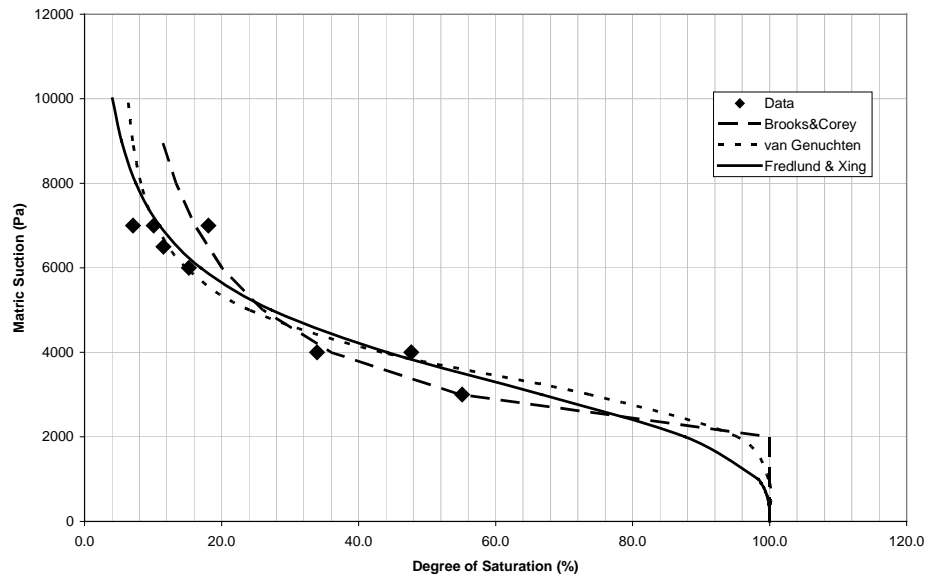
Figure 3. 21: *Soil Water Characteristic Curve Models for F-75 Ottawa Sand (e=0.60)*

Table 3. 2: *Summary of SWCC modeling parameters.*

Parameters	Brooks and Corey (1964)					
	F-75		F-55		F-40	
	Loose	Dense	Loose	Dense	Loose	Dense
λ	3.3	1.5	2.3	2.5	3.1	3.1
Sr	0.00	0.01	0.01	0.01	0.00	0.00
Ψb (kPa)	3.5	2.0	1.8	2.0	3.0	2.8
van Genuchten (1980)						
α (kPa-1)	0.25	0.29	0.42	0.4	0.25	0.25
n	5.0	5.0	4.0	4.0	8.0	9.0
m	0.80	0.80	0.75	0.75	0.88	0.89
θs	0.37	0.43	0.37	0.43	0.43	0.43
θr	0.1	0.1	0.1	0.1	0.1	0.1
e	0.75	0.6	0.75	0.6	0.75	0.75
Fredlund and Xing (1994)						
a	9.0	4.0	5.0	5.0	4.5	4.5
n	5.0	3.0	2.0	2.5	8.0	8.0
m	50	3	8	8	4	5

3.3 Direct Shear Testing

3.3.1 Apparatus Description

The direct shear test is one of several methods available for measuring the shear strength of soils. The apparatus consists of a shear box, carriage, and loading frame. The shear box used is a split horizontally and holds a soil specimen with a circular cross section. The diameter of the specimen is approximately 2.4 inches (6.13 cm). Figure 3.22 shows a schematic of a typical direct shear apparatus. The specimen is seated between two porous stones that allow drainage. The contact surfaces between the specimen and the porous stones are grooved to prevent slippage between the specimen and the stones during shearing. For testing, the specimen is subjected to a vertical load per unit of area

applied to the upper loading platen. Lateral force is then applied to the lower half of the box using a constant rate of deformation until shear failure is induced. Shear stress may then be plotted as a function of lateral displacement to determine the peak shear stress sustained.
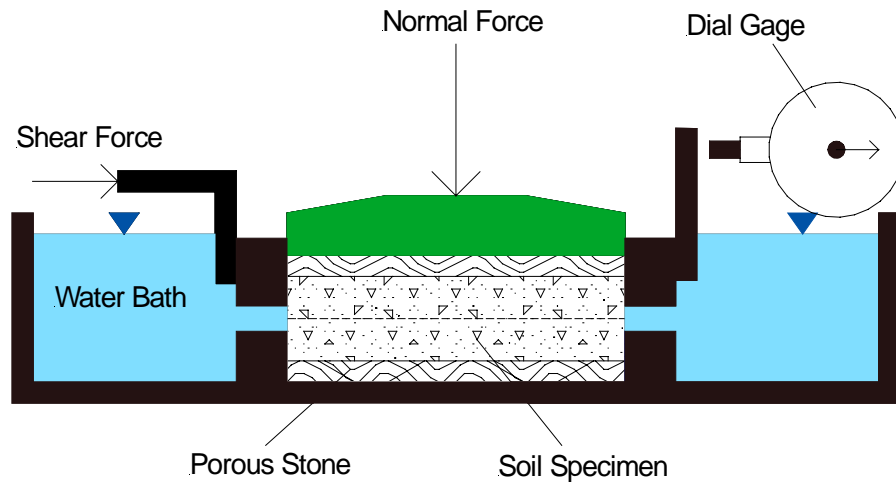
Figure 3. 22: *Schematic of typical direct shear testing setup*

Tests conducted for this research were performed using a Wykeham-Farrance direct shear machine equipped to record vertical deformations, horizontal deformations, and shearing force, as well as to control the rate of deformation (Figure 3.23). Specimens were compacted directly into the shear box at pre-prepared water contents (16-hour cure time) using a special sliding hammer designed to provide energy equivalent to standard energy Proctor compaction. Similar sliding hammers were also designed to compact specimens directly into the tensile strength testing apparatus (Section 3.4), and the Tempe cells used to determine SWCCs (Section 3.2). Table 3.3 summarizes the properties of these hammers and associated molds, including compactive energy, volume of the mold, and drop distance. Figure 3.24 shows photographs of the three sliding hammers.

Figure 3. 23: *Photograph of direct shear testing apparatus*

Table 3. 3: *Summary of sliding hammer and compaction mold Properties*

Standard Proctor 6042 cm-g/cm^3	Sliding Hammer		
	Tensile Strength Box	Direct Shear	Tempe Cell
Hammer Wt. (g)	1659.3	1202.2	1202.2
Disc (g)	516.3	264.5	264.5
Lifts (#)	7	3	3
Blows (#)	25	15	15
Drop (cm)	49	7.5	6.2
Volume of Mold (cm^3)	2433.5	81.4	67.2
Energy Per unit volume (cm-g/ cm^3)	6061	7062	6097
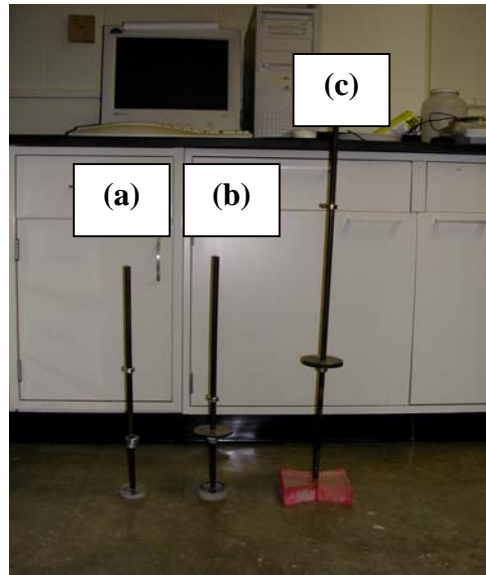
Figure 3. 24: *Sliding Hammers designed for compacting specimens into: (a) Tempe cell, (b) direct shear system, and (c) Tensile Strength system*

3.3.2 Experimental Program

The experimental program for direct shear testing included all three gradations of Ottawa Sand compacted to two different void ratios: a relatively dense condition ($e \sim 0.60$) and a relatively loose condition ($e \sim 0.75$). In addition to tests performed on saturated specimens, tests for specimens prepared to eight different gravimetric water contents were performed: 2%, 4%, 6%, 8%, 10%, 12%, 15%, and 18%. Table 3.4 summarizes the complete direct shear testing program.

Table 3. 4: *Summary of direct shear testing program*

Test	Soil Type	Density	W%
Direct Shear Tests	Ottawa Sand F-40 Ottawa Sand F-55 Ottawa Sand F-75	Loose (e ~ 0.75) & Dense (e ~ 0.60)	Dry
			2%
			4%
			6%
			8%
			10%
			12%
			15%
			18%

3.3.3 Procedure

Three magnitudes of normal stresses were applied to develop failure envelopes: 5psi (~35 kPa), 15 psi (~103 kPa), and 40 psi (~276 kPa). All specimens were sheared at a constant rate of deformation of 0.5 mm/min. Horizontal displacement, vertical displacement, and shear load were measured during shear.

Specimens were pluviated by gravity using a small funnel to obtain relatively loose compaction conditions for the dry sand specimens. A belt sander was used to vibrate the sides of the shearing device to obtain relatively dense conditions for the dry specimens. An undercompaction method and the sliding hammer shown as Figure 3.24b were used to achieve homogeneous specimens and reproducible densities for the partially saturated specimens. Here, three individual soil layers (lifts) were compacted to a lower density than the final desired value ($e = 0.75$ or $e = 0.60$) to normalize the cumulative

compaction effect as each subsequent layer is compacted. The expression used to

compute percent undercompaction was as follows:

$$U_n = U_{ni} - \left[\frac{(U_{ni} - U_{nt})}{n_t - 1}(n-1) \right]$$
(3.4)

where U_n is the undercompaction percentage, U_{ni} is the percent undercompaction of the

first layer, U_{nt} is the percent undercompaction of the last layer, n is the number of the

current layer, n_t is the total number of layers ($n_t = 3$). Table 3.5, for example, shows

relevant data for direct shear tests conducted at 8% water content and $e \sim 0.60$ for F-55

sand. A similar undercompaction method was used to prepare specimens for the tensile

strength testing series and the SWCC testing series.

Table 3. 5: *Undercompaction data for F-55 Ottawa sand (w = 8%, e = 0.60)*

Layer	U_{ni}	U_{nt}	n_t	n	U_n
1	5	0	3	1	5
2	5	0	3	2	2.5
3	5	0	3	3	0

Lift	
1	cm
Volume	
81.4	cm^3

Dry Unit weight	Water Content	Total Vol.	Total Wt	Layer Wt
γd (g/cm^3)	wa	Vm (cm^3)	Wt (g)	Wl (g)
1.71	0.08	81.4	150.3	50.1

Layer	h_t (cm)	n_t	n	U_n	Height of layer h_n (cm)
1	2.76	3	1	5	0.97
2	2.76	3	2	2.5	1.86
3	2.76	3	3	0	2.76

3.4 Tensile Strength Testing

3.4.1 Apparatus Description

The tensile strength testing device used for this research was based on the direct tension device described by Kim (2001). The sample container (Figure 3.25) consists of a 6-in by 6-in by 6-in box split in two equal halves. The front part is mounted on two sets of precision roller bearings sliding on two guide rails attached to the bottom of the device and 8.9 cm apart. The rear half of the box rests on two solid spacers to position it at the same height as the front half. Four 20º wedges were attached inside the box to facilitate contact between the specimen and the internal walls as tension develops across the plane of separation. Both halves of the box rest on a loading table with two pulleys installed to connect loading wires (Figure 3.26). Wires are attached to the bottom of the (movable) front half and connected to the buckets through pulleys (Figure 3.27). A dial gage with a precision of 0.0001 inches (2.54×10^{-4} cm) was installed to measure deformations parallel to the plane of separation during tensile loading (Figure 3.28).

Figure 3. 25: *Plan view of tensile strength testing device*
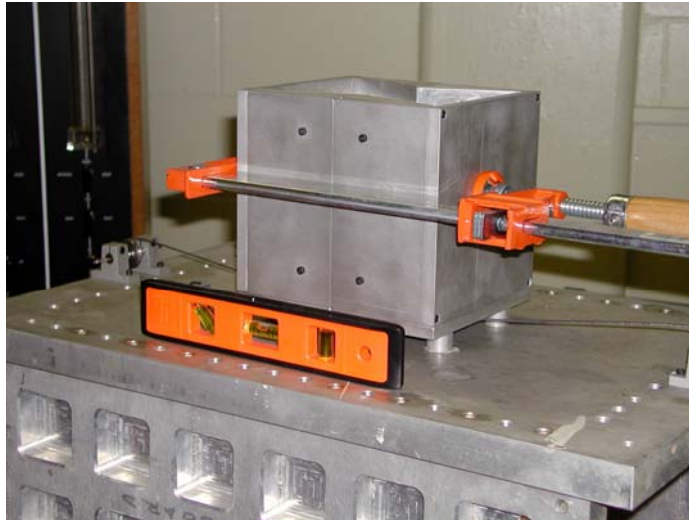
Figure 3. 26: *Side view of tensile strength testing device*

Figure 3. 27: *Loading system used to apply tensile stress*
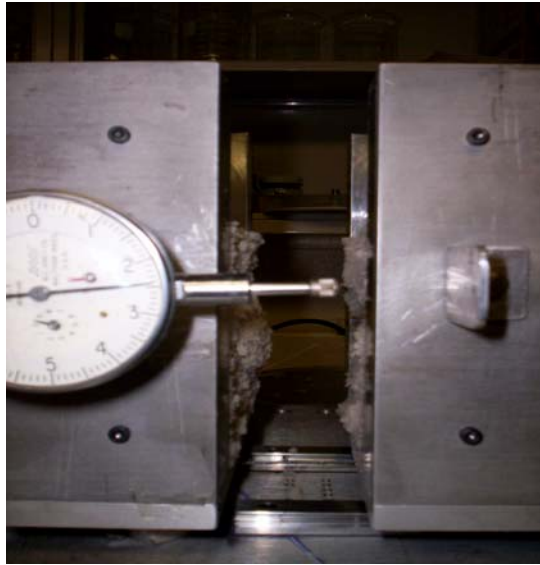
Figure 3. 28: *Dial gage used to measure deformations parallel to failure plane*

3.4.2 Experimental Program

The direct tension testing series included tests for all three gradations of Ottawa compacted at relatively dense and relatively loose void ratios ($e \sim 0.60$ and 0.75, respectively). Specimens were compacted to the same water contents as for the direct shear testing program (2%, 4%, 6%, 8%, 10%, 12%, 15%, and 18%). Table 3.6 summarizes the complete direct tension testing program.

Table 3. 6: *Summary of tensile strength testing program*

Test	Soil Type	Density	W%
Tensile Strength	*Ottawa Sand F-40* *Ottawa Sand F-55* *Ottawa Sand F-75*	*Loose (e ~ 0.75) & Dense (e ~ 0.60)*	2%
			4%
			6%
			8%
			10%
			12%
			15%
			18%

3.4.3 Procedure

Specimens for direct tension testing were prepared using the sliding hammer shown as Figure 3.24c and the undercompaction method with eight layers (lifts). Table 3.6, for example, summarizes undercompaction calculations for a loose F-75 Ottawa sand specimen preparation at water content of 10%. The two halves of the box were clamped to prevent movement during compaction. The rear loading container was partially filled with water to initialize the system against the front loading bucket to prevent movement at the initial stage of tensile loading. Tensile loading was then applied by introducing water into the front loading bucket at a rate of approximately 13g/sec until tensile failure occurred. Deformation readings were taken from the dial gage every 10 seconds.

Table 3. 7: *Undercompaction data for F-75 Ottawa sand (w = 10%, e = 0.75)*

Layer	U_{ni}	U_{nt}	n_t	n	U_n
1	10	0	8	1	10
2	10	0	8	2	8.57
3	10	0	8	3	7.14
4	10	0	8	4	5.71
5	10	0	8	5	4.29
6	10	0	8	6	2.86
7	10	0	8	7	1.43
8	10	0	8	8	0

Lift	
1.27	cm
Volume	
1426.1	cm^3

Dry Unit Wt	Water Content	Volume	Total Wt	Layer Wt
γd (g/ cm^3)	wa	Vm (cm^3)	Wt (g)	Wl (g)
1.66	0.1	1426.1	2604.1	325.5

Layer	h_t (cm)	n_t	n	U_n	Height of layer h_n (cm)
1	10.16	8	1	10	1.40
2	10.16	8	2	8.57	2.65
3	10.16	8	3	7.14	3.90
4	10.16	8	4	5.71	5.15
5	10.16	8	5	4.29	6.40
6	10.16	8	6	2.86	7.66
7	10.16	8	7	1.43	8.91
8	10.16	8	8	0	10.16

3.4.4 Data Reduction

The following expression was used to calculate tensile load as a function of time

$$L = LR * t - f - BB + FB \qquad (3.5a)$$

$$f = -0.01 * t^2 + 4.632t \qquad (3.5b)$$

where L is the tensile force (g), LR is the loading rate, t is time, f is a friction function determined by conducting a series of tests without soil present, BB is the back bucket mass, and FB is the front bucket mass. A series of twenty six tests was performed without soil present in the specimen box to calculate the friction function (eq. 3.5b and Figure 3.29). A series of tests where weights were placed in the movable half of the box demonstrated that the weight of the soil specimen should not significantly affect the friction function. Loading rate for use in eq. (3.5a) was calculated as the mass of the front bucket at the end of the test minus the mass of the front bucket at the start of the test divided by the total test time. To determine tensile strength, the tensile force at failure was divided by the cross sectional area of the specimen at the division between the two halves of the box.
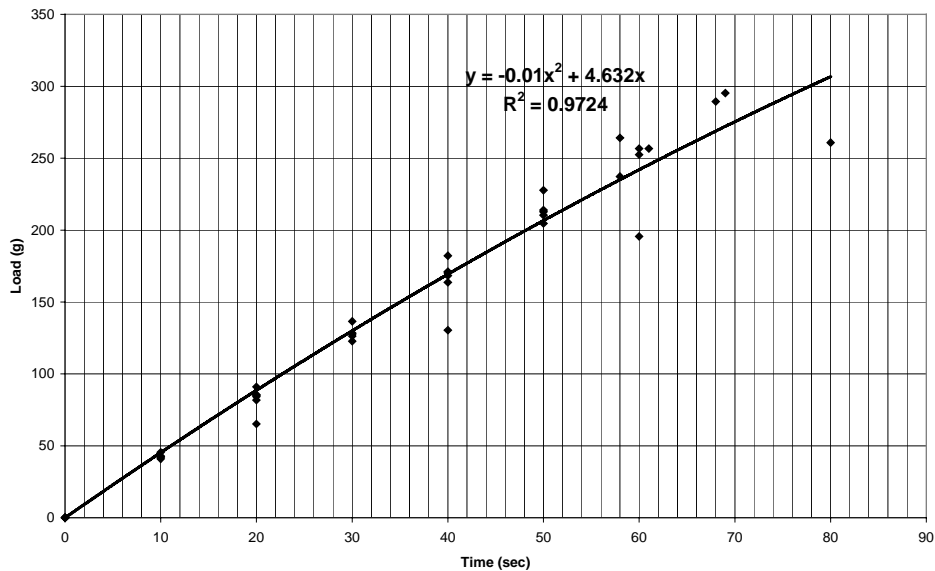
Figure 3. 29: *Results from preliminary testing of system to determine system friction*

4 Results

4.1 Direct Shear Results

Direct shear tests were performed at eight different water contents and two different void ratios for the three gradations of Ottawa sand. Relatively loose ($e = 0.75$) and relatively dense ($e = 0.60$) specimens were prepared at 0%, 2.0%, 4.0%, 6.0%, 8.0%, 10%, 12.0%, 15%, and 18.0% water content. Failure envelopes were obtained by plotting shear stress as a function of normal stress during the tests and drawing a tangent line to the peak shear stress observed.

Detailed testing results from the entire direct shear testing series are included in the Appendix A. For illustration, Figures 4.1 and 4.2 show failure envelopes determined for dry F-75 Ottawa sand compacted to dense and loose conditions, respectively. Figure 4.3 shows shear stress as a function of horizontal displacement for dense F-75 Ottawa sand at 15psi (103 kPa) normal stress prepared to different water contents. Figure 4.4 shows similar results for loose compaction conditions and a normal stress of 40 psi (276 kPa). Tables 4.1 and 4.2 summarize results from the entire series of direct shear tests for F-75 and F-55 Ottawa Sand. Results are interpreted in Chapter 5.
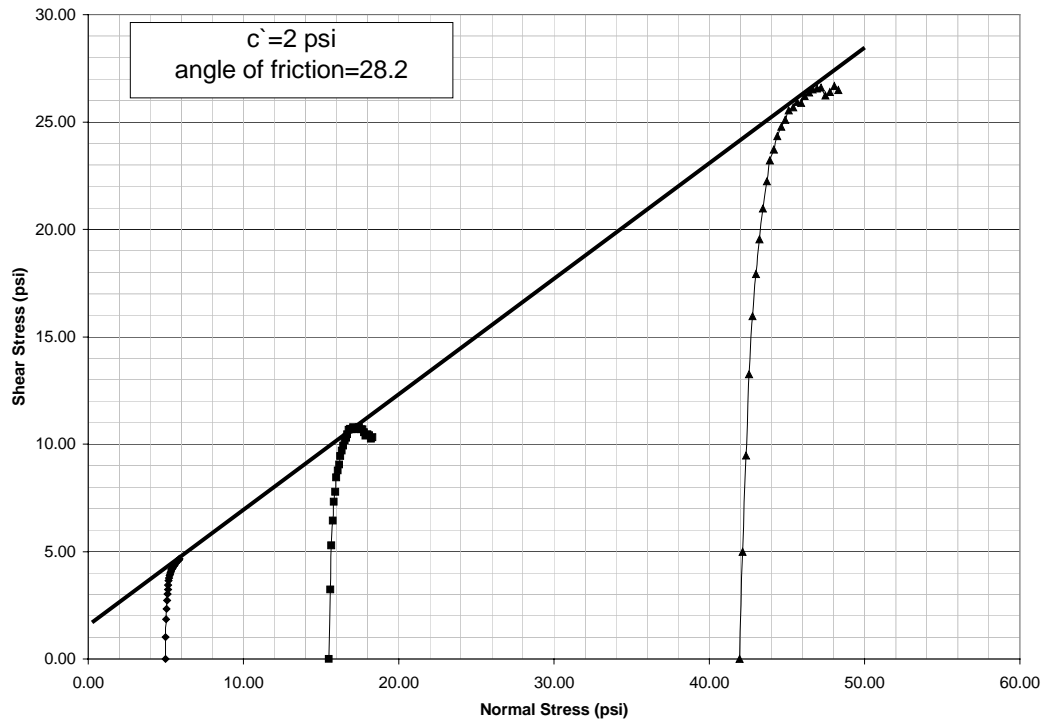
Figure 4. 1: *Failure envelope for loose dry F-75 Ottawa sand (e= 0.60)*
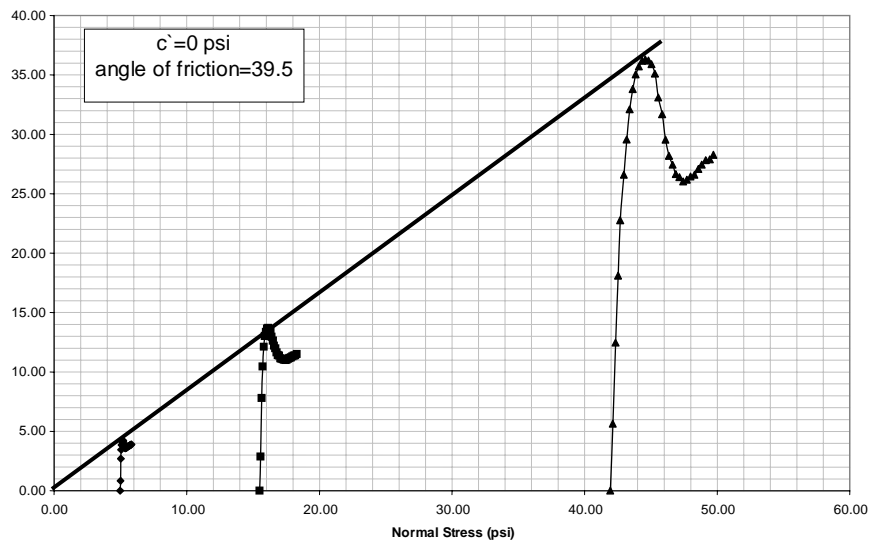
Figure 4. 2: *Failure envelope for dense dry F-75 Ottawa sand (e= 0.75)*
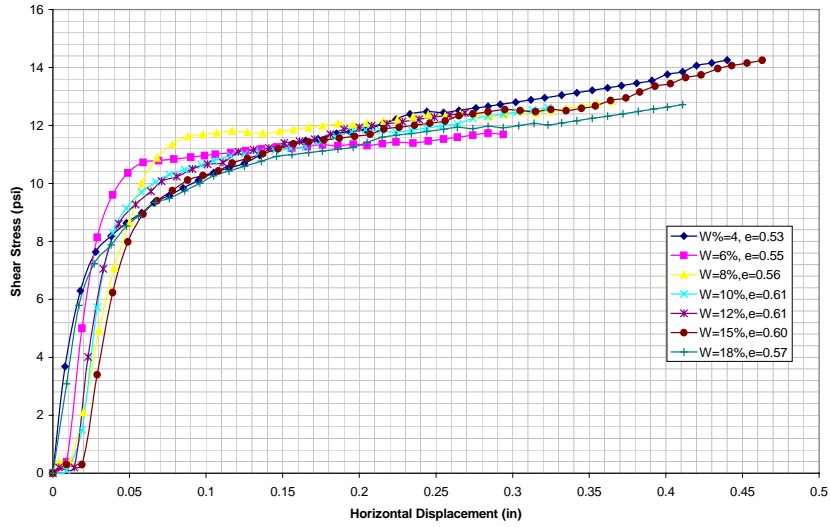
Figure 4. 3: *Shear stress as a function of horizontal displacement at different water contents for dense F-75 Ottawa sand ($\sigma_n = 15$ psi)*
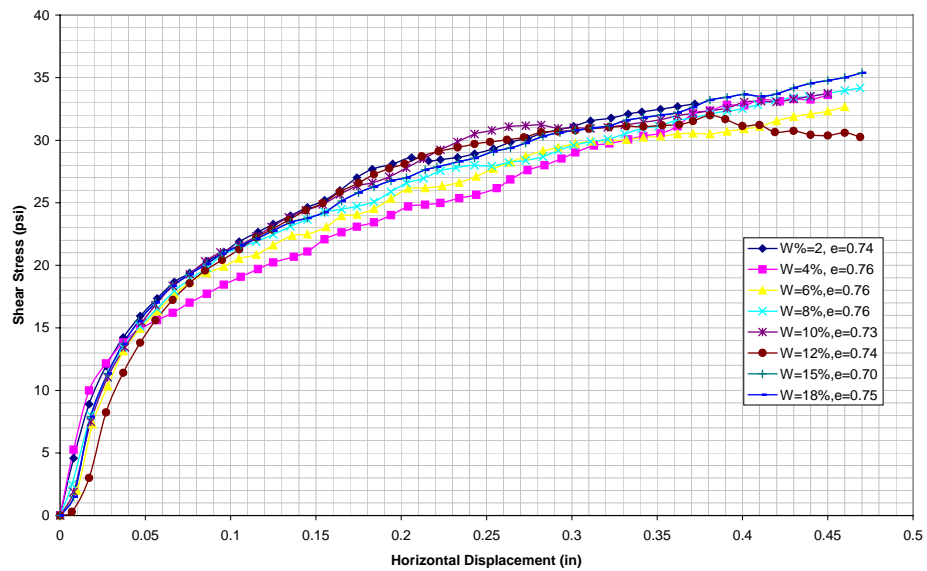
Figure 4. 4: *Shear stress as a function of horizontal displacement at different water contents for loose F-75 Ottawa sand ($\sigma_n = 40$ psi)*

Table 4. 1: *Direct Shear Results for F-75 Ottawa Sand*

Water Content (Target)						2%					
F-75	**Dense**					**Loose**					
Normal Stress (Target) (psi)	5		15		40		5		15		40	
Normal Stress (Failure) (psi & kPa)							6.24	43	20.94	144	56.96	392
Corrected Area (sq in & sq cm)							3.91	25	3.63	23	3.68	23
Shear Force (lb& N)							15.36	68	46.98	208	121.1	538
Shear Stress (psi & kPa)							3.92	27	12.93	89	32.9	226
Horizontal Displacement (in & cm)							0.27	0.7	0.39	1.0	0.37	1.0
Volumetric Strain (%)							-1.88		-3.07		-2.96	
Initial Void Ratio							0.73		0.76		0.74	
Final Void Ratio							0.7		0.71		0.69	
Angle of Friction (degrees)							29.4					
Capillary Cohesion (psi)							0.87 (5998 Pa)					
Actual Water Content							1.6% (1.8% Mix)					
Saturation(%)							6.1		6.0		6.1	
Volumetric Water Content (%)							2.6		2.6		2.6	

(continued)

Water Content (Target)	4%											
F-75	**Dense**						**Loose**					
Normal Stress (Target) (psi)	5		15		40		5		15		40	
Normal Stress (Failure) (psi & kPa)	6.39	44	21.63	149	57.75	398	6.39	44	21.19	146	58.92	406
Corrected Area (sq in & sq cm)	3.82	25	3.52	23	3.57	23	3.82	25	3.59	23	3.49	22
Shear Force (lb& N)	16.71	74	50.14	223	119.3	530	15.81	70	46.53	207	117.4	522
Shear Stress (psi & kPa)	4.37	30	14.25	98	33.45	231	4.13	28	12.95	89	33.61	232
Horizontal Displacement (in & cm)	0.31	0.79	0.44	1.12	0.42	1.07	0.31	0.79	0.41	1.04	0.45	1.14
Volumetric Strain (%)	0.93		-1.53		-0.8		-1.82		-2.97		-3.22	
Initial Void Ratio	0.55		0.56		0.63		0.75		0.76		0.76	
Final Void Ratio	0.57		0.53		0.61		0.71		0.71		0.7	
Angle of Friction (degrees)	28.8						28.9					
Capillary Cohesion (psi)	1.74 (11997 Pa)						1.13 (7791 Pa)					
Actual Water Content	4.2%						3.2 % (3.3% Mix)					
Saturation(%)	19.5		21.0		18.2		11.9		11.9		12.1	
Volumetric Water Content (%)	6.9		7.5		7.1		5.1		5.2		5.2	

Water Content (Target)	6%											
F-75	**Dense**						**Loose**					
Normal Stress (Target) (psi)	5		15		40		5		15		40	
Normal Stress (Failure) (psi & kPa)	5.58	38	19.69	136	58.57	404	6.24	43	21.49	148	59.33	409
Corrected Area (sq in & sq cm)	4.38	28	3.86	25	3.52	23	3.91	25	3.54	23	3.47	22
Shear Force (lb& N)	19.42	86	45.17	201	119.7	533	15.81	70	45.62	203	113.4	504
Shear Stress (psi & kPa)	4.44	31	34.05	235	119.7	825	4.04	28	12.88	89	32.67	225
Horizontal Displacement (in & cm)	0.08	0.20	0.29	0.74	0.44	1.12	0.27	0.69	0.43	1.09	0.46	1.17
Volumetric Strain (%)	-0.08		0.12		-0.8		-2.54		-2.85		-2.85	
Initial Void Ratio	0.56		0.55		0.55		0.76		0.76		0.76	
Final Void Ratio	0.55		0.55		0.54		0.72		0.71		0.71	
Angle of Friction (degrees)	29.3						27.6					
Capillary Cohesion (psi)	1.18 (8135 Pa)						1.69 (11652 Pa)					
Actual Water Content	5.2% (5.2% Mix)						5.2 % (5.7% Mix)					
Saturation(%)	25.1		25.1		25.5		19.1		19.4		19.4	
Volumetric Water Content (%)	9.0		8.9		9.1		8.3		8.4		8.4	

(continued)

Water Content (Target)	8%										
F-75	**Dense**						**Loose**				
Normal Stress (Target) (psi)	5		15		40		5		15		40	
Normal Stress (Failure) (psi & kPa)	5.64	39	20.59	142	59.73	412	6.24	43	20.68	143	59.69	412
Corrected Area (sq in & sq cm)	4.33	28	3.7	24	3.45	22	3.92	25	3.68	24	3.45	22
Shear Force (lb& N)	20.33	90	47.43	211	131.9	589	15.36	68	47.43	211	117.9	524
Shear Stress (psi & kPa)	4.7	32	12.83	89	38.27	264	3.92	27	12.89	89	34.18	236
Horizontal Displacement (in & cm)	0.1	0.25	0.37	0.94	0.45	1.14	0.27	0.69	0.37	0.94	0.47	1.19
Volumetric Strain (%)	-0.13		0.06		-0.46		-2.42		-3.22		-3.07	
Initial Void Ratio	0.56		0.56		0.56		0.76		0.75		0.76	
Final Void Ratio	0.56		0.56		0.55		0.72		0.69		0.71	
Angle of Friction (degrees)	27.6						29					
Capillary Cohesion (psi)	1.06 (7308 Pa)						1.11 (7653 Pa)					
Actual Water Content	7.6% (7.6% Mix)						6.7% (7.3% Mix)					
Saturation(%)	36.0		36.0		36.6		24.7		25.7		25.0	
Volumetric Water Content (%)	12.9		12.9		13.1		10.6		11.0		10.8	

Water Content (Target)	10%											
F-75	**Dense**						**Loose**					
Normal Stress (Target) (psi)	5		15		40		5		15		40	
Normal Stress (Failure) (psi & kPa)	6.06	42	20.05	138	56.4	389	6.48	45	20.32	140	58.92	406
Corrected Area (sq in & sq cm)	4.03	26	3.8	25	3.65	24	3.77	24	3.75	24	3.49	23
Shear Force (lb& N)	18.07	80	47.88	213	121.5	541	15.81	70	49.24	219	117.9	525
Shear Stress (psi & kPa)	4.48	31	12.62	87	33.28	230	4.19	29	13.14	91	33.74	233
Horizontal Displacement (in & cm)	0.22	0.56	0.32	0.81	0.38	0.97	0.33	0.84	0.34	0.86	0.45	1.14
Volumetric Strain (%)	0.11		-0.56		-1.2		-1.98		-2.49		-3	
Initial Void Ratio	0.61		0.61		0.61		0.76		0.76		0.73	
Final Void Ratio	0.61		0.6		0.59		0.72		0.72		0.68	
Angle of Friction (degrees)	29.7						28.9					
Capillary Cohesion (psi)	1.11 (7653 Pa)						1.22 (8411 Pa)					
Actual Water Content	9.4% (9.9%)						0.095					
Saturation(%)	40.8		41.5		42.2		35.0		35.0		37.0	
Volumetric Water Content (%)	15.5		15.7		16.0		15.1		15.1		15.6	

(continued)

Water Content (Target)						12%					
F-75		**Dense**						**Loose**			
Normal Stress (Target) (psi)	5		15		40		5		15		40	
Normal Stress (Failure) (psi & kPa)	6.1	42	19.39	134	60.53	417	6.47	45	12.23	84	56.29	388
Corrected Area (sq in & sq cm)	4.01	26	3.92	25	3.4	22	3.78	24	3.42	22	3.66	24
Shear Force (lb& N)	18.07	80	48.78	217	124.2	553	16.71	74	46.07	205	117	520
Shear Stress (psi & kPa)	4.51	31	12.43	86	36.52	252	4.43	31	13.46	93	31.98	220
Horizontal Displacement (in & cm)	0.23	0.58	0.27	0.69	0.45	1.14	0.33	0.84	0.48	1.22	0.38	0.97
Volumetric Strain (%)	-0.05		-0.57		-1.45		-1.69		-2.75		-3.59	
Initial Void Ratio	0.61		0.61		0.59		0.73		0.73		0.74	
Final Void Ratio	0.6		0.6		0.57		0.7		0.68		0.69	
Angle of Friction (degrees)	30.1						28.5					
Capillary Cohesion (psi)	1.37 (9445 Pa)						1.38 (9514 Pa)					
Actual Water Content	11.4% (12.0% Mix)						11.7% (12.1% Mix)					
Saturation(%)	50.4		50.4		53.0		44.3		45.6		44.9	
Volumetric Water Content (%)	19.1		19.1		19.7		18.7		19.2		19.1	

Water Content (Target)	15%										
F-75	**Dense**						**Loose**				
Normal Stress (Target) (psi)	5		15		40		5		15		40	
Normal Stress (Failure) (psi & kPa)	6.19	43	21.97	151	60.53	417	6.32	44	20.43	141	59.73	412
Corrected Area (sq in & sq cm)	3.95	25	3.46	22	3.4	22	3.86	25	3.72	24	3.45	22
Shear Force (lb& N)	18.97	84	49.69	221	123.8	551	16.26	72	45.17	201	122	542
Shear Stress (psi & kPa)	4.81	33	14.35	99	36.38	251	4.21	29	12.13	84	35.38	244
Horizontal Displacement (in & cm)	0.26	0.66	0.46	1.17	0.49	1.24	0.29	0.74	0.35	0.89	0.47	1.19
Volumetric Strain (%)	0.06		-0.94		-2.55		-1.79		-1.63		-2.28	
Initial Void Ratio	0.59		0.6		0.6		0.69		0.66		0.7	
Final Void Ratio	0.59		0.59		0.56		0.66		0.63		0.67	
Angle of Friction (degrees)	28.3						30.6					
Capillary Cohesion (psi)	1.71 (11790 Pa)						1.0 (6895 Pa)					
Actual Water Content	14.5% (14.0 % Mix)						0.143					
Saturation(%)	65.1		65.1		68.6		57.4		60.2		56.6	
Volumetric Water Content (%)	24.2		24.4		25.7		23.4		23.9		23.3	

Water Content (Target)						18%					
F-75	**Dense**						**Loose**				
Normal Stress (Target) (psi)	5		15		40		5		15		40	
Normal Stress (Failure) (psi & kPa)	6.24	43	21.22	146	59.73	412	6.32	44	20.43	141	59.73	412
Corrected Area (sq in & sq cm)	3.92	25	3.59	23	3.45	22	3.86	25	3.72	24	3.45	22
Shear Force (lb& N)	18.52	82	45.62	203	121.5	541	16.26	72	45.17	201	122	543
Shear Stress (psi & kPa)	4.73	33	12.72	88	35.25	243	4.21	29	12.13	84	35.38	244
Horizontal Displacement (in & cm)	0.27	0.69	0.41	1.04	0.47	1.19	0.29	0.74	0.35	0.89	0.47	1.19
Volumetric Strain (%)	-0.05		-0.9		-1.66		-1.79		-1.63		-2.28	
Initial Void Ratio	0.58		0.57		0.58		0.73		0.7		0.75	
Final Void Ratio	0.58		0.56		0.55		0.7		0.68		0.71	
Angle of Friction (degrees)	29.7						30.6					
Capillary Cohesion (psi)	1.25 (8618 Pa)						0.75 (5171 Pa)					
Actual Water Content	17.9 % (17.9% Mix)											
Saturation(%)	81.8		84.7		86.2							
Volumetric Water Content (%)	30.0		30.8		31.7							

Table 4. 2: *Direct Shear Results for F-55 Ottawa Sand*

Water Content (Target)	2%											
F-55	**Dense**						**Loose**					
Normal Stress (Target) (psi)	5		15		40		5		15		40	
Normal Stress (Failure) (psi & kPa)							6.63	46	20.05	138	59.69	412
Corrected Area (sq in & sq cm)							3.68	24	3.8	25	3.45	22
Shear Force (lb& N)							15.36	68	45.62	203	116.1	517
Shear Stress (psi & kPa)							4.17	29	12.02	83	33.66	232
Horizontal Displacement (in & cm)							0.37	0.94	0.32	0.81	0.47	1.19
Volumetric Strain (%)							-1.53		-2.43		-2.83	
Initial Void Ratio							0.73		0.76		0.76	
Final Void Ratio							0.7		0.72		0.71	
Angle of Friction (degrees)							28.6					
Capillary Cohesion (psi)							1.09 (7515 Pa)					
Actual Water Content							1.2% (1.4% Mix)					
Saturation(%)							4.5		4.4		4.5	
Volumetric Water Content (%)							1.9		1.9		1.9	

Water Content (Target)	4%											
F-55	**Dense**						**Loose**					
Normal Stress (Target) (psi)	5		15		40		5		15		40	
Normal Stress (Failure) (psi & kPa)							6.32	44	19.68	136	53.25	367
Corrected Area (sq in & sq cm)							3.87	25	3.87	25	3.87	25
Shear Force (lb & N)							14.16	63	41.1	183	119.3	530
Shear Stress (psi & kPa)							3.62	25	10.63	73	30.84	212
Horizontal Displacement (in & cm)							0.29	0.74	0.29	0.74	0.29	0.74
Volumetric Strain (%)							-1.59		-1.87		-2.64	
Initial Void Ratio							0.76		0.76		0.76	
Final Void Ratio							0.73		0.73		0.72	
Angle of Friction (degrees)							30.1					
Capillary Cohesion (psi)							0					
Actual Water Content							3.8% (3.6% Mix)					
Saturation(%)							13.8		13.8		14.0	
Volumetric Water Content (%)							6.0		6.0		6.0	

(continued)

Water Content (Target)	6%								
F-55	**Dense**				**Loose**				
Normal Stress (Target) (psi)	5		15		40	5		15		40	
Normal Stress (Failure) (psi & kPa)						6.24	43	20.16	139	58.88	406
Corrected Area (sq in & sq cm)						3.91	25	3.77	24	3.5	23
Shear Force (lb& N)						12.65	56	45.62	203	121.5	541
Shear Stress (psi & kPa)						3.23	23	12.09	83	34.75	240
Horizontal Displacement (in & cm)						0.27	0.69	0.33	0.84	0.45	1.14
Volumetric Strain (%)						-0.96		-2.58		-2.88	
Initial Void Ratio						0.75		0.76		0.76	
Final Void Ratio						0.73		0.72		0.71	
Angle of Friction (degrees)						30.5					
Capillary Cohesion (psi)						0					
Actual Water Content						5.4% (5.6% Mix)					
Saturation(%)						19.6		19.9		20.2	
Volumetric Water Content (%)						8.4		8.6		8.7	

Water Content (Target)						8%					
F-55	**Dense**					**Loose**					
Normal Stress (Target) (psi)	5		15		40		5		15		40
Normal Stress (Failure) (psi & kPa)							6.24	43	19.45	134	54.52	376
Corrected Area (sq in & sq cm)							3.91	25	3.91	25	3.78	24
Shear Force (lb& N)							15.36	68	25.75	115	118.4	526
Shear Stress (psi & kPa)							3.93	27	6.58	45	31.34	216
Horizontal Displacement (in & cm)							0.27	0.69	0.27	0.69	0.33	0.84
Volumetric Strain (%)							-2.23		-2.17		-2.51	
Initial Void Ratio							0.75		0.76		0.78	
Final Void Ratio							0.71		0.73		0.74	
Angle of Friction (degrees)							29.9					
Capillary Cohesion (psi)							0					
Actual Water Content							7.1% (7.7% Mix)					
Saturation(%)							26.5		25.8		25.4	
Volumetric Water Content (%)							11.4		11.1		11.1	

(continued)

Water Content (Target)	10%											
F-55	**Dense**						**Loose**					
Normal Stress (Target) (psi)	5		15		40		5		15		40	
Normal Stress (Failure) (psi & kPa)	6.24	43	19.67	136	54.52	376	6.36	44	20.15	139	57.37	396
Corrected Area (sq in & sq cm)	3.91	25	3.87	25	3.78	24	3.84	25	3.78	24	3.59	23
Shear Force (lb& N)	16.71	74	45.17	201	113.4	504	15.36	68	46.98	209	117	520
Shear Stress (psi & kPa)	4.27	29	11.67	80	30.02	207	4	28	12.44	86	32.6	225
Horizontal Displacement (in & cm)	0.27	0.69	0.29	0.74	0.33	0.84	0.3	0.76	0.33	0.84	0.41	1.04
Volumetric Strain (%)	0.19		-0.43		-1.3		-1.37		-2.43		-2.67	
Initial Void Ratio	0.6		0.61		0.6		0.74		0.75		0.74	
Final Void Ratio	0.61		0.6		0.58		0.72		0.7		0.7	
Angle of Friction (degrees)	27.6						28.3					
Capillary Cohesion (psi)	1.57 (10824 Pa)						1.66 (11445 Pa)					
Actual Water Content							9.6%					
Saturation(%)							35.3		36.3		36.3	
Volumetric Water Content (%)							15.0		15.6		15.5	

Water Content (Target)	12%										
F-55	**Dense**						**Loose**				
Normal Stress (Target) (psi)	5		15		40		5		15		40	
Normal Stress (Failure) (psi & kPa)	6.32	44	19.45	134	58.92	407	6.24	43	20.16	139	55.92	386
Corrected Area (sq in & sq cm)	3.86	25	3.91	25	3.49	23	3.91	25	3.77	24	3.68	24
Shear Force (lb& N)	16.71	74	45.62	203	117.4	522	14.91	66	46.07	205	120.1	534
Shear Stress (psi & kPa)	4.32	30	11.66	80	33.61	232	3.81	26	12.21	84	32.76	226
Horizontal Displacement (in & cm)	0.29	0.74	0.27	0.69	0.45	1.14	0.27	0.69	0.33	0.84	0.37	0.94
Volumetric Strain (%)	0.24		-0.74		-1.41		-1.61		-2.47		-2.45	
Initial Void Ratio	0.59		0.59		0.59		0.74		0.76		0.76	
Final Void Ratio	0.59		0.58		0.57		0.72		0.72		0.72	
Angle of Friction (degrees)	28.7						29.7					
Capillary Cohesion (psi)	1.32 (9101 Pa)						0.86 (5929 Pa)					
Actual Water Content							11.5% (11.9% Mix)					
Saturation(%)							42.3		42.3		42.3	
Volumetric Water Content (%)							18.0		18.3		18.3	

Water Content (Target)	15%										
F-55	**Dense**						**Loose**				
Normal Stress (Target) (psi)	5		15		40		5		15		40	
Normal Stress (Failure) (psi & kPa)							6.39	44	20.82	144	59.29	409
Corrected Area (sq in & sq cm)							3.82	25	3.66	24	3.47	22
Shear Force (lb& N)							15.81	70	46.53	207	115.6	514
Shear Stress (psi & kPa)							4.14	29	12.73	88	33.3	230
Horizontal Displacement (in & cm)							0.31	0.79	0.38	0.97	0.46	1.17
Volumetric Strain (%)							-2.06		-1.76		-2.9	
Initial Void Ratio							0.77		0.74		0.75	
Final Void Ratio							0.73		0.71		0.7	
Angle of Friction (degrees)							28.3					
Capillary Cohesion (psi)							1.35 (9307 Pa)					
Actual Water Content							14.5% (16.0% Mix)					
Saturation(%)							52.6		54.1		54.9	
Volumetric Water Content (%)							22.9		23.0		23.5	

Water Content (Target)	18%					
F-55	**Dense**			**Loose**		
Normal Stress (Target) (psi)	5	15	40	5	15	40
Normal Stress (Failure) (psi & kPa)				6.24 | 43	19.9 | 137	58.92 | 406
Corrected Area (sq in & sq cm)				3.91 | 25	3.82 | 25	3.49 | 23
Shear Force (lb& N)				15.81 | 70	46.98 | 209	118.8 | 528
Shear Stress (psi & kPa)				4.04 | 28	12.28 | 85	34 | 234
Horizontal Displacement (in & cm)				0.27 | 0.69	0.31 | 0.79	0.45 | 1.14
Volumetric Strain (%)				-1.6	-1.64	-2.61
Initial Void Ratio				0.77	0.77	0.75
Final Void Ratio				0.74	0.74	0.7
Angle of Friction (degrees)				29.2		
Capillary Cohesion (psi)				1.12 (7722 Pa)		
Actual Water Content				17.3% (17.6% Mix)		
Saturation(%)				62.0	62.0	65.5
Volumetric Water Content (%)				27.0	27.0	28.1

Vertical deformations were recorded and used to determine volumetric strain.

Figure 4.5, for example, shows volumetric strain as a function of horizontal displacement

for saturated F-75 Ottawa sand at the loose condition. Figure 4.6 shows similar results for

the dense condition. Positive volumetric strain represents dilation of the specimen

whereas negative volumetric strain represents contraction.
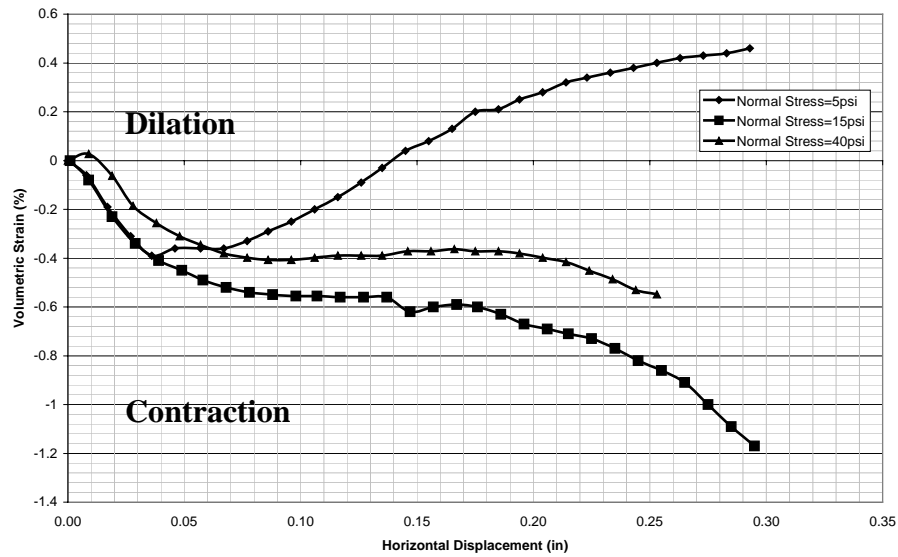
Figure 4. 5: *Volumetric strain as a function of horizontal displacement for saturated loose F-75 Ottawa sand (e=0.75)*
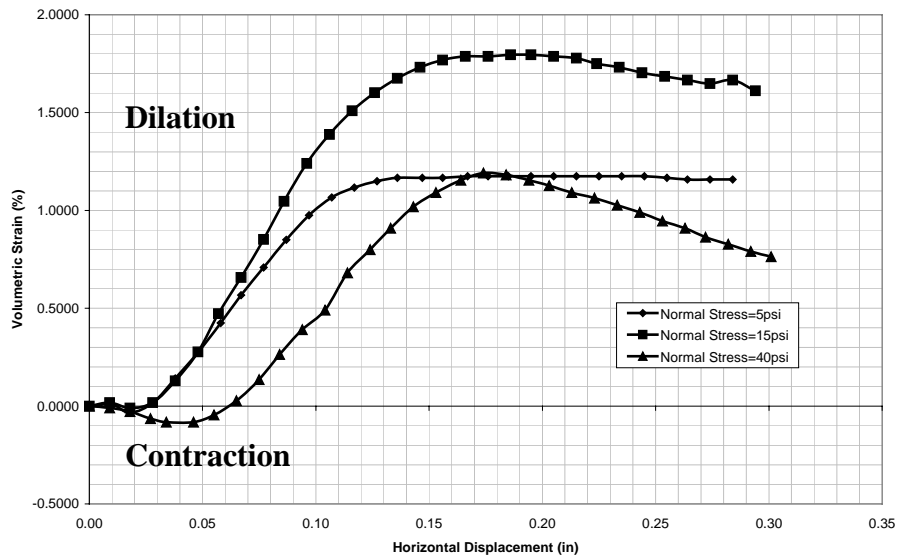
Figure 4. 6: *Volumetric strain as a function of horizontal displacement for saturated dense F-75 Ottawa sand (e=0.60)*

Figures 4.7, 4.8, 4.9 show volumetric strain as a function of horizontal displacement at different water contents for F-75 Ottawa sand and the dense condition under 5 psi, 15 psi, and 40 psi normal stresses respectively. Figures 4.10, 4.11, and 4.12 show similar results for the loose condition.
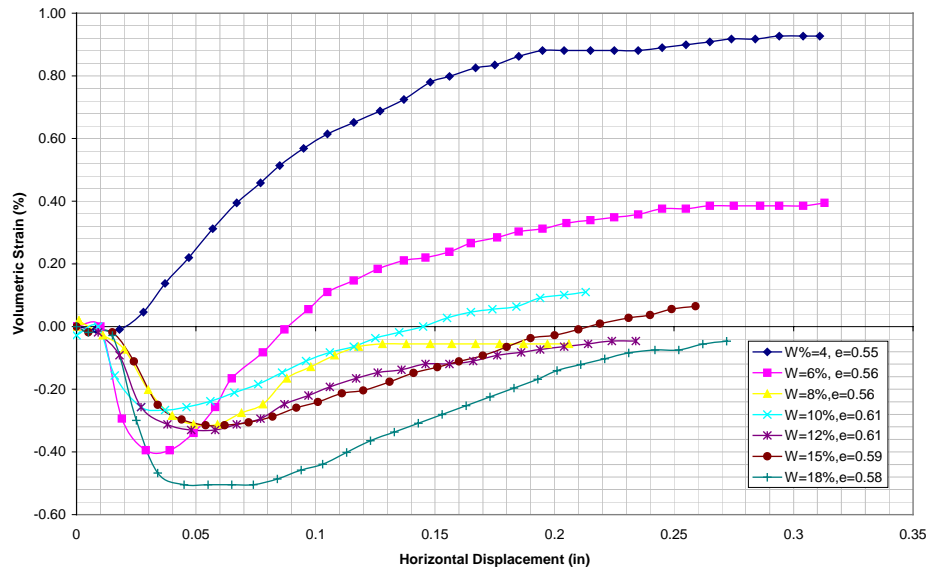
Figure 4. 7: Volumetric strain as a function of horizontal displacement at different water contents for dense F-75 Ottawa sand (σ_n =5psi)
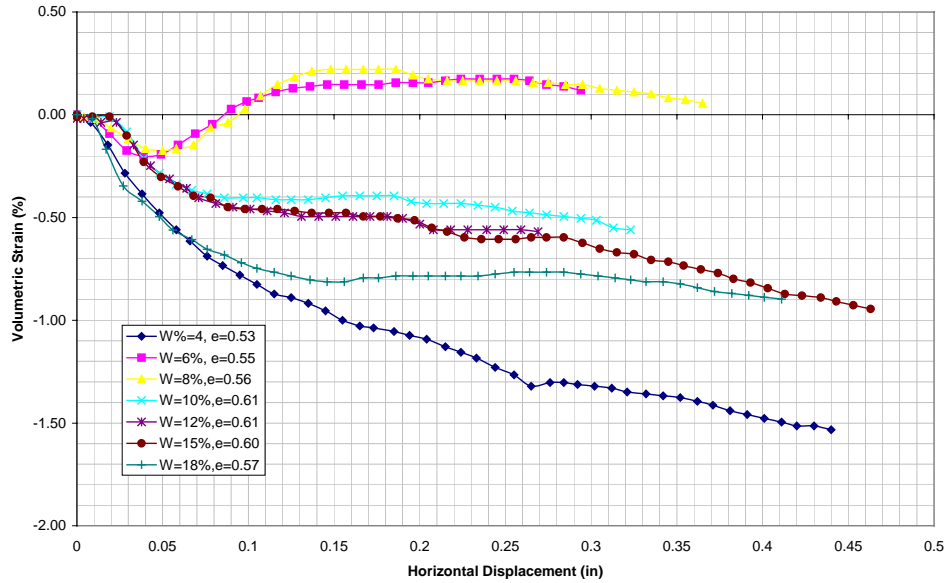
Figure 4. 8: *Volumetric strain as a function of horizontal displacement at different water contents for dense F-75 Ottawa sand (σ_n =15psi)*

Figure 4. 9: *Volumetric strain as a function of horizontal displacement at different water contents for dense F-75 Ottawa sand (σ_n =40psi)*

Figure 4. 10: *Volumetric strain as a function of horizontal displacement at different water contents for loose F-75 Ottawa sand (σ_n =5psi)*

Figure 4. 11: *Volumetric strain as a function of horizontal displacement at different water contents for loose F-75 Ottawa sand (σ_n =15psi)*
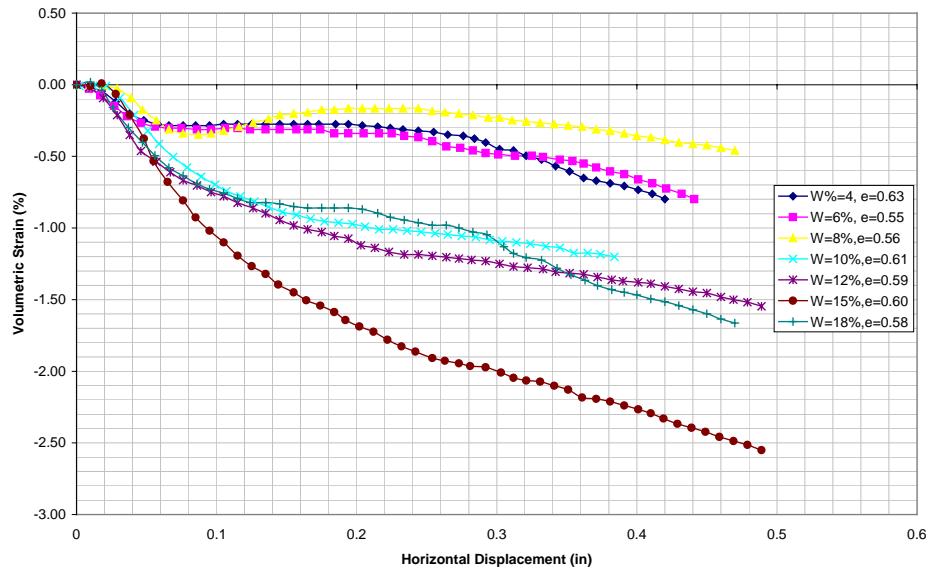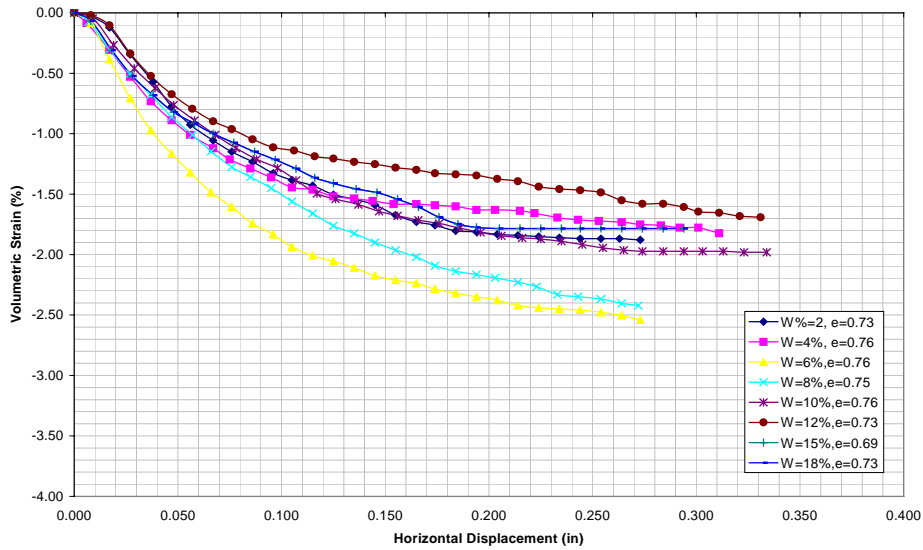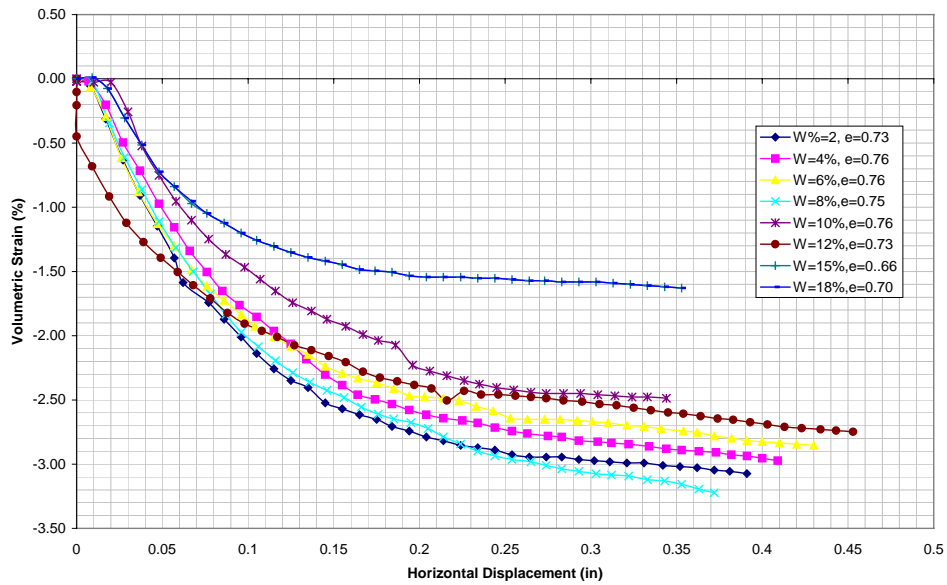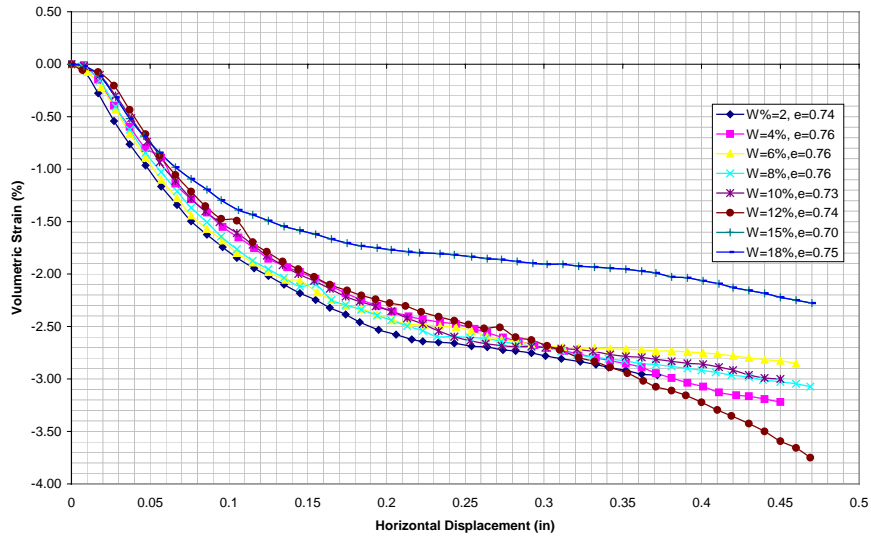
Figure 4. 12: *Volumetric Strain as a function of Horizontal Displacement at different water contents for loose F-75 Ottawa Sand (σ_n =40psi)*

4.2 Tensile Strength Results

A series of tensile strength tests were performed at eight different water contents, and two different void ratios. F-75 Ottawa sand, F-55 Ottawa sand, and F-40 Ottawa sand compacted to loose ($e \sim 0.75$) and dense ($e \sim 0.60$) conditions were prepared at 2.0%, 4.0%, 6.0%, 8.0%, 10%, 12.0%, 15.0%, and 18.0% water contents. The data obtained was reduced and the tensile strength was calculated for each test. Tensile strength was determined by calculating the ultimate tensile stress obtained from the test after the friction of the system was subtracted. Tables 4.3, 4.4, and 4.5 show results obtained for the tensile strength tests for F-40, F-55, and F-75 Ottawa sand. Tensile strength values for F-40 Ottawa sand are plotted as a function of degree of saturation and water content in Figure 4.13. Similar results are shown in Figures 4.14 and 4.15 for F-55 and F-75 Ottawa sand.

Table 4. 3: *Summary of tensile strength results for F-40 Ottawa sand*

F-40	Tensile Strength (Pa)		Saturation (%)	
Water Content	Dense	Loose	Dense	Loose
2%	3035	3248	8%	7%
4%	2762	2905	18%	14%
6%	2752	2665	27%	21%
8%	2845.	2337	35%	28%
10%	2372	3843	44%	35%
12%	3515	3637	53%	42%
15%	3872	3561	66%	53%
18%	5643	5481	80%	64%
Void Ratio	0.60	0.75	0.60	0.75
Porosity	38%	43%	38%	43%

Table 4. 4: *Summary of tensile strength results for F-55 Ottawa sand*

F-55	Tensile Strength (Pa)		Saturation (%)	
Water Content	Dense	Loose	Dense	Loose
2%	3073	2987	8%	7%
4%	2651	3220	18%	14%
6%	3412	3586	27%	21%
8%	3697	3687	35%	28%
10%	3173	3421	44%	35%
12%	3532	3812	53%	42%
15%	4343	5018	66%	53%
18%	4909	4682	80%	64%
Void Ratio	0.60	0.75	0.60	0.75
Porosity	38%	43%	38%	43%

Table 4. 5: *Summary of tensile strength results for F-75 Ottawa sand*

F-75	Tensile Strength (Pa)		Saturation (%)	
Water Content	*Dense*	*Loose*	*Dense*	*Loose*
2%	3246	2689	8%	7%
4%	3483	3117	18%	14%
6%	6483	4640	27%	21%
8%	4106	4192	35%	28%
10%	3016	3361	44%	35%
12%	3554	3554	53%	42%
15%	4700	5807	66%	53%
18%	7168	4487	80%	64%
Void Ratio	0.60	0.75	0.60	0.75
Porosity	38%	43%	38%	43%
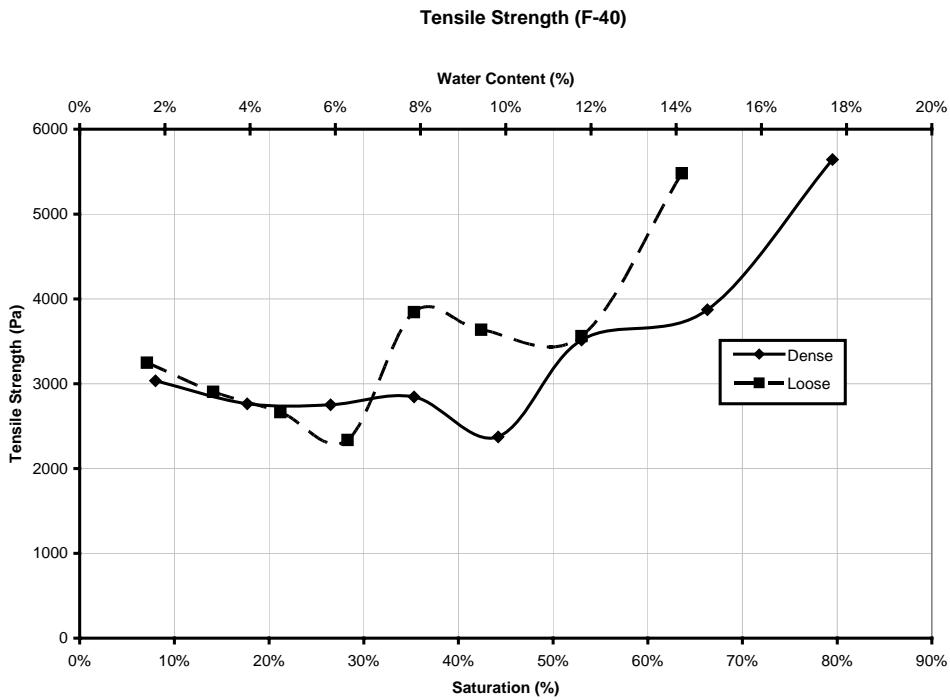
Figure 4. 13: *Tensile strength as a function of degree of saturation for F-40 sand*

Tensile Strength (F-55)
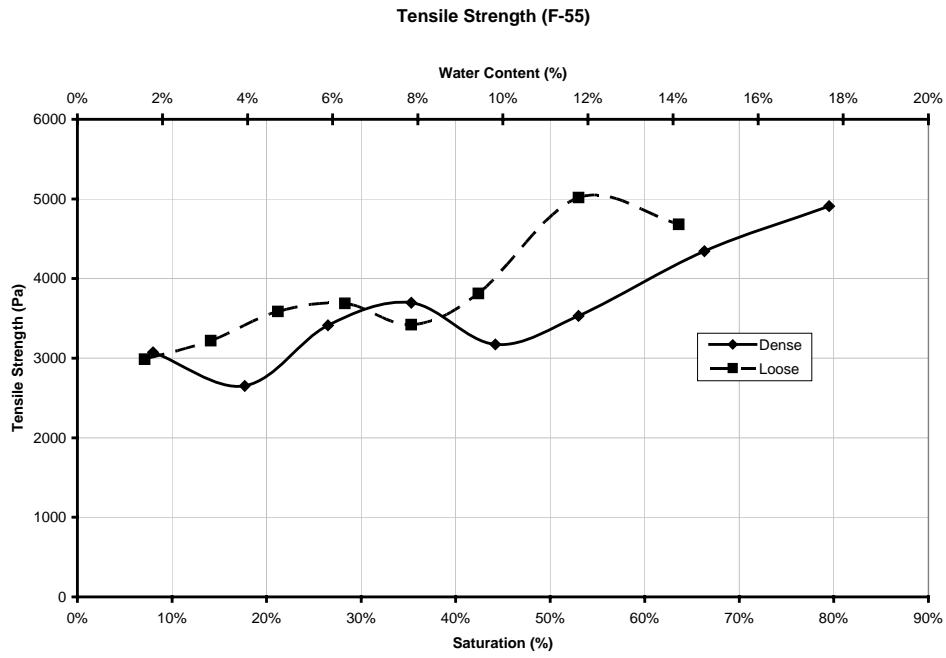
Figure 4. 14: *Tensile strength as a function of degree of saturation for F-55 Ottawa sand*

Tensile Strength (F-75)
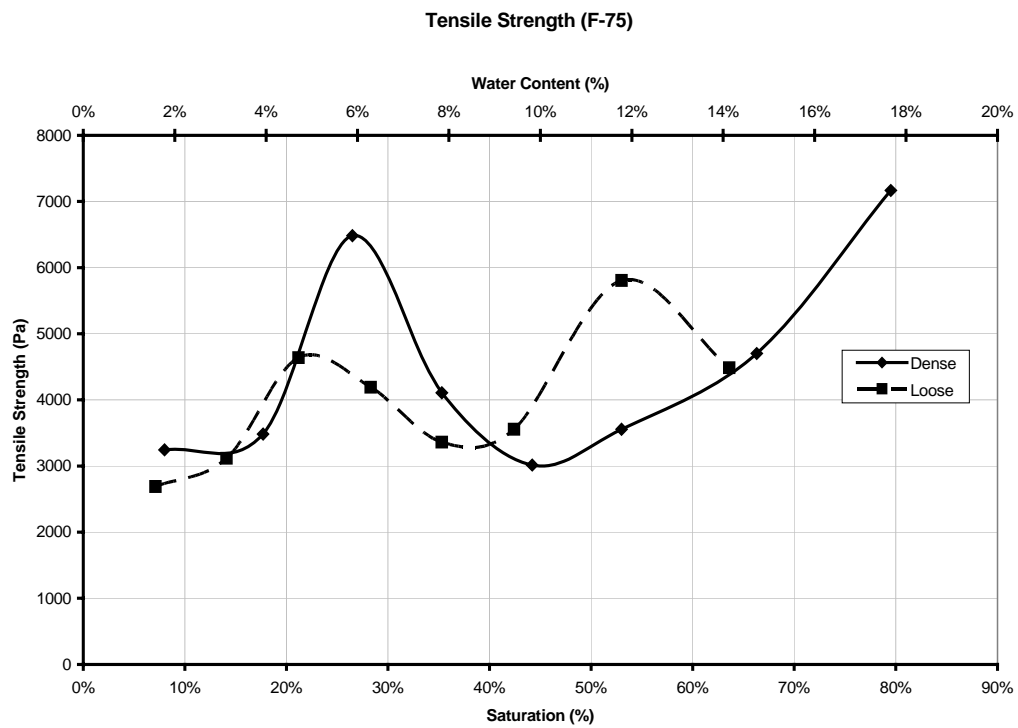
Figure 4. 15: *Tensile strength as a function of degree of saturation for F-75 Ottawa sand*

Figures 4.16 and 4.17 show displacement measured during tensile testing (horizontal box separation) as a function of tensile load for F-75 Ottawa sand at 2% water content and in the dense and loose condition, respectively. Figure 4.18 shows displacement at failure as a function of degree of saturation for all three types of sand prepared at the dense condition. Figure 4.19 shows similar results for the loose condition. Tensile displacement results from the entire suite of tension tests are summarized in the Appendix B.
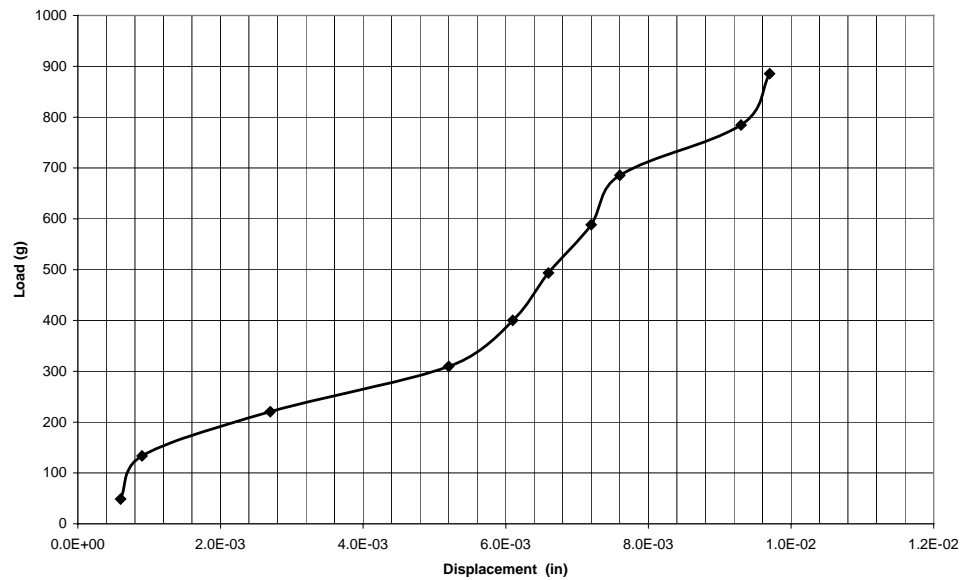
Figure 4. 16: *Load as a function of displacement in a tensile strength test for dense F-75 Ottawa sand (e=0.60 and w=2%)*
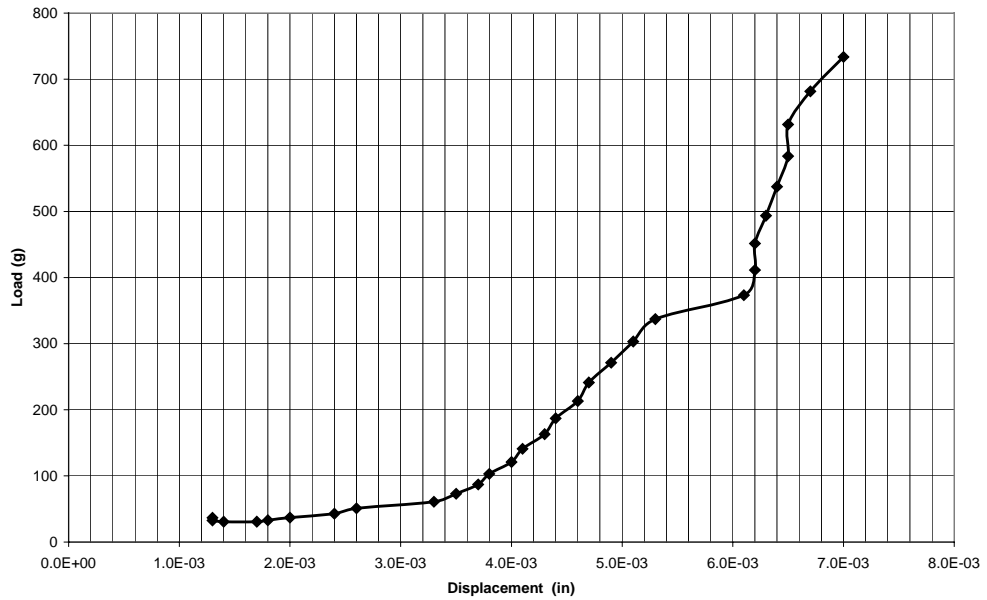
Figure 4. 17: *Load as a function of displacement in a tensile strength test for loose F-75 Ottawa sand (e=0.75 and w=2%)*
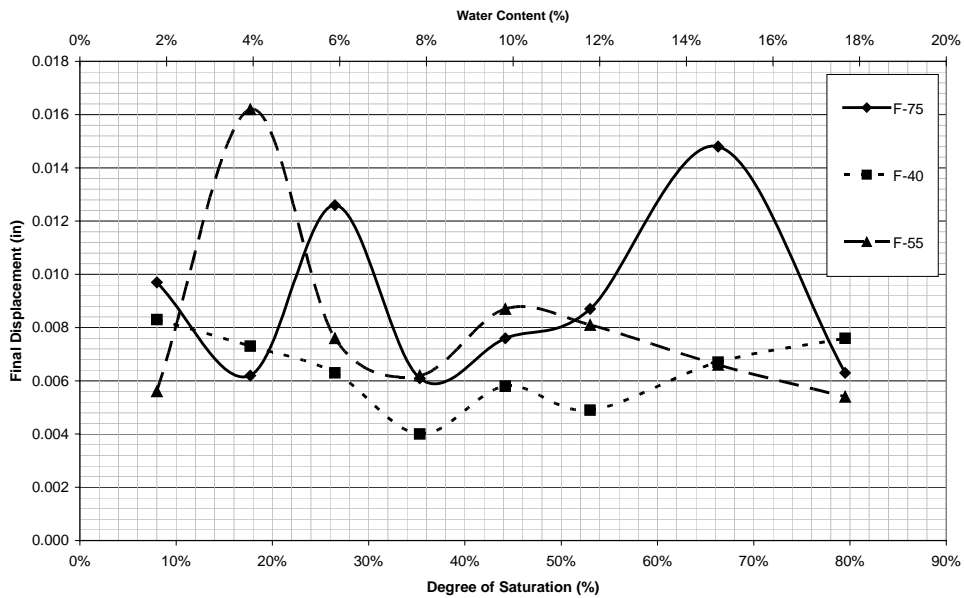
Figure 4. 18: *Horizontal displacement at failure as a function of degree of saturation in the tensile strength test for dense specimens (e=0.60)*

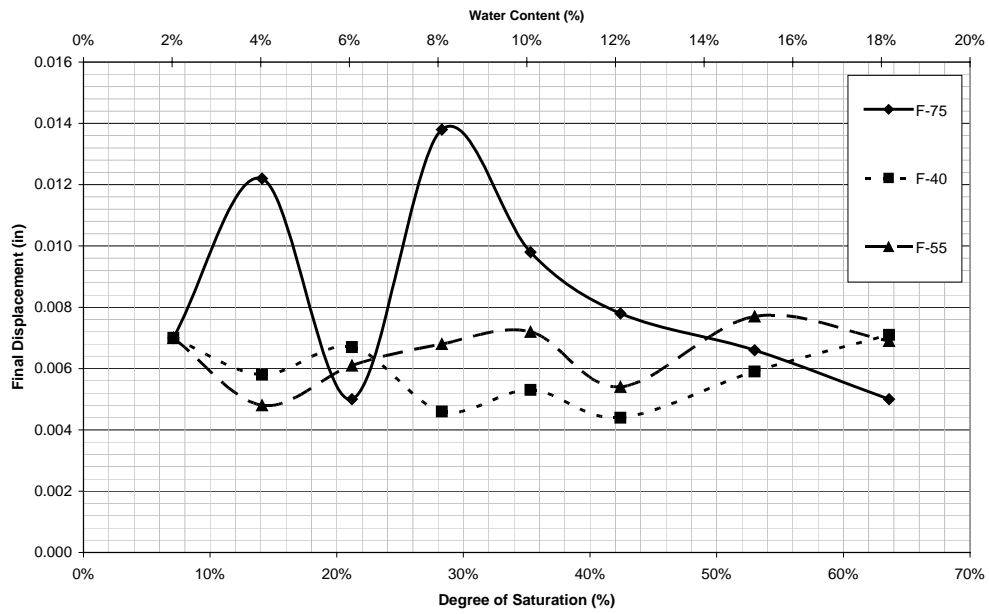**Figure 4. 19:Horizontal displacement at failure as a function of degree of saturation in the tensile strength test for loose specimens (e=0.75)**

5 Discussion and Analysis

5.1 Tensile Strength Model Predictions

Several models were described in Chapter 2 for predicting the tensile strength of bulk unsaturated particle systems in the pendular (σ_{tp}), funicular (σ_{tf}), and capillary (σ_{tc}) water content regimes. Rumpf's (1961) theory for the pendular regime (eq. 2.18) was derived for non-contacting spherical particles and requires estimates of bulk porosity (n), representative particle size (d), surface tension (T_s), contact angle (α), and particle separation distance (a/d). Tensile strength may be estimated as a function of bulk water content or degree of saturation using the filling angle (θ) by applying eqs. (2.14) and (2.17), respectively. Schubert (1984) presented expressions for tensile strength in the capillary regime (eq. 2.19) and funicular regime (eq. 2.21). The former relates tensile strength to degree of saturation and matric suction, which may be determined from the SWCC. The latter normalizes expressions for the pendular regime and capillary regime by establishing boundary degrees of saturation between the funicular and pendular regimes (S_f) and between the funicular and capillary regimes (S_c).

All three regimes (pendular, funicular and capillary) can be determined from the SWCC. Figure 5.1, for example, shows the SWCC determined for F-75 Ottawa sand at the loose condition. Boundaries between saturation regimes may be estimated by drawing tangent lines to estimate residual saturation (S_r) and air-entry saturation (S_{ae}) as shown, which are about 12% and 97%, respectively. Figure 5.2 shows similar estimates from the SWCC for densely compacted F-75 sand.
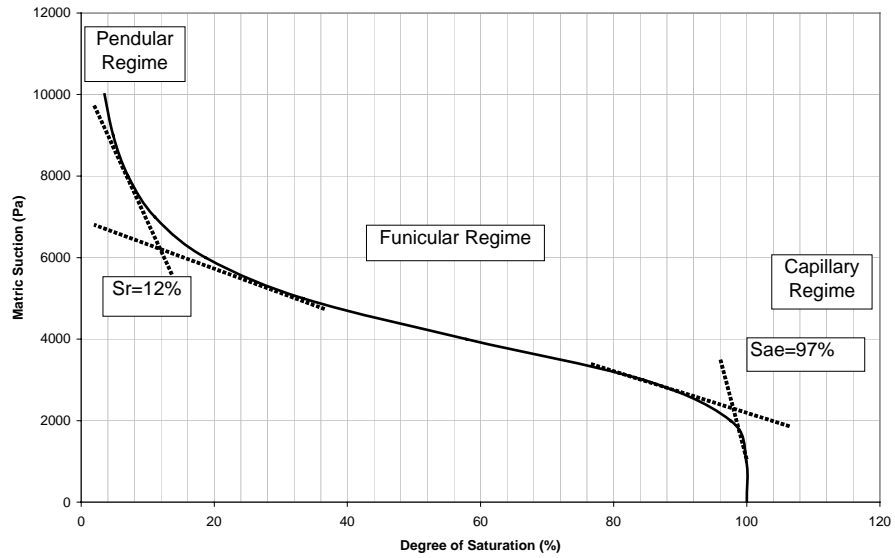
**Figure 5. 1:** *Pendular, Funicular, and Capillary regimes for F-75 Ottawa Sand Loose Specimens (e-0.75)*
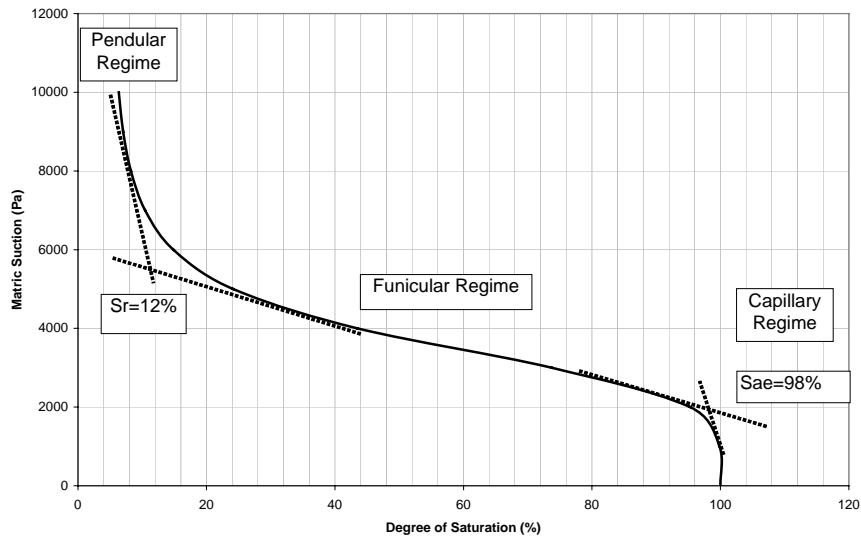
**Figure 5. 2:** *Pendular, Funicular, and Capillary regimes for F-75 Ottawa Sand Dense Specimens (e-0.60)*

For all models presented in this section, S_f (or S_r) and S_c (or S_{ae}) were estimated to be 15% and 90% for simplicity. Material constants selected for modeling in the pendular regime were $\alpha = 0°$, $T_s = 72$ mN/m, and $a/d = 0.025$. Porosity was measured directly from weight-volume relationships for the loose and dense compaction conditions ($n = 43\%$ and 37.5%, respectively). Particle size (d) was assumed a constant value equal to mean particle size (d_{50}) determined from sieve analysis, where $d_{50} = 0.35$ mm, 0.28 mm, and 0.22mm for F-40, F-55, and F-75 sand respectively.

Figure 5.3 summarizes theoretical estimates for all three soils at loose and dense compacted conditions. Within the pendular-dominated regime ($S < \sim30\%$), there is a clear correlation between particle size and tensile strength. Small particle sizes (e.g., F-75) result in significantly higher tensile strength. In addition, relatively densely compacted specimens result in higher tensile strength. At degrees of saturation approaching 50%, the tensile strength predictions begin to become dominated by matric suction. Specimens with higher matric suction for a given degree of saturation exhibit higher tensile strength. Specimens with relatively high-air entry pressure exhibit the largest tensile strength near saturation. In general, this should include either relatively fine-grained specimens or relatively densely compacted specimens, although this is not systematically the case for specimens shown on Figure 5.3. These discrepancies indicate the sensitivity of the model to accuracy in the determination of the SWCC, particularly near the air-entry pressure.
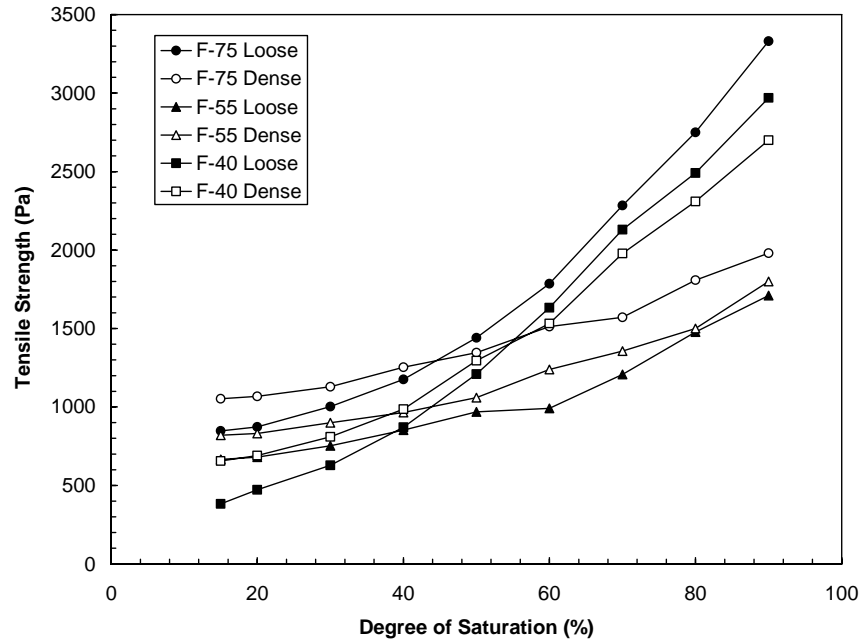
Figure 5. 3: *Tensile strength modeling results for all soil types and compaction conditions*

Figures 5.4 through 5.9 summarize comparisons between experimental tensile strength measurements and modeling results for all of the sand specimens. Comparison shows that the tensile strength models using Rumpf (1961) and Schubert (1984) underpredicted the measured tensile strength of the soil. The Kim (2001) empirical model for clean F-75 sand (eq. 2.27), which is included on Figures 5.8 and 5.9, also appears to underpredict the measured tensile strength but is in good agreement with the Rumpf-Schubert model. Both models do appear to capture the generally increasing trend in tensile strength of the range of saturation measured, but underpredict tensile strength by about 2000 Pa. In addition, none of the predictions characterize the apparent double-peak behavior observed in the tests.
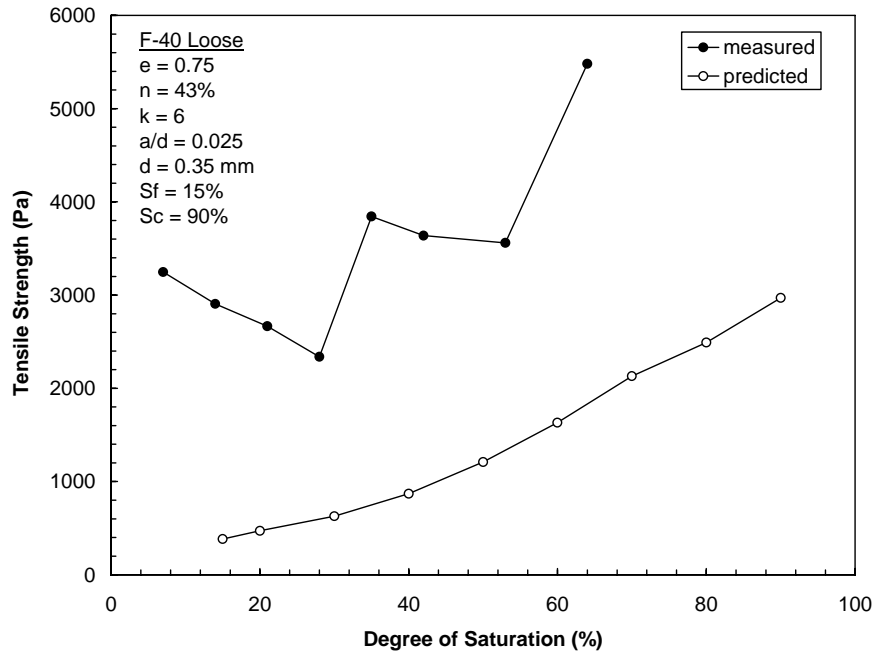
Figure 5. 4: *Measured and predicted tensile strength for loose F-40 sand*
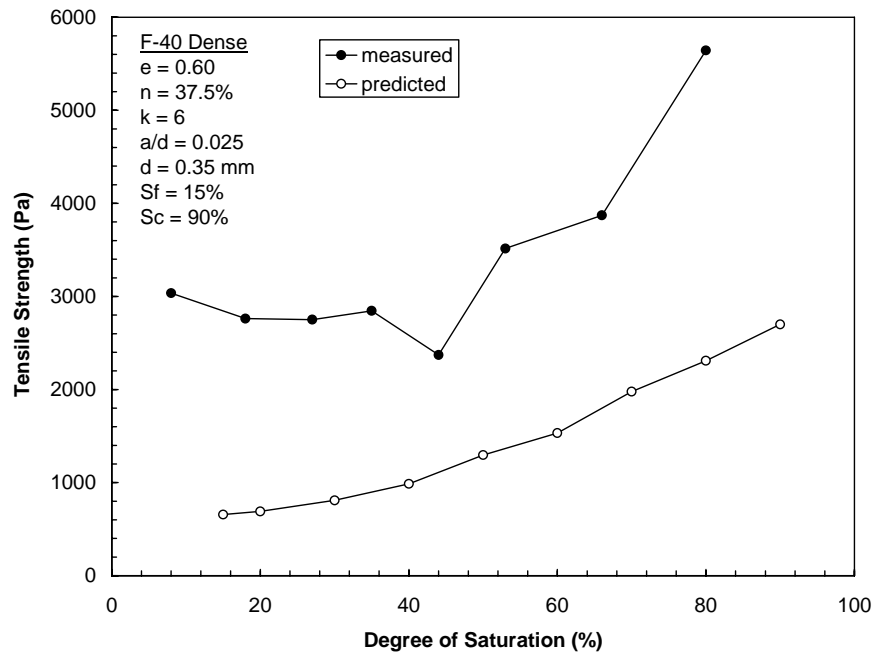
Figure 5. 5: *Measured and predicted tensile strength for dense F-40 sand*
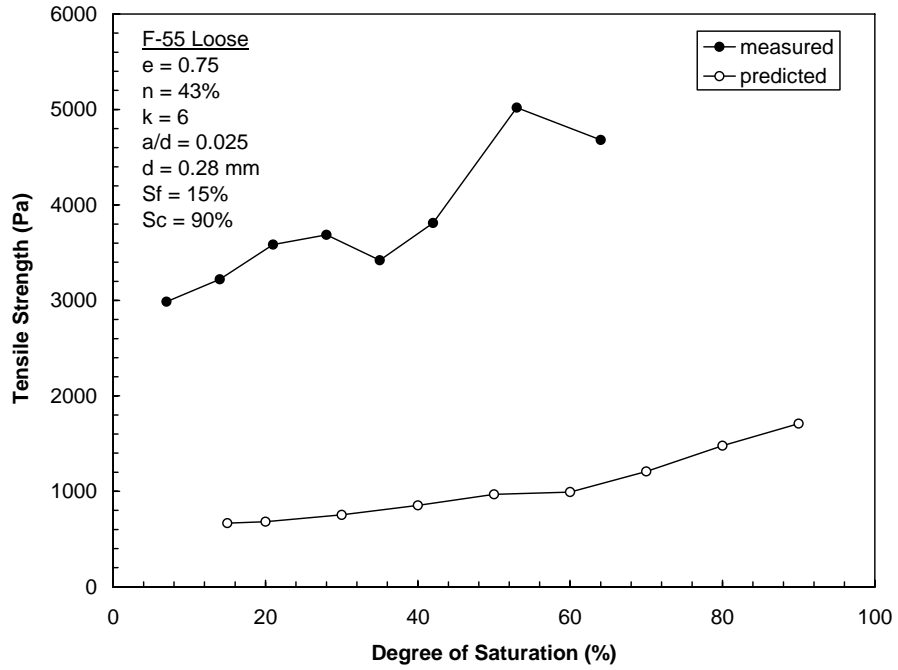
Figure 5. 6: *Measured and predicted tensile strength for loose F-55 sand*

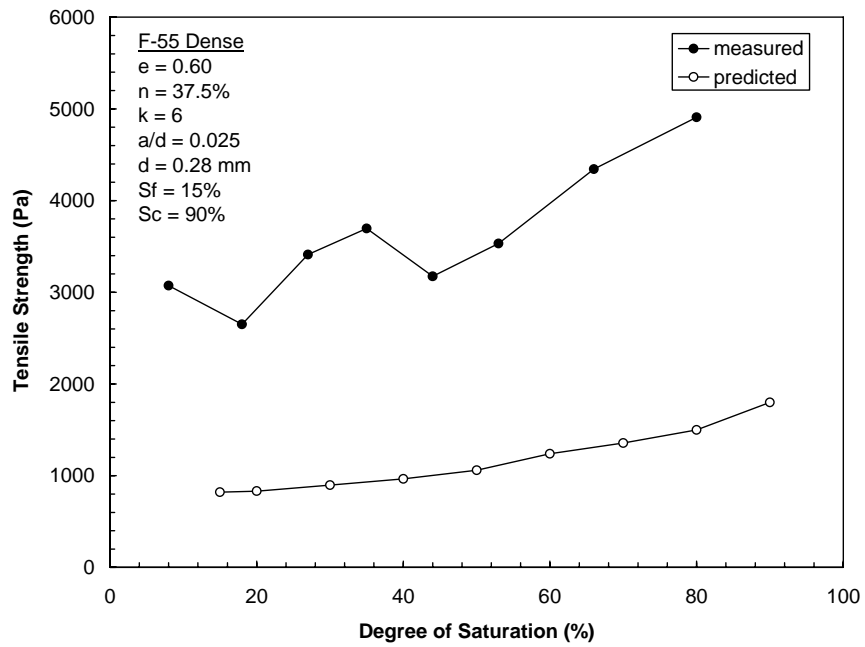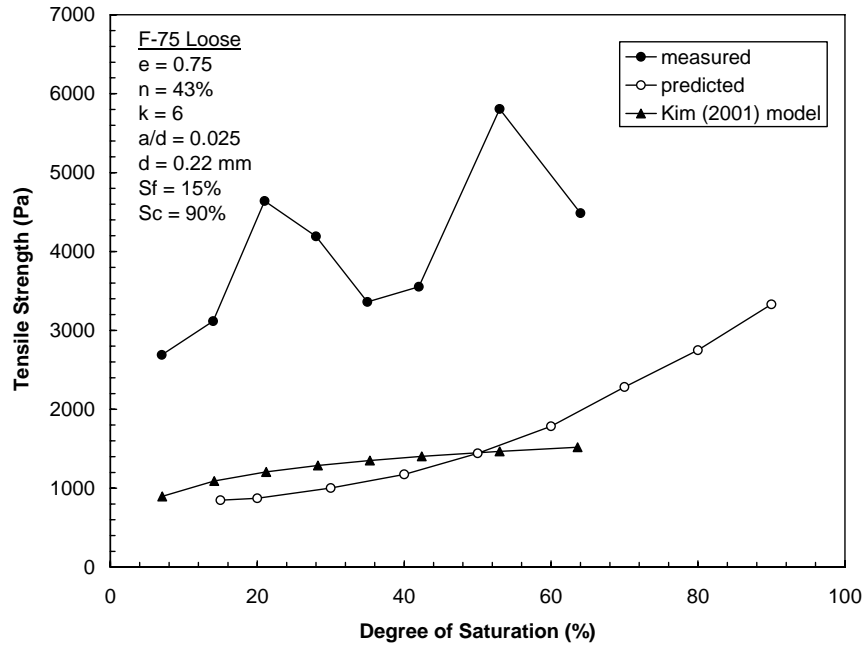**Figure 5. 7:** *Measured and predicted tensile strength for dense F-55 sand*
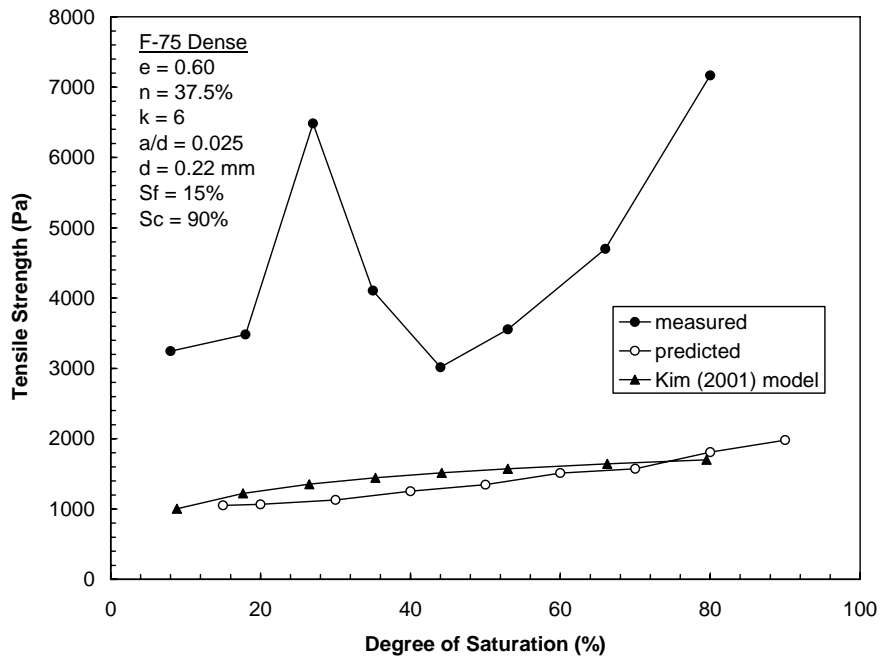
**Figure 5. 8:** *Measured and predicted tensile strength for loose F-75 sand*

Figure 5. 9: *Measured and predicted tensile strength for dense F-75 sand*

Figures 5.10 and 5.11 show measured tensile strength as a function of saturation for all three gradations of sand compacted to relatively loose and dense conditions, respectively. A general dependency on grain size may be observed. Smaller grain size results in higher tensile strength, which is consistent with theory for the pendular, funicular, and capillary regimes. Within the pendular/funicular regime, a smaller particle size for a given degree of saturation results in a greater interparticle bonding force, as described by eq. (2.14) and the first term in eq. (2.21). Within the funicular/capillary regime, a smaller particle size for a given degree of saturation results in a smaller pore size and consequently higher matric suction, which increases the contribution of the water-filled pores under negative pressure to tensile strength (*i.e.*, second term in eq. (2.21))

There are several possible reasons for the discrepancies observed between the modeling predictions and experimental results. The Rumpf-Schubert model is highly dependent on accurate characterization of SWCC over wide range, particularly near the air-entry pressure. In the absence of interparticle attractive mechanisms other than capillarity, tensile strength is generally not expected to exceed air-entry pressure. Difficulties encountered while measuring the SWCCs at low suction pressures, however, resulted in few data points near air-entry. Considering Figures 3.15 – 3.20, it is feasible that actual air-entry pressures for the soils could be up to 1000 to 2000 Pa higher than values estimated for use in the model, which would bring the modeling and experimental results into closer agreement. A second source of uncertainty for modeling in the pendular-dominated regime is the selection of particle separation distance (*a/d*), contact angle (*α*), and particle shape (spherical) and size (*d*). As illustrated previously by Figure

2.10, a one-order of magnitude decrease in particle size results in a one-order of

magnitude increase in predicted tensile strength. Predictions were based on an assumed

particle size equal to the mean measured particle size (d_{50}), but it is feasible that smaller

particles within the specimen control ultimate tensile strength at failure. A contact angle

equal to zero was assumed in the model but its value is highly uncertain for the actual

specimen and is dependent on wetting direction. Figure 2.12 indicates that, for 0.1 mm

particles, contact angle changing from 0º to 40º results in a difference of about 1000 Pa in

tensile strength prediction. Another source of uncertainty is in the experimental

measurement of tensile strength, most notable with regard to friction in the loading

system. While system friction was calibrated and corrections were made to measured

tensile force at failure, the system friction is appreciable and could result in systematic

overestimation of tensile strength.
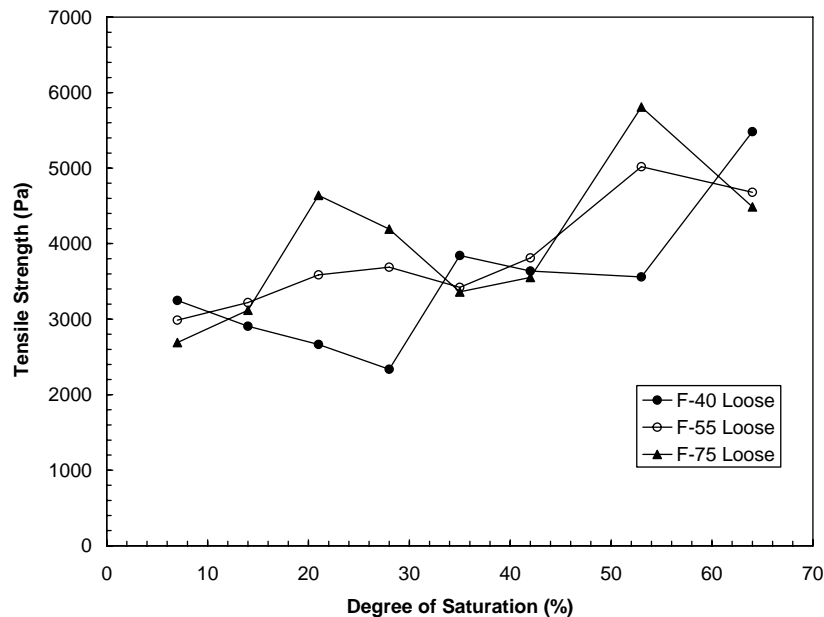
Figure 5. 10: *Measured tensile strength of all specimens in loose (e = 0.75) condition*
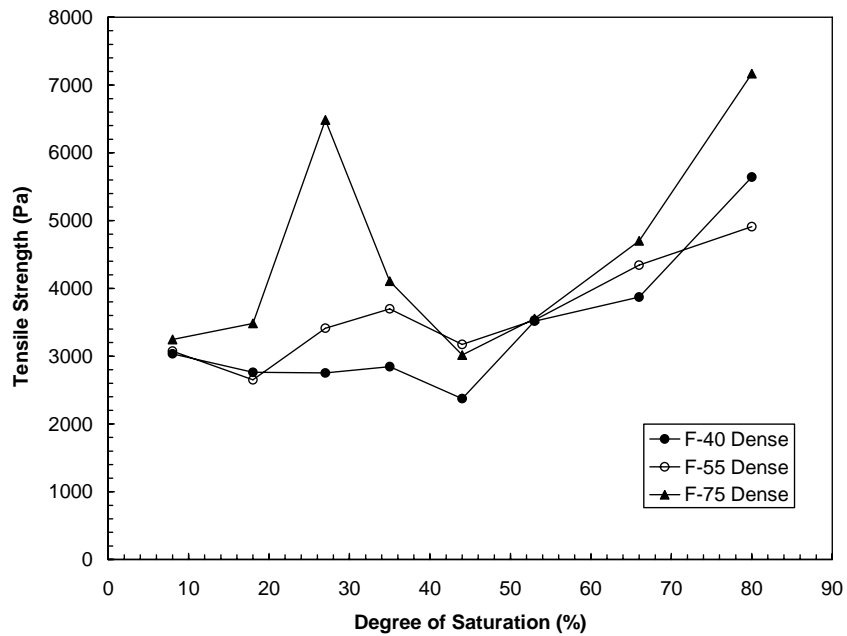
Figure 5. 11: *Measured tensile strength of all specimens in dense (e = 0.60) condition*

5.2 Relationship between Tensile Strength and Shear Strength

Results from tensile and shear strength tests are analyzed in this section to examine a hypothesis that the bulk tensile strength (σ_t) of granular unsaturated soil may be treated as an equivalent effective stress (σ'). For example, if soil is tested in direct tension, it fails when the net bonding force between particles along the failure plane is exceeded. Thus, if effective stress may be considered to describe the net interparticle force among soil particles, tensile strength may be treated as an equivalent effective stress. As illustrated conceptually on Figure 5.12, it follows that the shear strength (τ_f) of unsaturated soil could be predicted by treating tensile strength as a component of the total normal stress (σ_n) that contributes to frictional shear resistance. If tensile strength is measured as a function of water content, saturation, or matric suction, results from direct

shear tests for identically prepared specimens may then be interpreted in terms of effective stress by adding the measured tensile strength to the total normal stress applied during direct shear tests. An expression for this effective stress may be written as

$$\sigma' = \sigma_n + \sigma_t \tag{5.1}$$

which, following the Mohr-Coulomb failure criterion, may be used to predict shear strength as:

$$\tau_f = c' + \sigma' \tan\phi' = c' + (\sigma_n + \sigma_t)\tan\phi' \tag{5.2}$$

where c' is effective cohesion and ϕ' is the effective friction angle.
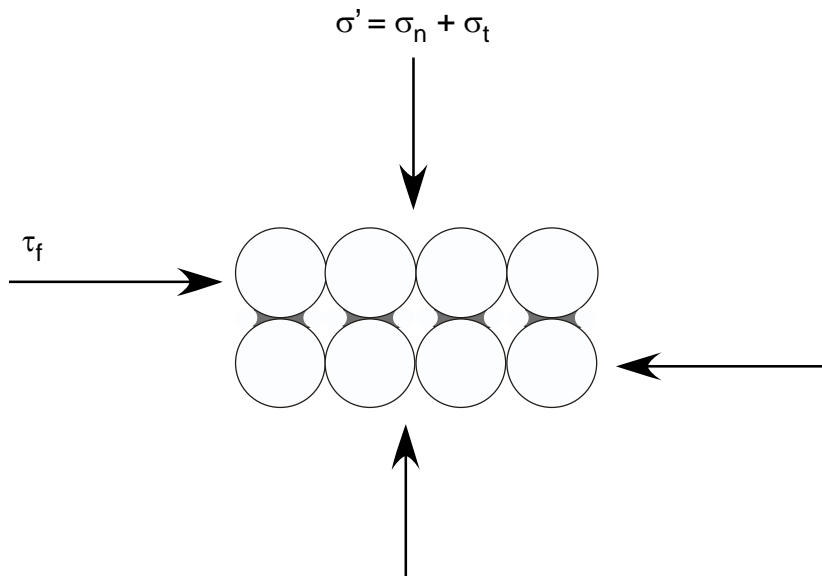
Figure 5. 12: *Effective stress (σ') conceptualized as the sum of total normal stress (σ_n) and tensile strength (σ_t).*

The validity of this conceptualization for effective stress may be evaluated in the relatively low normal stress range (100 Pa $< \sigma_n <$ 1000 Pa) by considering results from

direct tension and direct shear tests on Ottawa sand reported by Kim (2001). Validity in the relatively high normal stress range (35 kPa $< \sigma_n <$ 276 kPa) may be evaluated by considering results from the direct tension and direct shear tests reported here. Alternative expressions for quantifying effective stress in unsaturated soils may also be evaluated using both data sets.

Bishop's (1969) formulation for effective stress in unsaturated soil involves a modified form of Terzaghi's classic effective stress ($\sigma' = \sigma - u_w$) written as follows:

$$\sigma' = \sigma - u_a + \chi\left(u_a - u_w\right) \tag{5.3}$$

where the "effective stress parameter" χ is generally accepted to vary between zero and one as a function of degree of saturation, $\chi = f(S)$. The difference between total stress and pore air pressure ($\sigma - u_a$) is the "net normal stress" and the difference between the pore air pressure and the pore water pressure ($u_a - u_w$) is matric suction. For χ equal to zero (corresponding to dry conditions) and for χ equal to unity (corresponding to saturated conditions), eq. (5.3) reduces to Terzaghi's effective stress equation for air- or water-saturated soil. Macroscopic behavior is described using the modified effective stress within the general framework of saturated soil mechanics. Shear strength, for example, may be described by incorporating eq. (5.3) into the classical Mohr-Coulomb failure criterion:

$$\tau_f = c' + \left[(\sigma - u_a) + \chi(u_a - u_w)\right]\tan\phi' \tag{5.4}$$

Numerous theoretical, experimental, and empirical approaches have been proposed for determining the effective stress parameter χ. In a typical direct shear test, for example, the net total stress ($\sigma - u_a$) is known (controlled), shear strength τ_f is measured at failure, and c' and ϕ' may be determined by conducting tests for saturated or

- 115 -

dry specimens. Thus, by measuring or controlling matric suction $(u_a - u_w)$, the effective stress parameter χ can be evaluated as a function of matric suction (or corresponding degree of saturation) by rearranging equation (5.4) as follows:

$$\chi = \frac{\tau_f - c' - (\sigma - u_a)\ \tan \phi'}{(u_a - u_w)\ \tan \phi'} \tag{5.5}$$

Other applications of Bishop's effective stress have involved the simple assumption that χ is equal to the degree of saturation from zero to one $(0 < S < 1)$.

$$\chi = S \tag{5.6}$$

Khalili and Khabbaz (1998) considered a large series of experimental shear strength data and proposed a form of χ as a function of "suction ratio" $(u_a - u_w)/u_e$ as follows:

$$\chi = \left(\frac{u_a - u_w}{u_e} \right)^{-0.55} \quad \text{for} \quad (u_a - u_w) > u_e$$
$$\chi = 1 \qquad\qquad\quad \text{for} \quad (u_a - u_w) \le u_e \tag{5.7}$$

where u_e is the suction value marking the transition between saturated and unsaturated states, being the air-expulsion value for a wetting process and the air-entry value for a drying process. These values may be inferred from the SWCC.

The validity of several forms of χ as a function of the degree of saturation was also examined by Vanapalli and Fredlund (2000) using a series of shear strength test results for statically compacted mixtures of clay, silt, and sand from Escario and Juca (1989) (Lu and Likos, 2004). For matric suction ranging between 0 and 1,500 kPa, the following two forms showed a good fit to the experimental results:

$$\chi = S^\kappa = \left(\frac{\theta}{\theta_s} \right)^\kappa \tag{5.8}$$

where S is the degree of saturation, θ is volumetric water content, θ_s is the saturated water content, and κ is a fitting parameter used to obtain a best-fit between measured and predicted values. Vanapalli and Fredlund (2000) also proposed an expression for χ in terms of effective saturation or effective volumetric water content as follows:

$$\chi = \frac{S - S_r}{1 - S_r} = \frac{\theta - \theta_r}{\theta_s - \theta_r} \tag{5.9}$$

where θ_r is the residual volumetric water content and S_r is the residual degree of saturation and θ_s is the saturated volumetric water content ($\theta_s = n$).

5.2.1 Analysis at low normal stresses

Table 2.4 summarized direct shear results reported by Kim (2001) for F-75-C Ottawa sand (clean sand) at different water contents for loosely compacted specimens (D_r ~ 30%, e ~ 0.71). Figure 5.13 shows corresponding failure envelopes in terms of applied total normal stress versus measured shear stress at failure. A similar plot is shown on Figures 5.14 for F-75-F Ottawa sand (2% fines content). This data was summarized on Table 2.5.
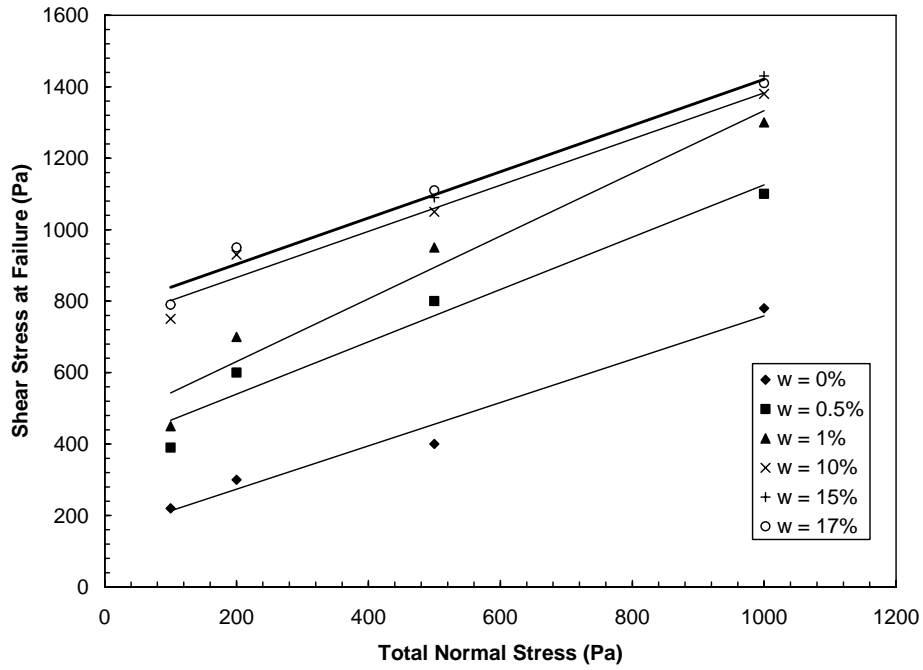
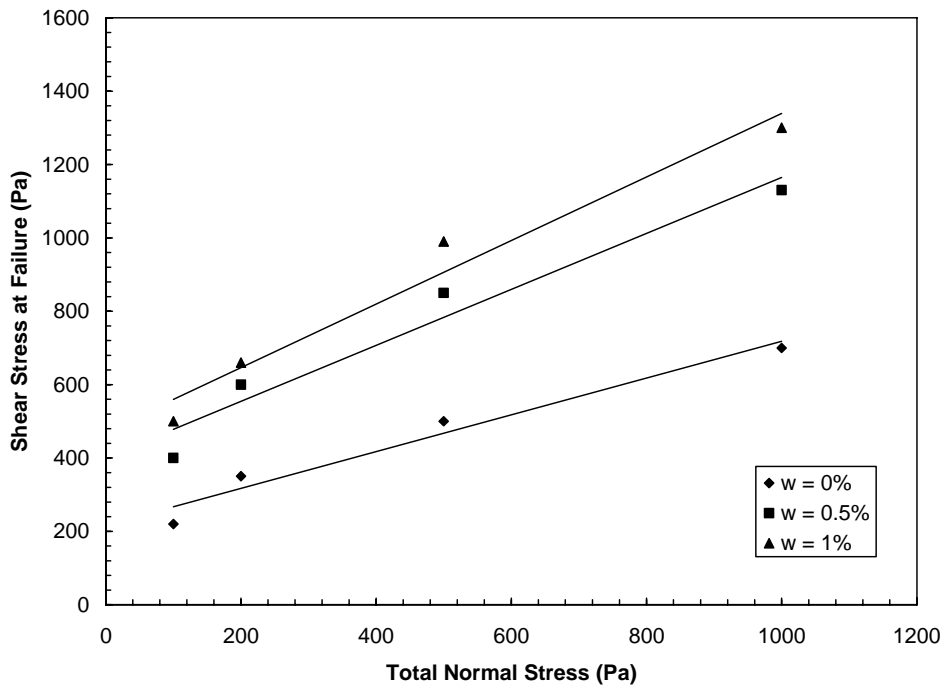**Figure 5. 13:** *Failure envelopes for F-75-C Ottawa sand measured from direct shear tests (e ~ 0.71)*

Figure 5. 14: *Failure envelopes for F-75-F Ottawa sand measured from direct shear tests (e ~ 0.71)*

While the failure envelopes may actually be non-linear at these values of low normal stress, the failure envelopes shown in the above figures were assumed linear as determined by least-squares linear regression. In general, it may be observed that the failure envelopes shift upward with increasing water content, which reflects an increase in apparent cohesion as water is added to the soil. If physicochemical and other effects such as particle interlocking are considered negligible, the source of the apparent cohesion is primarily attributable to capillary mechanisms. As indicated by the analyses in Chapter 2, the magnitude of capillary-induced interparticle force generally increases with increasing water content in the pendular regime, which is reflected in the failure envelopes as a macroscopic increase in shear strength. Friction angle is relatively constant as a function of water content, but the increase in effective stress due to capillary interparticle forces increases the frictional resistance of the soil.

To test the validity of the proposed expression for equivalent effective stress (eq. 5.1), tensile strength values determined from Kim's (2001) direct tension tests for similarly prepared specimens (Tables 2.2 and 2.3) were added to the values of total normal stress used in the direct shear tests. Corresponding effective stress failure envelopes were then plotted in terms of effective stress, as shown on Figure 5.15 for F-75-C sand. Figure 5.16 shows effective stress envelopes for the F-75-F sand. This procedure could be done only for specimens that were tested in both shear and tension at similar values of water content, which included $w \sim 0.5\%$ and $w \sim 1.0\%$. For $w = 0\%$, it was assumed that tensile strength was equal to zero.

It may be observed from Figs. 5.15 and 5.16 that the total stress failure envelopes converge to a relatively unique effective stress failure envelope (*i.e.*, total stress values shift to the right). Regression of the envelope for F-75-C sand (Figure 5.15) indicates an effective friction angle $\phi' = 36.3°$ and $c' = 92$ Pa, which are realistic values for Ottawa sand in this range of normal stress. Regression of the envelope for the F-75-F sand (Figure 5.16) indicates $\phi' = 35.2°$ and $c' = 123$ Pa. The decrease in friction angle and slight increase in cohesion may reflect the effect of the 2% fines. The fact that the effective stress failure envelopes are unique supports the validity of the equivalent effective stress concept defined as the sum of total normal stress and tensile strength.
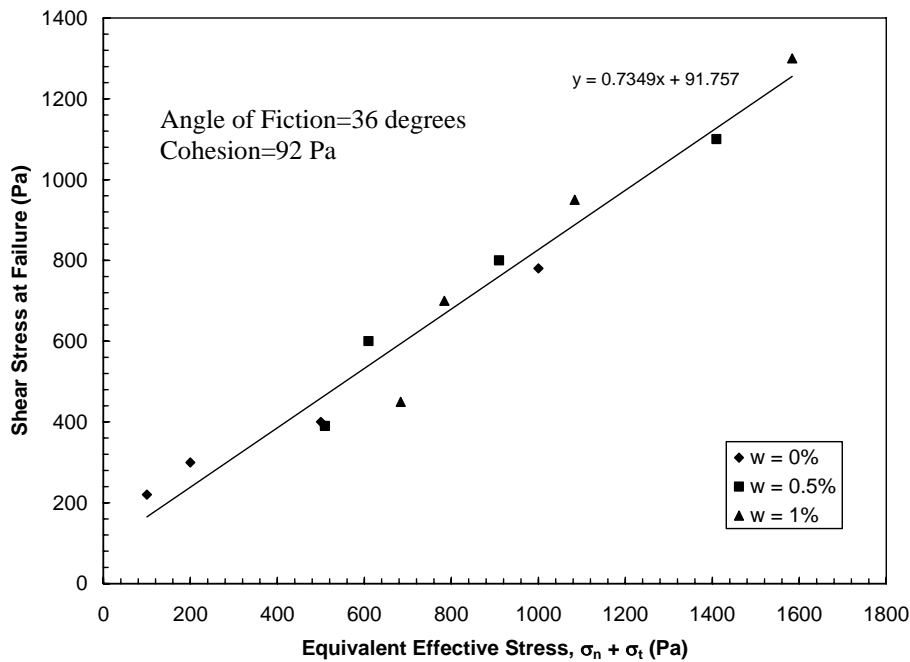
Figure 5. 15: *Failure envelope for direct shear tests on F-75-C sand in terms of effective stress defined as normal stress plus tensile stress*
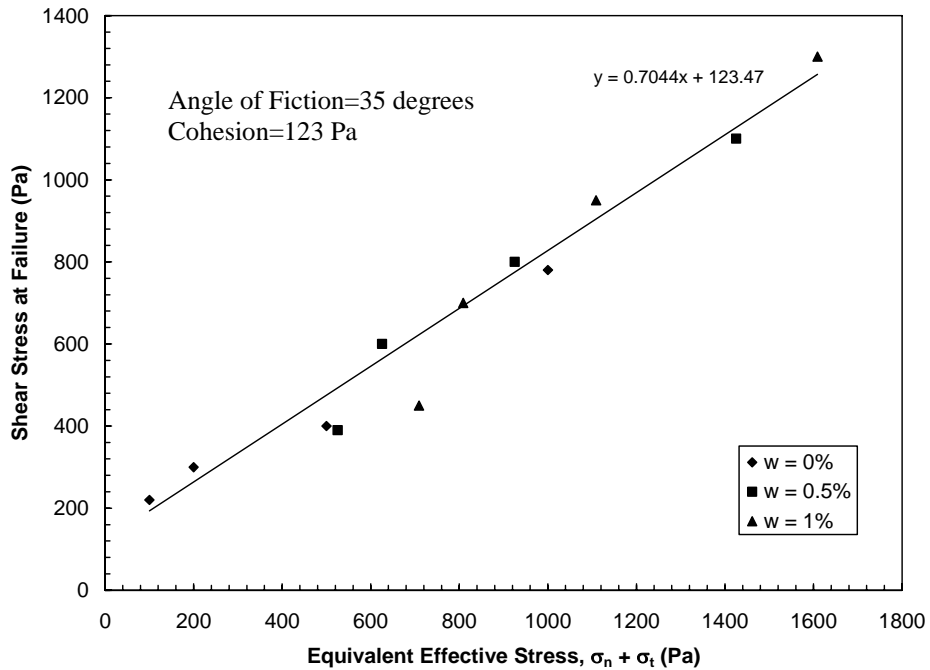
Figure 5. 16: *Failure envelope for direct shear tests on F-75-F (2% fines) sand in terms of effective stress defined as normal stress plus tensile stress*

Similar analyses were conducted to examine several alternative expressions for effective stress. Figure 5.17 and 5.18, for example, show effective stress failure envelopes obtained using Bishop's expression for effective stress (eq. 5.3). The effective stress parameter χ for these calculations was set equal to the degree of saturation (*i.e.*, eq. 5.6). Figures 5.19 and 5.20 show effective stress failure envelopes based on Bishop's formulation where the χ parameter was back-calculated from direct shear using eq. (5.5).

For the majority of cases, these procedures appear to result in reasonable representations for effective stress (i.e., the total stress envelopes converge). Note, however, that the $\chi = S$ approach for F-75-C sand (Figure 5.17) results in some deviation in the effective stress envelope at low water contents ($w < 1\%$). Here, the effect of adding even a small amount of water is significant in terms of shear strength; however the

associated change in saturation is very small. The relatively high friction angle at low

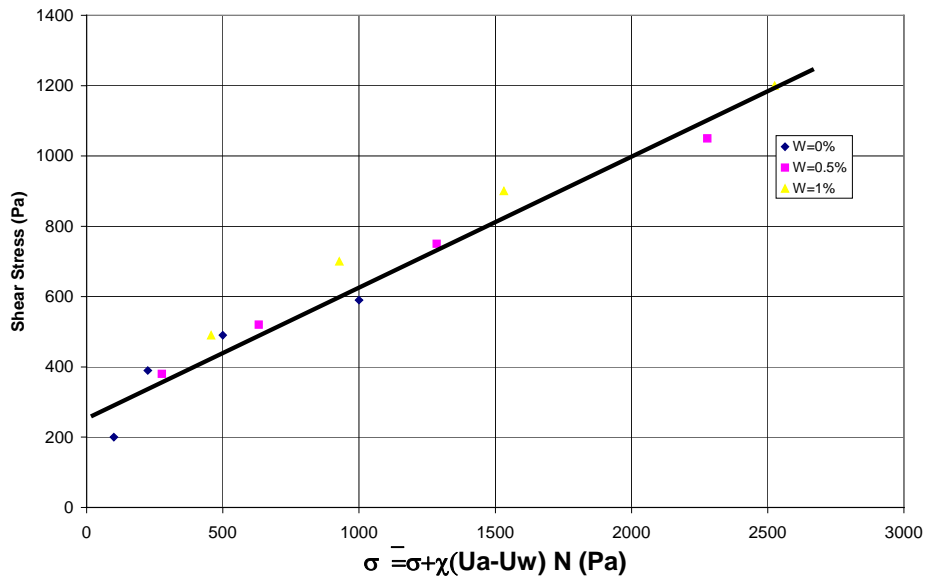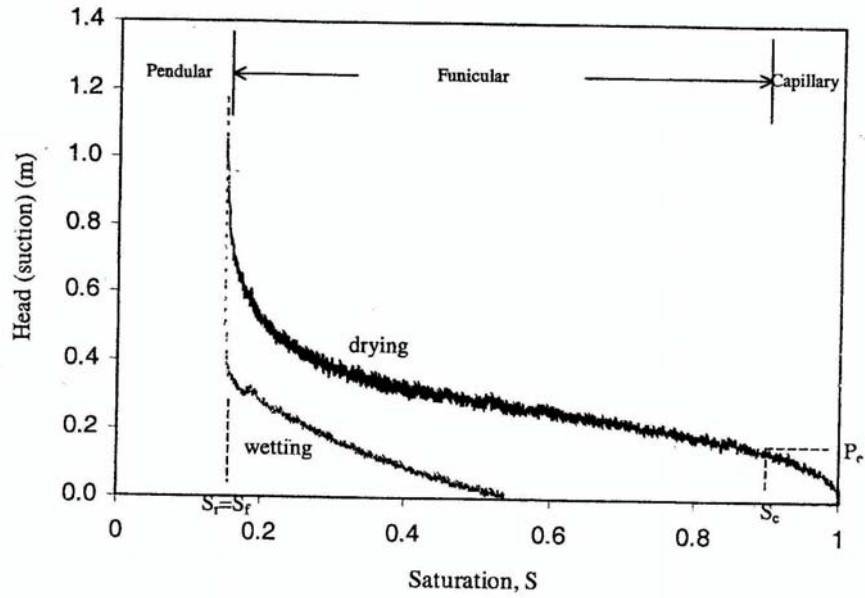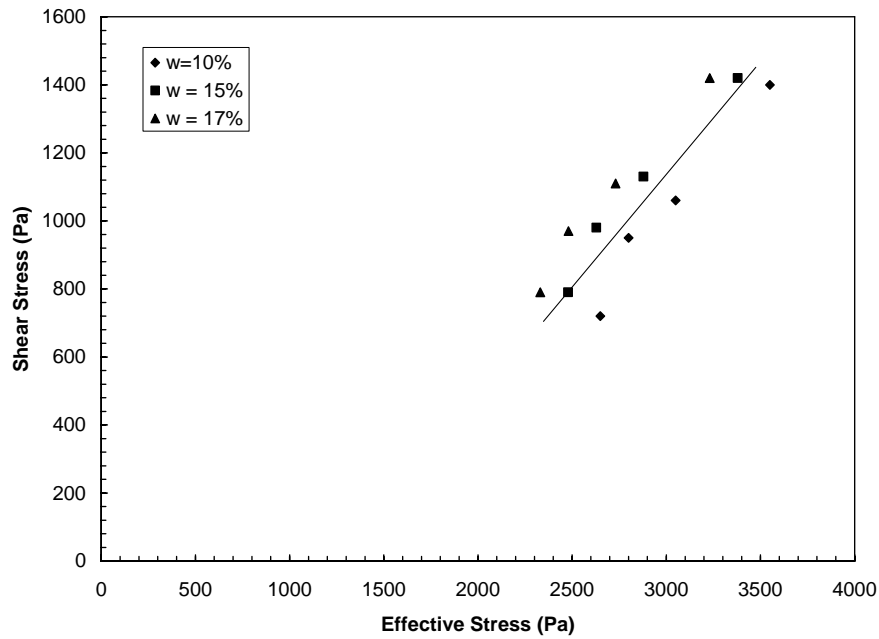effective stress may also reflect curvature in the actual failure envelope.
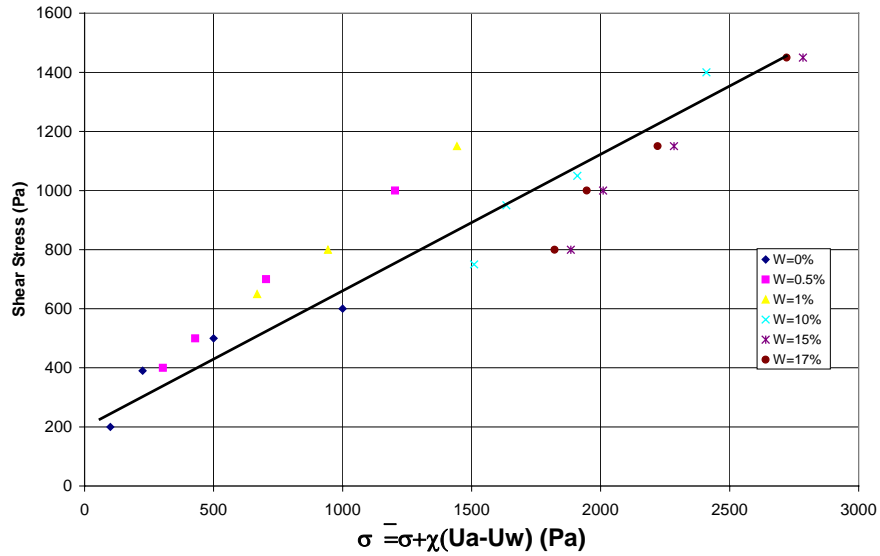
Figure 5. 17: *Failure envelope for direct shear tests on F-75-C sand in terms of effective stress defined using Bishop's effective stress and $\chi = S$)*
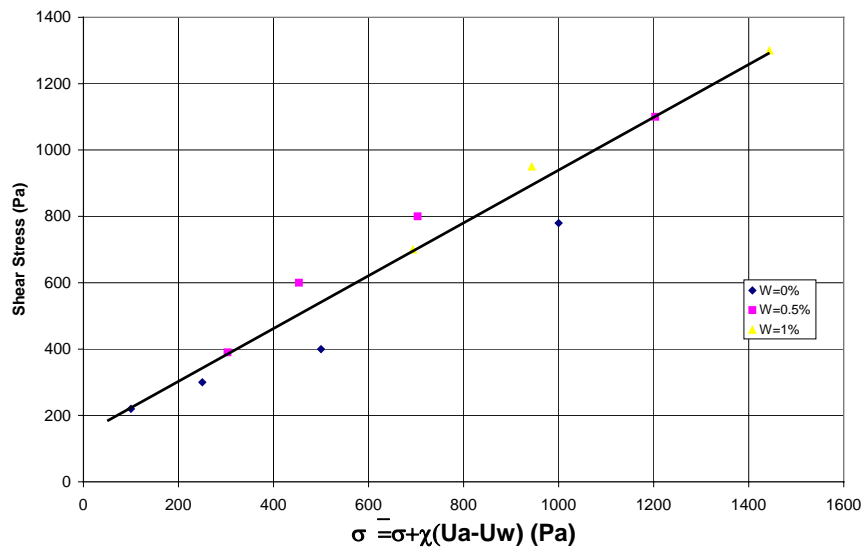
Figure 5. 18: *Failure envelope for direct shear tests on F-75-F sand in terms of effective stress defined using Bishop's effective stress and $\chi = S$).*
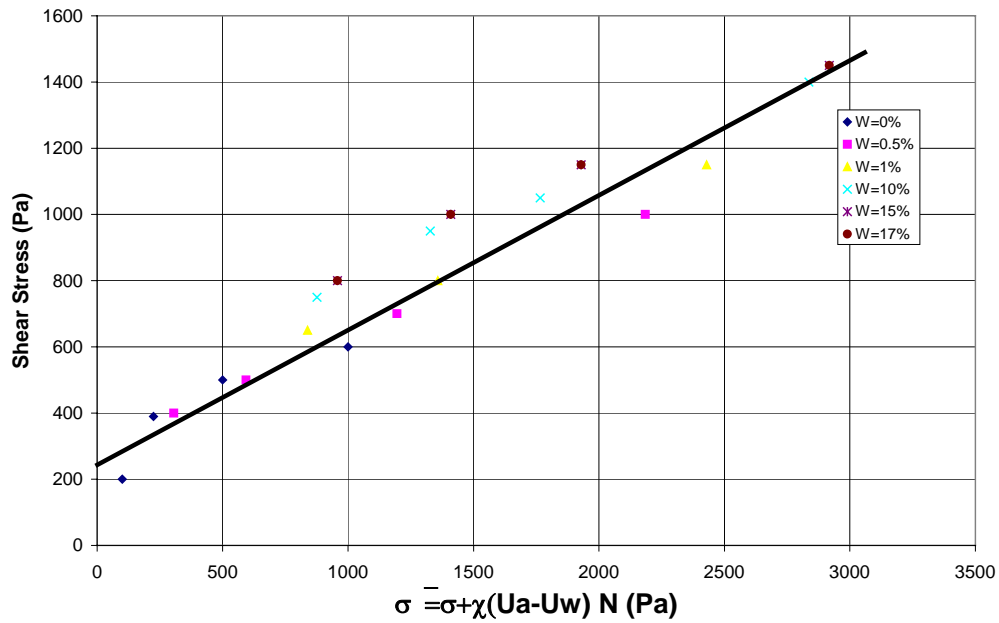
Figure 5. 19: *Failure envelope for direct shear tests on F-75-C sand in terms of effective stress defined using Bishop's effective stress and χ back-calculated from direct shear results)*

Figure 5. 20: *Failure envelope for direct shear tests on F-75-F sand in terms of effective stress defined using Bishop's effective stress and χ back-calculated from direct shear results)*

The effective stress parameter χ was also estimated using the Khalili and Khabbaz (1998) empirical expression (eq. 5.7), which requires knowledge of the SWCC to determine $(u_a - u_w) = f(S)$ and the air-entry value u_e. The SWCC for Kim's (2001) F-75-C sand is shown as Figure 5.21, which exhibits an air-entry value (u_e) of approximately 2000 Pa ($h = 0.2$ m). The drying loop of the SWCC was interpreted to determine χ at the different levels of saturation corresponding to direct shear test conditions. Water content values reported for direct shear tests were converted to degrees of saturation using $e = 0.71$ and $G_s = 2.65$. However, results could only be interpreted for relatively high water content values ($w = 10\%$, 15%, and 17% or $S = 0.37$, 0.56, and 0.63) where the SWCC is well defined.

Figure 5.22 shows the direct shear results in terms of corresponding effective stress. The data converges to a relatively unique failure envelope with an effective friction angle of 33.7°. However, the intercept with the shear stress axis is a significantly negative value. Use of this procedure is highly dependent on the accuracy of the SWCC, which may explain these results. In addition, the analysis is for low normal stresses, where a large suction stress $\chi(u_a - u_w)$ is added to a relatively small total normal stress such that uncertainty in either χ or $(u_a - u_w)$ results in significant uncertainty in their product.

Figure 5. 21: *Soil-water characteristic curve during wetting and drying for F-75C Ottawa sand [reproduced from Kim (2001); original data from Hwang (2001)]*

Figure 5. 22: *Failure envelope for direct shear tests on F-75-C sand in terms of effective stress defined using Bishop's effective stress and χ from Khalili and Khabbaz (1998)*

5.2.2 Analysis at high normal stresses

Table 4.1 and 4.2 summarized results from direct shear tests conducted for F-75, and F-55 Ottawa sand at various water contents and compacted to relatively loose (e ~ 0.75) and relatively dense (e~ 0.60) conditions. Figures 5.23 and 5.24 show total stress failure envelopes for the F-75 sand at loose and dense conditions, respectively. Unlike the previous results for low normal stress, the envelopes do not shift up appreciably from the influence of capillary cohesion. Results from the theoretical consideration (Section 5.1) and experimental consideration at low normal stress (Section 5.2) suggest that the magnitude of induced capillary stress is on the order of less than about 5000 Pa depending on grain size and degree of saturation. Thus, the relatively high total normal stress (35 kPa $< \sigma_n <$ 276 kPa) dominates the effective stress and the effects of capillarity are masked.
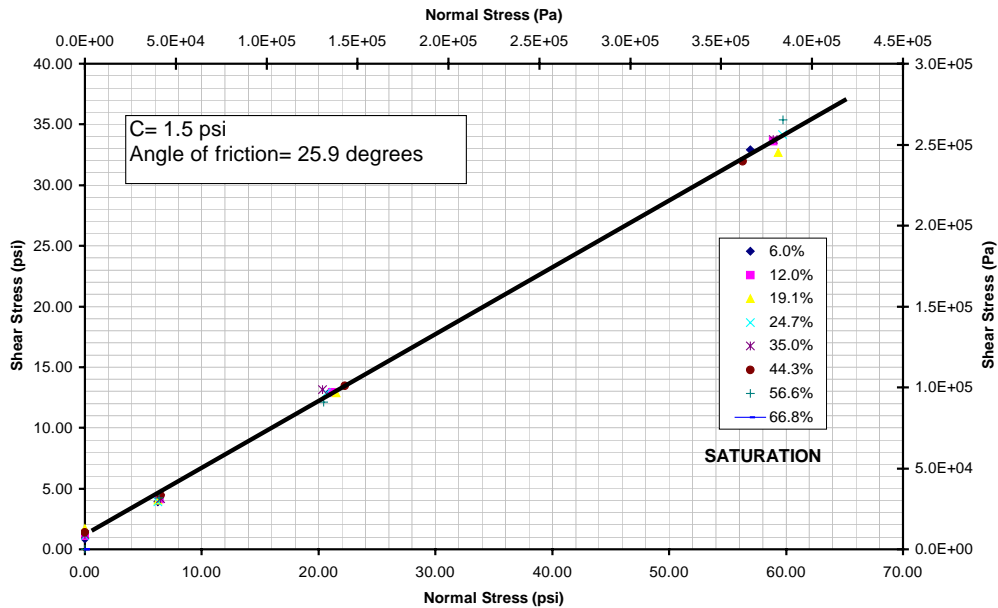
Figure 5. 23: *Total stress failure envelopes for loose F-75 Ottawa sand (e= 0.75)*
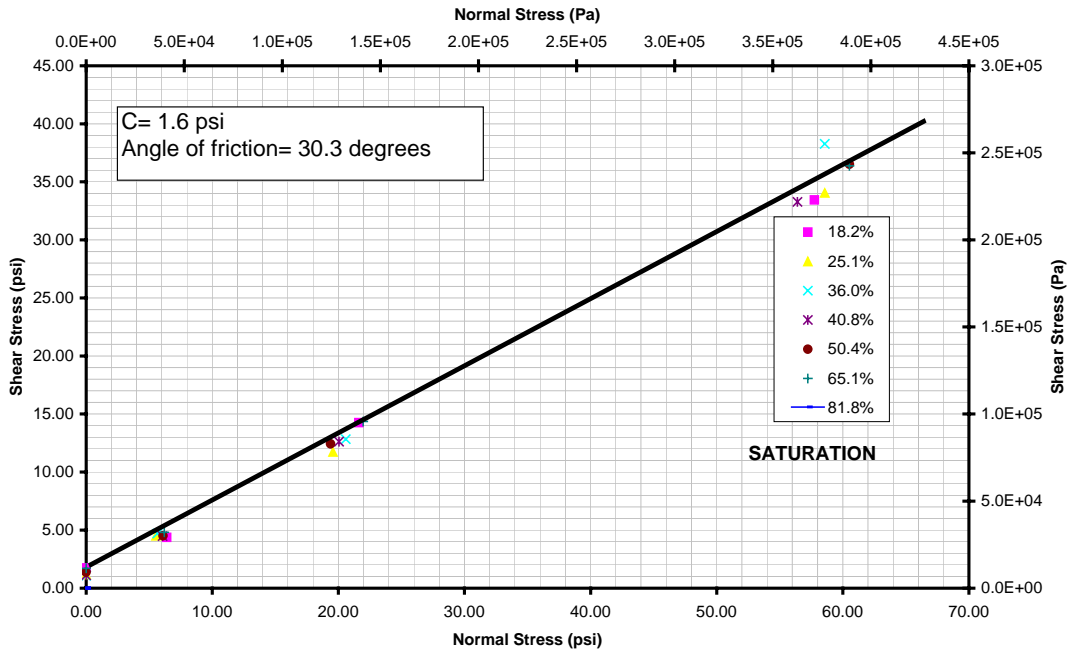
Figure 5. 24: *Total stress failure envelopes for dense F-75 Ottawa sand (e= 0.60)*

Figures 5.25 through 5.32 show effective stress envelopes for the F-75 sand calculating according to the several methods described above. Figure 5.25 and 5.26 show envelopes based on effective stress defined as normal stress plus tensile strength (eq. 5.1). Here, tensile strength was considered from the direct tension results for F-75 specimens prepared to the same water content and void ratio as the direct shear tests. Figure 5.27 and 5.28 show envelopes based on effective stress defined using Bishop's formulation and $\chi = S$. Figure 5.29 and 5.30 show envelopes based on effective stress defined using Bishop's formulation and χ back-calculated directly from the shear results. Finally, Figures 5.31 and 5.32 show failure envelopes based on effective stress defined using Bishop's formulation and χ calculated using the Khalili and Khabbaz (1998) empirical expression.
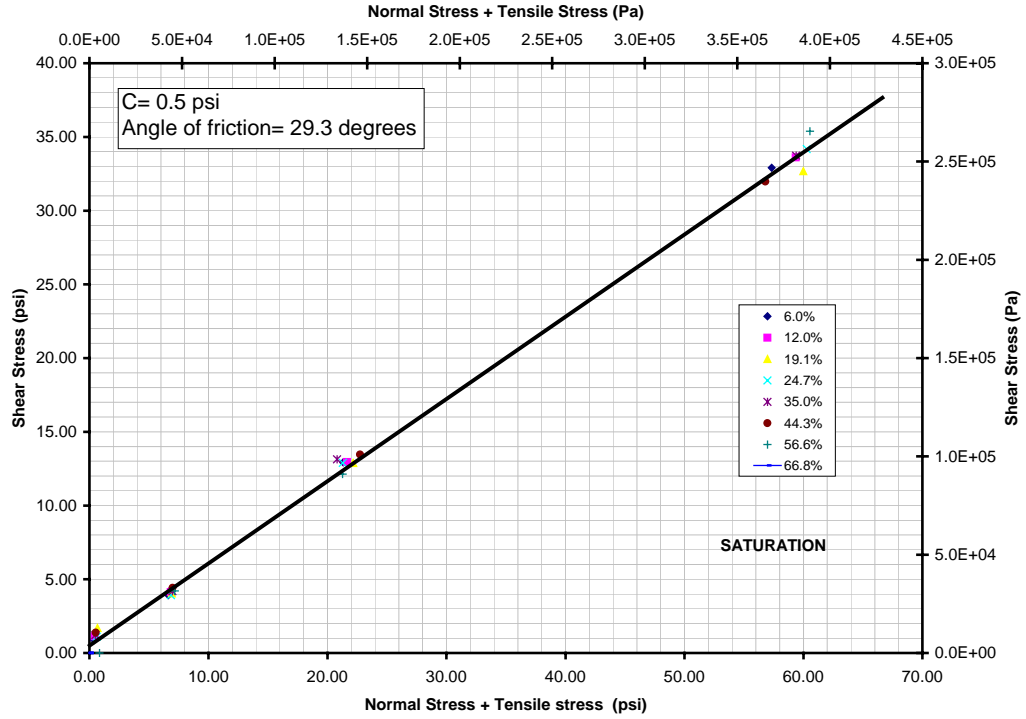
Figure 5. 25: *Failure envelope for direct shear tests on loose F-75 sand (e = 0.75) in terms of effective stress defined using normal stress plus tensile strength.*
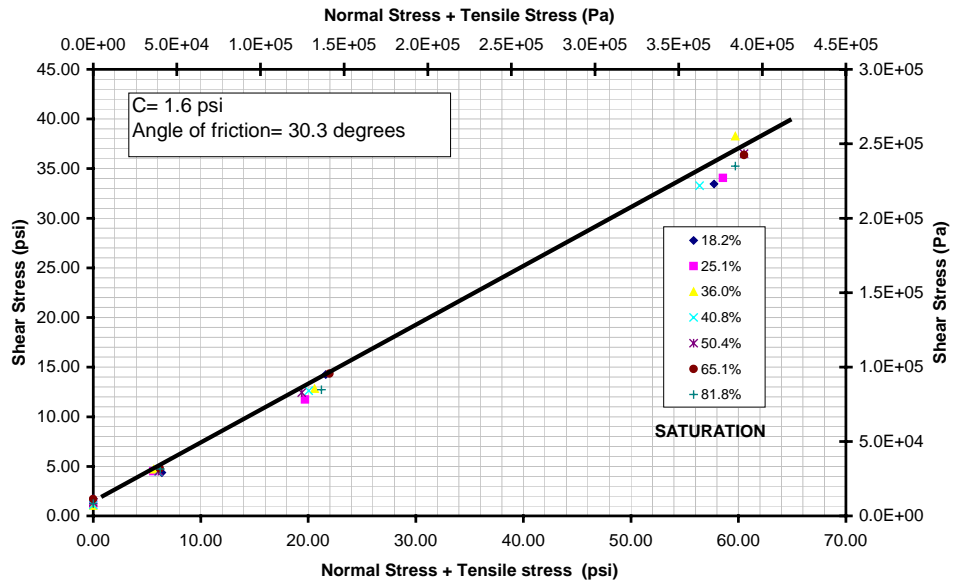
Figure 5. 26: *Failure envelope for direct shear tests on dense F-75 sand (e = 0.60) in terms of effective stress defined using normal stress plus tensile strength.*
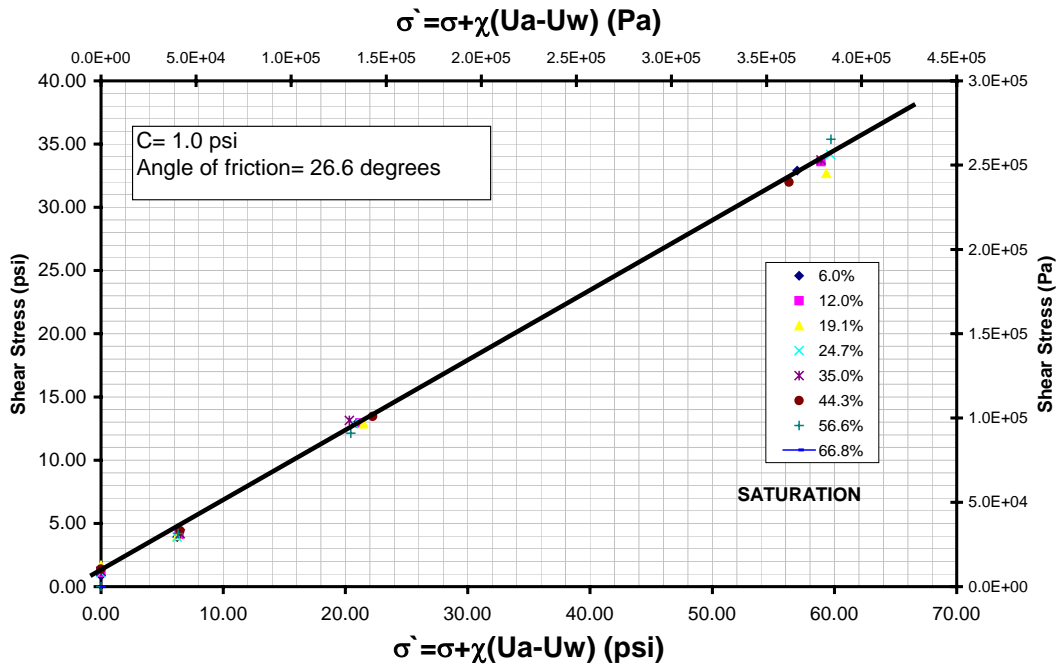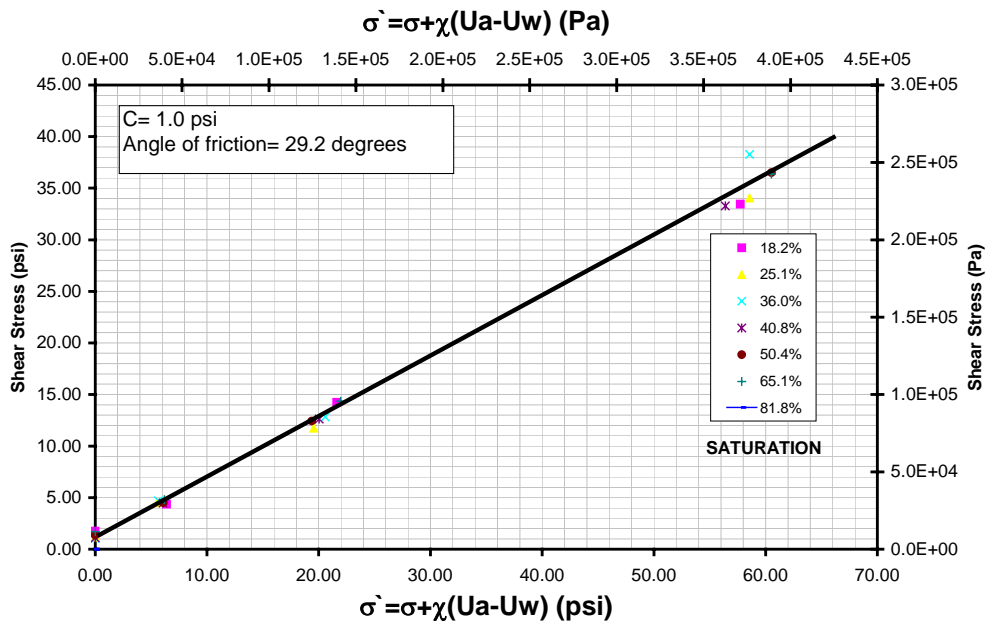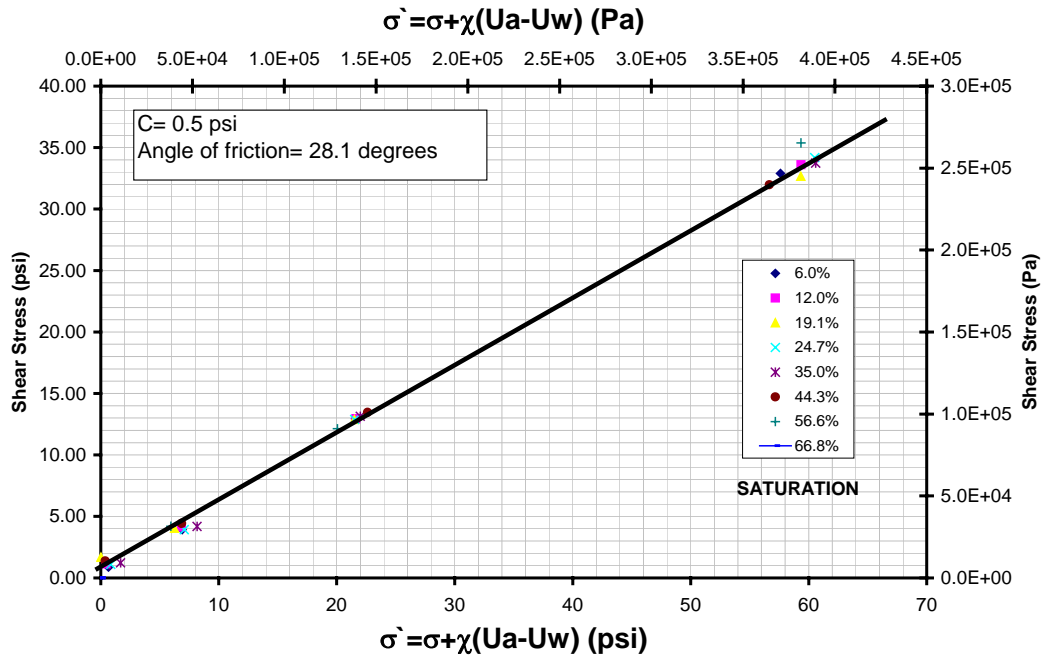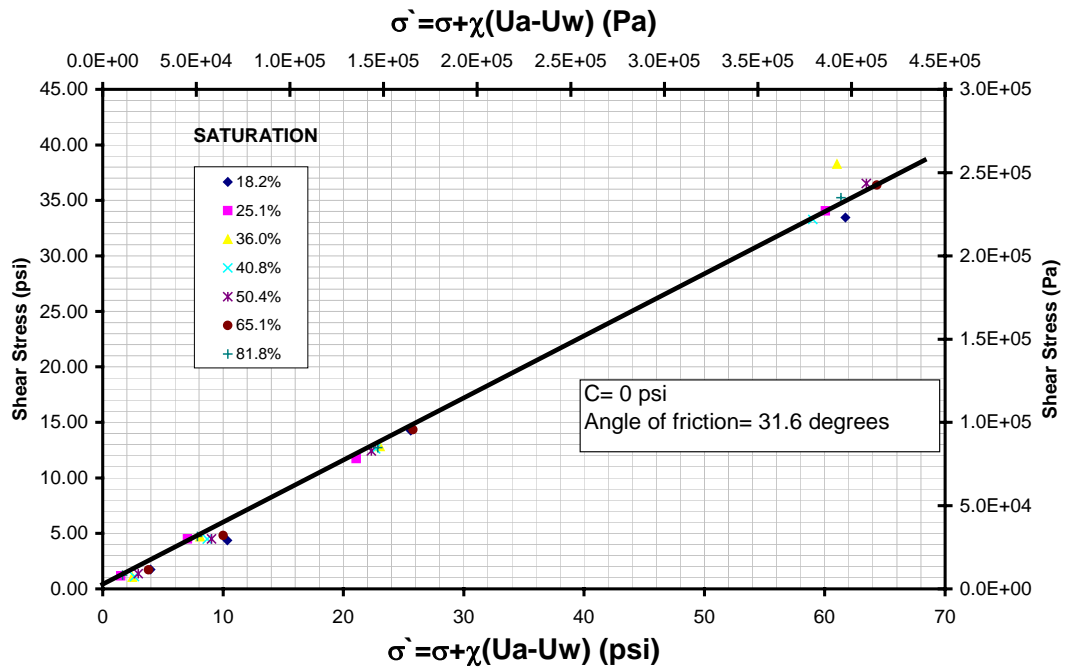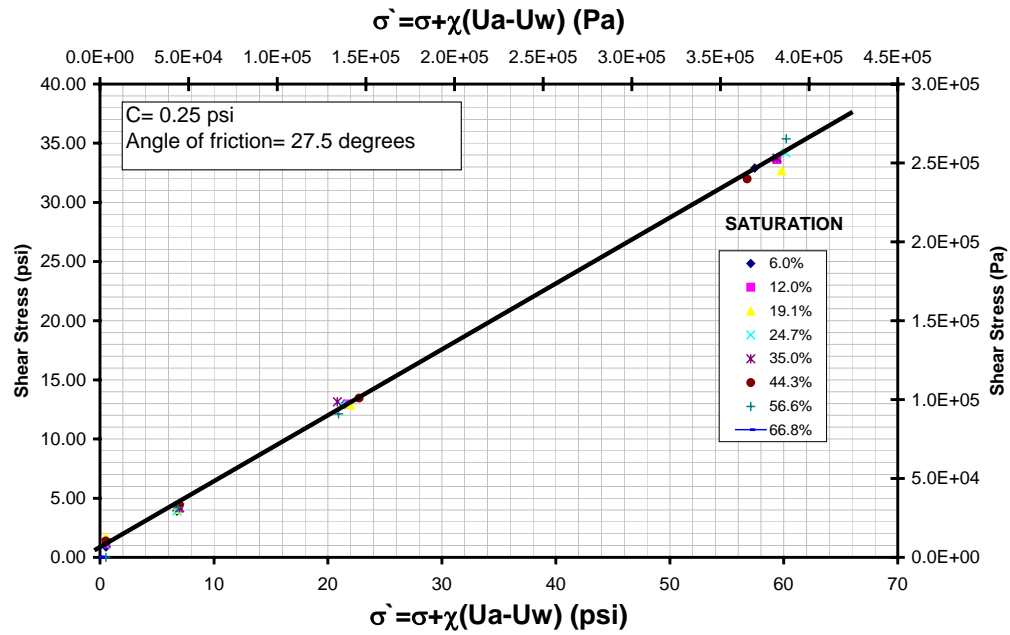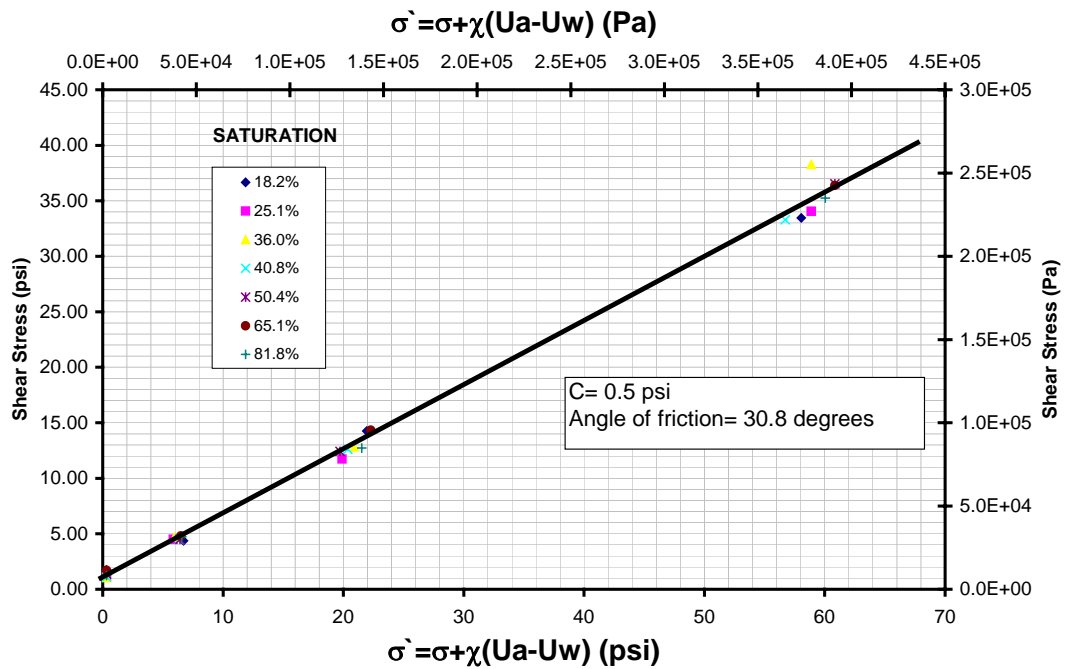
Figure 5. 27: *Failure envelope for direct shear tests on loose F-75 sand (e = 0.75) in terms of effective stress defined using Bishop's effective stress and χ = S.*

Figure 5. 28: *Failure envelope for direct shear tests on dense F-75 sand (e = 0.60) in terms of effective stress defined using Bishop's effective stress and χ = S.*

Figure 5. 29: *Failure envelope for direct shear tests on loose F-75 sand (e = 0.75) in terms of effective stress defined using Bishop's effective stress and χ from direct shear tests.*

Figure 5. 30: *Failure envelope for direct shear tests on dense F-75 sand (e = 0.60) in terms of effective stress defined using Bishop's effective stress and χ from direct shear tests.*

Figure 5. 31: *Failure envelope for direct shear tests on loose F-75 sand (e = 0.75) in terms of effective stress defined using Bishop's effective stress and Khalili and Khabbaz (1998)*


Figure 5. 32: *Failure envelope for direct shear tests on dense F-75 sand (e = 0.60) in terms of effective stress defined using Bishop's effective stress and Khalili and Khabbaz (1998)*

Figures 5.33 and 5.34 show effective stress parameter functions [$\chi = f(S)$ and $\chi = f(u_a - u_w)$] that were back-calculated from the direct shear results and used to calculate the effective stress envelopes shown as Figures 5.27 and 5.28. Both functions are highly non-linear and extend well beyond the range of $0 < \chi < 1$. This behavior reflects the fact that shear strength resulting from frictional resistance associated with total normal stress is much greater than that resulting from frictional resistance associated with matric suction. Considering eq. (5.5), these are quantified by the terms $(\sigma - u_a)tan\phi'$ and $(u_a - u_w)tan\phi'$, respectively. The large difference in these two terms makes the calculation of χ based on back-calculation from eq. (5.5) very sensitive.
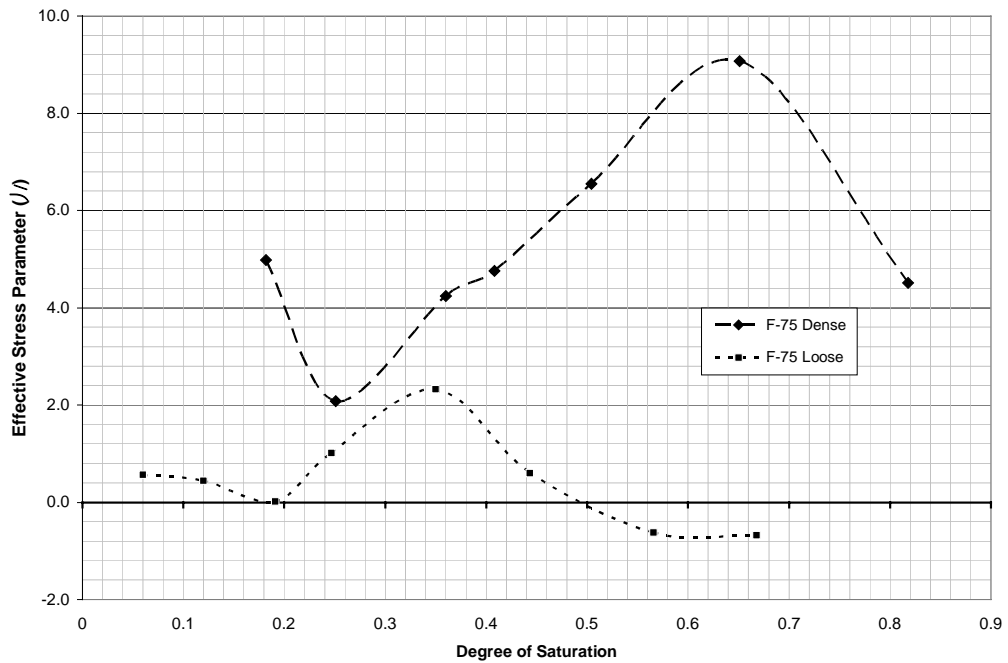
Figure 5. 33: Effective stress parameter function $\chi = f(S)$ for F-75 sand.
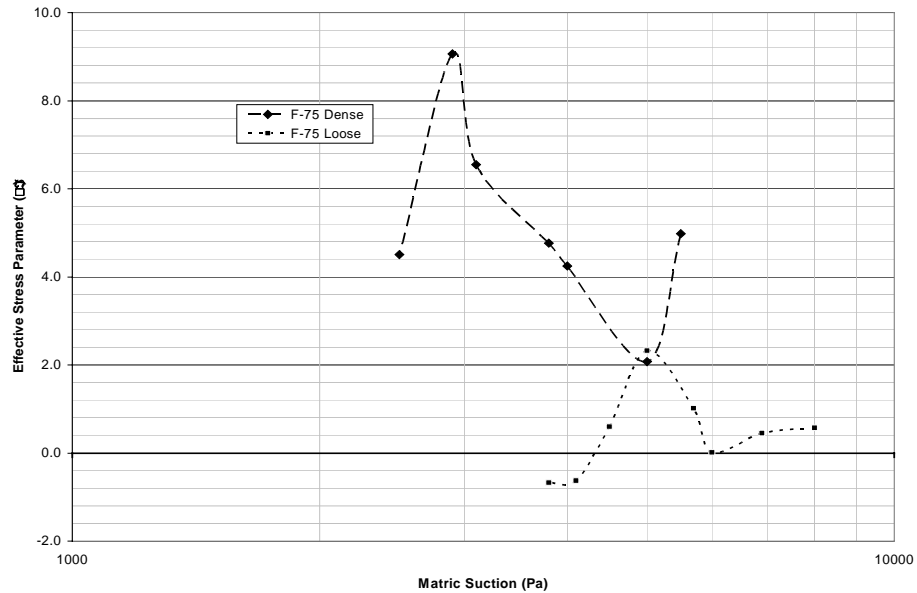
Figure 5. 34: Effective stress parameter function $\chi = f(u_a - u_w)$ for F-75 sand.

5.3 Analysis of Double-Peak Behavior

Figure 2.13 indicates that the contribution of tensile strength associated with the pendular regime and the capillary regime reach peak values near the residual water content and air-entry pressure, respectively. If tensile strength can be treated as an indirect measurement of effective stress, then this double-peak behavior may be reflected in the macroscopic strength and deformation behavior of unsaturated sand. Figure 5.35 shows conceptual relationships between saturation and matric suction (i.e., the SWCC) (5.35a), tensile strength (5.35b), and apparent cohesion (5.35c). Boundaries between the pendular, funicular, and capillary saturation regimes are included at the residual saturation S_r and air-entry saturation S_{ae}. The tensile strength and shear strength curves

- 133 -

are considered to reach peak values at these points to reflect the relatively high values of effective stress.
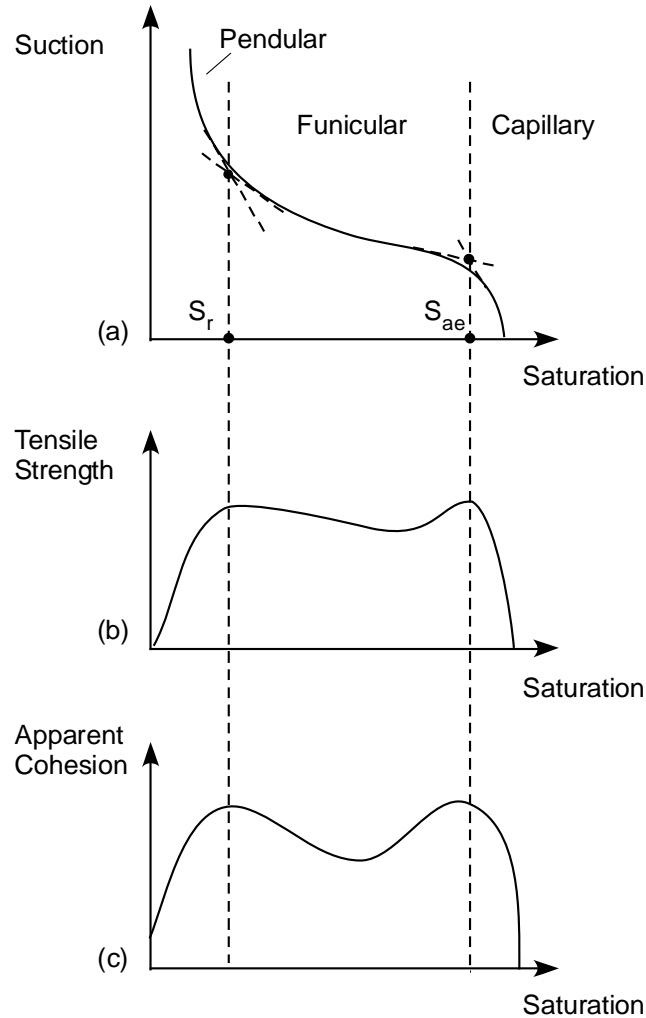
Figure 5. 35: Conceptual relationships between saturation and (a) suction, (b) tensile strength, and (c) apparent cohesion.

Figures 5.36 through 5.38 plot these relationships for several of the sands tested here. As indicated by the SWCC for F-75 sand (Fig. 5.36), residual saturation and air-entry pressure occur at about 12% and 97% saturation, respectively. These ranges were similar for all three sand gradations and compaction conditions. The tensile strength

results (Fig. 5.37) appear to display double-peak behavior, with a first peak occurring at saturation ranging from about 15% to 35%. A second peak occurs at about 50% to 65% saturation for the loose specimens. Although not well-defined, a second peak for the dense specimens appears to be approached at saturation from about 80% to 90%. Apparent cohesion (Fig. 5.38) based on the direct shear results appears to exhibit a first peak near 20% saturation for F-75 sand at both compaction conditions. A second peak occurs near 50% and 70% saturation for the loose and dense specimens, respectively. These ranges and the differences in loose and dense peak locations are consistent with those observed for the tensile strength behavior. The double-peak peak behavior in both tensile strength and apparent cohesion is also more pronounced in specimens prepared loose than those prepared dense.

The first peak in the tensile strength and apparent cohesion may be interpreted to result from a maximum increase in effective stress and corresponding shear strength that is derived from the interparticle forces developed in the pendular regime, i.e. liquid bridges. The second peak at higher saturation represents an increase in shear strength and corresponding effective stress due to the maximum interparticle forces developed in the capillary regime. The shape of the curves between these peaks (funicular regime) reflects the increase in shear resistance produced by a combination of pendular and capillary regime effects. Poorly-graded sand would be expected to exhibit a more pronounced valley between the two peaks because the pendular and capillary regimes are distinct. Well-graded sand would not be expected to exhibit clear double-peak behavior because pendular and capillary interparticle forces are both important over a wide range of saturation.
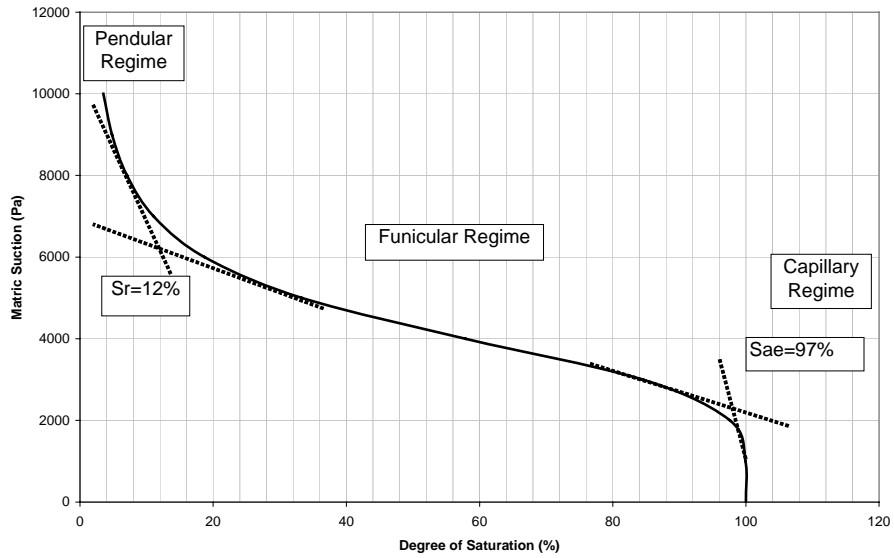
Figure 5. 36: Soil-water characteristic curve for F-75 sand
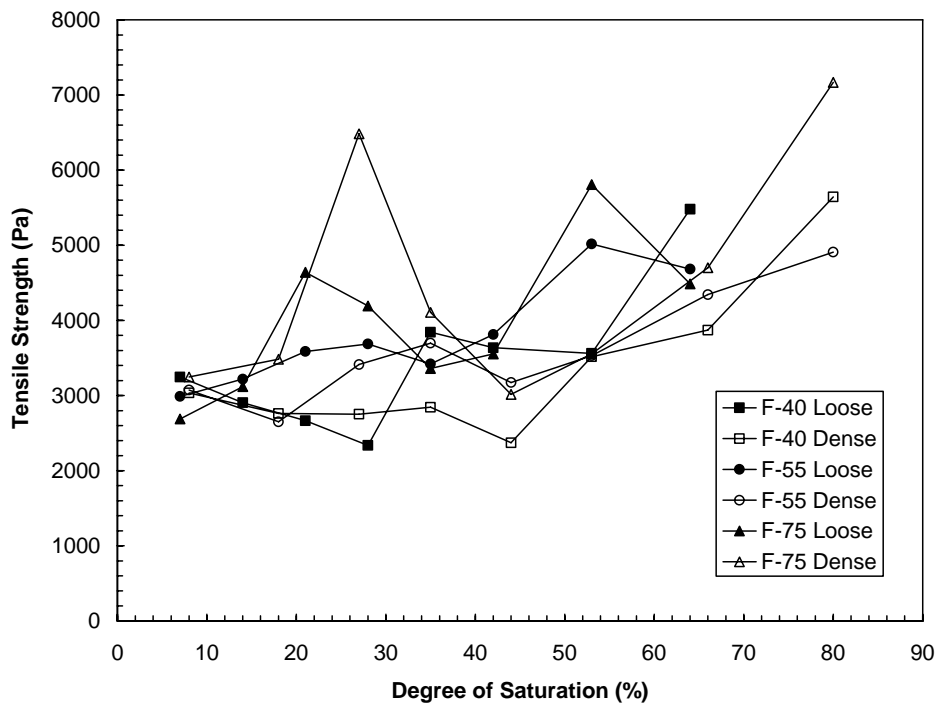
Figure 5. 37: Relationship between tensile strength and saturation measured for all sands and compaction conditions.
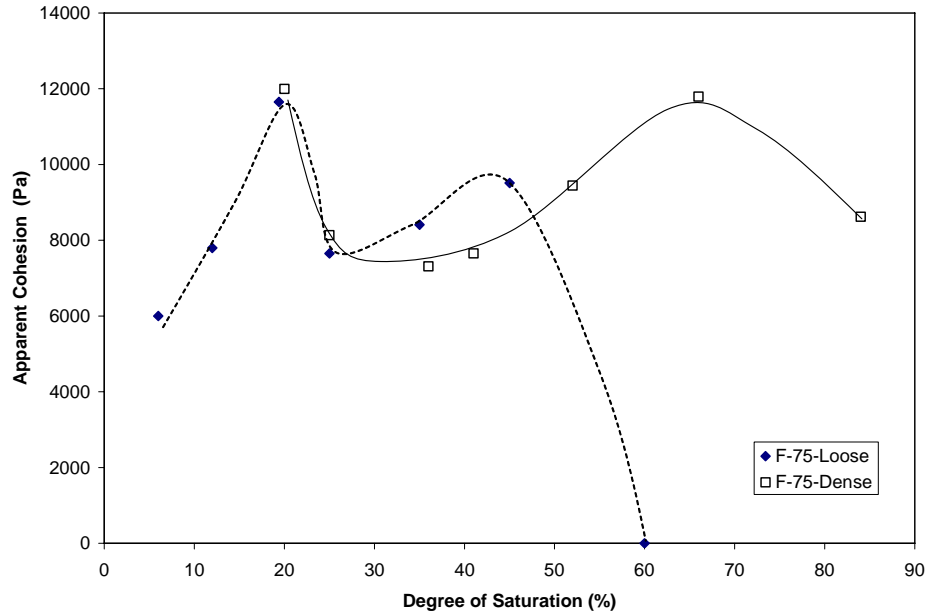
Figure 5. 38: *Apparent cohesion as a function of saturation for F-75 sand*

Double-peak behavior in compaction (Proctor) curves obtained over a wide range of saturation has also been noted by a number of researchers (*e.g*., Olson, 1963; Lee and Suedkamp, 1972; Hausmann, 1990). Lee and Suedkamp (1972) showed that double-peak behavior typically occurs for either highly plastic or completely non-plastic soils. Olson (1963) interpreted double-peak compaction behavior in the context of effective stress and frictional resistance.

Considering Figure 5.39, for example, Olson (1963) proposed that peak values on a double-peak compaction curve (B and D) indicate saturation conditions corresponding to relatively low effective stress. Because the compaction curve is a measure of the soil density for a given amount of compactive energy, larger densities may be interpreted to indicate lower frictional strength (and therefore lower effective stress) because a higher density is required to resist the load (*i.e.*, denser packing and more interparticle contact is required to develop strength). When the curve is increasing, shear strength is decreasing.

The points B, C, and D represent equilibrium points among factors which decrease strength and factors which increase strength.
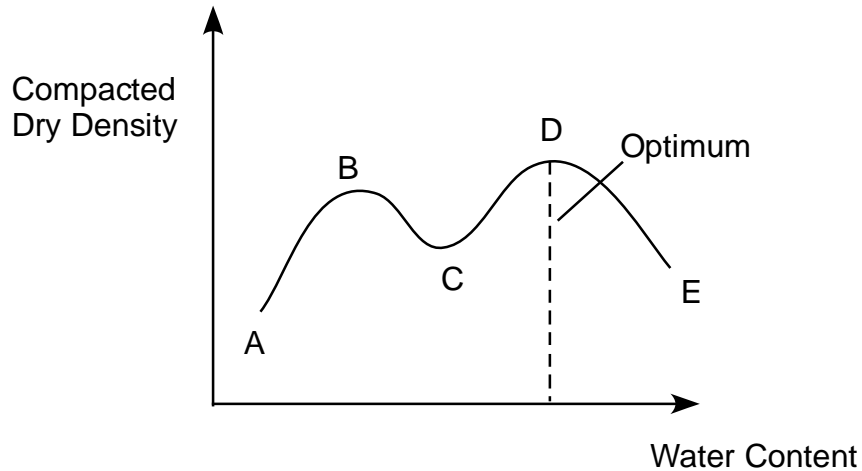
Figure 5. 39: *Conceptual double-peak behavior in Proctor compaction curve*

Figure 5.40 shows the detailed compaction curve for F-40 Ottawa sand obtained using standard Proctor energy. Dry density is plotted as a function of degree of saturation, which was determined for each water content from the compacted void ratio. Peaks are apparent at about 20% saturation and 70% saturation. The locations of these peaks are in fairly good agreement with those noted in the tensile strength and apparent cohesion, which were interpreted to be conditions of high effective stress. According to Olson's effective stress interpretation, however, the peaks in the compaction curve would be expected to occur at saturation conditions where effective stress reaches a minimum. These results suggest that the increase in effective stress resulting from capillary forces acts to increase density rather than provide shear strength to resist densification.
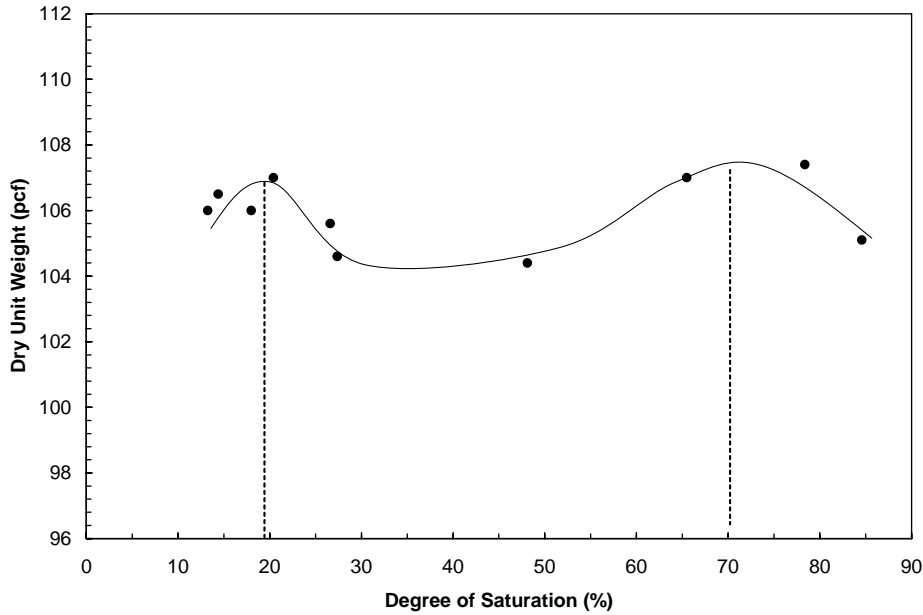
Figure 5. 40: *Double-peak behavior in compaction curve for F-40 sand.*

5.4 Analysis of Failure Surfaces

Figure 5.41 shows a photograph of the post-test failure surface for dense (e~0.60) F-75 sand from direct tension testing at S =8%. Figure 5.42 shows a similar photo for the same soil at S=80% These degrees of saturation were interpreted previously to be near the pendular regime boundary and capillary regime boundary, respectively. The soil near the pendular regime boundary exhibits a smooth tensile failure surface, while the soil near the capillary regime boundary exhibits a rough failure surface. Comparison of densely and loosely compacted specimens showed similar patterns but they occurred at different degrees of saturation because the saturation boundaries depend on the density and grain size of the soil.

Figure 5. 41: *Pattern of failure surface in a tensile strength test for dense F-75 sand (e = 0.60; S = 8%). Pendular regime boundary*

Figure 5. 42: *Pattern of failure surface in a tensile strength test for dense F-75 sand (e = 0.60; S = 80%). Capillary regime boundary*

Lu et al. (2005) observed similar behavior from tensile strength tests on cohesionless sand and interpreted the patterns to reflect the anisotropic nature of capillary-induced stress. Within the pendular saturation regime, sand particles are bonded together by surface tension and the lowered pore water pressure within isolated water bridges between the particles. Tensile failure occurs when the applied uniaxial normal

stress perpendicular to the failure plane exceeds the bonding force along the failure plane. Because the water phase is in the form of isolated water bridges and because tensile stress is not applied in directions parallel to the failure plane, however, the strength of the soil in these directions is not exceeded. Thus, failure occurs only on the plane to which the external tensile stress is applied and the failure plane is smooth. Within the funicular regime, water bridges and pores filled with water are present concurrently, which means both capillary forces due to the water bridges and capillary forces due to regions filled with water contribute to the total bonding force. Because the water phase is not isolated in the form of liquid bridges, the applied uniaxial tensile stress induces a change in stress in three dimensions and failure may occur on a more complex three-dimensional surface. Thus, the observed failure plane is rough.

Figures 5.43 and 5.44 show photographs of failure surfaces for F-40 sand after direct shear testing at degrees of saturation near the pendular regime boundary and capillary regime boundary, respectively. In contrast with the tensile strength results, the surface in the pendular regime is characterized by a rough surface, while that for the capillary regime is characterized by a smooth surface. Failure occurs when the shear strength on the horizontal failure plane is exceeded; however, the three-dimensional state of stress at failure is more complex than in the case of uniaxial tension. The smoother surface for the case of higher saturation probably reflects the more uniform distribution of pore water on the failure surface and a more uniform state of stress.

Figure 5. 43: *Pattern of failure surface in a direct shear test for F-40 sand (e = 0.60; S = 35%)*

Figure 5. 44: *Pattern of failure surface in a direct shear test for F-40 sand (e = 0.60; S = 80%).*

5.5 Analysis of Stress-Deformation Behavior

5.5.1 Shear stress - horizontal displacement behavior

Figure 5.45 shows the relationship between horizontal displacement and shear stress from direct shear tests for densely ($e \sim 0.60$) compacted F-75 specimens at water contents of 6% and 18% ($S = 28.4\%$ and $S = 82.2\%$) and the lowest level of applied total normal stress (5 psi or 34.5 kPa). Direct shear specimens compacted to a relatively dense state are generally expected to exhibit a peak in shear stress and then experience a residual strength at large deformations (*e.g.*, Terzaghi & Peck, 1960).

While both specimens on Figure 5.45 are at approximately the same density, the relatively dry specimen exhibits peak behavior more characteristic of a densely compacted sand specimen. The relatively wet specimen exhibits non-peak behavior more characteristic of a loosely compacted sand specimen. This behavior may be related to the apparent double-peak behavior observed from the results of tensile strength tests. For F-75 sand in either loose or dense conditions, these two peaks occurred at water contents around 6% and 18%. For specimens with water contents close to the first peak (near the pendular regime), the soil exhibits behavior more characteristic of dense sand behavior. As the water content approaches the second peak (near the capillary regime) the soil starts to exhibit behavior more characteristic of loose sand. The more brittle response of the sand near the pendular regime probably reflects relatively uniform failure of the interparticle water bridges at small levels of strain. The peak in shear stress occurs at horizontal displacement of about 0.05 in (1.27 mm).
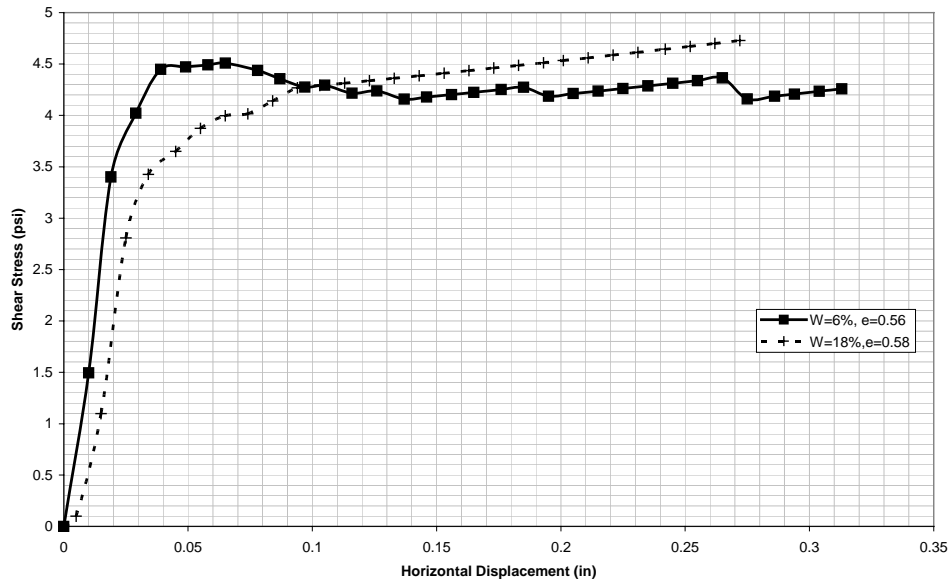
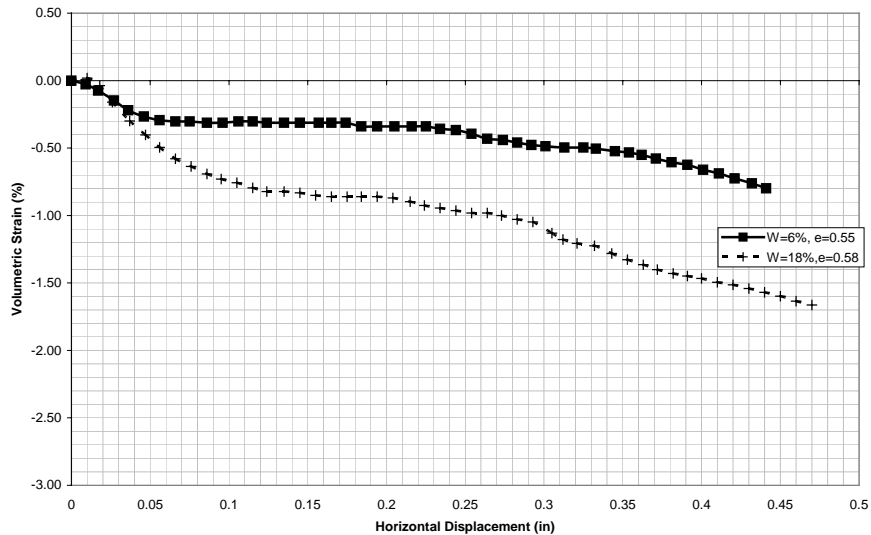**Figure 5. 45:** *Shear stress vs. horizontal displacement for dense F-75 Ottawa sand (σ_n = 5 psi)*

Figures 5.46 and 5.47 show shear stress as a function of horizontal displacement for the same soil at higher values of applied normal stress (15 psi and 40 psi or 103 kPa and 276 kPa). Here, the specimen with water content near the pendular regime does not show a peak in shear stress. This behavior is expected for loose specimens but not for dense specimens. It is possible that in addition to the mechanisms already described, the deformation behavior of the sand might be affected by an increase in the effective normal stress that can produce a dense specimen to behave as a loose one.
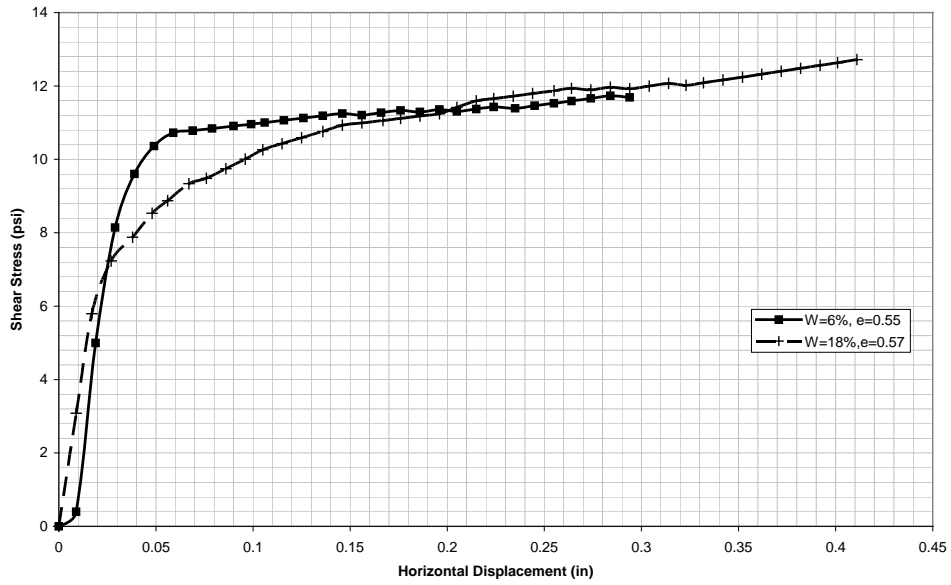
Figure 5. 46: *Shear stress vs. horizontal displacement for dense F-75 Ottawa sand (σ_n = 15 psi)*
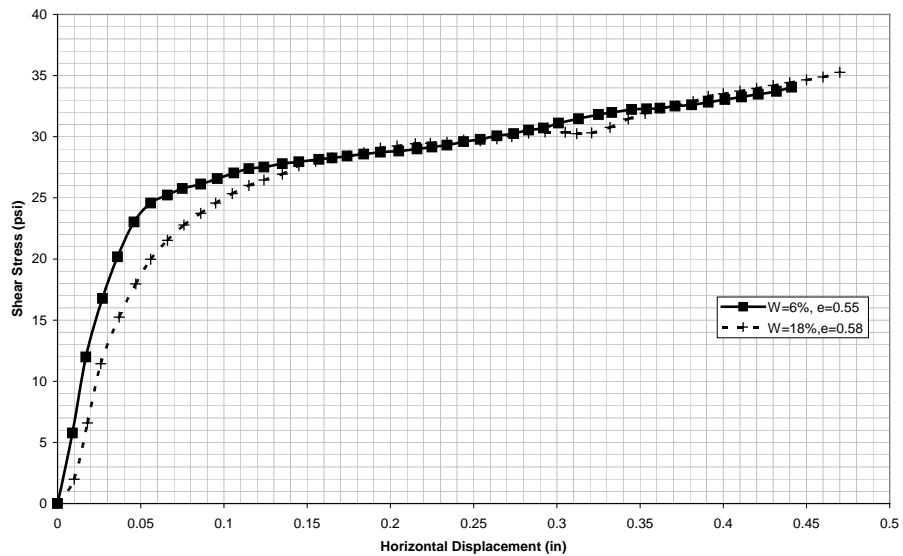
Figure 5. 47: *Shear stress vs. horizontal displacement for dense F-75 Ottawa sand (σ_n = 40 psi)*

5.5.2 Volumetric strain behavior

A dense sand specimen tested in direct shear will typically compress at relatively small horizontal displacements and then expand at higher displacements. Figure 5.48 shows the relationship between volumetric strain and horizontal displacement for densely compacted F-75 sand at 6% and 18% water content and applied normal stress of 5 psi (34.5 kPa). Both specimens first contract and then dilate as the horizontal displacement increases. However, the specimen with water content near the pendular regime ($w = 6\%$) shows initially a decrease in volume and then an increase that exceeds the decrease, thus resulting in a higher void ratio at the end of the test than at the beginning. The initial compression of the specimen at higher water content ($w = 18\%$) is both larger in magnitude than that for the dryer specimen and is not fully recovered. The final void ratio is smaller that the initial.
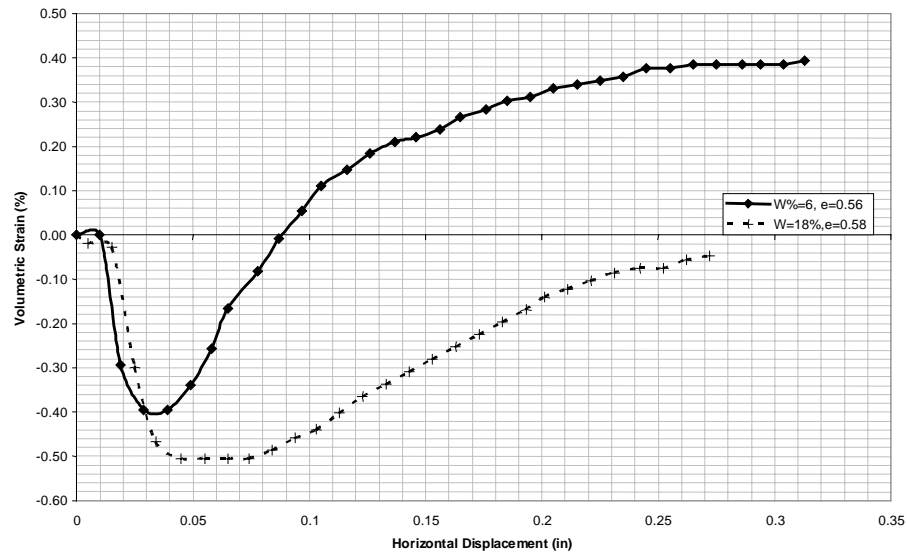
Figure 5. 48: *Volumetric strain vs. horizontal displacement for dense F-75 Ottawa sand (σ_n = 5 psi)*

Figures 5.49 and 5.50 show results for higher values of normal stress. The specimen at 6% water content behaves in a similar manner as before, but the initial compression is smaller than at the smaller value of normal stress. The specimen at 18% water content behaves in a manner characteristic of a loose specimen, even though the density and normal stresses have not changed. Both specimens experience compression over the entire measured range of horizontal displacement. The soil deformation behavior observed can be affected by the saturation regime mechanisms involved as well as the increase in effective normal stress due to those mechanisms. These observations are may be interpreted in terms of critical state behavior.
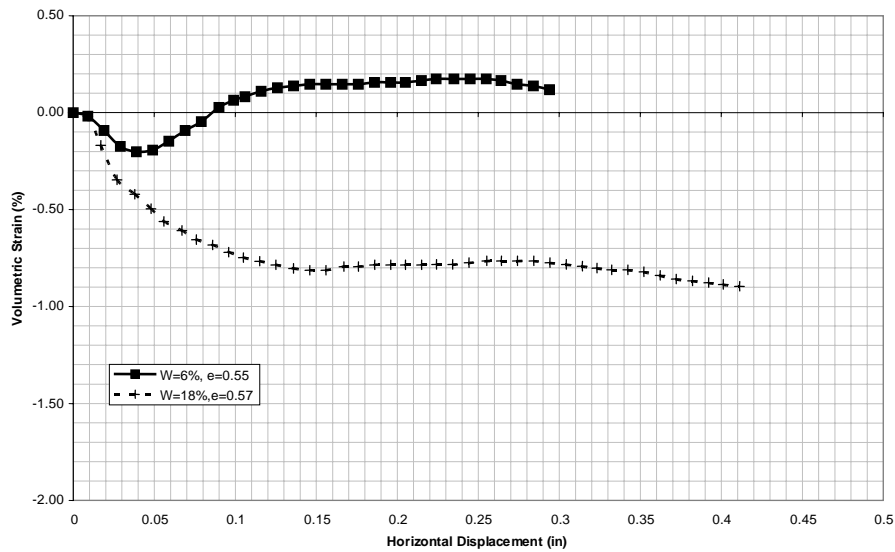
Figure 5. 49: *Volumetric strain vs. horizontal displacement for dense F-75 Ottawa sand (σ_n = 15 psi)*

Figure 5. 50: *Volumetric strain vs. horizontal displacement for dense F-75 Ottawa sand ($\sigma_n = 40$ psi)*

5.5.3 Critical State Line

Wood (1990) defines the critical state line as the ultimate condition in which shearing could continue indefinitely without changes in volume or effective stress. Atkinson & Bransby (1978) said the critical state line is a single and unique line of failure points for both drained and undrained tests. They added that its crucial property is that failure will occur once the stress states of the specimens reach the line, independently of the path followed on their way to the critical state line. This means that for a given confining stress, the critical void ratio is the void ratio at which the specimen will end up at large strains. This critical void ratio is independent of initial void ratio and confining stress.

Wood (1990) mentioned that for dense sand the shear stress reaches a maximum value and if the deformation continues, the shear stress will drop to a smaller value. When this value is reached it will remain constant for all further displacement. During this drop in shear stress the sand continues to expand until the critical void ratio is achieved. At this point continuous deformation is possible at constant shear stress. When loose sand is sheared under constant normal stress the shear stress will increase until it reaches the maximum value. However, if the displacement continues the shear stress will remain the same. Thus, if the same material is tested at loose and dense conditions the curves representing the volume change during shearing meet at the critical state line.

Vertical deformations were recorded during the direct shear tests. Since the initial void ratio is known, it is possible to determine the final void ratio, and thereby determine if the specimen experiences a net decrease or an increase in volume. Figures 5.51 and 5.52 show the critical state line for F-55 and F-75 sand determined by examining the behavior of each of the specimens during shearing. These lines were determined by analyzing if the specimen dilated or contracted during shearing. If the initial void ratio is smaller than the critical void ratio the specimen will tend to dilate. If the initial void ratio is greater than the critical void ratio the specimen will tend to contract. It was observed that some specimens that were prepared to a void ratio of 0.60 (dense) behaved as loose specimens (contraction). This can be explained if it is considered that the critical void ratio is not a constant but a function of the effective normal stress. Since the effective stress varies with suction stress, and this varies with degree of saturation, it can be expected that as the effective normal stress is increased it might be enough to relocate the normal stress on the loose (contraction) side of the critical state line. It is more likely for

a specimen with a high normal stress to be on the contraction side of the critical stress line, and if an increase due to the suction stress is present, this is even more likely. It is also likely that the specimens prepared to higher water content will show higher effective normal stresses, since the suction stress is greater, thus increasing the likelihood of having a specimen on the contraction side of the critical state line. However, it is important to mention that the effective stress increase due to the suction stress at this range of normal stresses was determined to be minimal. This can lead to the thinking that for unsaturated sands not only the normal stress but the mechanisms involved in the unsaturated regimes acting in the specimen affect the deformation behavior of the soil.
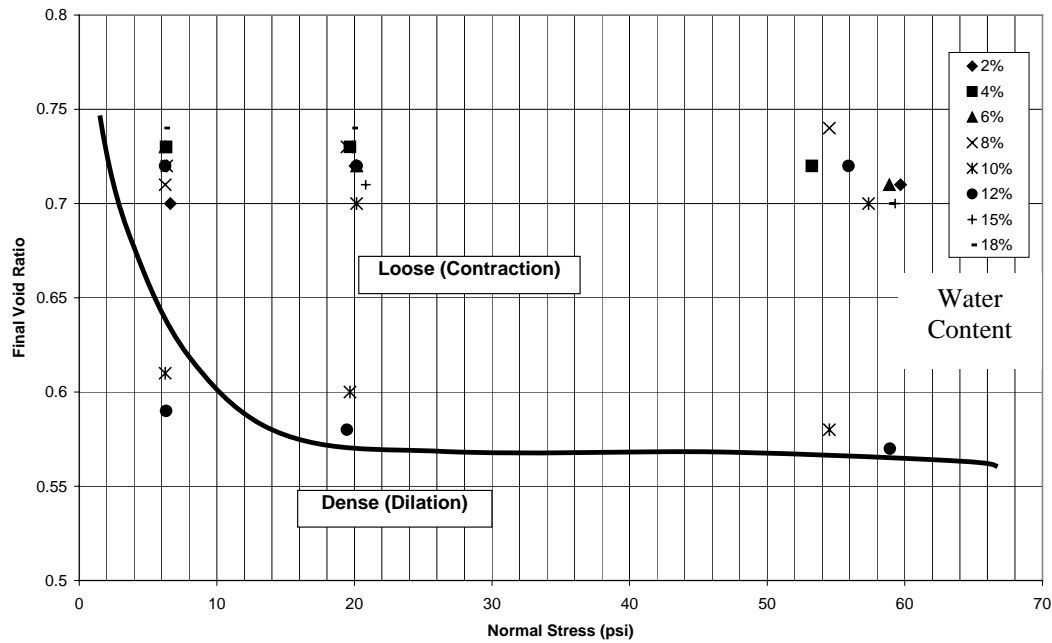
Figure 5. 51: *Critical state line for F-55 Ottawa sand.*
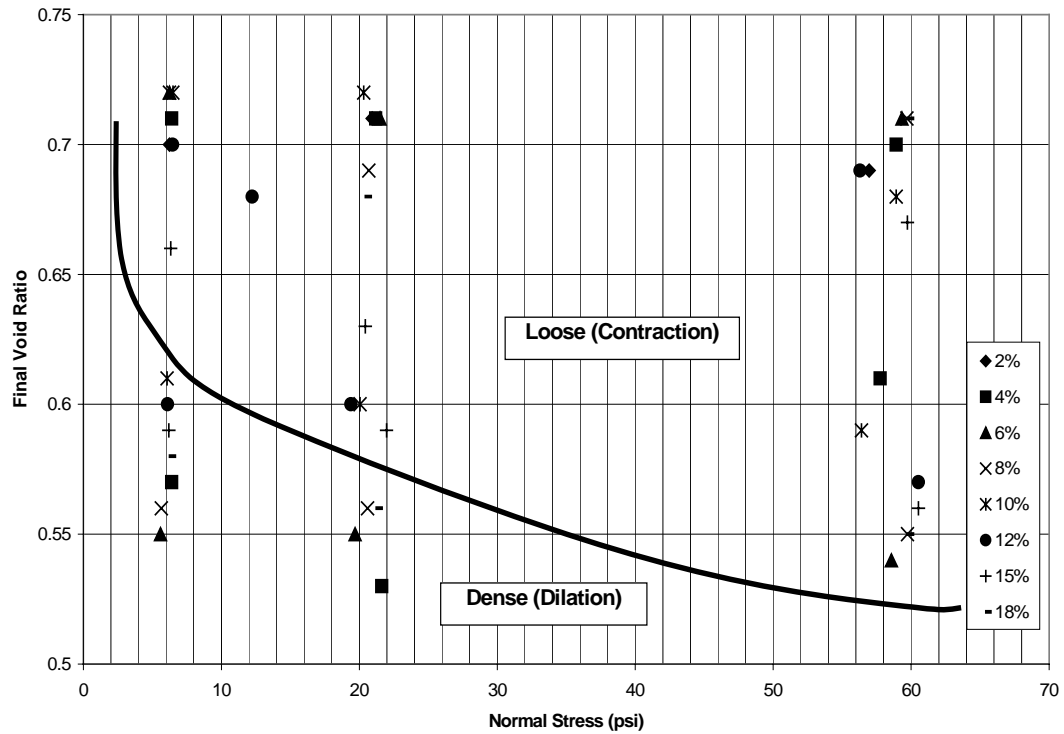
Figure 5. 52: *Critical state line for F-75 Ottawa sand*

5.5.4 Tensile Deformations

Figure 5.53 shows results obtained from tensile strength tests for loose and dense

F-75 sand in terms of tensile displacement (separation of box) measured at failure as a

function of degree of saturation. Peak tensile displacement over the entire range of

saturation is similar for the loose and dense cases and it ranges from about 0.006 inches

to 0.014 inches (0.15 mm to 0.36 mm). Peak displacement for the loose specimen appears

to decrease at higher saturation. The measured range of displacement at failure is on the

same order of magnitude as the mean grain size for the F-75 sand ($d_{50} = 0.22$ mm). For an

ideally smooth failure plane in the pendular regime, this suggests that the liquid bridges

bonding the particles on either side of the failure plane break when the ratio of particle

separation to particle diameter (*a/d*) is about 0.68 to 1.63. It is more likely that the liquid

bridges fail non-uniformly at much smaller separation distances on a failure plane having

roughness on the scale of individual particles.
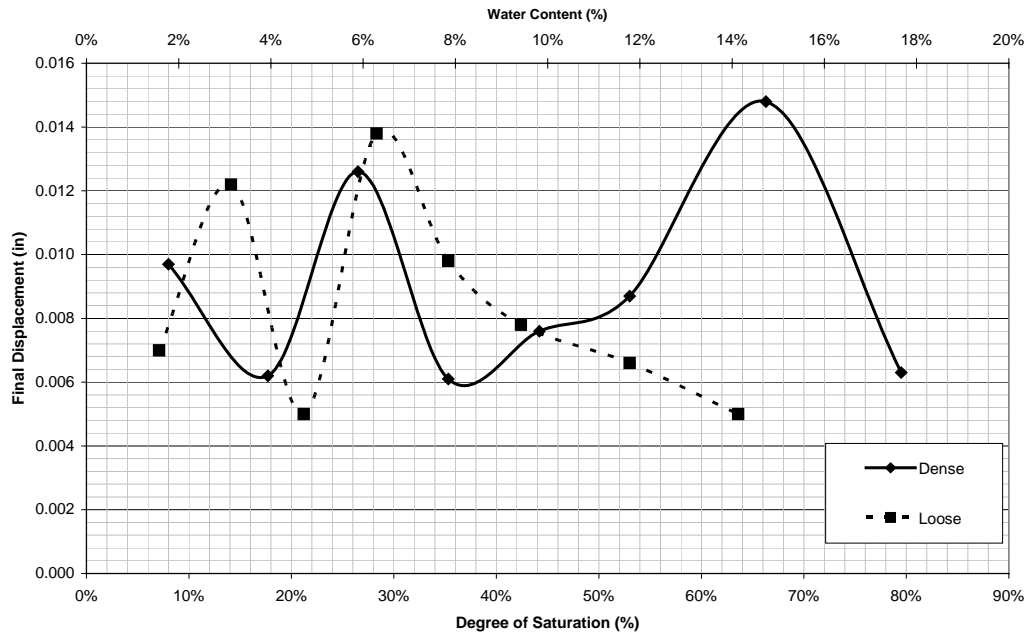
Figure 5. 53: *Horizontal displacement at failure in the tensile strength test for F-75 Ottawa Sand*

Figures 5.54 and 5.55 show peak tensile displacement for all three sand gradations

at dense and loose compaction, respectively. Two observations can be made: (1) the peak

tensile displacement generally increases as particle size decreases; and (2) peak tensile

displacement tends to be more uniform (constant) with changing saturation for larger

particle sizes. The first observation is consistent with Rumpf's (1961) tensile strength

theory for the pendular regime (Chapter 2), which indicates that for a given degree of

saturation, relatively small particles have greater tensile strength at higher separation

distances (*a/d*). The second observation was also evident in the tensile strength

measurements, which also show a more constant value as a function of saturation for the larger grain sizes.
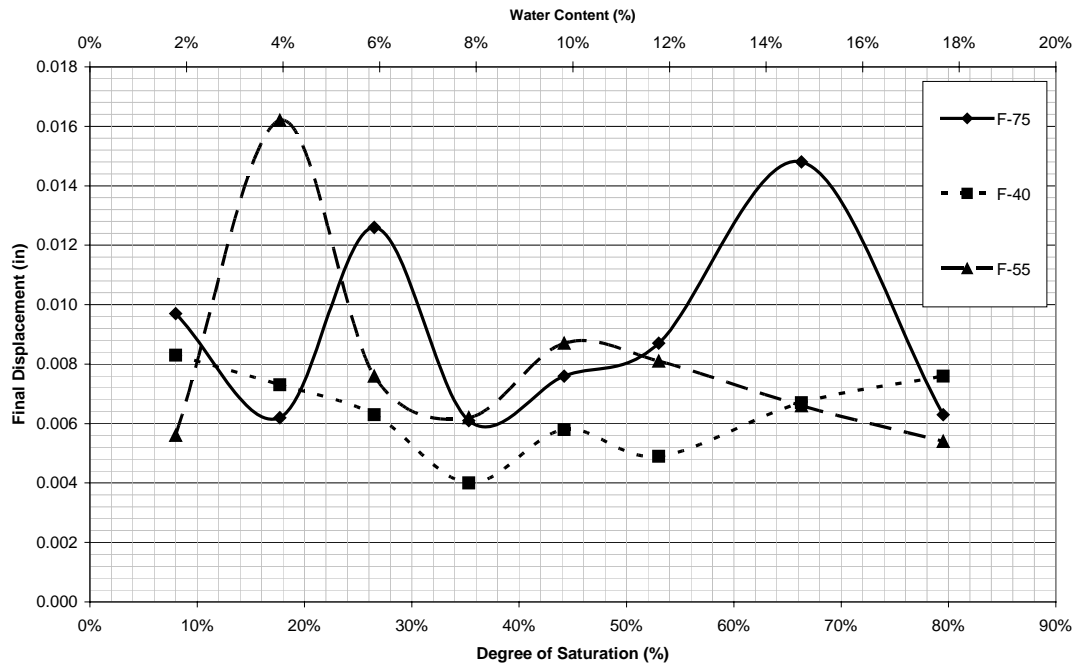
Figure 5. 54: *Horizontal displacement at failure in the tensile strength test (e = 0.60)*
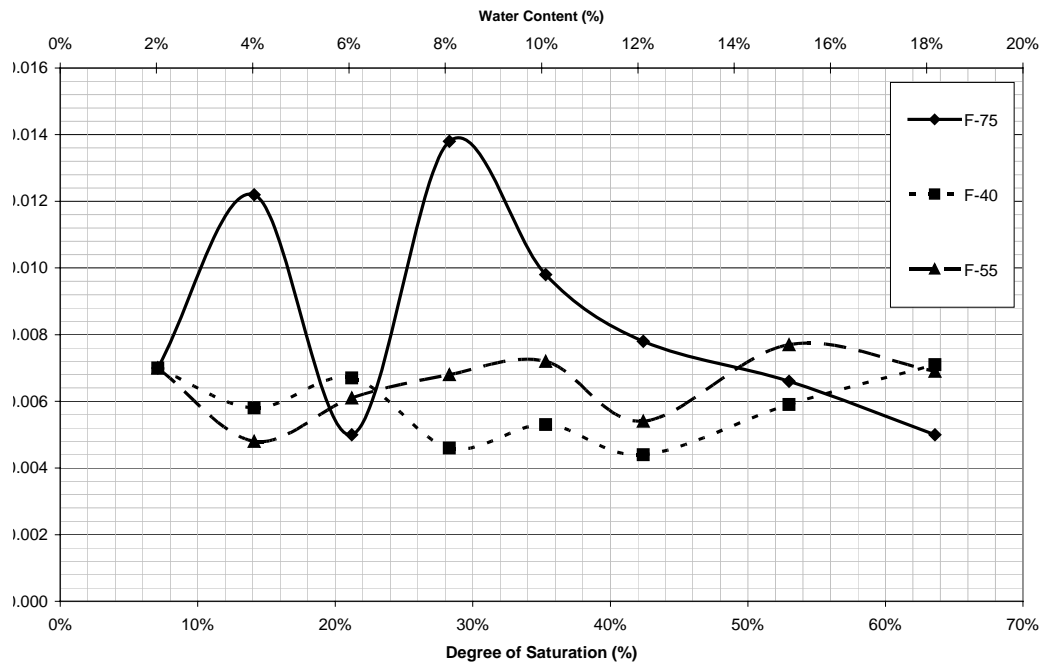
Figure 5. 55: *Horizontal displacement at failure in the tensile strength test (e=0.75)*

6 Conclusions and Recommendations

6.1 Conclusions

Direct tension and direct shear tests were conducted to better understand the role of capillary-induced interparticle forces and their manifestation to the strength and deformation behavior of sand. Three gradations of Ottawa sand were compacted to relatively dense (e ~ 0.60) and relatively loose (e ~ 0.75) conditions and tested for tensile strength and shear strength at degrees of saturation ranging from about 10% to 80%. The major conclusions obtained from this research are:

1. Theoretical models based on interparticle forces in the pendular, funicular, and capillary saturation regimes tended to underpredict measured tensile strength from direct tension tests. Discrepancies may be attributable to the requirement for accurate characterization of the soil-water characteristic curve over a wide saturation range, modeling assumptions about particle size, shape, gradation, contact angle, and particle separation at failure, and experimental limitations resulting from system friction.

2. Analysis of results from direct tension and direct shear tests conducted at relatively low total normal stress (0.01 psi or 100 Pa $< \sigma_n <$ 0.15 psi or 1000 Pa) (Kim, 2001) indicates that tensile strength may be treated as an equivalent effective stress. If total normal stress applied during direct shear tests is added to tensile stress measured at failure during direct tension tests, the total stress envelopes collapse to a unique effective stress envelope. Shear strength may be

reasonably predicted using the sum of tensile strength and total normal stress as an equivalent effective stress ($\sigma' = \sigma_t + \sigma_n$).

3. Analysis of direct shear tests at low normal stress also indicates that Bishop's (1959) effective stress formulation is a reasonable representation for effective stress by setting $\chi = S$ and by back-calculating χ from shear tests. Failure envelopes calculated using the Khalili and Khabbaz (1998) suction ratio method showed limitations in that the total stress failure envelopes did not collapse to a unique failure envelope.

4. Results from theoretical considerations suggest that the magnitude of capillary-induced stress for Ottawa sand is on the order of less than about 0.73 psi (5 KPa) depending on grain size and degree of saturation. Direct tension and direct shear results conducted for high total normal stress (5.1 psi or 35 kPa $< \sigma_n <$ 40 psi or 276 kPa) do not indicate an appreciable impact of capillary forces on direct shear failure envelopes. The high normal stress dominates the effective stress and the effects of capillarity are masked. This suggests that the influence of capillary forces in sand at values of total stress characteristic of many field conditions is negligible.

5. For high normal stresses the effective stress parameter χ back-calculated from the direct shear results was not constrained between zero and one.

6. Tensile strength and apparent cohesion measured from direct tension and direct shear tests, respectively, exhibited double-peak behavior as a function of saturation. A first peak at degree of saturation between about 15% and 30% was interpreted to indicate the peak influence of capillary forces associated with the

pendular regime. A second peak at degree of saturation between about 50% and 90% was interpreted to indicate the peak influence of capillary forces associated with the capillary regime. The peak dominated by capillary mechanisms showed higher tensile strength than the other one. However, the capillary cohesion values for that same point are lower or similar to the peak near the pendular regime boundary. It is important to mention that due to long specimen preparation times tests were not repeated in order to reach some statistical significance. However, there is some confidence that the double-peak behavior is real because it seems to follow that trend at most series of tests.

7. The double-peak peak behavior in tensile strength is more pronounced in specimens prepared loose than those prepared dense. The smaller the grain size, the larger the tensile strength peak value at the same density. Dense specimens showed larger tensile strength magnitudes than the loose specimens. These observations are consistent with the theoretical considerations.

8. Peaks in the Proctor compaction curve for F-40 sand were apparent at about 20% saturation and 70% degree of saturation. The locations of these peaks are in some agreement with those noted in the tensile strength and apparent cohesion. These results suggest that the increase in effective stress resulting from capillary forces acts to increase density by pulling the soil particles closer to each other rather than provide shear strength to resist densification.

9. Sands at saturations near the pendular regime boundary exhibit a smooth tensile failure surface. Sands near the capillary regime boundary exhibit a rough failure surface. Within the pendular saturation regime, sand particles are bonded together

by surface tension and the lowered pore water pressure within isolated water bridges between the particles. Because the water phase is in the form of isolated water bridges and the tensile stress is not applied in directions parallel to the failure plane, but the strength of the soil in these directions is not exceeded, the failure plane is smooth. Within the funicular regime, water bridges and pores filled with water are present concurrently. Because the water phase is not isolated in the form of liquid bridges, the applied uniaxial tensile stress induces a change in stress in three dimensions and failure may occur on a more complex three-dimensional surface. Thus, the observed failure plane is rough. It was observed from the direct shear tests that the rougher failure surface in this test represents the tensile strength peak dominated by the pendular regime mechanisms. The smoother failure surface in this test represents the tensile strength peak dominated by the capillary regime mechanisms.

10. Relatively dense specimens with water contents close to the pendular regime exhibited peak shear stress followed by residual shear stress, which is consistent with the more general behavior of dense sands. However, as the water content starts approaching the capillary regime the soil starts behaving as a loose specimen. The deformation behavior might be affected by an increase in the effective stress that can produce a dense specimen to behave as a loose one.

11. For the same density and normal stress, specimens sheared with water content near the pendular regime showed initially a decrease in volume and then an increase that exceeded the decrease, thus resulting in a higher void ratio at the end of the test. Specimens dominated by capillary regime mechanisms also showed

first a decrease in volume and then an increase. The increase in volume was smaller than the decrease, thus resulting in a final void ratio smaller that the initial.

12.   Horizontal displacement (failure plane separation) at failure in tension exhibited double-peak behavior as a function of degree of saturation. For the dense specimens, the two peaks occurred at higher degrees of saturation than the loose ones. The second peak (higher degree of saturation) showed higher horizontal deformation at failure. The two-peak behavior tends to flatten out as the grain size increases. This behavior is consistent with that observed for tensile strength.

6.2 Recommendations

1.   It is recommended to use a suction controlled tensile strength test device to assure the matric suction remains constant during the test.

2.   Reduce the friction of the system for the tensile strength box used for this research.

3.   Perform direct shear tests at low normal stresses where the horizontal and vertical displacements are measured in order to investigate soil behavior at this range of stress.

4.   Investigate at what ratios of normal stress to suction stress the increase in effective stress should be accounted for in practical geotechnical engineering problems and discuss how dependable these increases can be in practice.

5.   Use the tensile strength test device to evaluate fiber reinforced soil and its behavior and shear strength. Compare to see if the conclusions of this research are applicable to reinforced soils.

6. Perform tensile strength tests on cohesive soils to evaluate the effect of suction stress in the effective stress when forces other than capillary are involved.

7 References

Aitchison, G.D. 1960. "Relationship of Moisture Stress and Effective Stress Functions in Unsaturated Soil" *Pore Pressure and Suction in Soils,* Conference British National Society of International Soil Mechanics and Foundation Engineering: 47-52, Butterworths, London

Akazawa, T. 1953. "Tension Test Method for Concrete" Bulletin No. 16, Nov. 1953. *The International Union of Testing and Research Laboratory for Material and Construction (RILEM),* Paris, France: 11-23

Al-Hussaini, M.M.; Townsend, F.C. 1974. *Investigation of Tensile Testing of Compacted Soils.* U.S.Army Engineer Waterways Experiment Station, Soils and Pavements Laboratory. Vicksburg, Mississippi.

Atkinson, J.H. and P.L. Bransby 1978. *The Mechanics of Soils: An Introduction to Critical State soil Mechanics*. Maidenhead, McGraw-Hill.

Bishop, A.W., 1959, "The principle of effective stress*" Teknisk Ukeblad I Samarbeide Med Teknikk**, Oslo, Norway, 106(39): 859-863*

Bishop, A.W.; Garga, V.K. 1969. "Drained Tests on London Clay" *Geotechnique, Vol. 19, No. 2:* 309-312.

Bofinger, H.E. 1970. *"The Measurement of the Tensile Properties of Soil Cement"* RRL Report LR 365. Road Research Laboratory, Ministry of Transport, Crowthorne, Berkshire.

Brooks, R.H.; and Corey, A.T. 1964. "Hydraulic properties of porous media" *Colorado State University, Hydrology Paper No. 3*, March

Carneiro, F.L.L., and Barcellos, A. 1953. " Tensile Strength of Concrete". Bulletin No. 13, Mar. 1953. *The International Union of Testing and Research Laboratory for Material and Construction (RILEM),* Paris, France: 97-125

Chen, W.F.; and Drucker, D.C. 1969. "Bearing Capacity of Concrete Block or Rock" *Journal of the Engineering Mechanics and Foundations Division*, American Society of Civil Engineers. Vol 96, No. EM4, Aug 1969: 955-978

Cho, G.C.; Santamarina, J.C. 2001. "Unsaturated Particulate Materials-Particle Level Studies" *Journal of Geotechnical and Geoenvironmental Engineering.* Vol. 127, No.3: 84-109.

Conlon, R.T. 1966. "Landslide on the Toulnustone River Quebec" *Canadian Geotechnical Journal, Vol. 3, No.3:* 113-144.

Dallavalle, J.M. 1943. *Micrometrics*. Pitman, London.

Dobbs, H.T.; Jeomans, J.M. 1992. "Capillary condensation and prewetting between spheres" *Journal of Physics: Condensed Matter, 4: 10113-10138*

*Escario***, V.; Juca, J.; and Coppe, M.S. 1989**. "Strength and deformation of partly saturated soils" *in Proceedings of the 12th International Conference on Soil Mechanics and Foundation Engineering,* Vol. 3, Rio de Janeiro: 43-46

Fisher , R.A. 1926. "On the capillary forces in an ideal soil; correction of formula given by W.B. Haines" *Journal Agricultural Science, 16: 492-505*

Fredlund, D.G.; Rahardjo, H. 1993. *Soil Mechanics for Unsaturated Soils.* Wiley & Sons Inc. New York.

Fredlund, D.G.; Xing, A.; and Huang 1994. "Predicting the shear strength of unsaturated soil-water characteristic curve" *Canadian Geotechnical Journal*, 31, 533-546

Hausmann, M.R., 1990, *Engineering Principles of Ground Modification***,** McGraw-Hill, Inc. New York

Hwang, C.S. 2001. *Doctoral Thesis Proposal.*

Khalili, N; Khabbaz, M.H. 1998. "A unique relationship for χ fot the determination of the shear strength of unsaturated soils" *Geotechnique, 48(5): 681-687*

Kim, Tae-Hyung 2001. *Moisture-Induced Tensile Strength and Cohesion in Sand.* Doctoral Dissertation, University of Colorado.

Kumar, S.; Malik, R.S. 1990. "Verification of quick capillary rise approach for determining pore geometrical characteristics in soil of varying texture" *Soil Science. 150(6): 883-888*

Laroussi, C.H.; DeBacker, L.W. 1979. "Relations between geometrical properties of glass bead media and their main $\psi(\theta)$ hysteresis loops" *Soil Science Society of America Journal, 43: 646-650*

Lechman, J., Lu, N., and Wu, D. 2005. "Hysteresis of matric suction and capillary stress in monodisperse disk-shaped particles" *Journal of Engineering Mechanics, Vol. 131 (9), 2005*

Lee, P.Y., and Suedkamp, R.J., 1972, "Characteristics of Irregularly Shaped Compaction Curves of Soils" *Highway Research Record, No. 381, National Academy of Sciences, Washington, D.C.:1-9*

Letey J.; Osborn, J. Pelishek, R.E. 1962. "Measurement of liquid-solid contact angles in soil and sand" *Soil Science. 93: 149-153*

Lian, G; Thornton, C.; Adams, M.J. 1993. "A theoretical study of the liquid bridge forces between two rigid spherical bodies" *Journal of Colloid and Interface Science, 161: 138-147*

Likos, William John 2000. *Total Suction-Moisture Content Characteristics for Expansive Soils.* Doctoral Dissertation, Colorado School of Mines.

Lu, Ning; Likos, William J. 2004. *Unsaturated Soil Mechanics.* Wiley & Sons Inc. New Jersey.

Lu, Ning; Wu, B.; Tan, C. 2005. "A Tensile Strength Apparatus for cohesionless soils" *Proceedings of Experus 2005, Trento, Italy, p.p. 105-110.*

Mesbah, A.; Morel, J.C.; Walker, P.; Ghavami, Kh. 2004. "Development of a Direct Tensile Test for Compacted Earth Blocks Reinforced with Natural Fibers". *Journal of Materials in Civil Engineering:* 95-98.

Mikulitsch, W.A.; Gudehus, G. 1995. "Uniaxial tension, biaxial loading and wetting tests on loess" *Proceedings of 1st International Conference on Unsaturated Soils, Alonso & Delage:* 145-150.

Molenkemp, F.; Nazemi, A.H. 2003. "Interaction between two rough spheres, water bridge, and water vapour" *Geotechnique, 53(2): 255-264*

Munkholm, Lars J.; Schjonning, Per; Kay, Bev D. 2002. "Tensile Strength of Soil cores in relation to aggregate strength, soil fragmentation and pore characteristics" *Soil & Tillage Research:* 125-135

Olson, R.E. 1963. "Effective Stress Theory of Soil Compaction" *Journal of the soil mechanics and foundation division. ASCE. Vol. 89, No SM2, Paper 3457, Ann Arbor, Michigan.*

Orr, F.M.; Scriven, L.E.; and Rivas, A.P. 1975. "Pendular rings between solids: meniscus properties and capillary force" *Journal of Fluid Mechanics. 67(4), 723-744*

Perkins, S.W. 1991. *"Modeling of Regolith Structure Interaction in Extraterrestrial Constructed Facilities"* Doctoral Dissertation. University of Colorado at Boulder.

Piestch, P.; Agrawal, D.K. and Caram, H.S. 1997. "Haftkraft, Kapillardruck, Flussigkestisvolumen und Grenzwinkel einer Flussigkeitsbrucke zwischen Kugeln" *Chemie Ingenieur Technik*, Vol 39, No. 15: 885-893

Rumpf, H. 1961. "The Strength of Granules and Agglomerates". *Agglomeration W.A.Knepper, Interscience:* 379-418

Schubert, Helmar 1975. "Tensile Strength of Agglomerates" *Powder Technology, Elsevier Sequoia S.A:* 107-119

Schubert, Helmar 1984. "Capillary forces-Modeling and application in particulate Technology" *Powder Technology, Elsevier Sequoia S.A:* 105-116.

Tamrakar, Surendra B.; Toshiyuki Mitachi; Yasuo Toyosawa; Kazuya Itoh 2005. "Development of a New Soil Tensile Strength Test Apparatus" *GSP 138 Site Characterization and Modeling. ASCE.*

Tang, Gary X.; Graham, James 2000. "A Method for Testing Tensile Strength in Unsaturated Soils". *Geotechnical Testing Journal:* 377-381.

Terzaghi, Karl; Peck, Ralph B 1960. *" Soil Mechanics in Engineering Practice"* Wiley & Sons Inc. New Jersey.

van Genuchten, M.T. 1980. " A closed form equation for predicting the hydraulic conductivity of unsaturated soils" *Soil Science Society of America Journal*, 44: 892-898

Vanapalli, S.K. Fredlund, D.G. 2000. "Comparison of empirical procedures to predict the shear strength of unsaturated soils using the soil-water characteristic curve" *in Advances in Unsaturated Geotechnics, Shackelford, C.D. Houston, S.L.; and Chang , N.Y. edsGSP No 99, ASCE, Reston VA: 195-209*

Wang, X.; Benson, CH. 2004. "Leak-Free Pressure Plate Extractor for measuring the Soil Water Characteristic Curve" *Geotechnical Testing Journal.* Vol. 27, Issue 2.

Wood, D.M. 1990. *Soil Behaviour and Critical State Soil Mechanics*. Cambridge, England, Cambridge University Press.

Appendix A:

Direct Shear Failure Envelopes
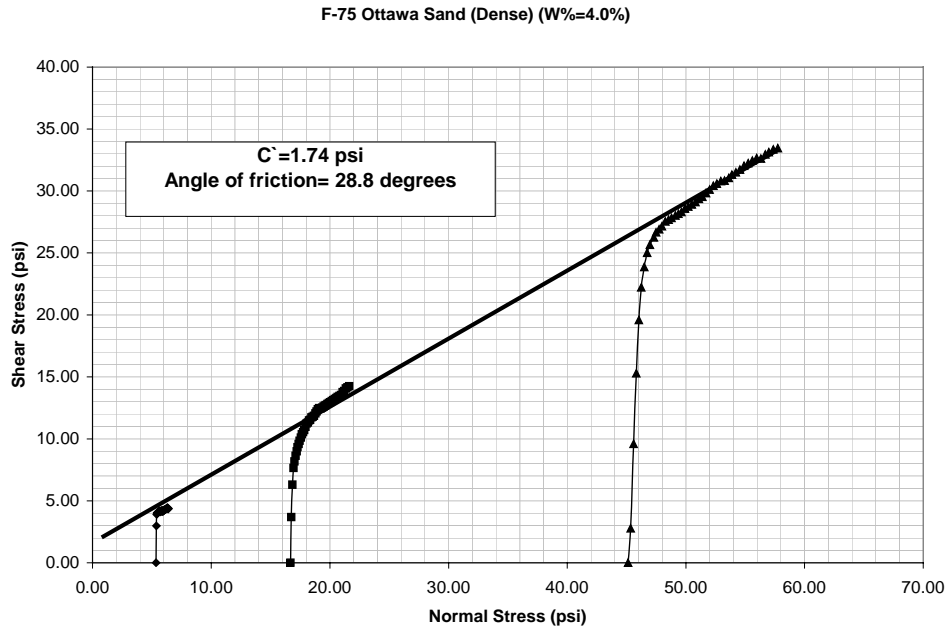
Figure A. 1: *Failure envelope for dense W=4% F-75 Ottawa sand (e= 0.60)*
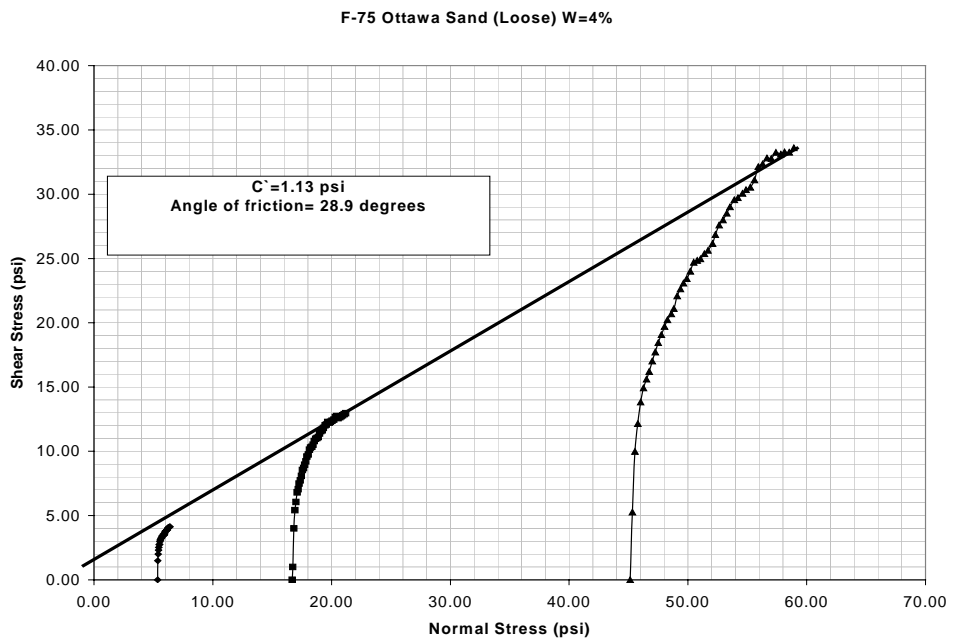
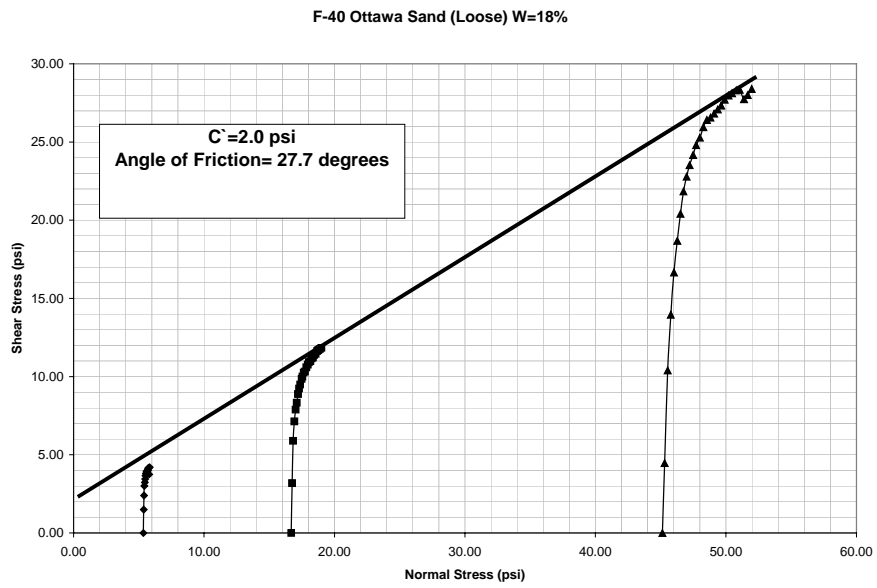**Figure A. 2:** *Failure envelope for loose W=4% F-75 Ottawa sand (e= 0.75)*
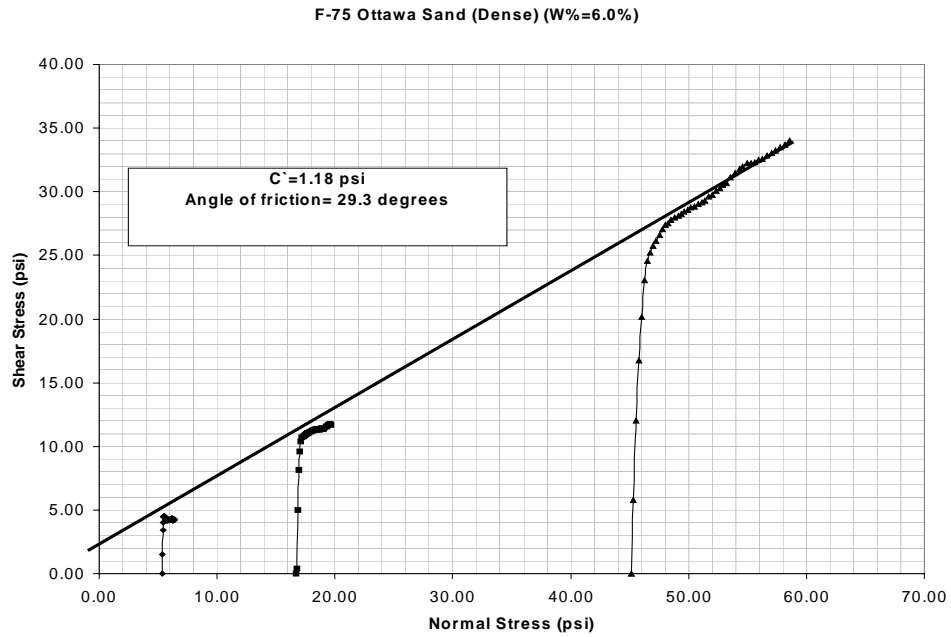
Figure A. 3: *Failure envelope for dense W=6% F-75 Ottawa sand (e= 0.60)*
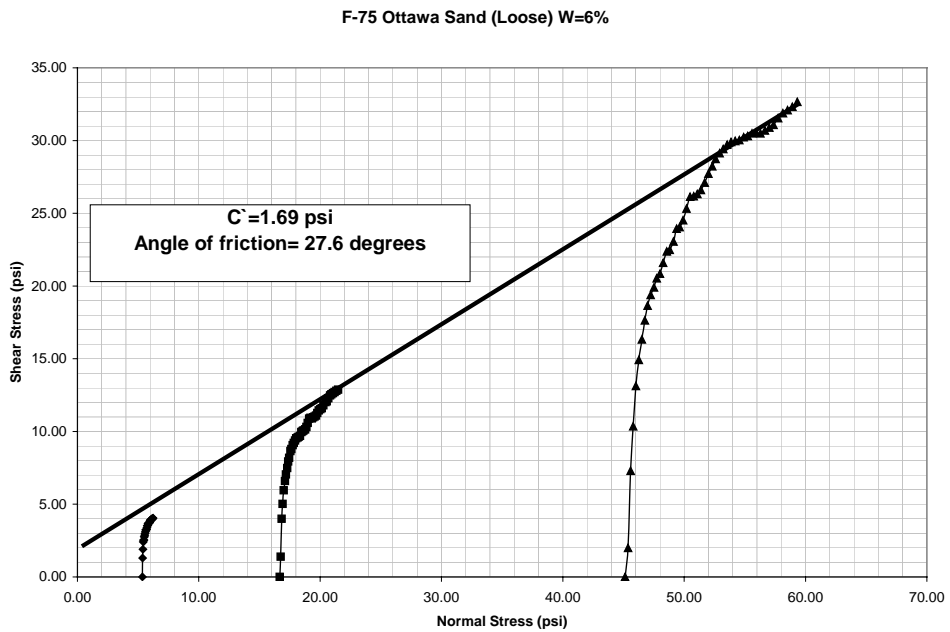
**Figure A. 4:** *Failure envelope for loose W=6% F-75 Ottawa sand (e= 0.75)*

F-75 Ottawa Sand (Dense) (W%=8.0%)

C`=1.06 psi
Angle of friction= 27.6 degrees
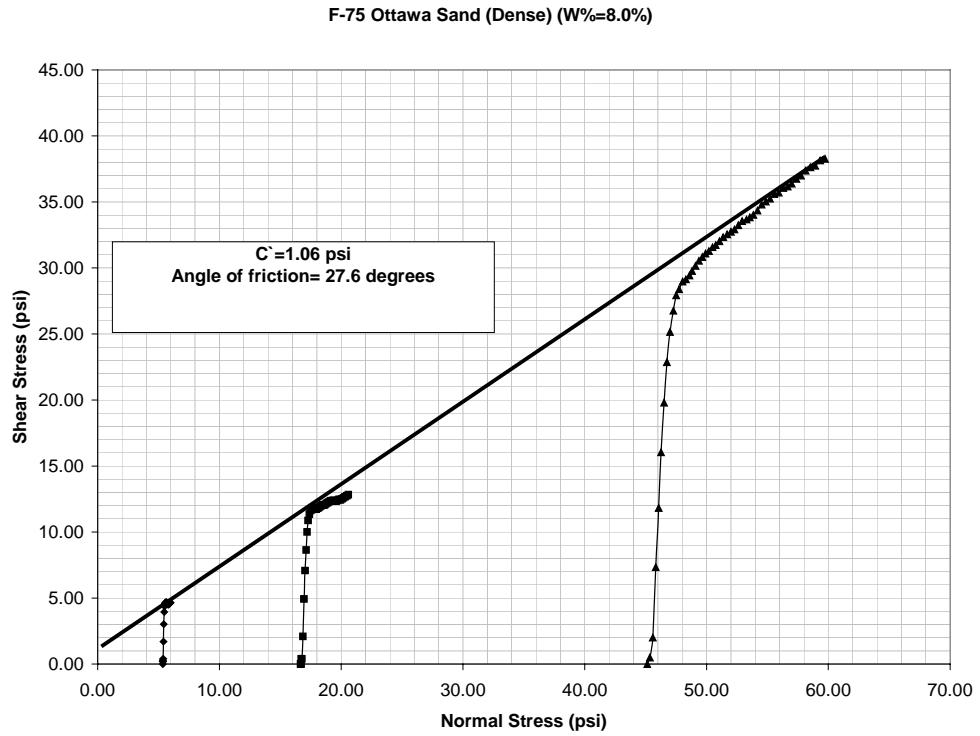
Figure A. 5: *Failure envelope for dense W=8% F-75 Ottawa sand (e= 0.60)*

F-75 Ottawa Sand (Loose) W=8%

C`=1.11 psi
Angle of friction= 29.0 degrees
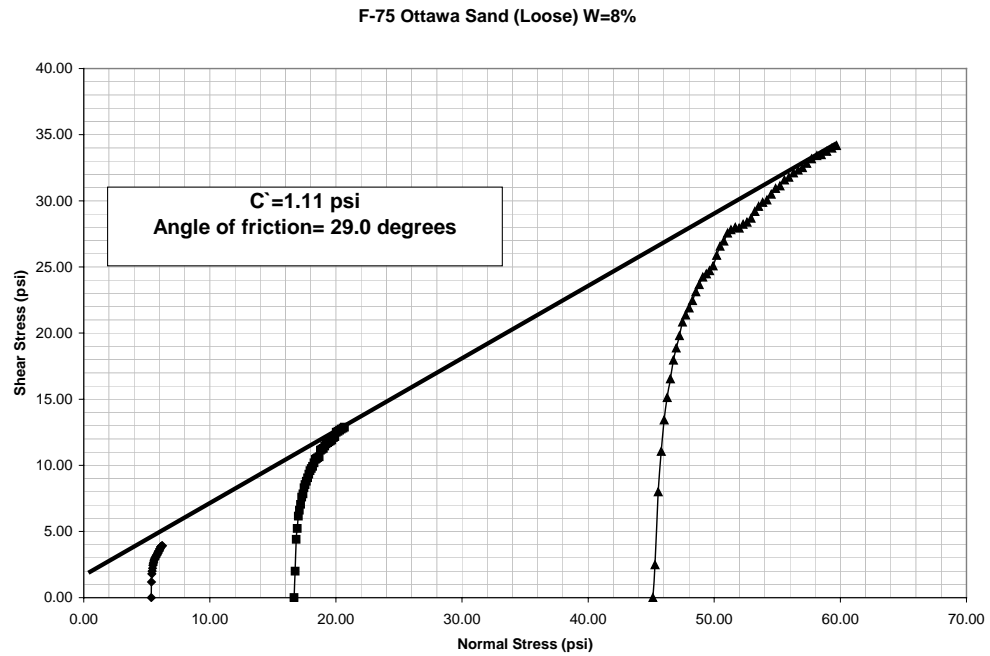
Figure A. 6 :*Failure envelope for loose W=8% F-75 Ottawa sand (e= 0.75)*
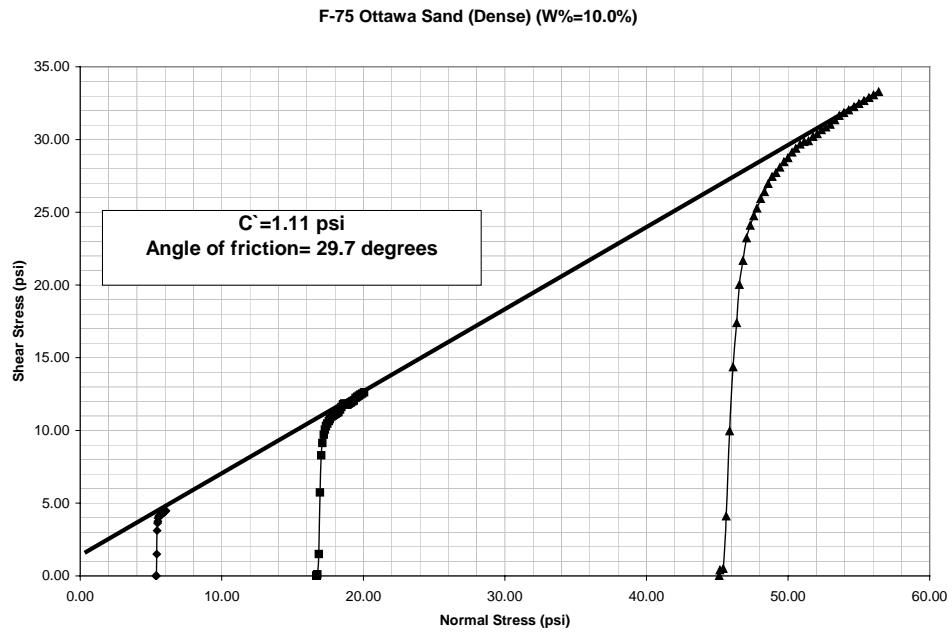
Figure A. 7: *Failure envelope for dense W=10% F-75 Ottawa sand (e= 0.60)*
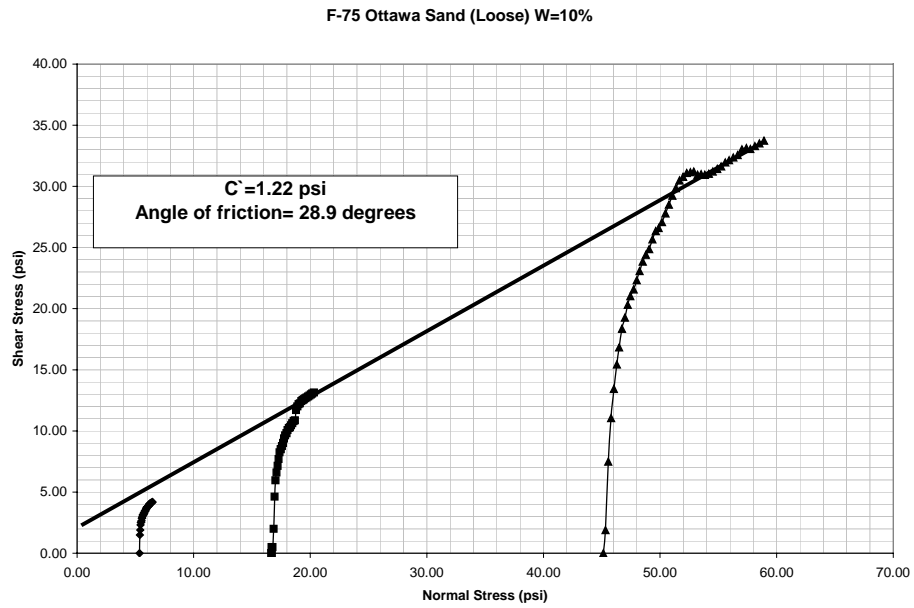
Figure A. 8: *Failure envelope for loose W=10% F-75 Ottawa sand (e= 0.75)*
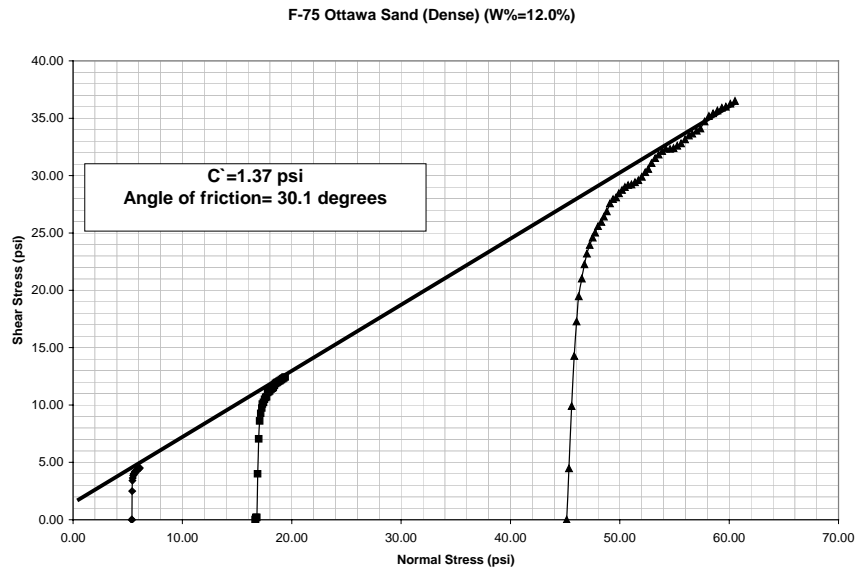
Figure A. 9: *Failure envelope for dense W=12% F-75 Ottawa sand (e= 0.60)*
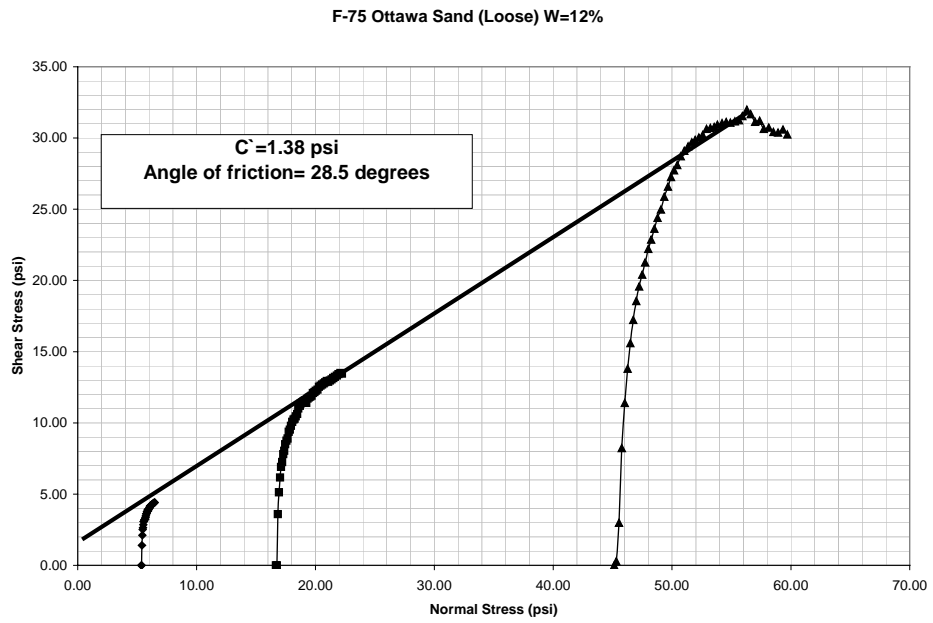
Figure A. 10: *Failure envelope for loose W=12% F-75 Ottawa sand (e= 0.75)*
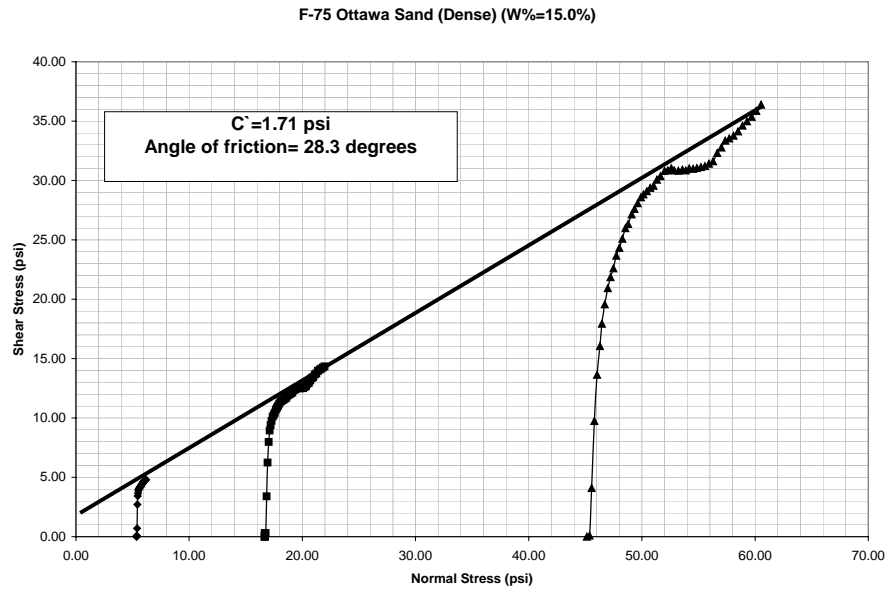
Figure A. 11: *Failure envelope for dense W=15% F-75 Ottawa sand (e= 0.60)*
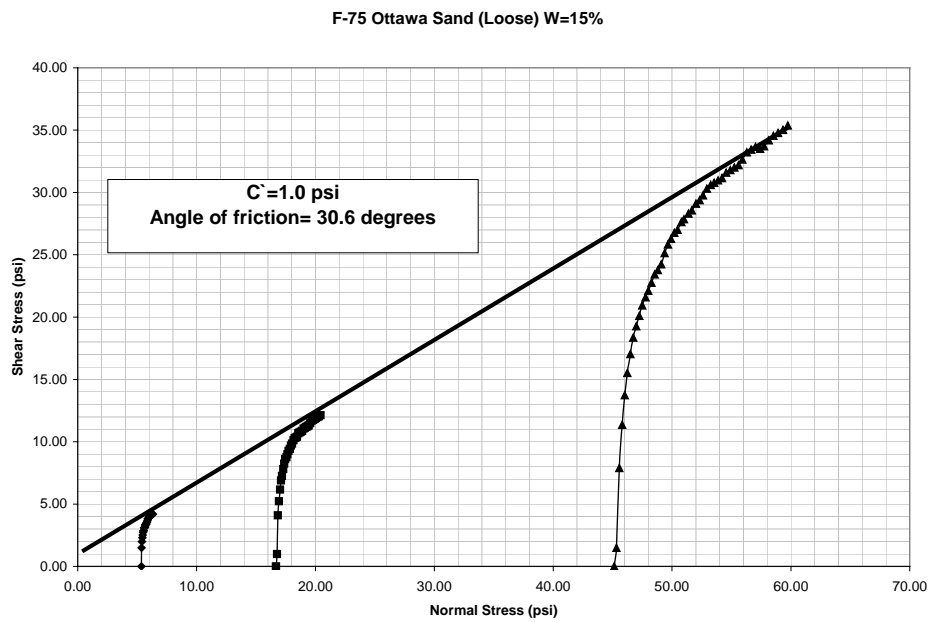
Figure A. 12: *Failure envelope for loose W=15% F-75 Ottawa sand (e= 0.75)*
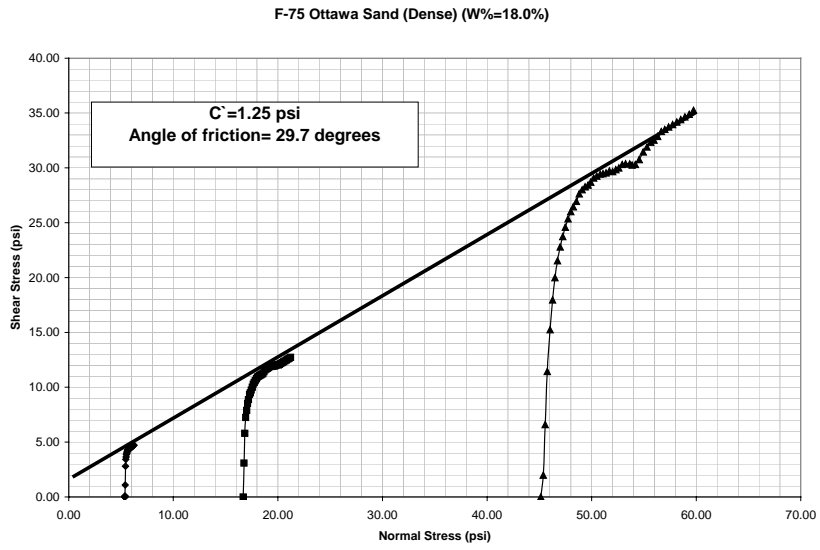
Figure A. 13: *Failure envelope for dense W=18% F-75 Ottawa sand (e= 60)*
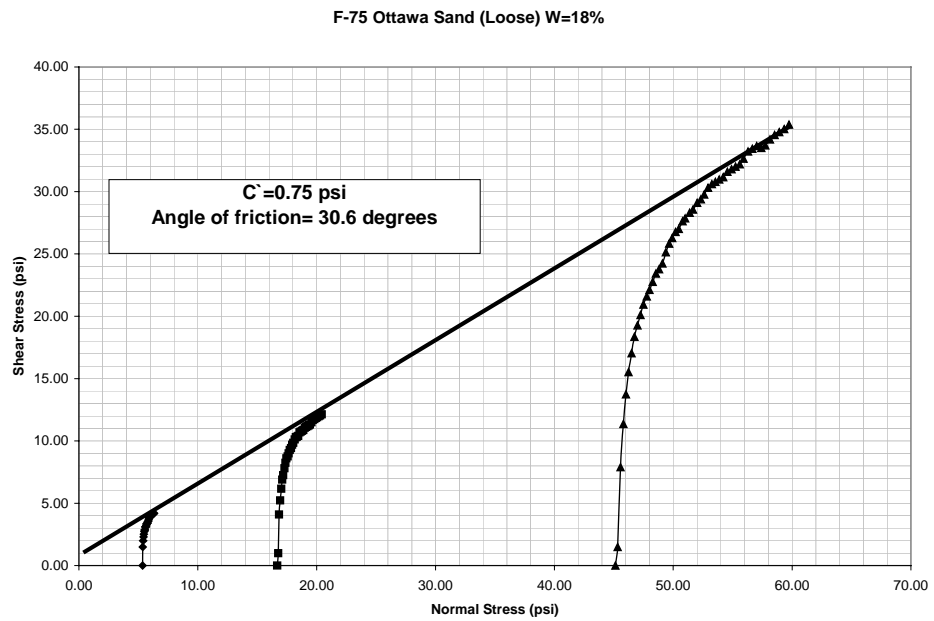
Figure A. 14: *Failure envelope for loose W=18% F-75 Ottawa sand (e= 0.75)*

F-55 Ottawa Sand (Loose) W=2%

C`=1.09 psi
Angle of friction= 28.6 degrees
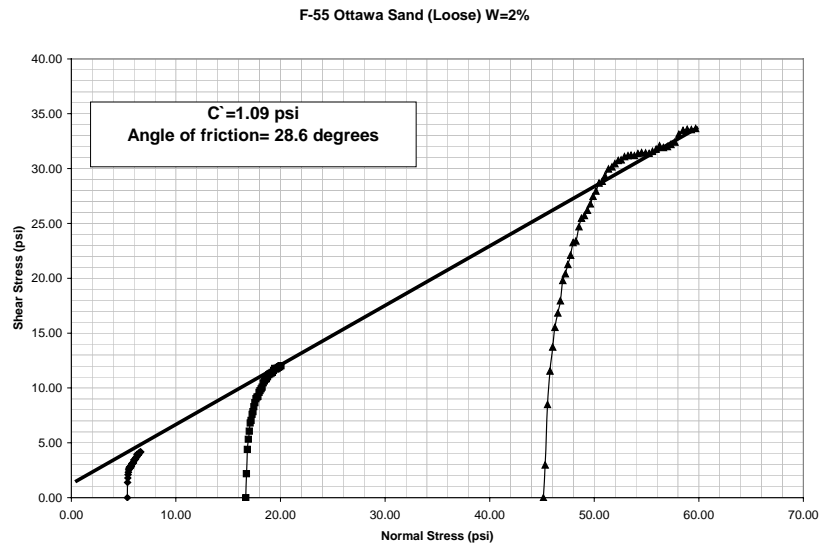
Figure A. 15: *Failure envelope for loose W=2% F-55 Ottawa sand (e= 0.75)*

F-55 Ottawa Sand (Loose) W=4%

C`=0 psi
Angle of friction= 30.1 degrees
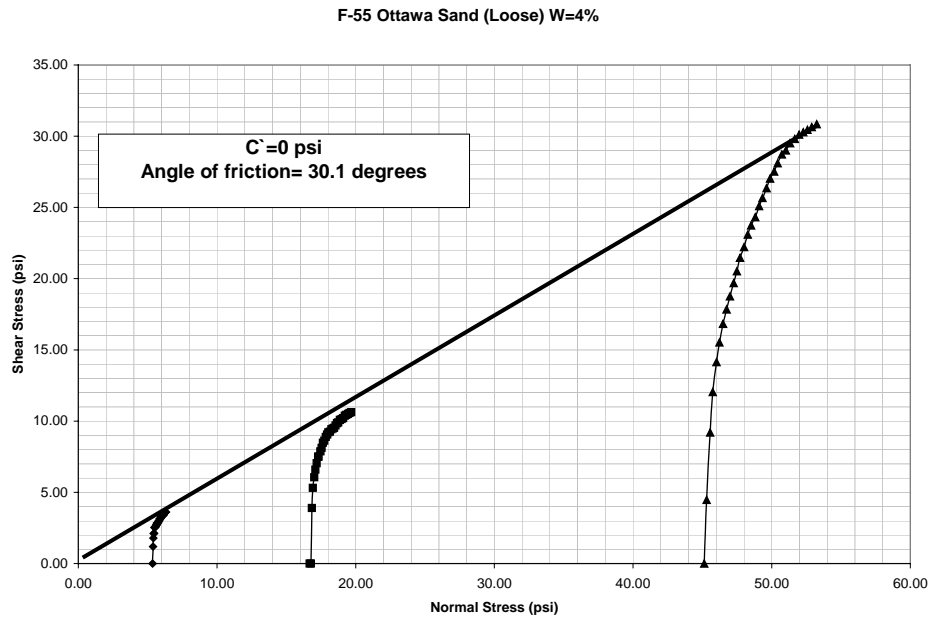
Figure A. 16: *Failure envelope for loose W=4% F-55 Ottawa sand (e= 0.75)*
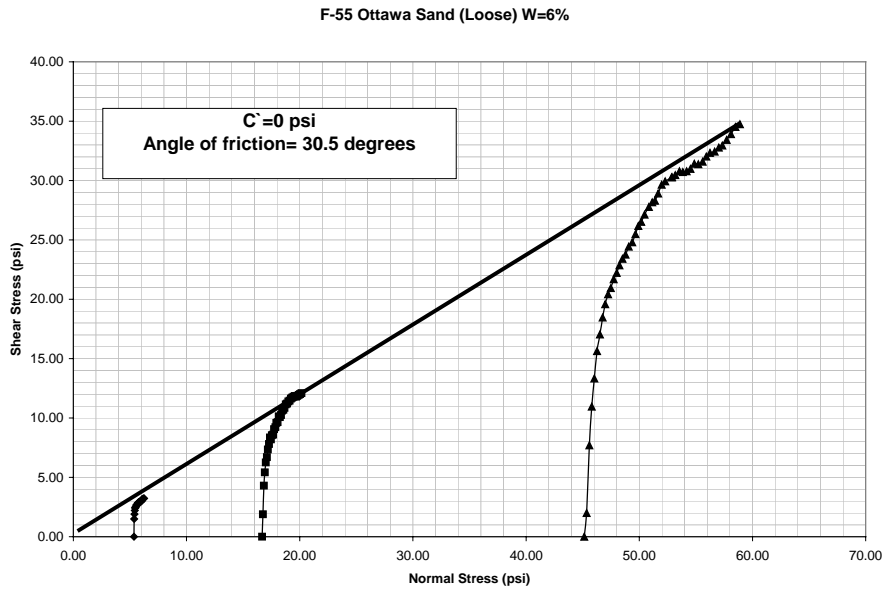
Figure A. 17: *Failure envelope for loose W=6% F-55 Ottawa sand (e= 0.75)*
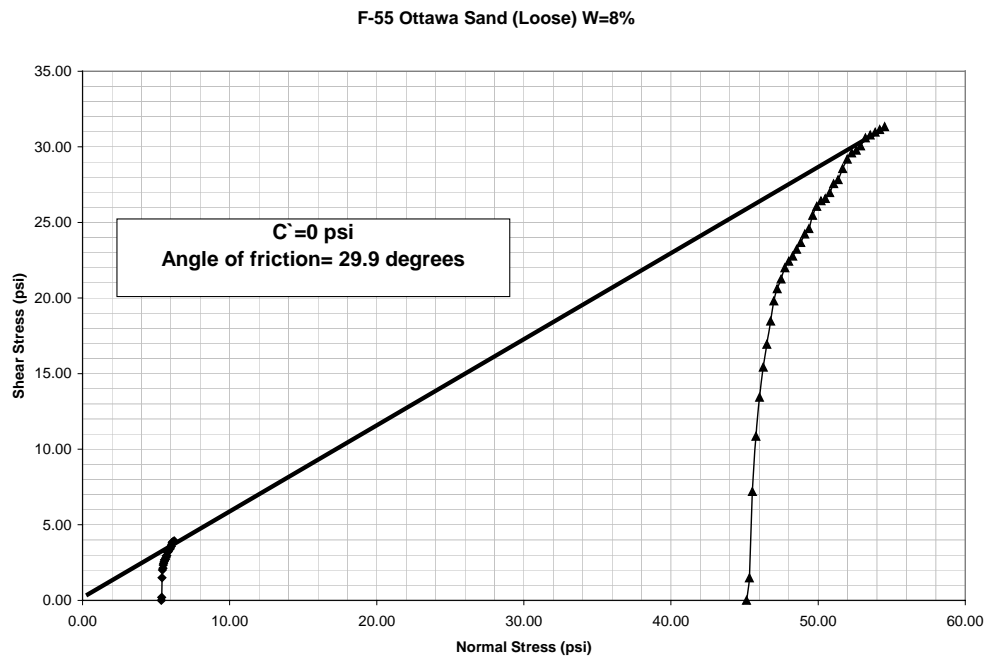
Figure A. 18: *Failure envelope for loose W=8% F-55 Ottawa sand (e= 0.75)*
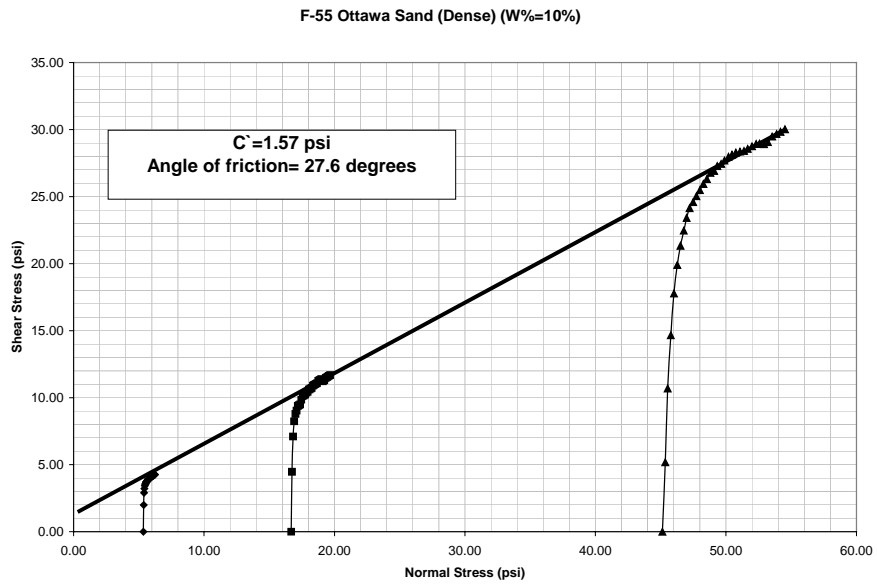
Figure A. 19: *Failure envelope for dense W=10% F-55 Ottawa sand (e= 0.60)*
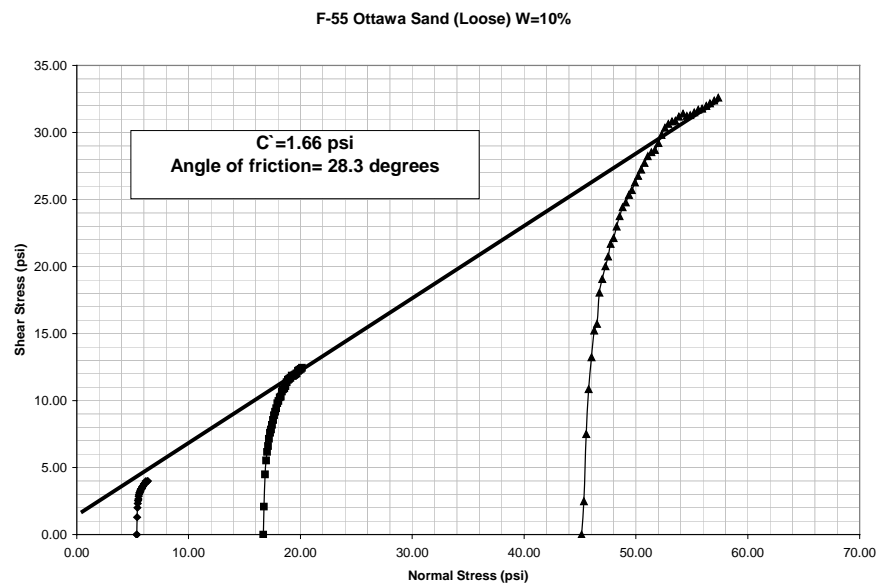
Figure A. 20: *Failure envelope for loose W=10% F-55 Ottawa sand (e= 0.75)*
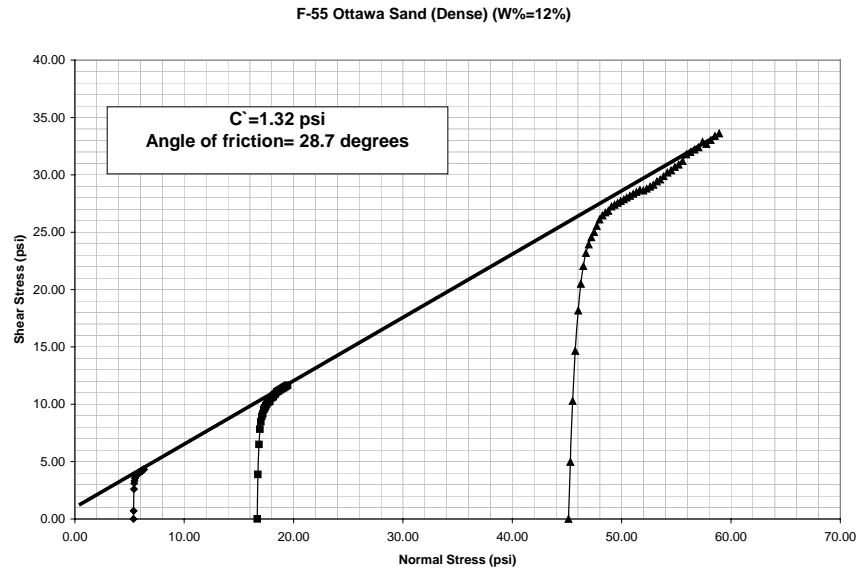
Figure A. 21: *Failure envelope for dense W=12% F-55 Ottawa sand (e= 0.60)*
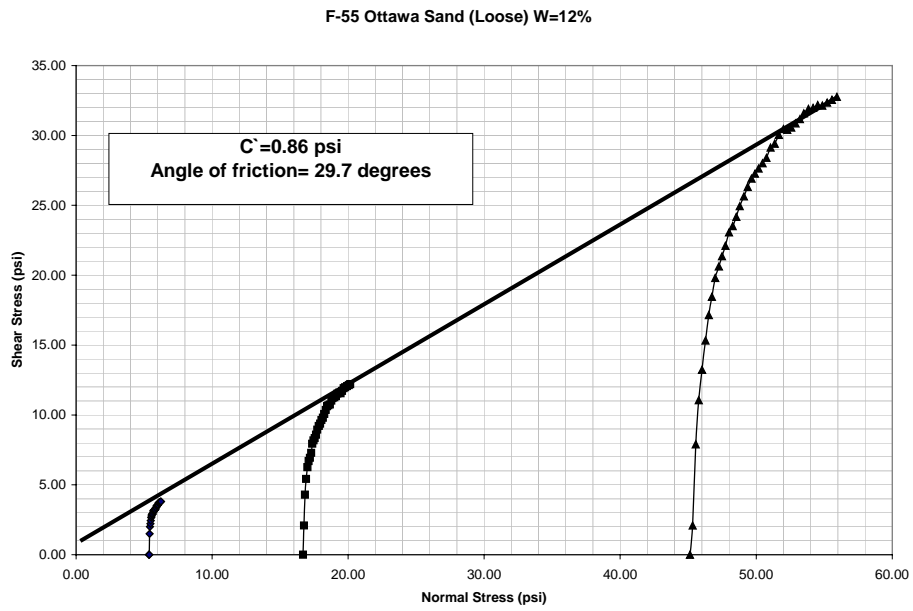
Figure A. 22: *Failure envelope for loose W=12% F-55 Ottawa sand (e= 0.75)*

F-55 Ottawa Sand (Loose) W=15%

C`=1.35 psi
Angle of friction= 28.35 degrees
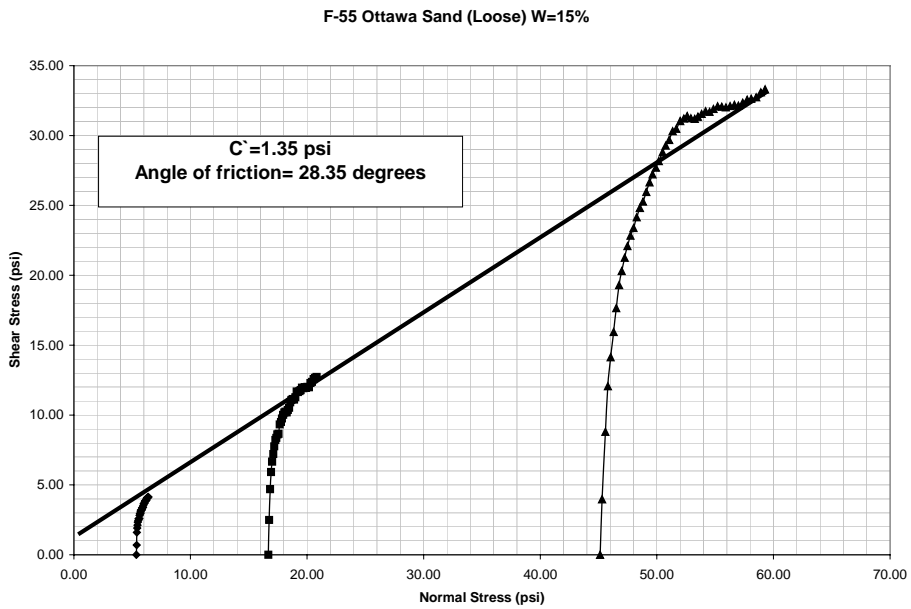
Figure A. 23: *Failure envelope for loose W=15% F-55 Ottawa sand (e= 0.75)*

F-55 Ottawa Sand (Loose) W=18%

C`=1.12 psi
Angle of friction= 29.2 degrees
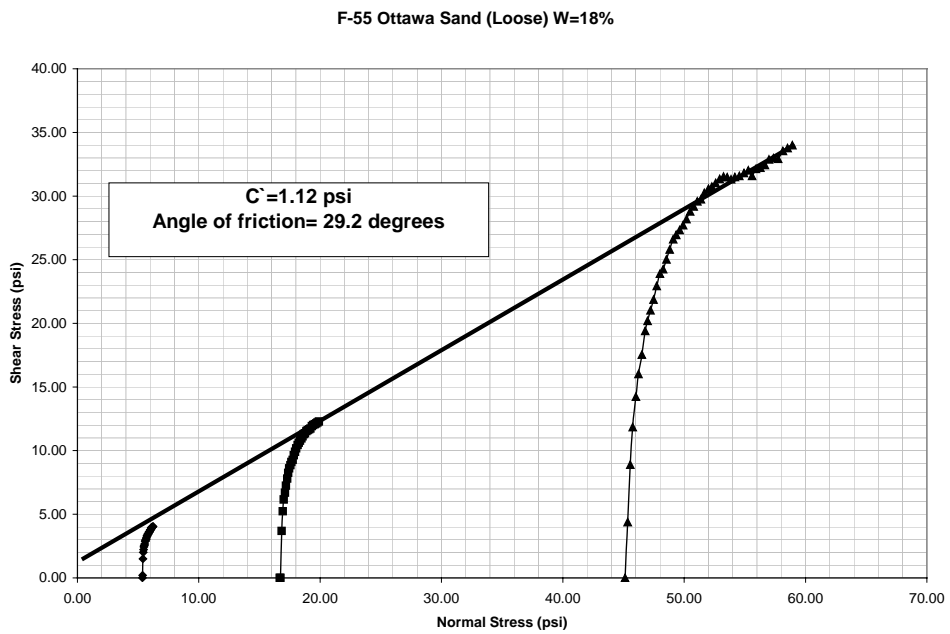
Figure A. 24: *Failure envelope for loose W=18% F-55 Ottawa sand (e= 0.75)*
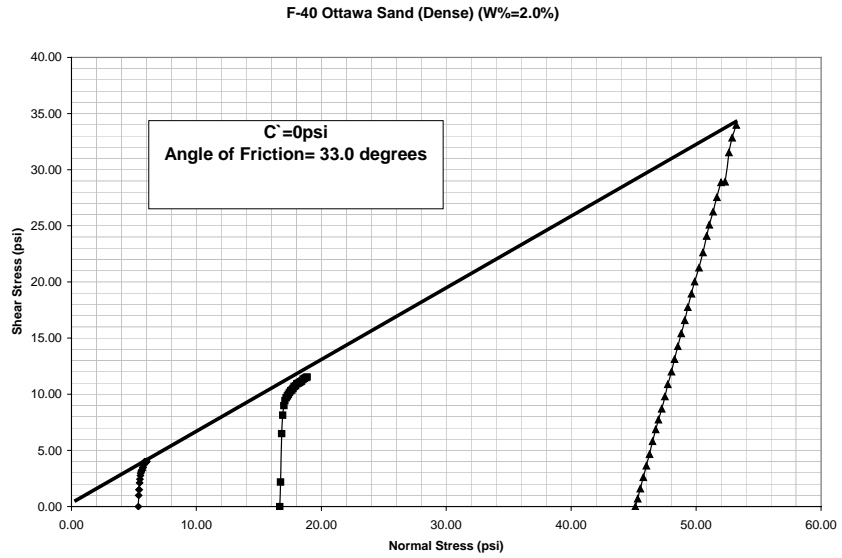
Figure A. 25: *Failure envelope for dense W=6% F-40 Ottawa sand (e= 0.60)*
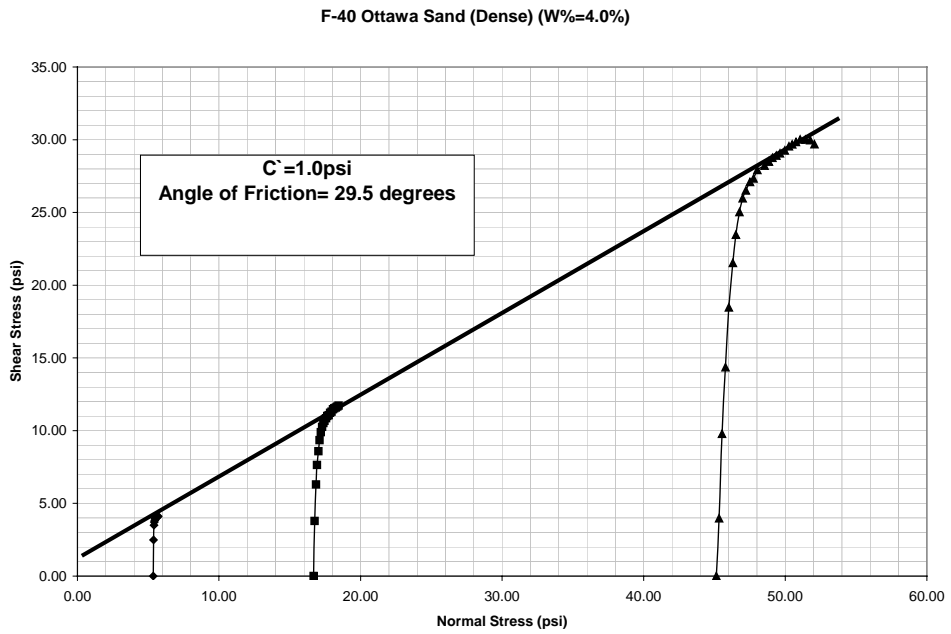
Figure A. 26: *Failure envelope for dense W=4% F-40 Ottawa sand (e= 0.60)*
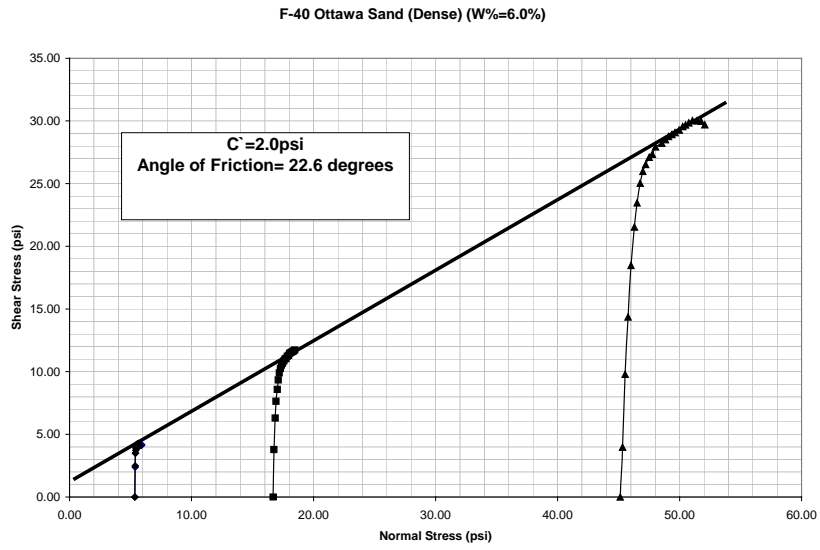
Figure A. 27: *Failure envelope for dense W=6% F-40 Ottawa sand (e= 0.60)*
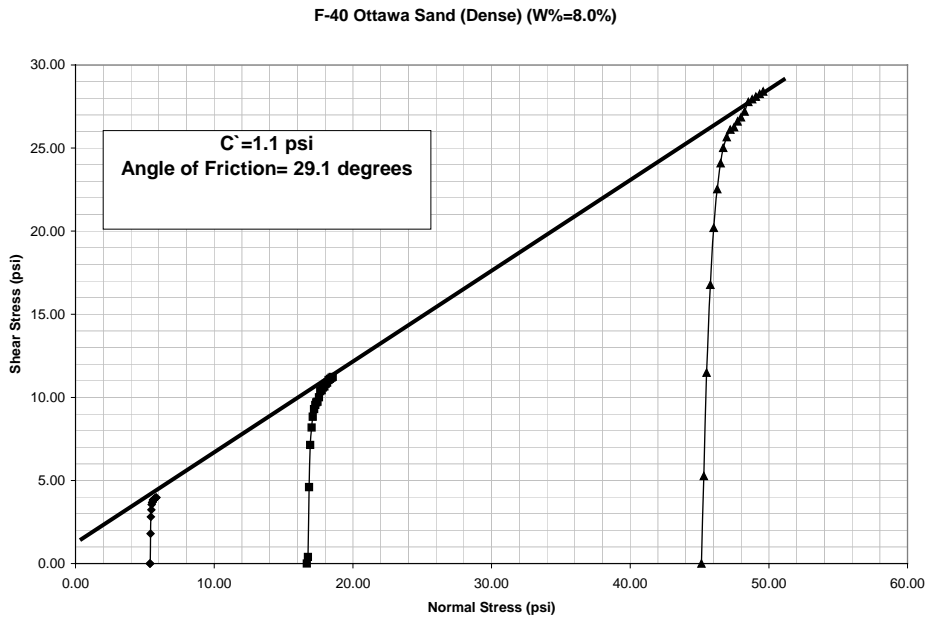
Figure A. 28: *Failure envelope for dense W=8% F-40 Ottawa sand (e= 0.60)*

F-40 Ottawa Sand (Dense) (W%=10.0%)

C`=1.4 psi
Angle of Friction= 28.5 degrees
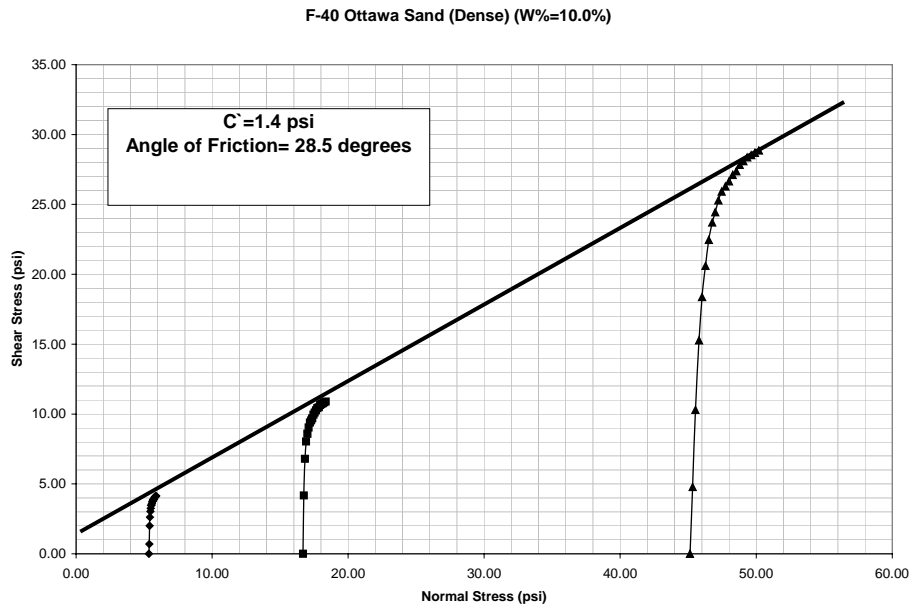
Figure A. 29: *Failure envelope for dense W=10% F-40 Ottawa sand (e= 0.60)*

F-40 Ottawa Sand (Loose) W=10%

C`=1.0 psi
Angle of Friction= 29.7 degrees
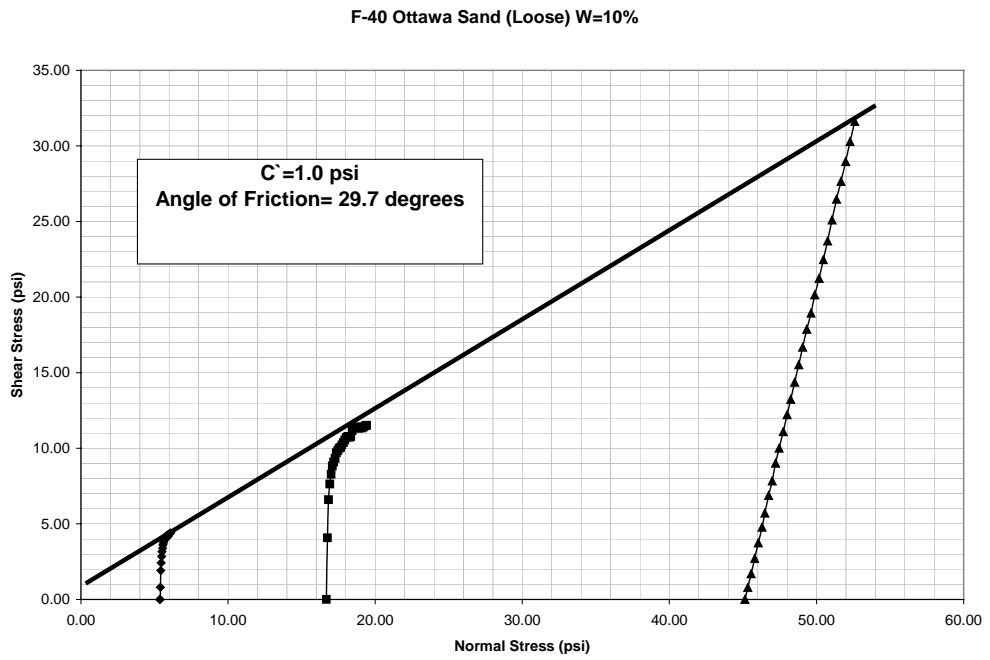
Figure A. 30: *Failure envelope for loose W=10% F-40 Ottawa sand (e= 0.75)*
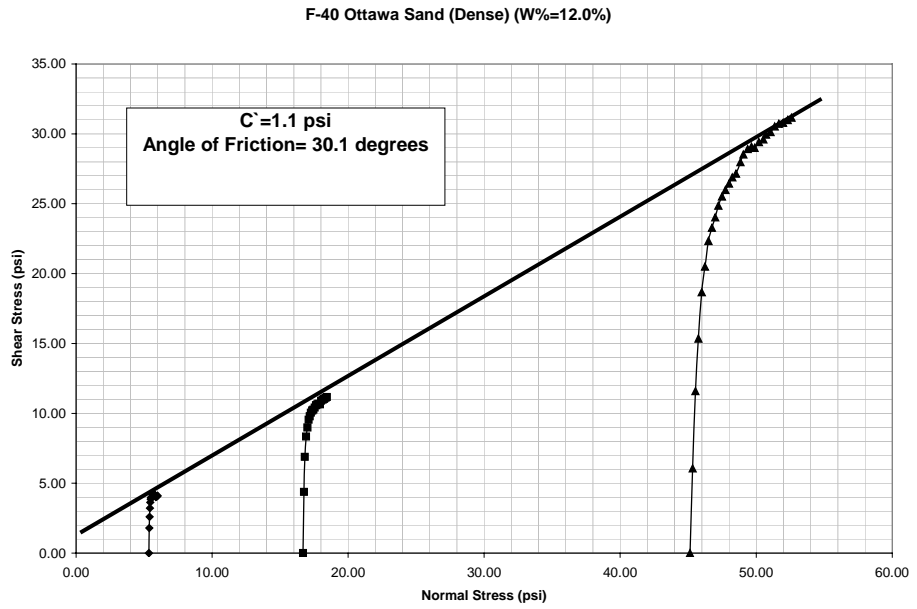
Figure A. 31: *Failure envelope for dense W=12% F-40 Ottawa sand (e= 0.60)*
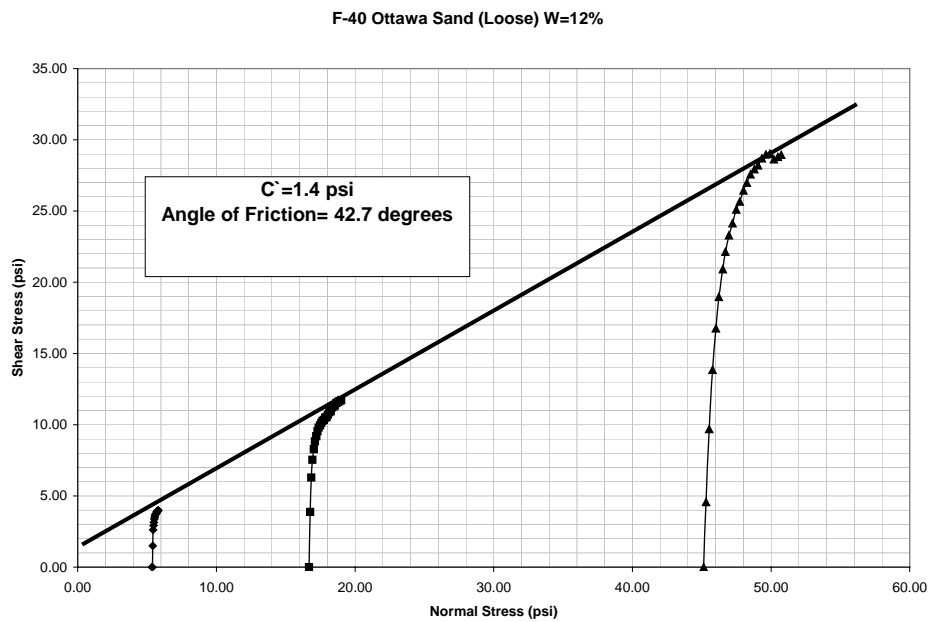
Figure A. 32: *Failure envelope for loose W=12% F-40 Ottawa sand (e= 0.75)*
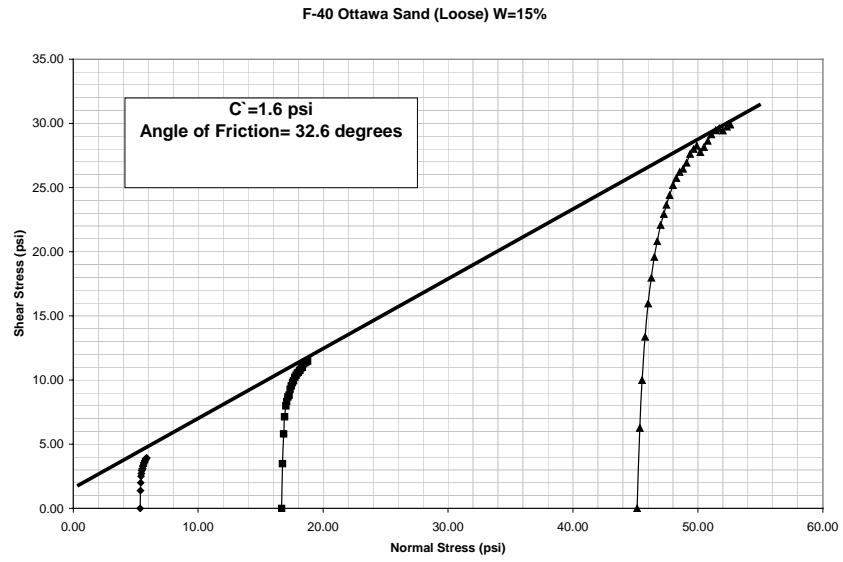
Figure A. 33: *Failure envelope for loose W=15% F-40 Ottawa sand (e= 0.75)*

Figure A. 34: *Failure envelope for loose W=18% F-40 Ottawa sand (e= 0.75)*

Appendix B:

Tensile Strength Test Results
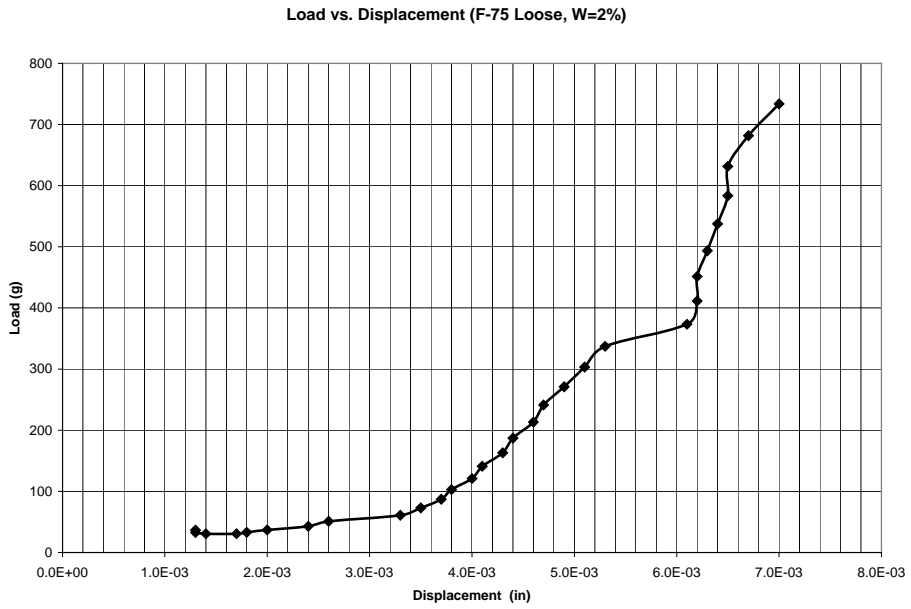
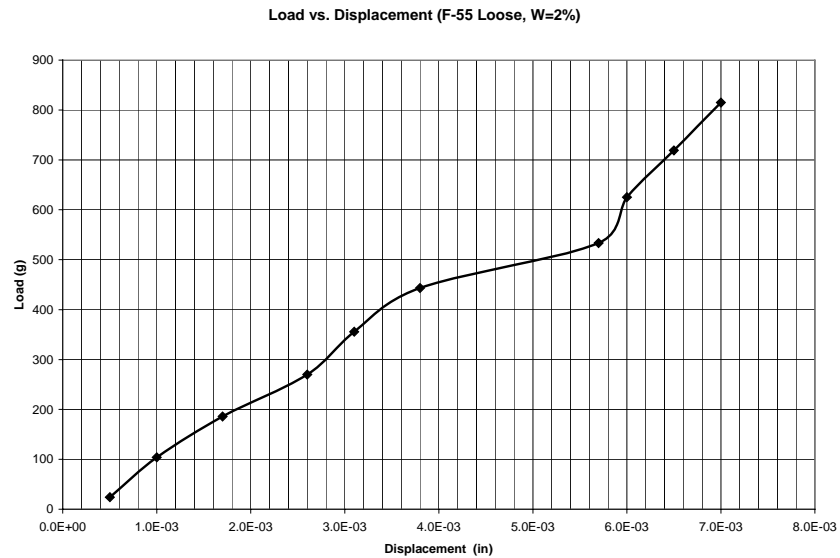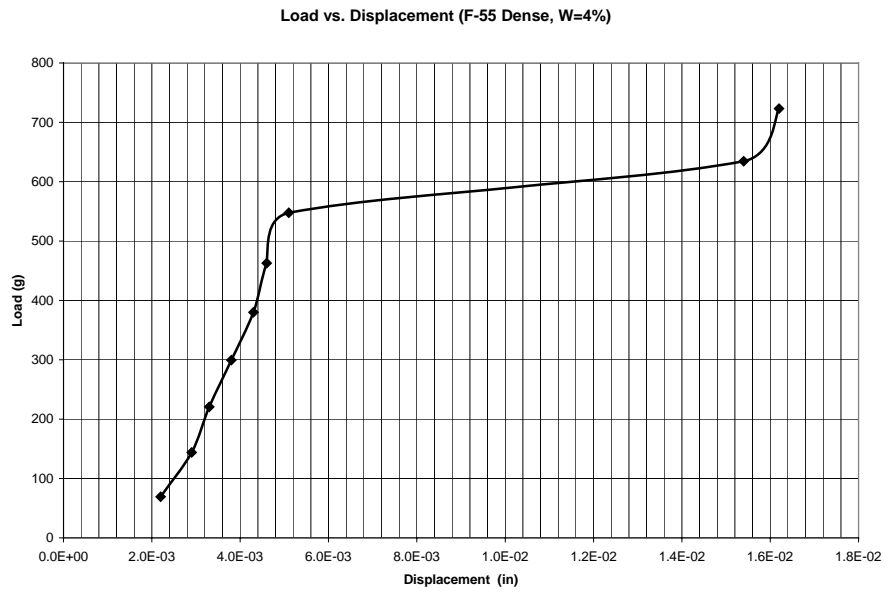**Figure B. 1:** *Load as a function of displacement in a tensile strength test for loose F-75 Ottawa sand (e=0.75 and w=2%)*
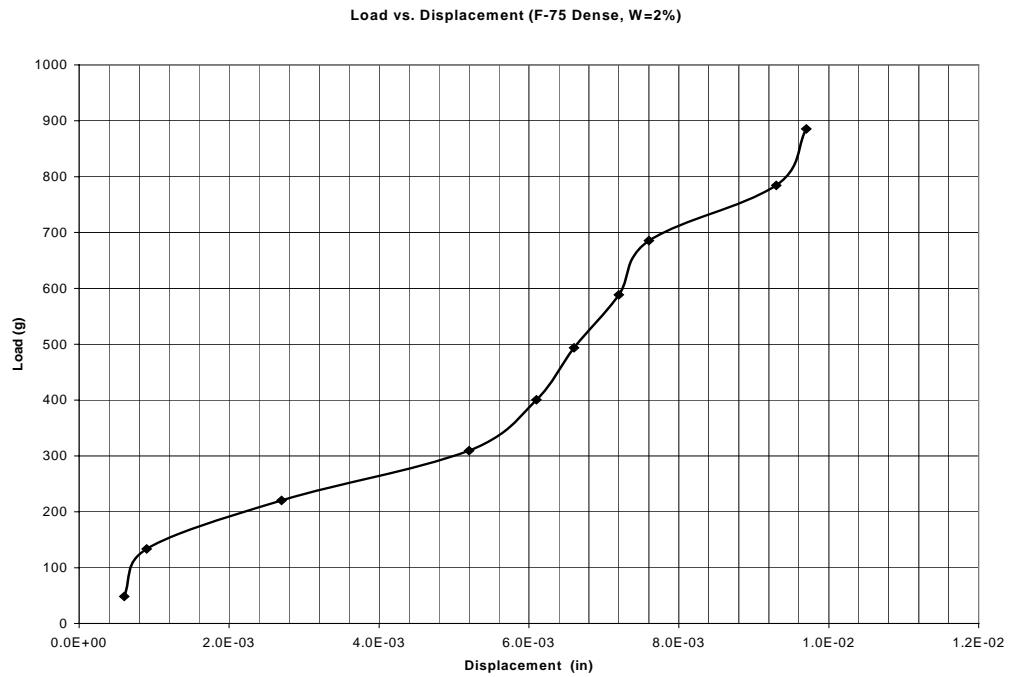
Figure B. 2: *Load as a function of displacement in a tensile strength test for dense F-75 Ottawa sand (e=0.60 and w=2%)*
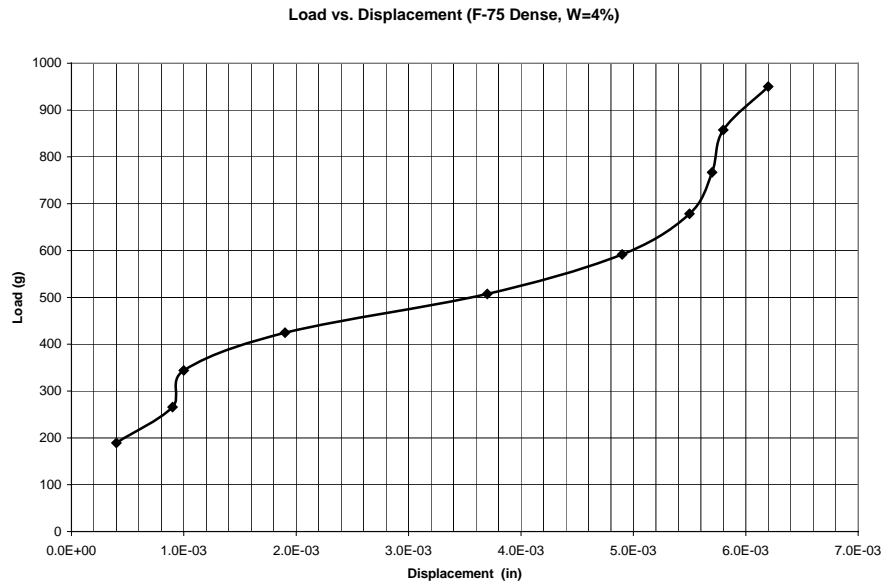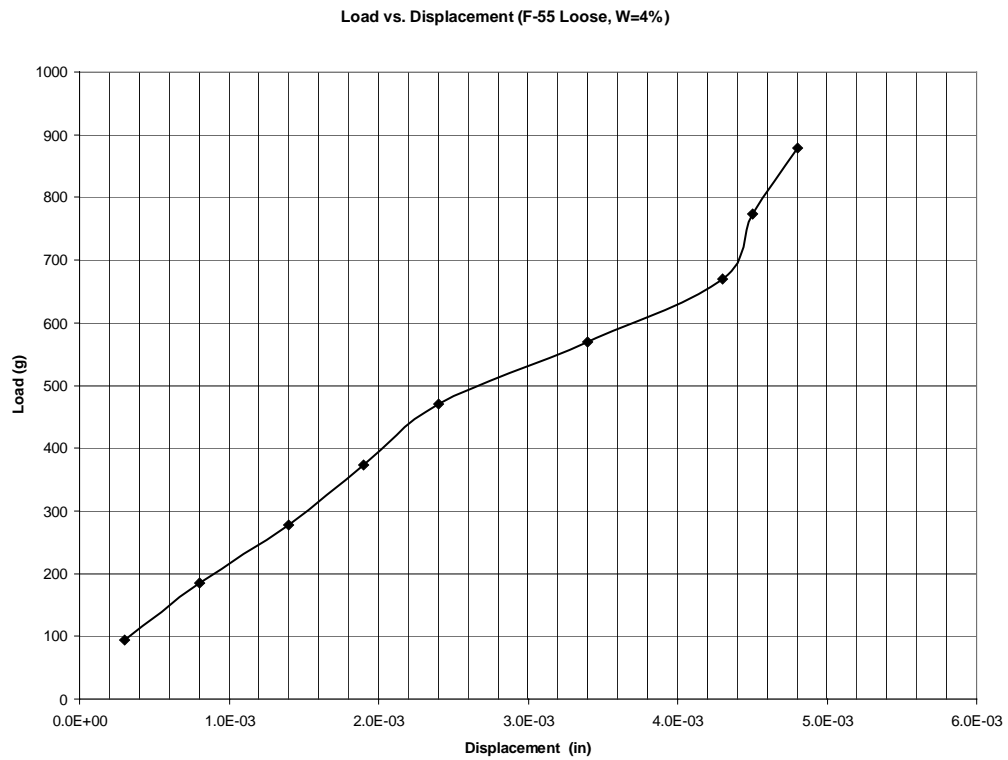
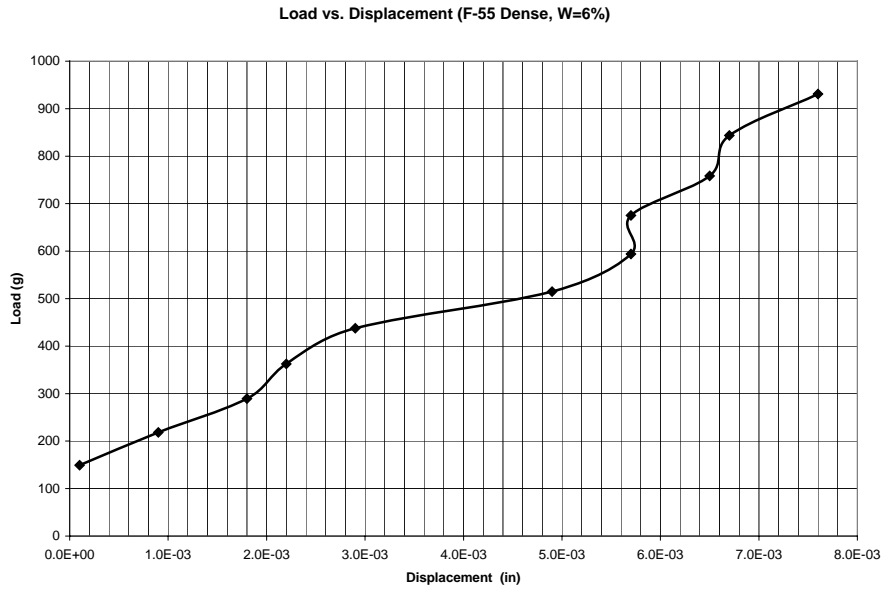**Figure B. 3:** *Load as a function of displacement in a tensile strength test for dense F-75 Ottawa sand (e=0.60 and w=4%)*
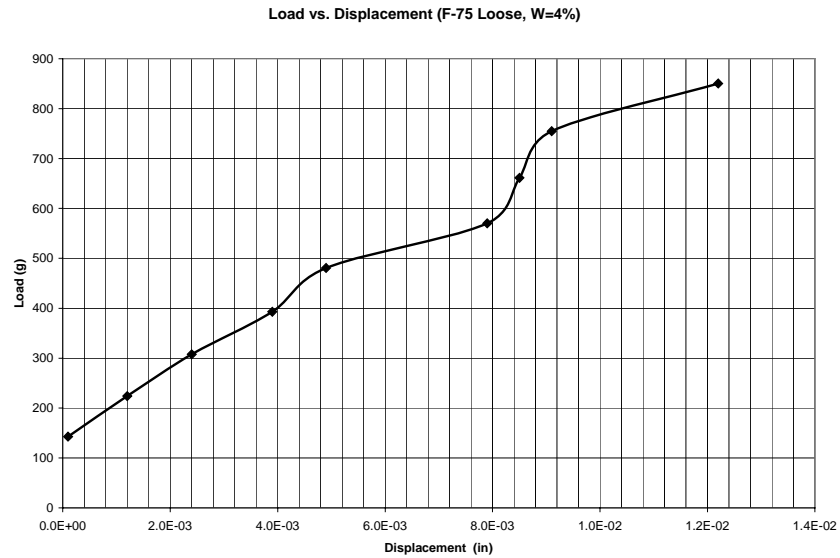
Figure B. 4: *Load as a function of displacement in a tensile strength test for loose F-75 Ottawa sand (e=0.75 and w=4%)*
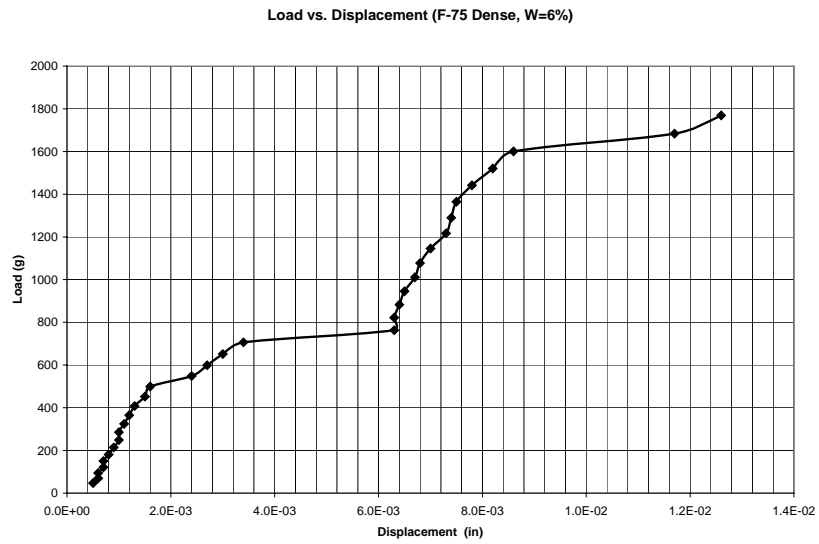
Figure B. 5: *Load as a function of displacement in a tensile strength test for dense F-75 Ottawa sand (e=0.60 and w=6%)*
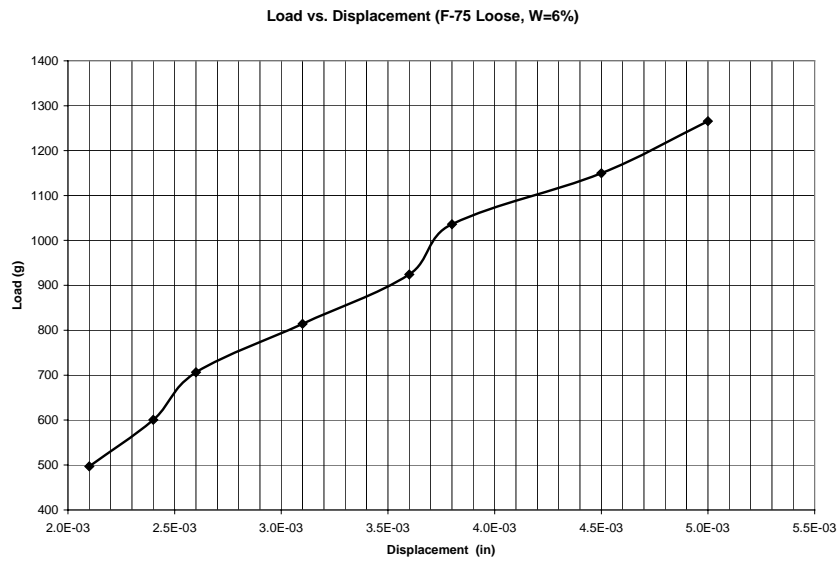
Figure B. 6: *Load as a function of displacement in a tensile strength test for loose F-75 Ottawa sand (e=0.75 and w=6%)*
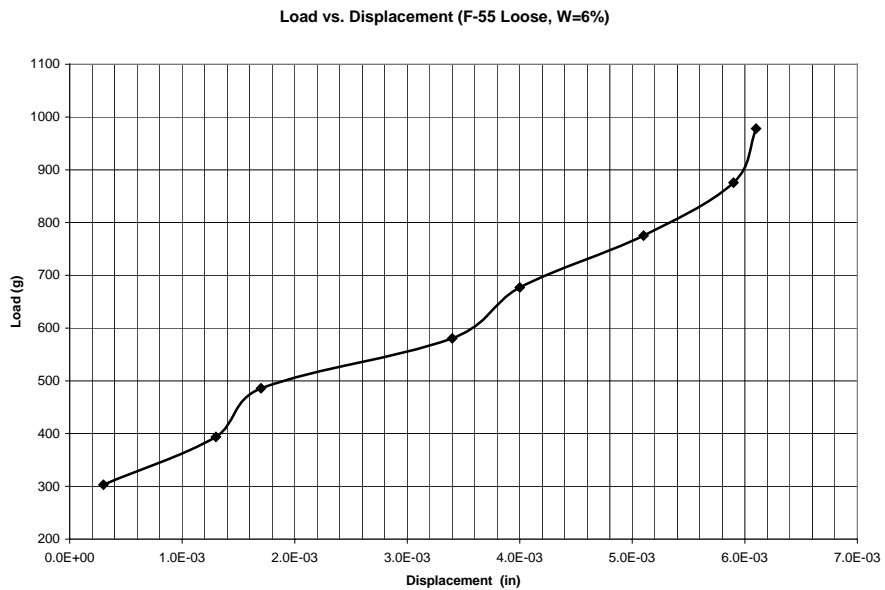
- 188 -
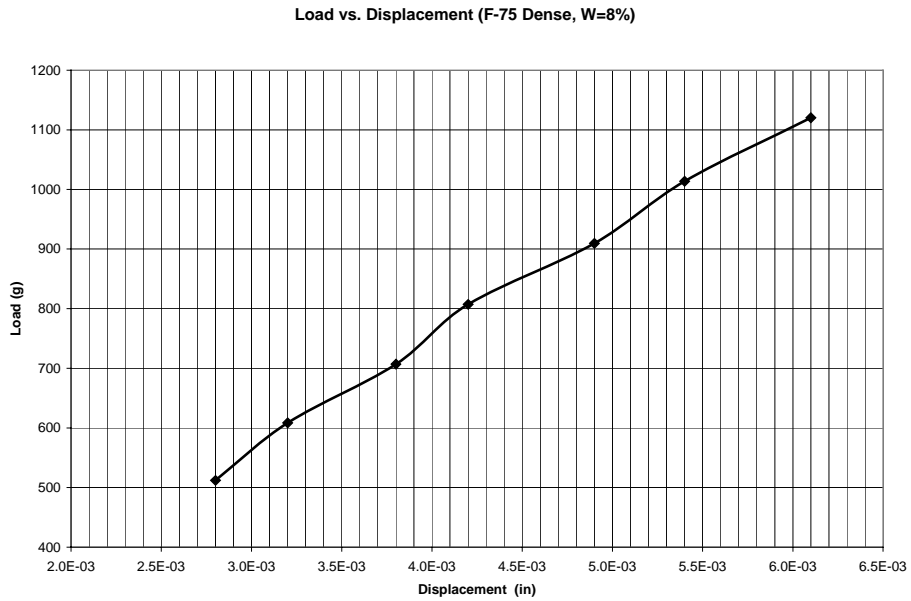
Figure B. 7: *Load as a function of displacement in a tensile strength test for dense F-75 Ottawa sand (e=0.60 and w=8%)*
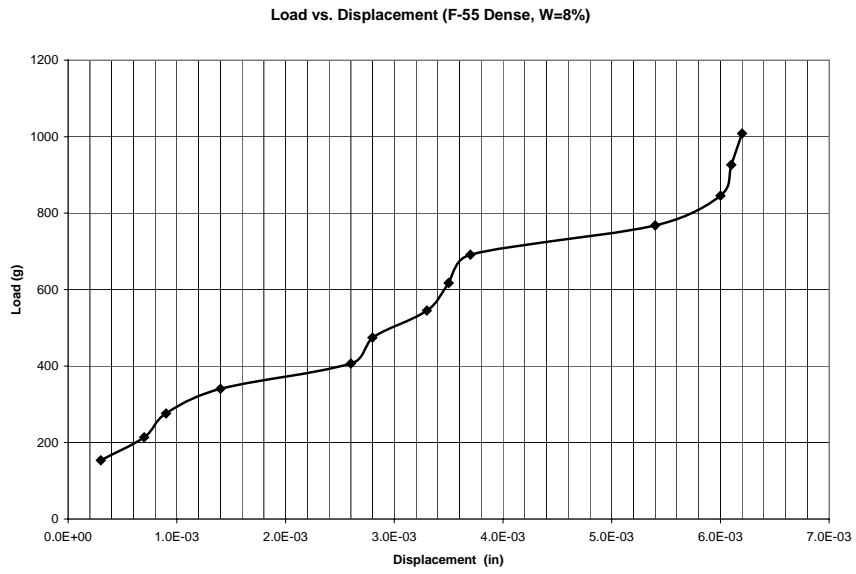

Figure B. 8: *Load as a function of displacement in a tensile strength test for loose F-75 Ottawa sand (e=0.75 and w=8%)*

Load vs. Displacement (F-75 Dense, W=10%)
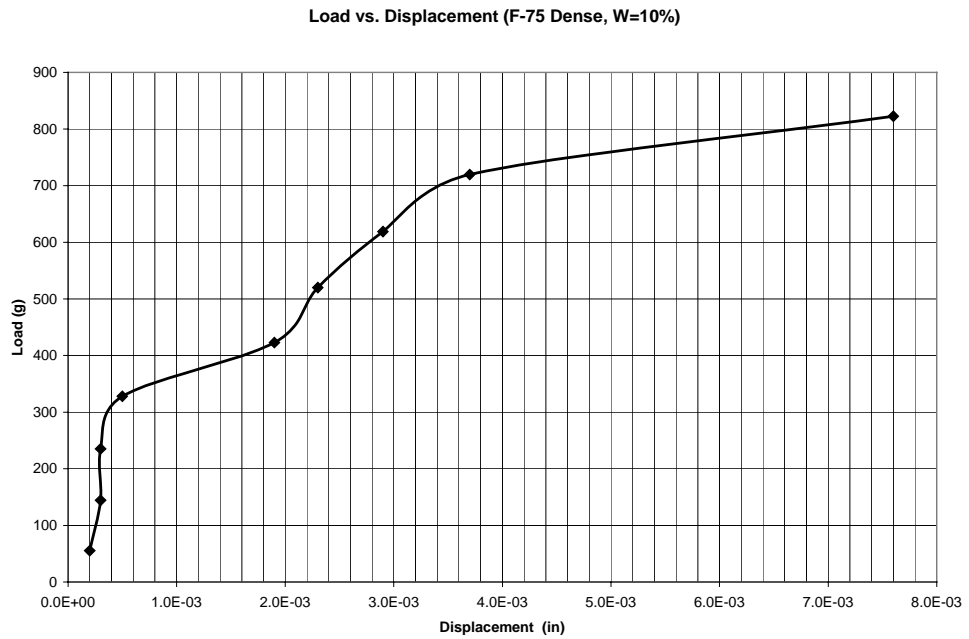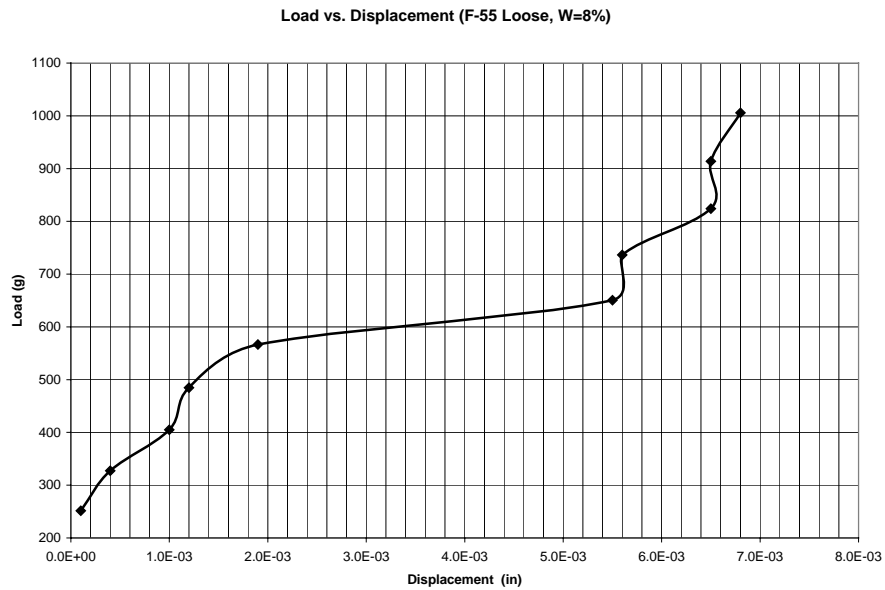

Figure B. 9: *Load as a function of displacement in a tensile strength test for dense F-75 Ottawa sand (e=0.60 and w=10%)*

Load vs. Displacement (F-75 Loose, W=10%)

Figure B. 10: *Load as a function of displacement in a tensile strength test for loose F-75 Ottawa sand (e=0.75 and w=10%)*

Load vs. Displacement (F-75 Dense, W=12%)
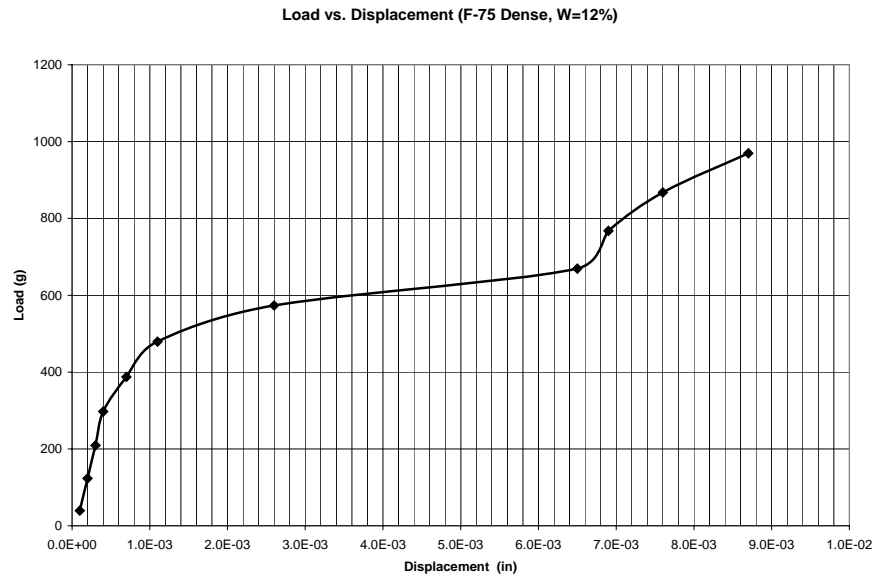
Figure B. 11: *Load as a function of displacement in a tensile strength test for dense F-75 Ottawa sand (e=0.60 and w=12%)*
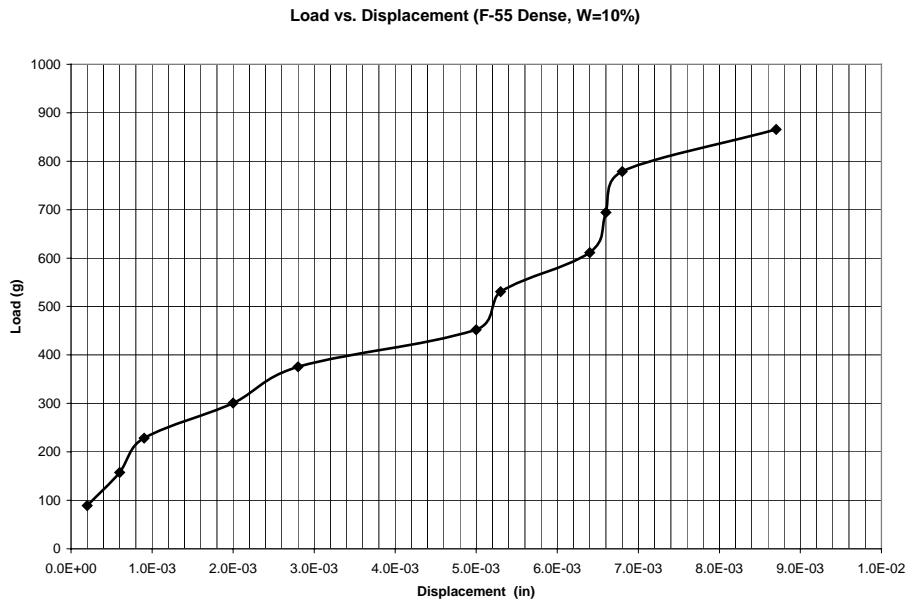
Load vs. Displacement (F-75 Loose, W=12%)

Figure B. 12: *Load as a function of displacement in a tensile strength test for loose F-75 Ottawa sand (e=0.75 and w=12%)*
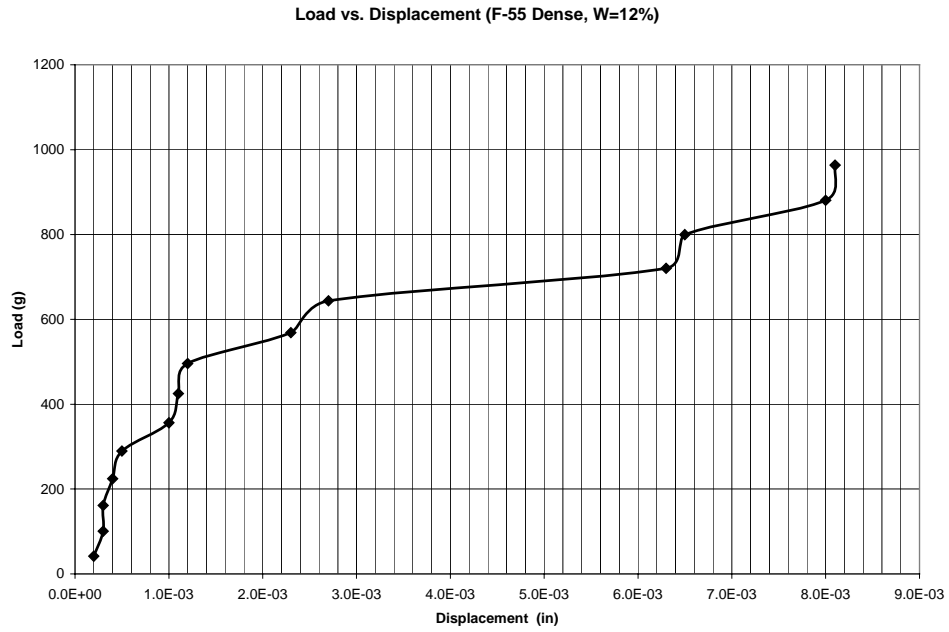
- 191 -

Figure B. 13: *Load as a function of displacement in a tensile strength test for dense F-75 Ottawa sand (e=0.60 and w=15%)*
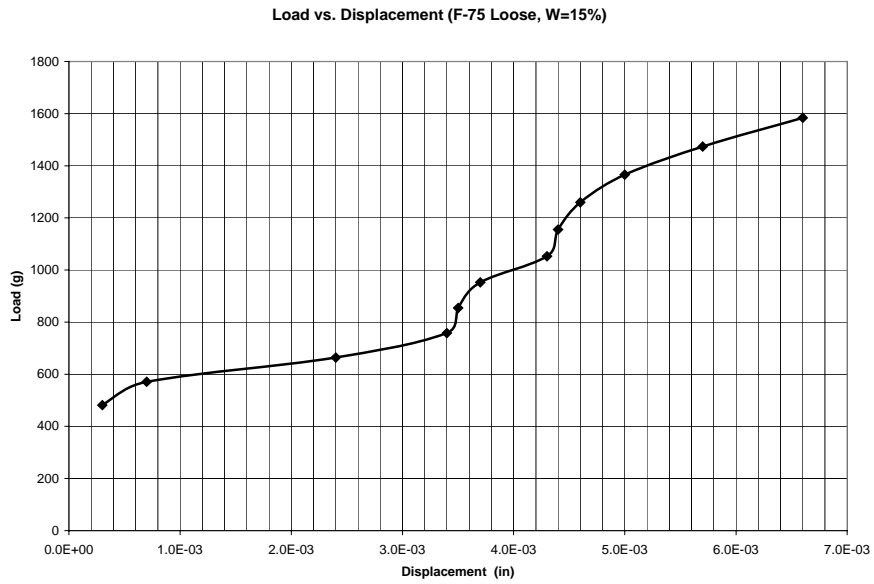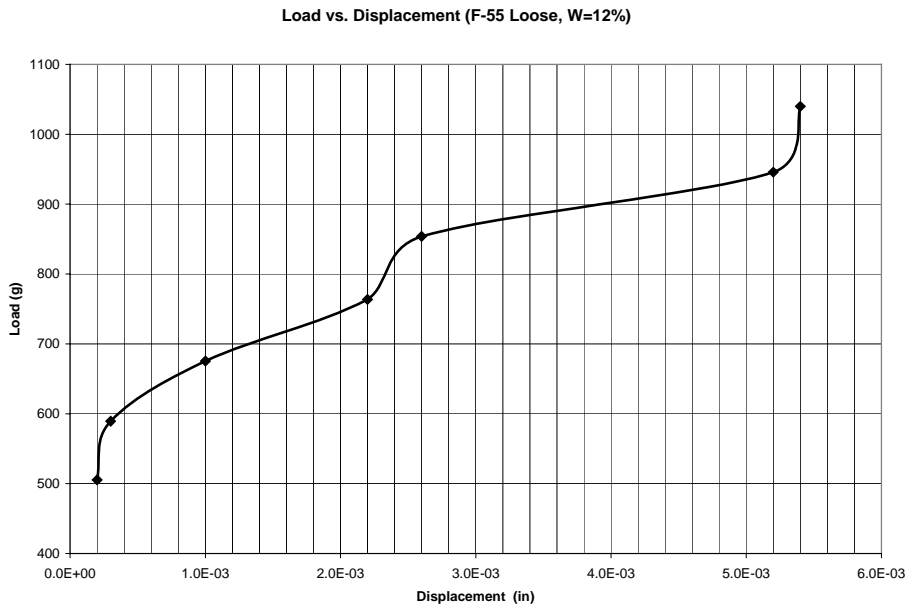

Figure B. 14: *Load as a function of displacement in a tensile strength test for loose F-75 Ottawa sand (e=0.75 and w=15%)*
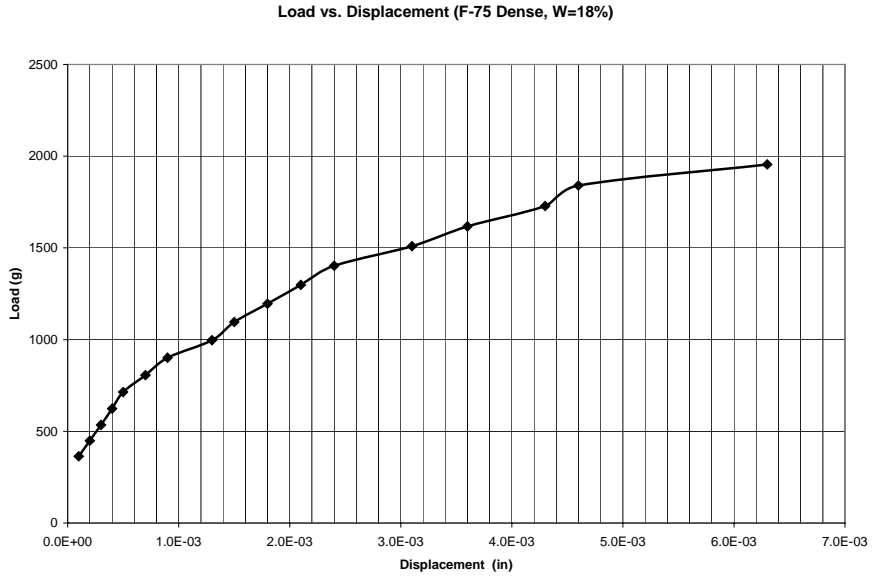
Figure B. 15: *Load as a function of displacement in a tensile strength test for dense F-75 Ottawa sand (e=0.60 and w=18%)*

Figure B. 16: *Load as a function of displacement in a tensile strength test for loose F-75 Ottawa sand (e=0.75 and w=18%)*
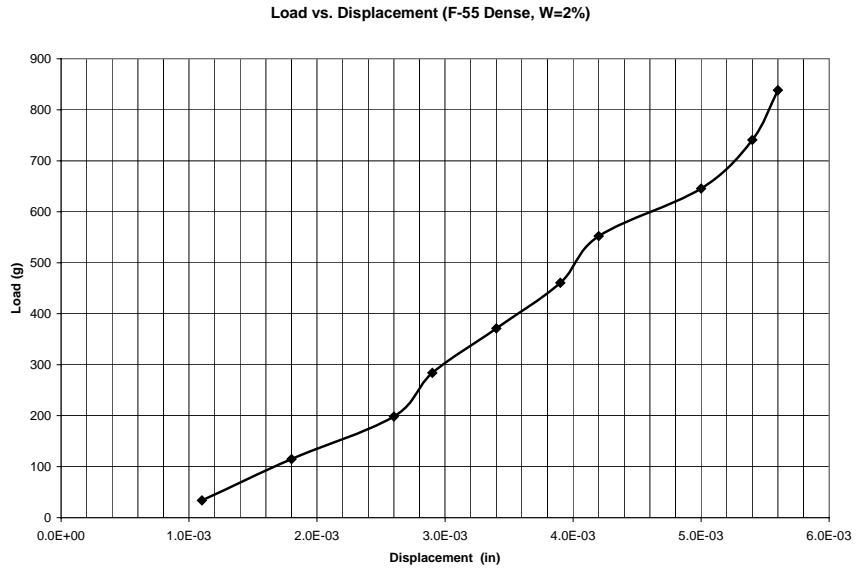
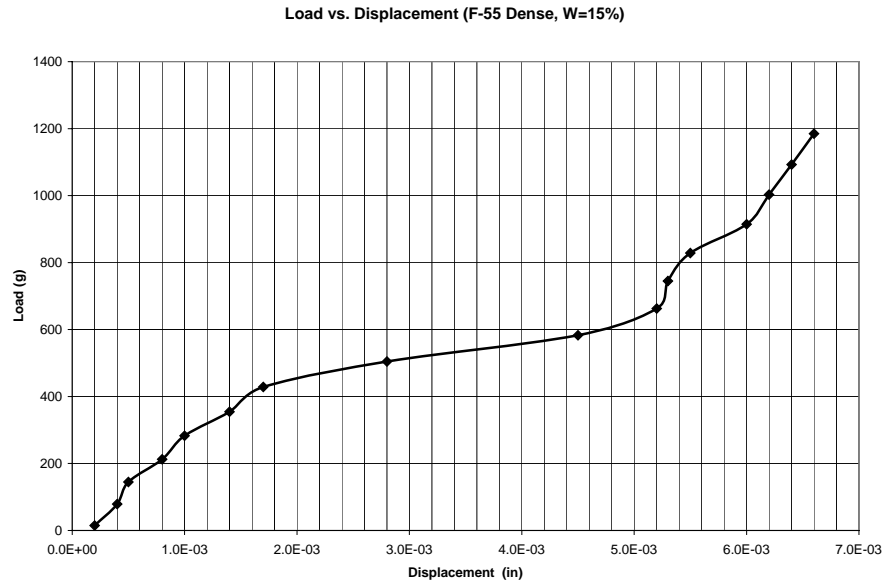**Figure B. 17:** *Load as a function of displacement in a tensile strength test for dense F-55 Ottawa sand (e=0.60 and w=2%)*
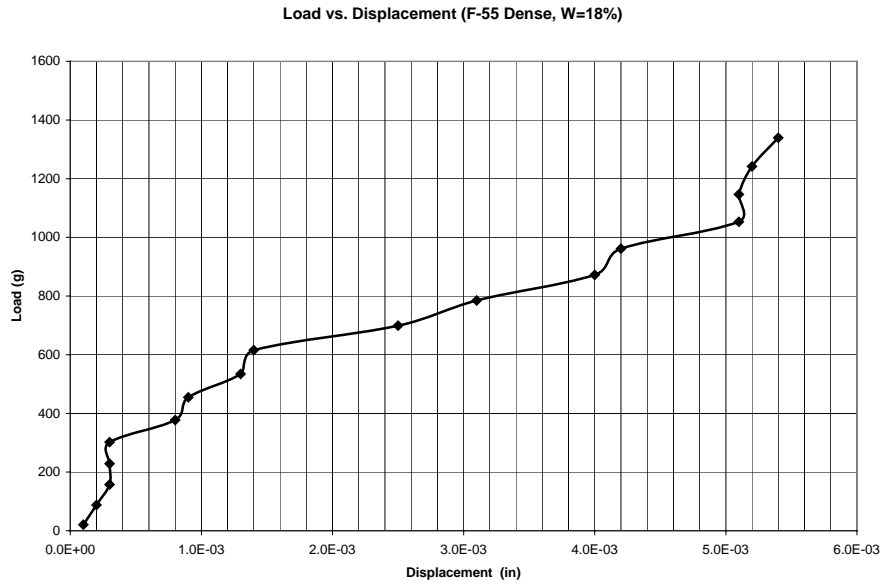

Figure B. 18: *Load as a function of displacement in a tensile strength test for loose F-55 Ottawa sand (e=0.75 and w=2%)*

Figure B. 19: *Load as a function of displacement in a tensile strength test for dense F-55 Ottawa sand (e=0.60 and w=4%)*

Figure B. 20: *Load as a function of displacement in a tensile strength test for loose F-55 Ottawa sand (e=0.75 and w=4%)*
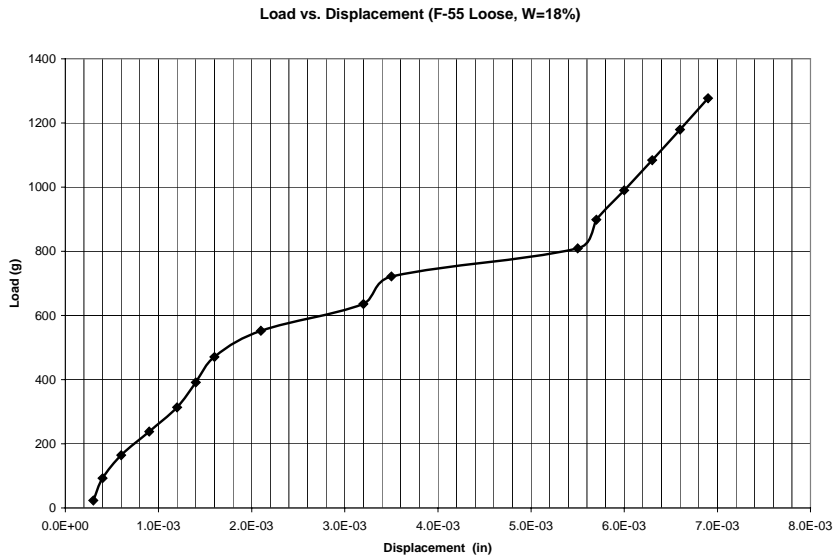
Figure B. 21: *Load as a function of displacement in a tensile strength test for dense F-55 Ottawa sand (e=0.60 and w=6%)*
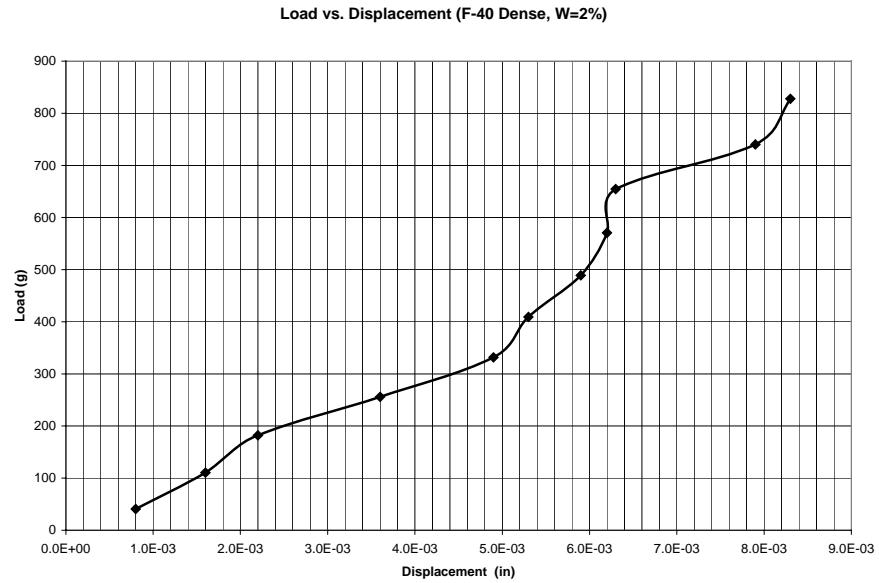

Figure B. 22: *Load as a function of displacement in a tensile strength test for loose F-55 Ottawa sand (e=0.75 and w=6%)*
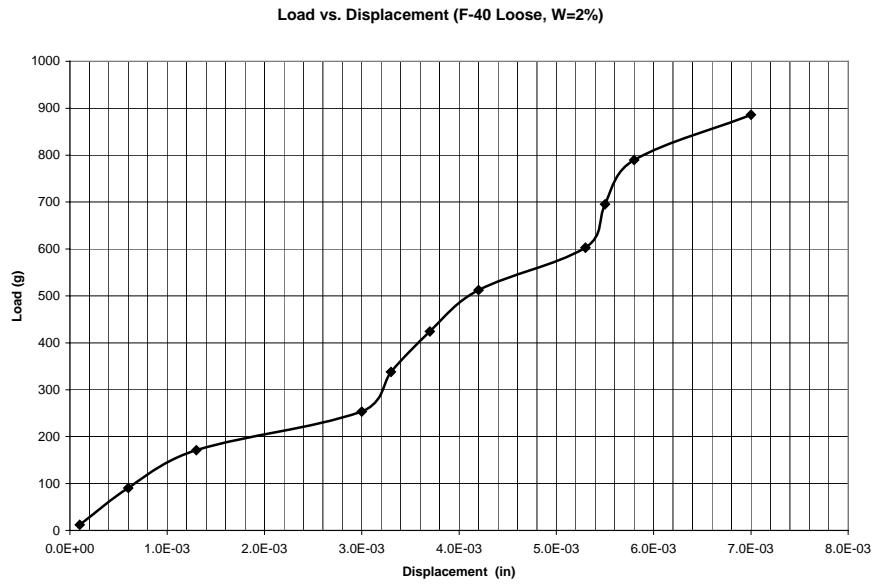
Figure B. 23: *Load as a function of displacement in a tensile strength test for dense F-55 Ottawa sand (e=0.60 and w=8%)*

Figure B. 24: *Load as a function of displacement in a tensile strength test for loose F-55 Ottawa sand (e=0.75 and w=8%)*

Load vs. Displacement (F-55 Dense, W=10%)

Figure B. 25: *Load as a function of displacement in a tensile strength test for dense F-55 Ottawa sand (e=0.60 and w=10%)*

Load vs. Displacement (F-55 Loose, W=10%)
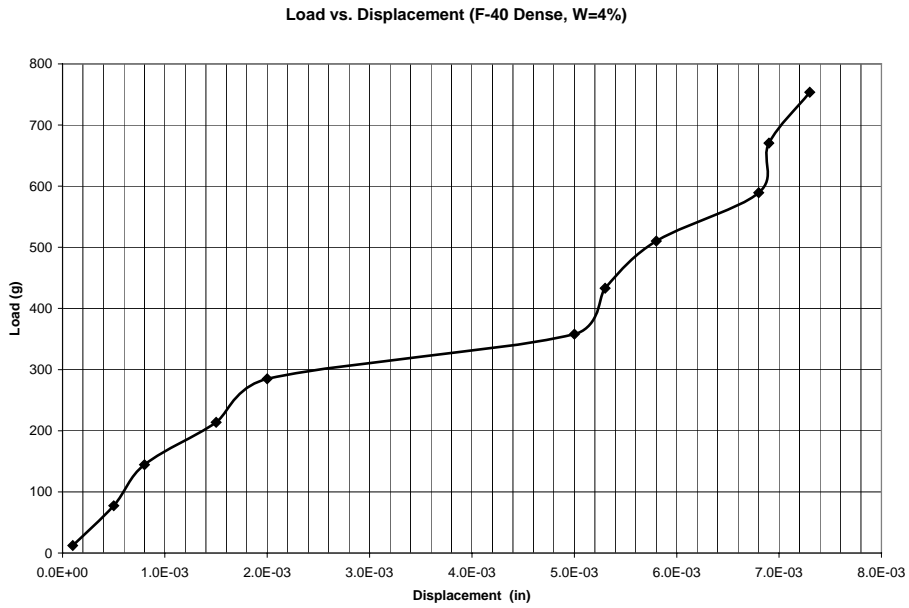

Figure B. 26: *Load as a function of displacement in a tensile strength test for loose F-55 Ottawa sand (e=0.75 and w=10%)*
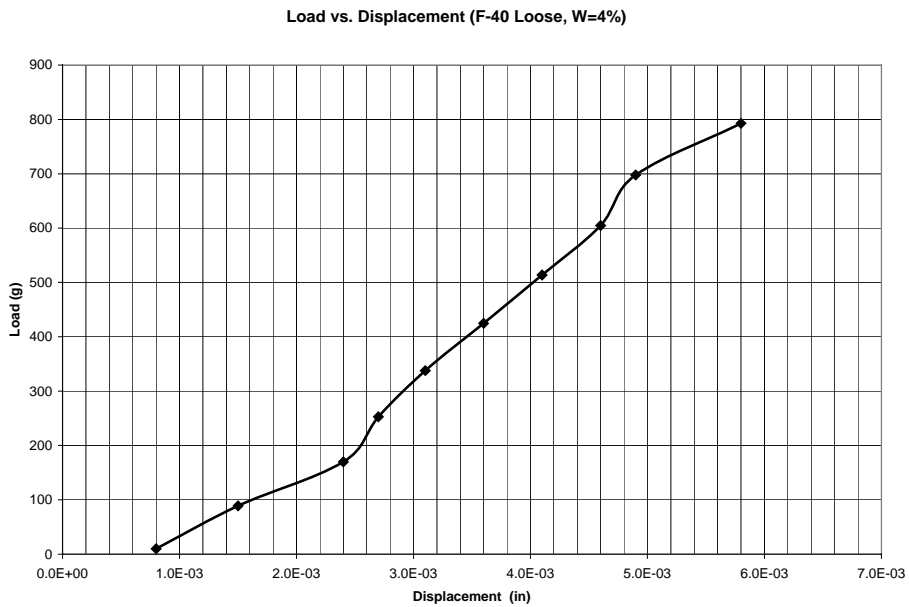
Figure B. 27: *Load as a function of displacement in a tensile strength test for dense F-55 Ottawa sand (e=0.60 and w=12%)*
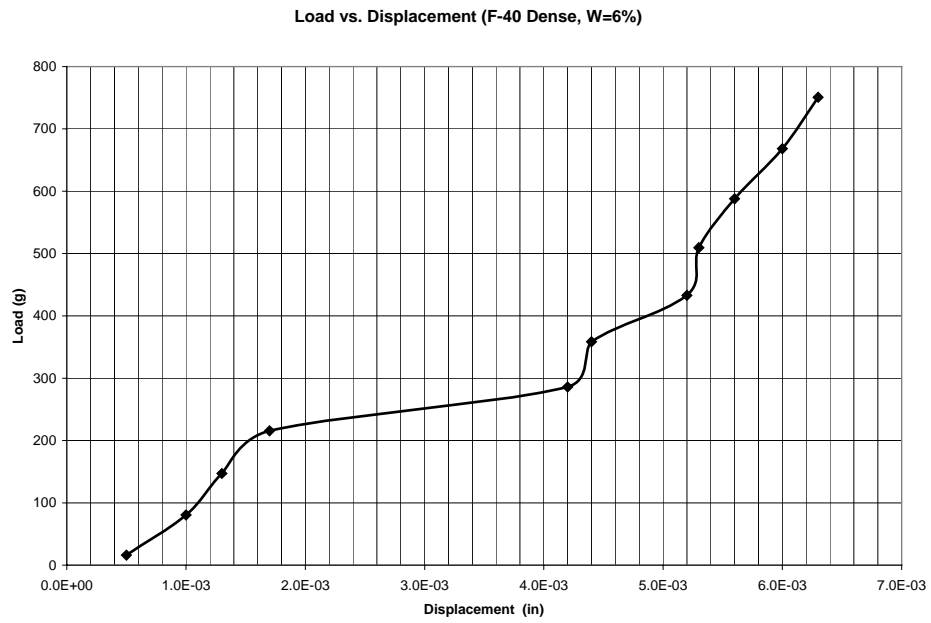

Figure B. 28: *Load as a function of displacement in a tensile strength test for loose F-55 Ottawa sand (e=0.75 and w=12%)*

Figure B. 29: *Load as a function of displacement in a tensile strength test for dense F-55 Ottawa sand (e=0.60 and w=15%)*

Figure B. 30: *Load as a function of displacement in a tensile strength test for loose F-55 Ottawa sand (e=0.75 and w=15%)*
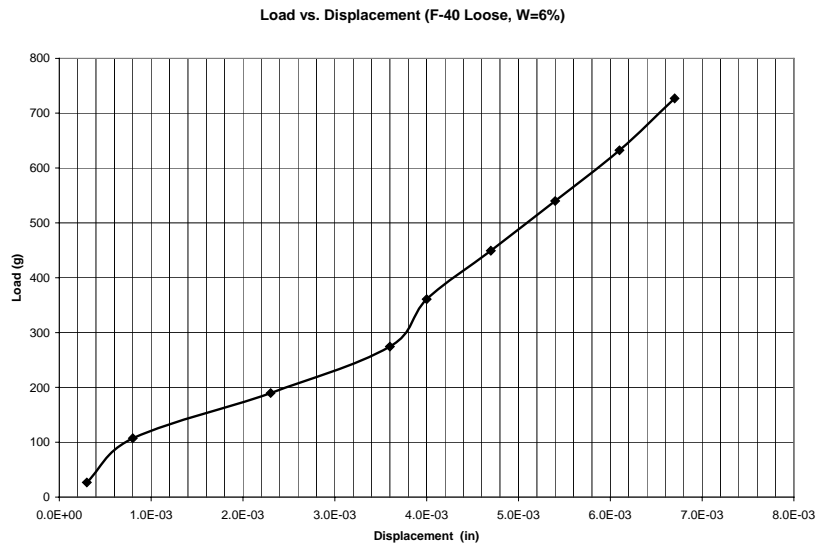
Load vs. Displacement (F-55 Dense, W=18%)

Figure B. 31: *Load as a function of displacement in a tensile strength test for dense F-55 Ottawa sand (e=0.60 and w=18%)*

Load vs. Displacement (F-55 Loose, W=18%)

Figure B. 32: *Load as a function of displacement in a tensile strength test for loose F-55 Ottawa sand (e=0.75 and w=18%)*

Figure B. 33: *Load as a function of displacement in a tensile strength test for dense F-40 Ottawa sand (e=0.60 and w=2%)*

Figure B. 34: *Load as a function of displacement in a tensile strength test for loose F-40 Ottawa sand (e=0.75 and w=2%)*

Figure B. 35: *Load as a function of displacement in a tensile strength test for dense F-40 Ottawa sand (e=0.60 and w=4%)*
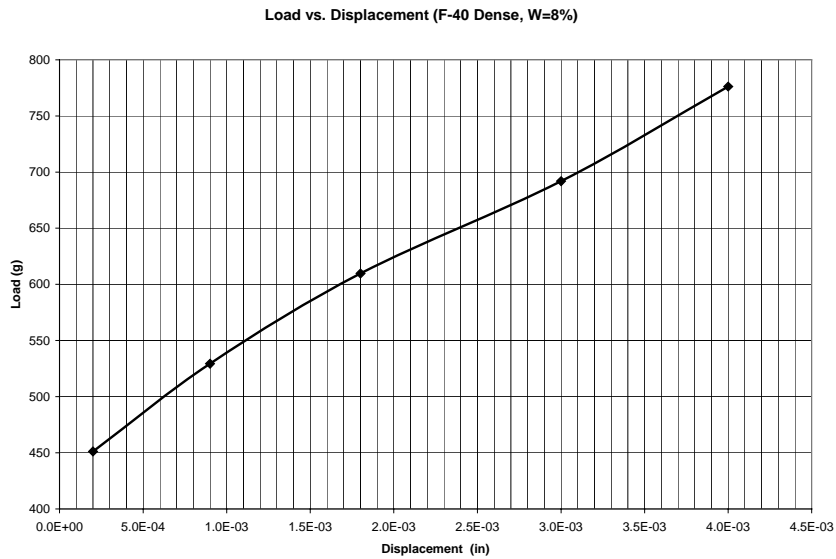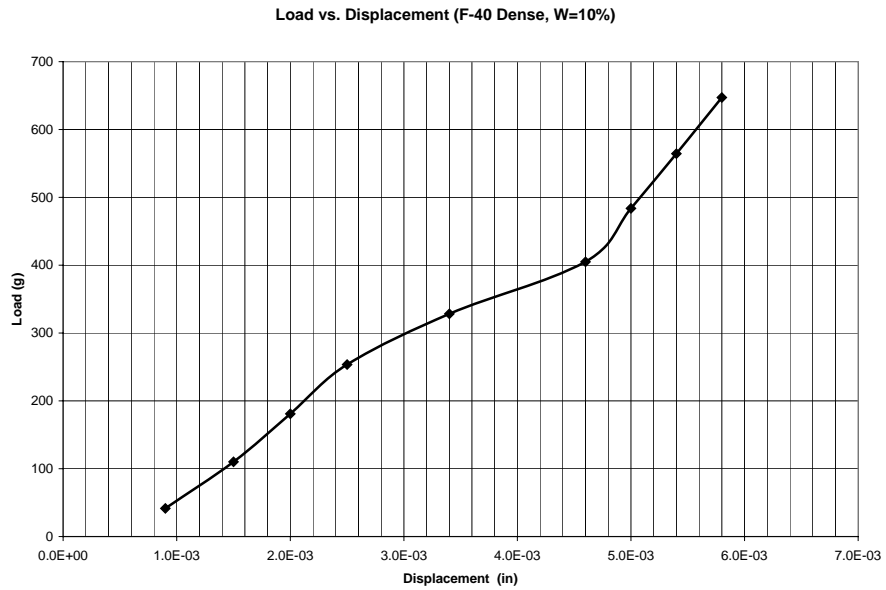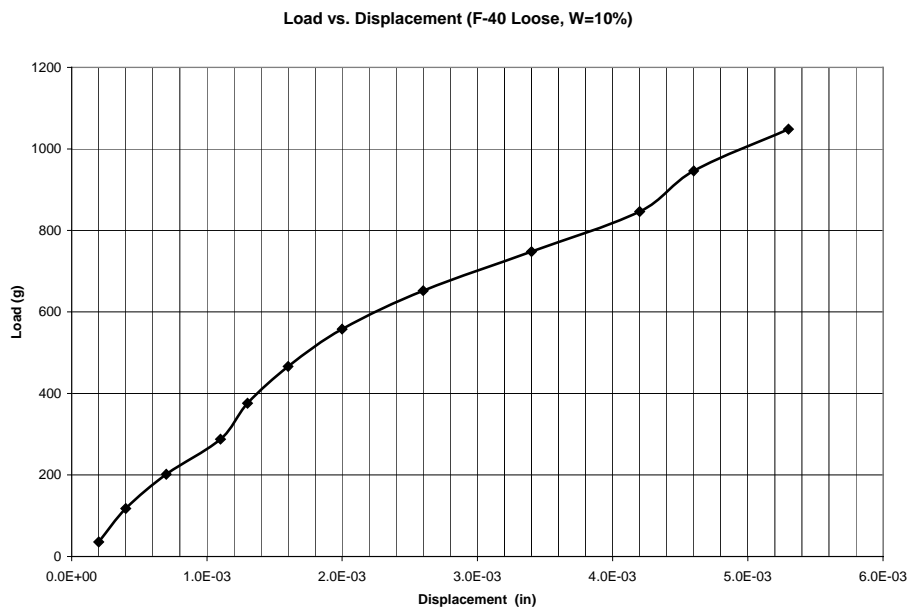

Figure B. 36: *Load as a function of displacement in a tensile strength test for loose F-40 Ottawa sand (e=0.75 and w=4%)*

Figure B. 37: *Load as a function of displacement in a tensile strength test for dense F-40 Ottawa sand (e=0.60 and w=6%)*

Figure B. 38: *Load as a function of displacement in a tensile strength test for loose F-40 Ottawa sand (e=0.75 and w=8%)*
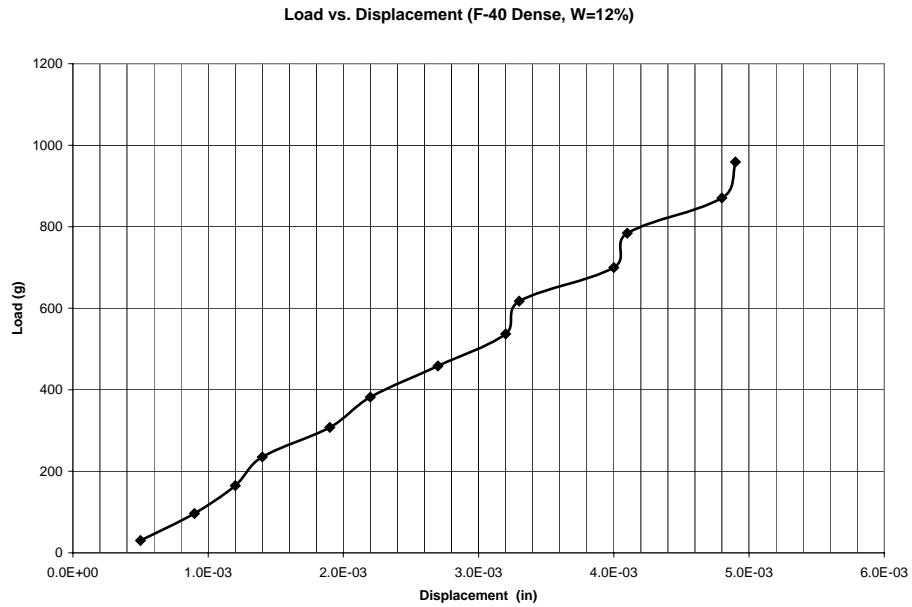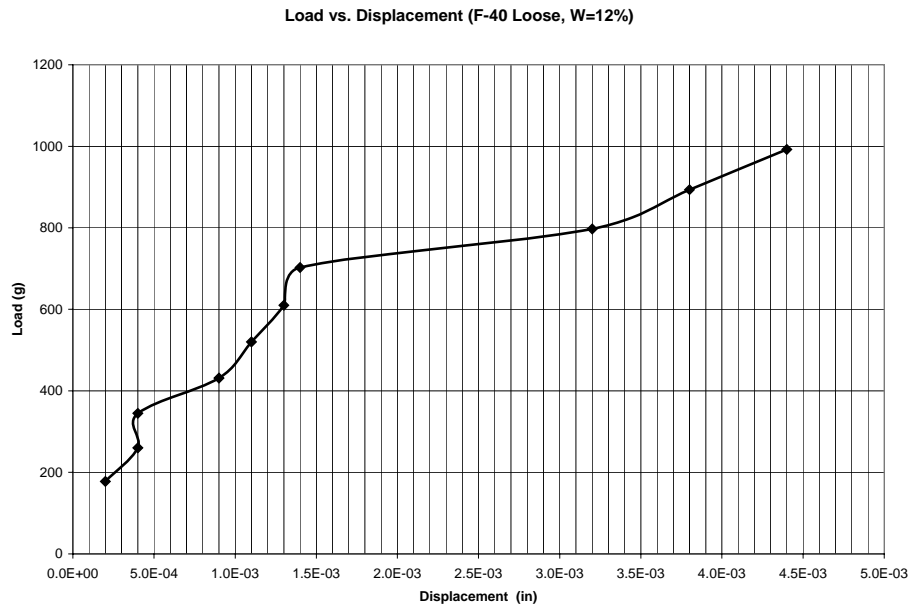
Figure B. 39: *Load as a function of displacement in a tensile strength test for dense F-40 Ottawa sand (e=0.60 and w=8%)*

Figure B. 40: *Load as a function of displacement in a tensile strength test for loose F-40 Ottawa sand (e=0.75 and w=8%)*

Load vs. Displacement (F-40 Dense, W=10%)

Figure B. 41: *Load as a function of displacement in a tensile strength test for dense F-40 Ottawa sand (e=0.60 and w=10%)*

Load vs. Displacement (F-40 Loose, W=10%)

Figure B. 42: *Load as a function of displacement in a tensile strength test for loose F-40 Ottawa sand (e=0.75 and w=10%)*
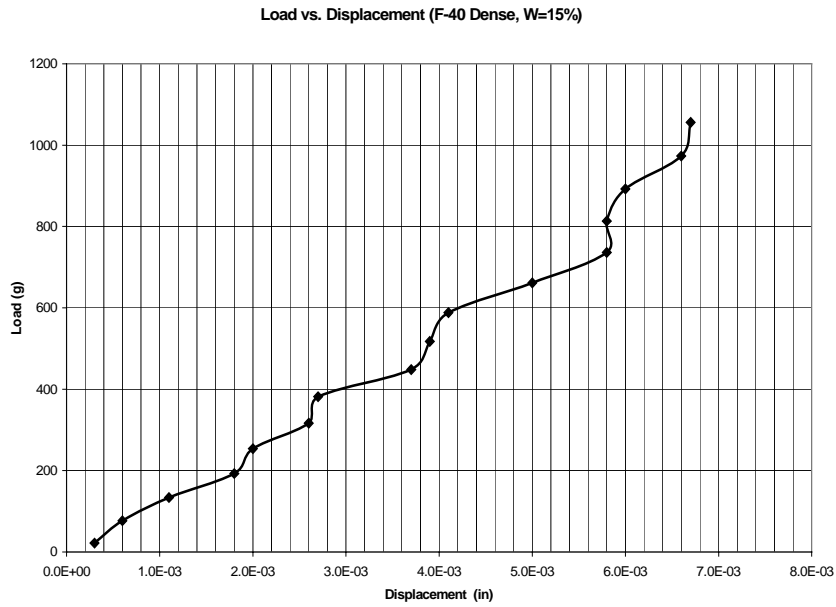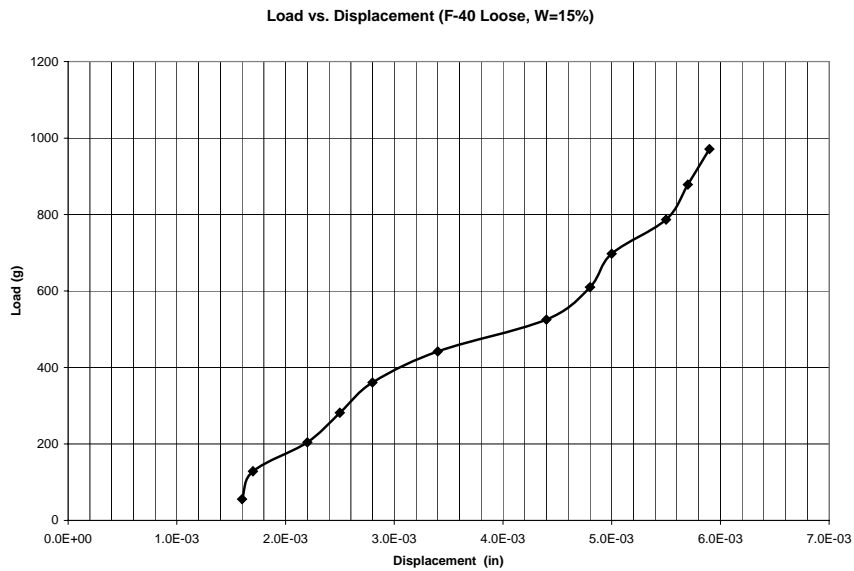
Load vs. Displacement (F-40 Dense, W=12%)

Figure B. 43: *Load as a function of displacement in a tensile strength test for dense F-40 Ottawa sand (e=0.60 and w=12%)*

Load vs. Displacement (F-40 Loose, W=12%)

Figure B. 44: *Load as a function of displacement in a tensile strength test for loose F-40 Ottawa sand (e=0.75 and w=12%)*
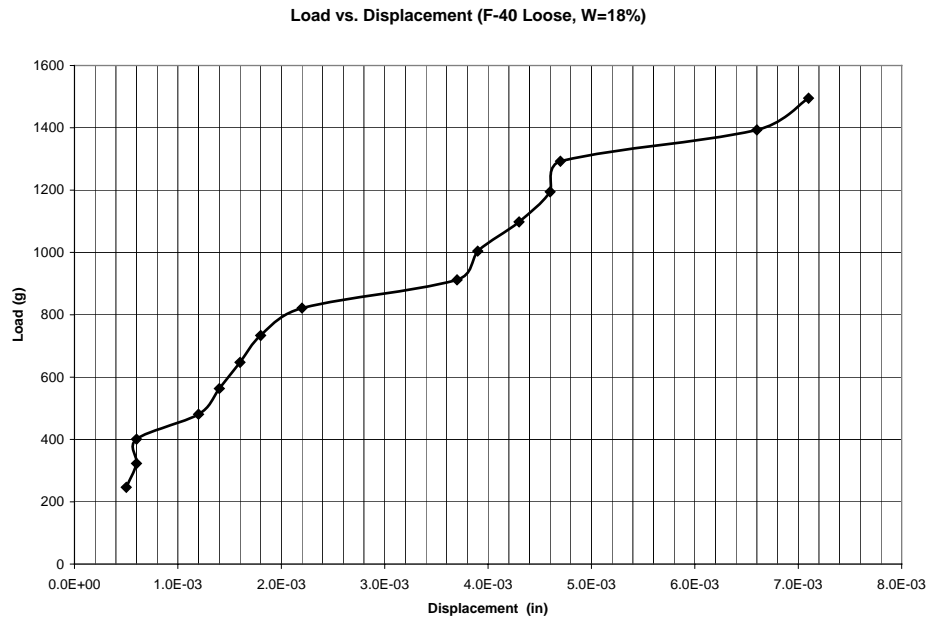
Figure B. 45: *Load as a function of displacement in a tensile strength test for dense F-40 Ottawa sand (e=0.60 and w=15%)*

Figure B. 46: *Load as a function of displacement in a tensile strength test for loose F-40 Ottawa sand (e=0.75 and w=15%)*

Load vs. Displacement (F-40 Dense, W=18%)

Figure B. 47: *Load as a function of displacement in a tensile strength test for dense F-40 Ottawa sand (e=0.60 and w=18%)*

Load vs. Displacement (F-40 Loose, W=18%)
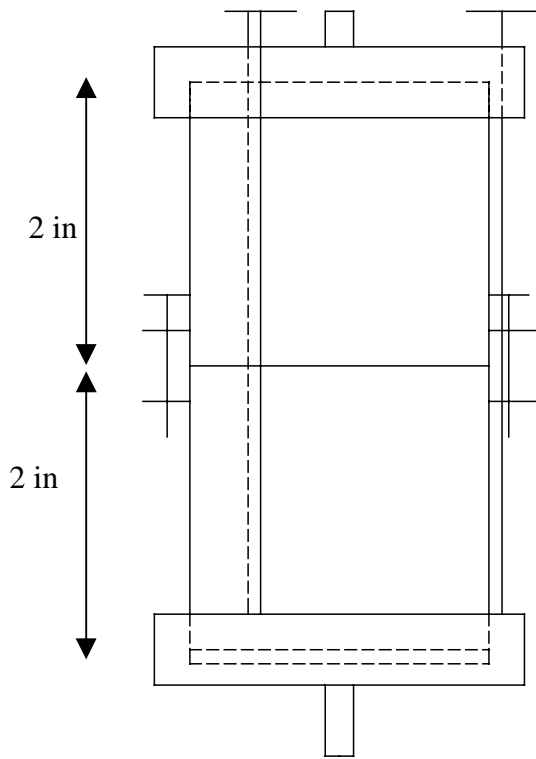

Figure B. 48: *Load as a function of displacement in a tensile strength test for loose F-40 Ottawa sand (e=0.75 and w=18%)*
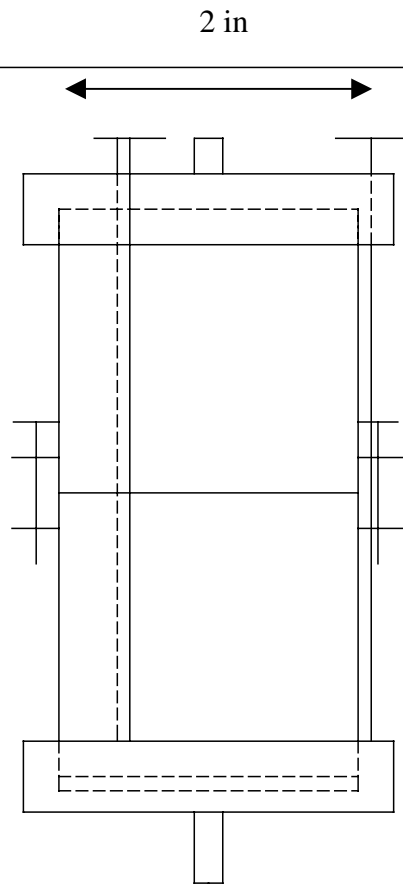
Appendix C:

Suggested Suction Controlled Tensile Strength Test Device

Map View
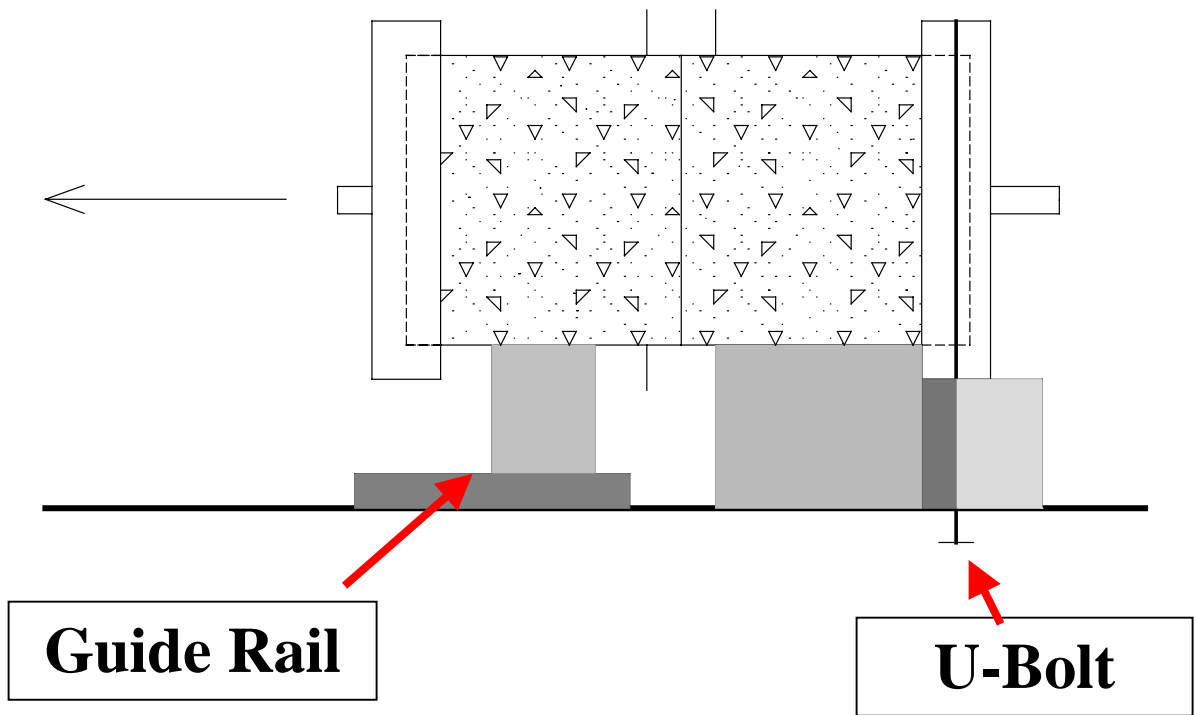
2 in

2 in

2 in
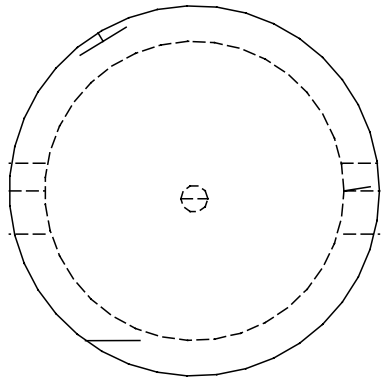
Front View

Side View

Guide Rail

U-Bolt

VITA

Mr. Baltodano Goulding obtained a "Licenciatura" (BSCE) degree in Civil Engineering in 1998 and a Business degree from Costa Rica. Then I worked for the Public Works and Transportation Ministry-Agriculture Ministry-German Technical Cooperation Program (GTZ) agreement at the Technical Support Unit of the Rural Roads Construction and Maintenance Program.

In 2000 he entered the MSCE with emphasis in Geotechnical Engineering Program at the University of Costa Rica. In 2001 he decided to pursue a graduate degree in the USA in Geotechnical Engineering, resulting in a MSCE degree from The University of Kansas in 2002. Then he came to the Geotechnical Engineering Program of the University of Missouri-Columbia to pursue a PhD degree.

He is a register civil engineer and a patent evaluator in Costa Rica and certified as an E.I.T. in the State of California. His experience includes activities such as road construction management, research (GRA) in the Transportation Engineering and Geotechnical Engineering Fields, public works quality assurance inspector, college instructor, community training.